A FRAMEWORK FOR MULTI-PLATFORM ANALYTICAL AND EXPERIMENTAL SIMULATIONS OF REINFORCED CONCRETE STRUCTURES

by

Vahid Sadeghian

A thesis submitted in conformity with the requirements
for the degree of Doctor of Philosophy

Graduate Department of Civil Engineering
University of Toronto

A FRAMEWORK FOR MULTI-PLATFORM ANALYTICAL AND EXPERIMENTAL SIMULATIONS OF REINFORCED CONCRETE STRUCTURES

Vahid Sadeghian

Degree of Doctor of Philosophy

Graduate Department of Civil Engineering

University of Toronto

2017

Abstract

This study presents a framework for multi-platform analysis and hybrid (experimental-analytical) simulation of reinforced concrete structures. In this approach, each potentially critical member, based on its mechanical characteristics, is modelled using the most suitable finite element analysis tool or is represented with a test specimen, while the rest of the structure is modelled with computationally fast global analysis software. The interaction between substructure modules is fully considered by satisfying compatibility and equilibrium requirements. The framework is based on object-oriented methodology and uses a standardized data exchange format, facilitating addition of new analysis tools or test equipment. The effectiveness of the framework is evaluated by several verification examples including analysis of structures repaired with fibre-reinforced polymer sheets. The multi-platform analysis computes the behaviour of structures with a level of accuracy that was previously difficult to achieve with most single-platform analysis software.

In addition, a new interface element, named F2M, is introduced to connect layered beam elements to membrane elements. Compared to existing methods, the F2M element provides more realistic stress distributions and allows for transverse expansion at the connection section between substructures. The accuracy of the proposed element is verified through mixed-dimensional modelling of a series of beam specimens presented in the literature.

A small-scale experimental program was conducted using a six degree-of-freedom hydraulic testing equipment to verify the hybrid simulation framework and provide additional data for small-scale testing of shear-critical reinforced concrete frames. The physical models were 1/3.23-scale representations of a beam and two columns. A multi-platform modelling technique was employed to analyze the remainder of the frames. The hybrid simulation results were compared against those obtained from a similar large-scale test and finite element analyses. The study found that, with proper precautions, small-scale hybrid testing can sufficiently well simulate the behaviour of shear-critical frames. However, to draw general conclusions, additional test data are required.

ACKNOWLEDGEMENTS

Firstly, I would like to express my sincere gratitude to my supervisors, Professor Frank J. Vecchio and Professor Oh-Sung Kwon, for their incredible support and advice over the course of my studies at the University of Toronto. Their guidance has not only helped me to think rationally about research problems, but has taught me invaluable lessons to carry on in my professional life.

I would like to thank all my advisory committee members: Professor Evan C. Bentz, Professor Oya Mercan, and Professor Daniel A. Kuchma for their thorough review of this thesis. Their valuable feedbacks and recommendations are gratefully acknowledged.

I would like to acknowledge the generous financial support provided for this research project by IC-IMPACTS, S-FRAME Inc., the Department of Civil Engineering at the University of Toronto, and my supervisors.

Also, I would like to express my appreciation to my friends and colleagues who have made this an enjoyable journey and supported me: Farhad Habibi, Arsalan Tavassoli, Arjang Tavassoli, Serhan Guner, Trevor D. Hrynyk, Fady ElMohandes, Seong-Cheol Lee, Andac Lulec, Anca Jurcut, Raymond Ma, Xu Huang, Stamatina Chasioti, Siavash Habibi, Mark Hunter, and Isojeh Benard.

Lastly and most importantly, I would like to give my heartfelt thanks to my parents and my brother for their unconditional support, help, and encouragement.

TABLE OF CONTENTS

CHAPTER 5: EXPERIMENTAL INVESTIGATION OF RC STRUCTURES USING SMALL-SCALE MULTI-AXIAL HYBRID SIMULATION

CHAPTER 6: SUMMARY, CONCLUSIONS AND RECOMMENDATIONS

LIST OF FIGURES

CHAPTER 3: MODELLING BEAM-MEMBRANE INTERFACE IN REINFORCED CONCRETE MEMBERS

CHAPTER 5: EXPERIMENTAL INVESTIGATION OF RC STRUCTURES USING SMALL-SCALE MULTI-AXIAL HYBRID SIMULATION

APPENDIX B

LIST OF TABLES

CHAPTER 5: EXPERIMENTAL INVESTIGATION OF RC STRUCTURES USING SMALL-SCALE MULTI-AXIAL HYBRID SIMULATION

APPEDNIX A

CHAPTER 1

INTRODUCTION

1.1 Background

Over the past few decades, significant progress has been made with respect to nonlinear analysis of reinforced concrete (RC) structures. These advancements have been mainly attributed to the great amount of research dedicated to constitutive modelling of reinforced concrete behaviour and development of sophisticated analysis procedures. A good measure of this progress is in the results of competitions conducted for predicting the response of experimental tests. Some examples are the prediction competitions involving panels tested at the University of Toronto (Collins et al., 1985), a large-scale shear wall tested by the Nuclear Power Engineering Corporation of Japan (1996), and more recently an informal competition organized by the ACI/ASCE Committee 447 focusing on a series of large-scale columns tested at the University of California at San Diego. Comparisons of the results clearly show that the ability to accurately model nonlinear behaviour of reinforced concrete has been substantially improved over the last 30 years.

With advancements in computing technology, nonlinear analysis procedures were implemented in various types of structural software with high-performance solvers, expanding the size and complexity of the problems that can be analyzed. Bentz (2000) investigated the influence of computing power growth on the analysis performance of a prestressed T-beam modelled with layered beam elements. Based on the analyses conducted on different types of central processing units (CPUs) developed from 1975 to 2000, it was found that the computing speed increased by five orders of magnitude over the span of 25 years.

Despite the great improvements in nonlinear analysis methods and computing technology, because of the complex behaviour of cracked reinforced concrete, there is no analysis software that can perform well for all types of structures and loading conditions. Each structural software has its own advantages and disadvantages and is only suitable for certain types of problems. Applications of reinforced concrete analysis tools can be different based on their analysis procedure (e.g., frame-type methods and finite element methods), crack representation method (e.g., smeared crack models and discrete crack models), and capabilities such as modelling repaired members or extreme loading conditions (e.g., blast and fire). In addition, some analysis software are limited in terms of material behaviour models (e.g., empirical models and fracture mechanics models) or element library (e.g., 2D elements and 3D elements).

For example, frame-type analysis methods are computationally fast and applicable to large structural systems. However, due to their simplified formulations, these methods may not be suitable for the analysis of structures with complex behaviour. Guner and Vecchio (2010b) used three nonlinear frame-type programs for the analysis of a clinker preheater tower built in Central America; namely, SAP2000 (CSI, 2005), RUAUMOKO (Carr, 2005), and VecTor5 (Guner and Vecchio, 2010a). To account for nonlinear behaviour, the first two programs used the lumped plasticity approach, while the third program was based on the distributed plasticity method. The analysis results showed large discrepancies in terms of the predicted failure mode and ductility, which were mainly attributed to difficulties in capturing shear behaviour. Compared to frame-type analysis procedures, finite element analysis methods are able to capture the nonlinear behaviour of complex structures with better accuracy. However, due to the high computational cost of their analysis procedure, these methods are mostly limited to component-level modelling. For example, with VecTor4, which is a nonlinear finite element program for shell structures, the dynamic analysis of a quarter slab modelled with 65 nine-noded shell elements can take about 75 hours for 2000 time steps using a desktop computer with the Intel Core 2 processor (Hrynyk and Vecchio, 2013).

Today, as reinforced concrete infrastructure around the world ages, many structures are reaching their design lifespan and are becoming in dire need of repair (FHWA, 2014). However, the nonlinear analysis of deficient or repaired structures poses several challenges. At the component-level, analyzing damage effects and mechanisms related to the externally attached repaired component requires finely detailed finite element models. At the system-level, force redistribution due to stiffness changes between different components can affect the response of the repaired member, especially when the structure experienced damage prior to retrofitting. Most of the existing studies are only conducted at the component-level due to the computational time and memory storage limitations of local analysis tools, neglecting the system-level behaviour. For a comprehensive analysis of such structures, a combination of two or more structural analysis programs is needed.

In addition to unique applications of different structural analysis tools, there are situations where the behaviour of a structure can be influenced by the surrounding soils and therefore a soil-structure interaction analysis is required. However, most structural programs do not have advanced soil modelling capabilities and geotechnical software cannot accurately model structural behaviour. Therefore, for accurate and practical analysis of large structures with complex behaviour or modelling multi-disciplinary systems, more advanced simulation methods are required.

1.2 Research Motivation

For many years, researchers employed the substructuring technique to develop methods which either improved the computational performance or increased modelling capabilities by combining different types of elements or analysis tools. Three types of commonly used methods are: global-local analysis methods, parallel computing methods, and mixed-dimensional methods. Although these techniques significantly improved the analysis accuracy of large complex structural systems, they have certain limitations. Global-local methods cannot fully capture the interaction between the substructures nor completely satisfy equilibrium requirements. Parallel computing methods, for complex systems with several substructures, require substantial amounts of computing resources which may not be available in a typical engineering design office. Mixed-dimensional methods, which involve combining different types of elements, are mostly used for linear elastic problems and are limited to single-platform analysis. The strengths and weaknesses of each method are discussed in detail in Section 2.2 of Chapter 2.

In recent years, several studies attempted to extend mixed-dimensional modelling to multi-platform simulation by combining global analysis software with local analysis tools or test specimens in a concurrent manner. In this approach, each potentially critical member, based on its mechanical characteristics, is modelled using the most suitable finite element analysis tool or is represented with a physical specimen, while the rest of the structure is modelled with a computationally fast global analysis software. The interface between numerical models is simulated using proper mixed-dimensional element coupling methods. An integrated simulation procedure is used to take into account the interaction between different modules and to satisfy compatibility and equilibrium requirements. Data are exchanged between the modules through network communication.

However, most of the published multi-platform studies have focused on hybrid simulation, which entails combining numerical models with physical specimens. The main objective of these studies was to provide a flexible testing module and little effort was made to extend the capabilities of the numerical module. A few studies that attempted to integrate different analysis tools have one or more of the following deficiencies: 1) limited to numerical simulation and not applicable to hybrid simulation, 2) only compatible with in-house programs and not applicable to other analysis tools, and 3) require high amounts of communication data and therefore not applicable to large structural systems. In addition, none of the existing studies specifically investigated the application of multi-platform analysis to reinforced concrete structures. Advanced reinforced concrete analysis tools use different types of solution schemes to compute the nonlinear response of a structure. To preform multi-platform simulation, integration of these solution schemes should be investigated.

1.3 Study Scope and Objectives

This research study was carried out in two phases: the analytical phase and the experimental phase.

The main objectives of the analytical phase can be stated as:

1) Developing a new multi-platform simulation framework which intends to address some of the deficiencies of the previous studies, allowing for a more realistic analysis of complex reinforced concrete structures or multi-disciplinary systems. This research objective had two goals:

I. Integration of the VecTor programs into the simulation framework.
II. Facilitating addition of other analysis tools into the simulation framework.

The specific tasks carried out for this objective were:

- Development of the integrated solution algorithm.
- Theoretical investigation of the combined secant-tangent solution scheme.
- Implementation of the modified Newton Raphson procedure into the framework.
- Implementation of three types of communication methods into the framework.
- Development of the graphical user interface for the simulation framework.
- Implementation of the communication methods and static condensation functions in the VecTor programs.
- Further development of the graphical user interface of the VecTor programs to accommodate multi-platform modelling.
- Implementation of the UTNP standardized data exchange format (Huang et al., 2015) into the simulation framework enabling communication with the interface program NICA (Kwon et al., 2008).
- Evaluating the computational performance of the simulation framework.
- Verification of the integration of the VecTor programs through multi-platform analysis of two experimental case studies reported in the literature.
- Verification of the integration of other analysis programs by multi-platform modelling of a geotechnical-structural system using VecTor2 and OpenSees.

2) Investigating the application of multi-platform analysis to reinforced concrete structures repaired with fibre-reinforced polymer (FRP) sheets. The focus of this objective was on:

- Investigation of the mechanisms influencing the component-level behaviour of FRP-confined RC members.
- Performance assessment of the multi-platform analysis of two experimental case studies reported in the literature.

3) Developing a new beam-membrane interface element, specifically formulated for the nonlinear analysis of reinforced concrete structures, eliminating some of the limitations associated with existing mixed-dimensional methods. The required tasks included:

- Identifying deficiencies of the existing mixed-dimensional methods for connecting frame and membrane elements.
- Development of a procedure that addresses the deficiencies of existing methods.
- Verification of the proposed interface element through mixed-dimensional modelling of a series of beam elements with different types of failure modes.
- Comparison of the performance of the proposed interface element against two other commonly used mixed-dimensional methods.

The experimental phase of the research study had two main objectives:

1) Further development of the simulation framework to accommodate hybrid testing. The required tasks included:

- Connecting the simulation framework to a generalized controller interface program, NICON (Zhan and Kwon, 2015), compatible with a wide range of test configurations.
- Modification of NICON to improve its performance and facilitate hybrid testing.
- Assembling a hardware box to provide communication between the actuator controller and NICON.

2) Conducting a small-scale experimental program to verify the hybrid simulation capability of the framework and provide additional samples for small-scale testing of reinforced concrete structures. The experimental program contained three parts:

I. Hybrid simulations of two steel frame structures within the linear elastic range.
II. Hybrid simulations of two RC frame structures with different failure modes.
III. Hybrid simulation of a shear-critical RC frame that had been previously tested as a full-frame specimen in a quasi-static manner.

The specific tasks carried out for this objective were:

- Testing floor construction.
- Loading platform preparation.
- Calibration process.
- Small-scale material preparation and material tests.

- Small-scale specimen preparation.
- Modelling the numerical modules.
- Comparison of the hybrid simulation results with numerical analyses and a previously conducted full-frame test.

1.4 Thesis Contents

Chapter 2 provides an overview of previous studies on the integrated simulation of structural systems. Details of the proposed multi-platform simulation framework are discussed. The integration of analysis tools with different solution schemes is investigated. The performance of the multi-platform analysis procedure is assessed using four case studies.

Chapter 3 discusses the strengths and weaknesses of current methods for coupling beam and membrane elements. A comprehensive description of the proposed beam-membrane interface element is presented. The accuracy of the interface element is compared against the experimental test results and two commonly used coupling methods presented in the literature.

Chapter 4 presents an overview of existing methods for modelling reinforced concrete structures repaired with FRP sheets. The mechanisms influencing the component-level behaviour of FRP-confined RC members are described in detail. The capabilities of the proposed multi-platform analysis procedure is assessed by modelling specimens from two experimental studies.

Chapter 5 provides a summary of previous studies on the small-scale testing of reinforced concrete structures. Details of the hybrid simulation experimental program including material preparation and tests, construction of the specimens, and test setup are fully presented. Comparisons and discussions regarding the results of the small-scale hybrid tests are provided.

Chapter 6 presents a summary of the thesis, the conclusions from the analytical and experimental studies, and recommendations for future investigations.

CHAPTER 2

DESCRIPTION OF THE SIMULATION FRAMEWORK, VERIFICATION AND APPLICATION EXAMPLES

2.1 Introduction

Nonlinear finite element analysis (NLFEA) of reinforced concrete structures has witnessed tremendous advancement over the past few decades. In addition to the standard design problems (e.g., computing conditions under service loads including deformations and maximum crack width), there are cases in which using advanced NLFEA tools is essential due to the complexity of an analysis or the required level of accuracy. For instance, a more comprehensive analysis may be warranted if a structure is subjected to unintended or extreme loads (e.g., fire, impact, or blast), if the codes or standards used for the design are deemed to be deficient today, if the structure was incorrectly designed or constructed in the first place, or if the structure is damaged and requires rehabilitation. However, in many NLFEA software, modelling an entire structural system in detail is not practical due to computational time and memory storage limitations, and therefore they are mainly applicable to component-level analysis.

For nonlinear analysis of large structural systems, engineers use frame-type analysis tools which are typically based on two types of approaches: the lumped plasticity methods and the distributed plasticity methods. The lumped plasticity methods consist of linear elastic frame members with zero-length nonlinear plastic hinges located at the ends. Although these methods are numerically efficient and stable, due to their oversimplified formulations, they have limitations including: 1) inability to consider the gradual change of nonlinear behaviour over the member length and 2) requiring the user to define hinge parameters prior to the analysis. Unlike lumped plasticity methods, distributed plasticity methods consider material nonlinearity effects at every section of an element, providing a more accurate simulation of the structural behaviour. However, these methods are based on various compatibility assumptions (e.g., “plane section remains plane”) and therefore may be unable to accurately capture nonlinear stress distributions, particularly at the disturbed regions (e.g., beam-column joints). In addition to the above-mentioned deficiencies, most frame-type analysis tools have certain restrictions when applied to the nonlinear analysis of a structure which is subjected to extreme loads or is damaged and requires rehabilitation. The latter is discussed in detail in Section 4.2 of Chapter 4.

One effective and practical approach for accurately assessing both the global and local behaviour of complex structural systems is to combine various types of structural analysis programs in a concurrent manner, known as multi-platform simulation. In this approach, the complex or potentially critical members are modelled using detailed NLFEA tools, while the remainder of the structure is modelled with computationally efficient global analysis programs. The compatibility and equilibrium requirements should be satisfied both at the component-level and at the system-level including the interface of sub-models. The multi-platform method provides a simulation environment that incorporates a broad range of analysis methods, element types, material models, and load options. Moreover, it enables the use of parallel processing techniques to improve computational time and memory storage limitations associated with sequential single-platform analyses. The application of multi-platform simulation can be extended by combining analysis tools from different disciplines. For example, structural analysis programs can be integrated with geotechnical analysis software for more realistic soil-structure interaction simulation. In addition, integration of physical test specimens with numerical analysis tools enables conducting hybrid simulation. This testing technique allows taking into account the interaction between the test specimen and other structural members which are numerically modelled, providing more accurate simulation of the test specimen and overall system behaviour.

This chapter begins with an overview of previous studies on the simulation of integrated structural systems. Then, a new multi-platform simulation framework which attempts to address some of the limitations of the existing integrated methods is presented in detail. Also, integration of analysis tools with different solution schemes is investigated. Lastly, the performance, application, and effectiveness of the proposed framework are illustrated by modelling and analyzing three structures. The multi-platform analysis results including load-deflection responses, failure modes, and crack patterns are compared against those reported from the stand-alone analyses and experimental tests.

2.2 Literature Review

Over the past few decades, researchers proposed different types of methods for analysis of large complex structural systems. These methods are mainly based on the substructuring technique whose origins goes back to a very early method in structural engineering called the Moment Distribution method developed by Hardy Cross (Cross, 1930). Cross explained his motivation for the method as:

"The reactions in beams, bents, and arches which are immovably fixed at their ends have been extensively discussed. They can be found comparatively readily by methods which are more or less standard. The method of analysis herein presented enables one to derive from these the moments, shears, and thrusts required in the design of complicated continuous frames."

The idea behind the method was to integrate known reactions of simple structural components such as beams and columns for analysis of more complicated structures like continuous frames.

However, the first pioneer of the substructuring method in the current form is Przemieniecki (1963). He introduced the substructuring technique for the finite element design of aircrafts at Boeing Company. Przemieniecki stated his motivation for dividing the structure into different components as:

"The necessity for dividing a structure into substructures arises either from the requirement that different types of analysis have to be used on different components, or because the capacity of the digital computer is not adequate to cope with the analysis of the complete structure."

These objectives have remained the focus of many research studies to this day for analysis of large complex structural systems. Researchers employed the substructuring technique to develop methods which either improve the computational performance of the analysis or increase its modelling capabilities by combining different types of elements or analysis tools. In general, these methods can be categorized into four types:

1. Global-local analysis methods.
2. Parallel computing methods.
3. Mixed-dimensional single platform analysis methods.
4. Multi-platform simulation methods.

In the following subsections, a summary of the related previous studies for each type of analysis methods is provided.

2.2.1 Global-Local Analysis Methods

The most common approach that has been used to analyze integrated structural systems is a two-step technique known as the global-local method. In this approach, first a global analysis of the entire structure is performed to determine the internal forces and displacements. Then, the critical components of the structure are analyzed using local models with boundary values being the displacements obtained from the global analysis. The original form of the global-local method was limited to linear elastic problems (Holand et al., 1969; Mote, 1971). Several researchers then proposed refined versions of the method. Hirai et al. (1985) developed a multi-level zooming method based on the static condensation technique. Figure 2.1 shows the application of this method for modelling a rectangular plate with a circular hole. According to stress concentration analyses that were performed by the authors, the method was sensitive to the configuration of the selected zooming areas. Noor (1986) employed reduction techniques to reduce the number of degrees of freedom (DOFs) in the global analysis, improving the computational performance of the global-local methods.

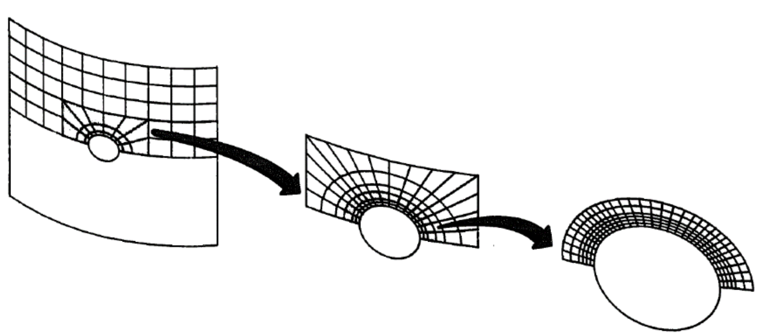

Figure 2.1 Application of zooming technique to a plate with a hole (taken from Noor, 1986)

The above-mentioned global-local methods are known as the direct types of global-local methods. These methods are based on compatibility conditions and only satisfy equilibrium requirements locally. Whitcomb (1991) proposed an iterative global-local method using the modified Newton Raphson procedure which accounted for the differences between the stiffnesses of members in the global model and local model. However, the study was limited to linear problems and the local refinement was only applicable to systems with a single critical region. Mao and Sun (1991) developed a three-step global-local method to improve the analysis results of the global model. The first two steps of the method were similar to the conventional global-local approach, previously discussed. In the third step, using the results of the local analysis, the global analysis was repeated, producing more refined results. To improve the accuracy and satisfy equilibrium at both the global-level and local-level, several iterations were required. Although the iterative methods captured the behaviour of integrated systems more accurately compared to the direct methods, they were limited to linear problems or simple nonlinear problems. In addition, since the analysis was not performed in a concurrent manner, the force redistribution due to the stiffness changes in the system was not fully considered.

2.2.2 Parallel Computing Methods

Some researchers developed parallel simulation methods to improve the computational performance of single-platform analysis tools enabling the modelling of large structural systems. In general, there are two types of parallel simulation methods: parallel equation solvers and parallel processing techniques. The parallel equation solvers use direct solution methods (Davis, 2004; Cho and Hall, 2012) or iterative solution methods (Balay et al., 2014) to efficiently solve the equilibrium equations of large structural systems using multiple computers. The parallel processing techniques, also known as domain decomposition methods, use the substructuring concept to partition the system into multiple components and then employ parallel computing techniques to solve the equilibrium equations at the interface nodes and in each substructure. The numerical solution of the interface problem is computationally expensive and requires substantial communication between the substructures. Several studies proposed methods to reduce the amount of data transfer (El-Sayed and Hsiung, 1990) and to minimize coupled computational operations between the substructures (Farhat, 1987; Fulton and Su, 1992).

Chen and Archer (2001) developed a new domain decomposition method suitable for nonlinear analysis which avoided the computationally expensive factorization procedure of the stiffness matrix at every load step. The method was implemented in a frame-type analysis program which had nonlinear rotational springs. The Message Passing Interface communication method was used to transfer data between the substructures.

Yang et al. (2012) adopted a multi-level substructuring method to improve the performance of parallel finite element analysis. An iterative multi-level mesh partitioning method was employed to optimize the work load between the computers by continuously updating the mesh partitioning configurations. Unlike the single-level substructuring method in which the equilibrium equation of all the interface nodes is solved in one step, in the multi-level substructuring method this process is performed in multiple steps, resulting in less overall analysis time. Figure 2.2 shows an overview of the multi-level substructuring method.

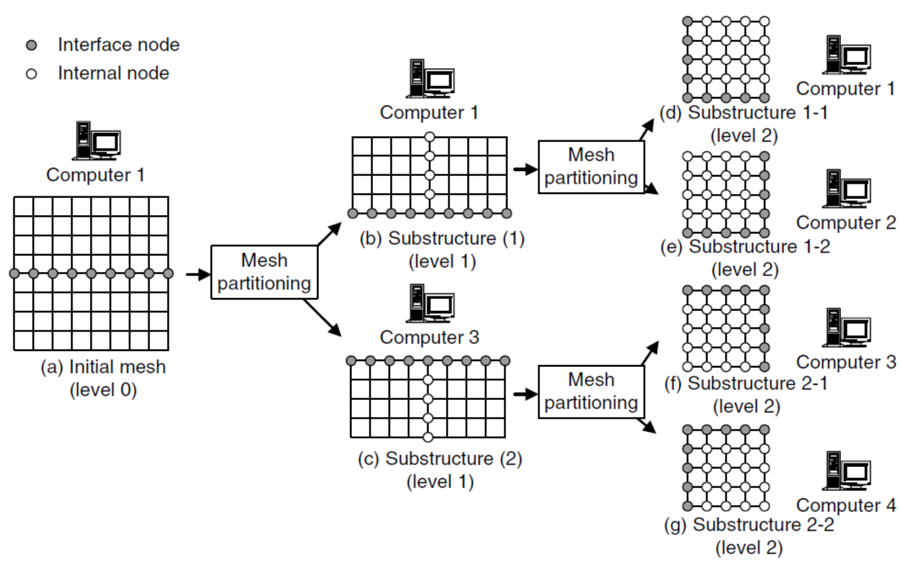

Figure 2.2 Overview of the multi-level substructuring method (taken from Yang et al., 2012)

Although parallel simulation methods can significantly improve the computational performance of the analysis, they require advanced computing facilities which are expensive and may not be available in a typical engineering design office. For medium size problems, using multiple cores of office computers may be adequate. However, for most large and complex structural systems, computing sites enhanced with supercomputers or a substantial number of processing units are required.

2.2.3 Mixed-Dimensional Single-Platform Analysis Methods

Another approach to accurately analyzing complex structural systems is mixed-dimensional analysis where low-dimensional elements (e.g., beam element) are coupled with high-dimensional elements (e.g., membrane and shell elements) in a single finite element model. The element coupling methods can be categorized into three types: Rigid Links (Mata et al., 2008), Multi-Point Constraints (MPC) (McCune et al., 2000; Wang et al., 2014), and Transition Elements (Surana, 1980; Kim and Hong, 1994). A comprehensive discussion of these methods is presented in Section 3.2 of Chapter 3. Several researchers successfully employed mixed-dimensional modelling methods for multi-scale analysis of large structural systems. Li et al. (2009) developed a mixed-dimensional model of a steel bridge structure in ABAQUS (2012) where joint panels were modelled with shell elements, while all other members were modelled with beam elements (see Figure 2.3). Beam and shell elements were connected using constraint equations. The mixed-dimensional analysis results were compared with those obtained from a full-beam model, a full-shell model, and laboratory testing of a reduced-scale specimen representing the truss structure. There was a good agreement between the computed and measured responses.

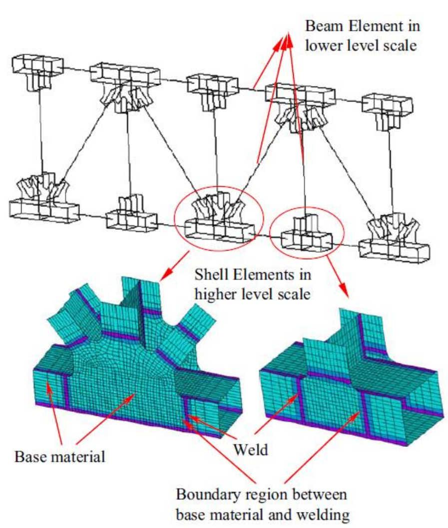

Figure 2.3 Mixed-dimensional model of a steel bridge (taken from Li et al., 2009)

Wang et al. (2014) developed an iterative method to formulate linear constraint equations based on the virtual work concept for connecting various types of elements. The application of the method was demonstrated by mixed-dimensional analysis of a steel frame structure using ANSYS (Kohnke, 1994) software where the joint panels were modelled with shell elements and the beam and columns were modelled with frame elements. Figure 2.4 shows the mixed-dimensional finite element model. The linear elastic analysis results, including the deflection at the mid-span of the beam and the stress distributions in the joint panels, were compared against those from other types of coupling methods and a full-shell model. Although the procedure was extended to nonlinear analysis, the expensive computations required to obtain the constraint equations prohibited its practical application.

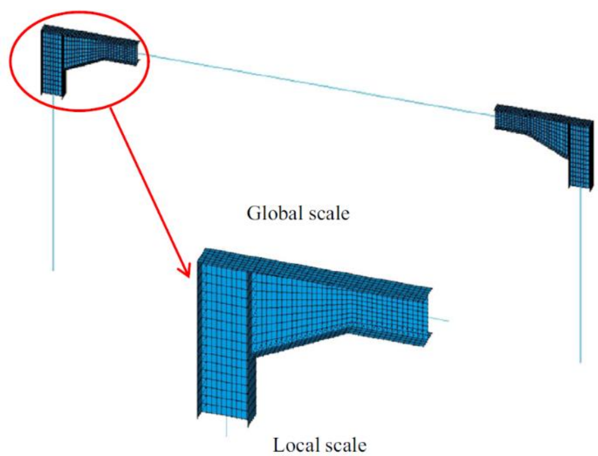

Figure 2.4 Mixed-dimensional model of a steel frame (taken from Wang et al., 2014)

2.2.4 Multi-Platform Simulation Methods

In recent years, several studies attempted to extend mixed-dimensional modelling to multi-platform simulation by combining global analysis software with local analysis tools or test specimens in a concurrent manner. In this approach, each potentially critical member, based on its mechanical characteristics, is modelled using the most suitable NLFEA tool or is represented with a physical specimen, while the rest of the structure is modelled with a computationally fast global analysis software. The interface between numerical models is simulated using proper mixed-dimensional element coupling methods. An integrated simulation procedure is used to take into account the interaction between different modules and to satisfy compatibility and equilibrium requirements. Data are exchanged between the modules through network communication.

Most of the published multi-platform studies have focused on hybrid simulation, which entails combining numerical models with physical specimens. Yang et al. (2002) incorporated a user-defined element in OpenSees (McKenna and Fenves, 1999; Mazzoni et al., 2007), representing the properties of the test specimen, with a data exchange framework to conduct pseudo-dynamic hybrid simulation. The dynamic effects were considered in OpenSees based on the α-Operator Splitting time integration method (Combescure and Pegon, 1997). The data exchange framework used the SQL objects to transfer information between the numerical and experimental modules. The application of the method was demonstrated by hybrid simulation testing of a multi-storey steel frame structure. The test specimen was a buckling restrained braced (BRB) member located at the base of the structure, while the remainder of the frame was modelled in OpenSees using linear elastic beam elements.

Takahashi and Fenves (2005) employed a similar approach to that proposed by Yang et al. (2002) and developed an object-oriented framework for geographically distributed hybrid simulation which was compatible with a wide range of testing facilities and configurations. The communication between the numerical and physical modules was established using TCP/IP sockets and through the Internet network. A geographically distributed hybrid simulation was carried out by connecting testing equipment at the University of Kyoto in Japan and a computational site at the University of California, Berkeley in USA to investigate the pseudo-dynamic response of a bridge pier with two seismic isolation bearings. The pier was analyzed in OpenSees based on a bilinear hysteresis model while the seismic isolation bearing was experimentally tested. The round trip communication time between the two universities at each load step was about 200 milliseconds. Figure 2.5 shows an overview of the hybrid simulation configuration.

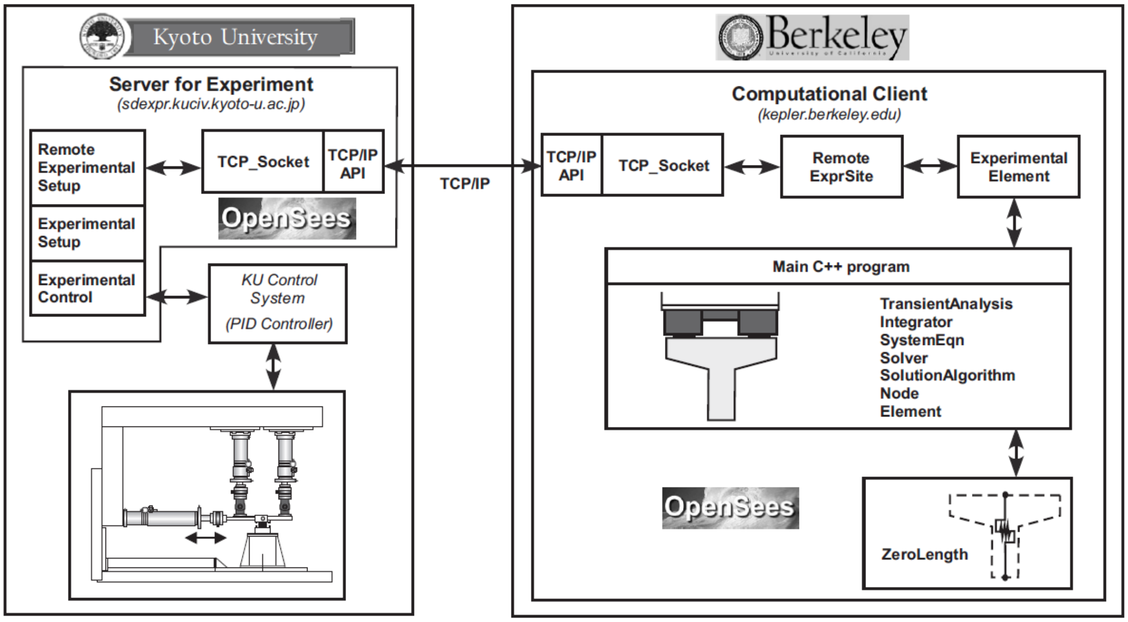

Figure 2.5 Hybrid simulation configuration for distributed testing of a bridge pier (taken from Takahashi and Fenves, 2005)

Pan et al. (2005) adopted a file sharing technique and proposed an online testing system for geographically distributed hybrid simulation. The numerical and physical modules transferred data through a series of temporary files stored in shared directories. The equation of motion for the entire structure was formulated in an in-house finite element analysis program using an implicit time integration method. A stiffness prediction procedure was developed based on the least square method to account for the control and measurement errors generated by the physical module. To examine the performance of the framework, a hybrid simulation was conducted on an eight-storey two-span steel frame structure isolated with rubber bearings at the base. The base isolation system was tested in the laboratory and the frame structure was numerically modelled using beam elements with nonlinear plastic hinges located at each end. Karavasilis et al. (2008), Saouma et al. (2012), and Castaneda et al. (2015) implemented nonlinear structural elements in the hybrid simulation frameworks aiming to carry out real-time testing. The nonlinear elements were limited to frame-type elements (plastic hinges and fibre elements) and no sophisticated element was incorporated into the simulation frameworks.

The main objective of the aforementioned hybrid simulation studies was to provide a flexible testing module and little effort was made to extend the capabilities of the numerical module.

Most hybrid simulation frameworks employ simplified frame-type analysis procedures to analyze the numerical models. However, there are situations where some of the critical members of the structure should be numerically modelled and the ability of the analysis procedure to do so is crucial. There have been only a few studies which focused on integrating different analysis tools to extend the modelling capabilities of single-platform programs. The majority of these studies were limited to numerical analysis and were not applicable to hybrid simulation. A brief overview of these studies are provided in the following.

Mata et al. (2008) combined a global frame-type analysis tool with a local finite element analysis program for integrated simulation of reinforced concrete structures. The rotational displacements of the beam elements were transferred to the equivalent translational displacements of the hexahedral elements based on the rigid body movement assumption at the interface section. As shown in Figure 2.6, the numerical modules were connected in a master-slave manner using a message passing interface (MPI). An iterative Newton Raphson scheme was used to consider the interaction between the global and local models. The integrated method was verified by nonlinear analysis of a one-storey one-span reinforced concrete frame structure. The beam and columns were modelled with a global frame-type analysis program, while the joint panels were modelled using a local finite element analysis software. The analysis results of the integrated model were compared against those obtained from the full-frame model. No verification study was reported against the stand-alone finite element analysis or experimental tests. Also, the proposed integrated method was employed in in-house programs and the application of the method to other potential analysis tools was not discussed.

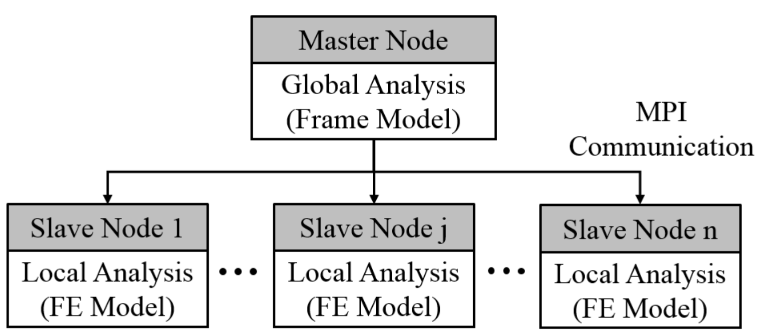

Figure 2.6 Schematic representation of master-slave method used in Mata et al. (2008)

Chen and Lin (2011) developed an internet-based computing framework for multi-scale simulation of structural systems. The framework was enhanced with two levels of parallel processing, enabling efficient numerical computations. Each module was analyzed in a cluster which contained multiple computers connected using a local network. The clusters communicated with each other in a master-slave manner through the Internet network. Figure 2.7 shows an overview of the computing framework. For multi-scale simulation, a simplified global model of the entire structure was connected to detailed finite element models of potentially critical members. The critical members were modelled twice, with beam elements and with detailed finite elements. In each load step, the boundary displacements resulting from the analysis of the global model were sent to the related finite element models to compute the local response of each component. The first-order and parabolic shear deformation theories were adopted to model the interface and transfer displacements between the global and local models.

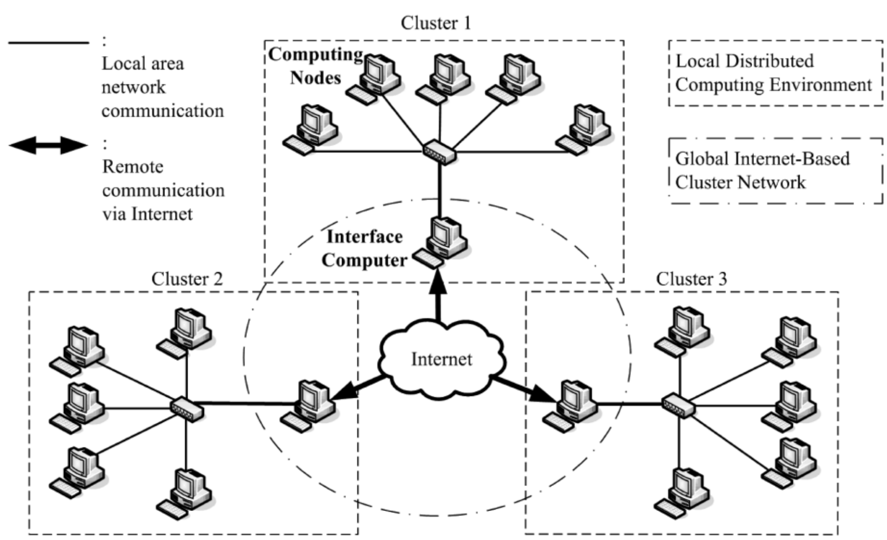

Figure 2.7 Multi-scale framework with two levels of parallel processing (taken from Chen and Lin, 2011)

The performance of the multi-scale framework was evaluated by a push-over analysis of a seven-storey two-bay frame structure. The global model was created using beam elements with plastic hinges located at each end. Two local models were made with detailed solid elements representing a beam and a column of the structure. All three models were analyzed using

ABAQUS. The multi-scale analysis results were compared against the response of a single-scale detail analysis. Although the framework was computationally efficient, it had some major limitations including: 1) the multi-scale simulation was based on displacement compatibility conditions and did not completely satisfy equilibrium requirements between the global and local models, 2) the data flowed only in a one-way path from the global model to the local models, compromising the ability of the method to accurately capture the interaction between the models, and 3) the simulation framework was only compatible with ABAQUS software and the addition of any other potential analysis tools required extensive changes to the system.

Kwon et al. (2008) proposed a multi-platform analytical-experimental simulation framework, named UI-SIMCOR, which enabled integration of various analysis tools and geographically distributed experimental equipment for pseudo-dynamic hybrid simulation. The framework adopts the α-Operator Splitting time integration method (Combescure and Pegon, 1997) to take into account dynamic effects. To exchange data between the simulation framework and substructure modules, TCP/IP sockets are used through the Internet network. The algorithm of the framework comprises three main parts: 1) the initial stiffness evaluation: the framework either reads the initial stiffness matrix of each module from an input file, or generates it by imposing a small displacement to each degree of freedom and receiving computed or measured restoring forces, 2) the static equilibrium: the structural system is analyzed under gravity loads, 3) the dynamic equilibrium: the structural system is analyzed under dynamic excitation using the time integration method. The main parts of the framework are shown in Figure 2.8. The modified Newton Raphson procedure is employed to satisfy equilibrium requirements at the system-level during the gravity load analysis stage.

The application of the multi-platform framework was demonstrated with several examples including: numerical simulation of a bridge structure (integration of OpenSees and Zeus-NL (Elnashai et al., 2008)), numerical simulation of a reinforced concrete high rise building (integration of Zeus-NL and VecTor2 (Wong et al., 2013)), and distributed hybrid simulation of a bridge structure (integration of Zeus-NL with two experimental test specimens). The framework was able to successfully simulate the response of the aforementioned structural systems. However, there are certain restrictions associated with the framework. The integrated procedure requires forces and displacements of all the degrees of freedom to be transferred between the framework and substructures which can result in a substantial amount of data exchange, particularly for large structural systems. In addition, for each iteration of the simulation at the system-level, each substructure module has to perform a full local analysis to compute restoring forces. However, most advanced reinforced concrete analysis tools use sophisticated numerical procedures with several iterations that can be time-consuming. Therefore, the practical application of the framework to multi-platform simulation of large reinforced concrete structures is disputable.

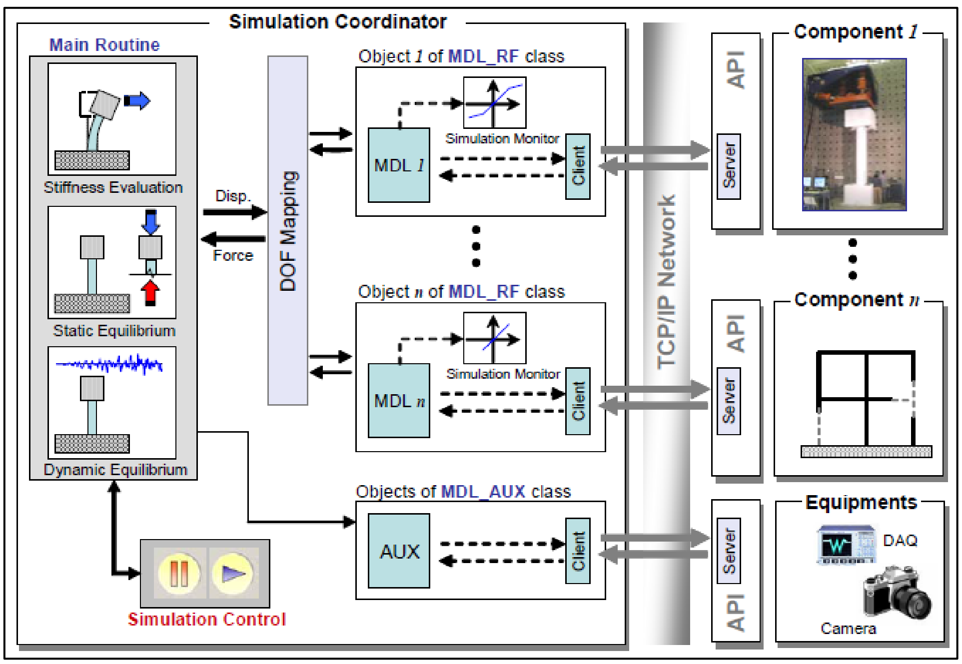

Figure 2.8 Main parts of UI-SIMCOR (taken from Kwon et al., 2008)

2.2.5 Conclusions

Based on the reviewed literature, the following conclusions can be drawn regarding the integrated simulation of large complex reinforced concrete structures:

1. Traditional global-local analysis approach cannot fully capture the interaction between different components since the data flow only in a one-way path from the global model to the local models. The refined versions of the global-local methods (e.g., multi-step methods, iterative methods) are more accurate, but cannot fully satisfy equilibrium requirements and are limited to linear and simple nonlinear problems.

2. Parallel computing methods are an effective approach for improving the computational performance of analysis programs and were successfully employed for nonlinear analysis of large structural systems. However, these methods require substantial amounts of computing resources (e.g., supercomputers, computer clusters) which are expensive and are not available in a typical engineering design office; thus, their application is limited.

3. Although a significant amount of research was carried out on developing methods to combine low-dimensional and high-dimensional elements (e.g., rigid links, multi-point constraints, and transition elements), the application of these methods to the analysis of large structural systems was mostly limited to linear elastic single-platform simulations.

4. Multi-platform simulation is an effective and practical approach to accurately capture the behaviour of large complex structural systems. The majority of existing multi-platform studies were focused on hybrid simulation which involves combining numerical models with physical test specimens. The main objective of these studies was to provide a flexible testing module and little effort was made to extend the capabilities of the numerical module. Most hybrid simulation frameworks analyze the numerical models using simplified frame-type programs which have major modelling limitations and cannot fully capture material nonlinearity effects or stress distributions at the disturbed regions.

5. In recent years, a few studies attempted to integrate global and local analysis tools in a concurrent manner aiming to extend the modelling capabilities of single-platform analysis, providing a more accurate simulation method for large complex structural systems. Although these methods were successfully employed for the simulation of several structural systems, they have one or more of the following deficiencies: 1) most of these methods are limited to numerical simulation and are not applicable to hybrid simulation, 2) the majority of them are only compatible with in-house programs and the addition of new analysis tools to their simulation procedure is challenging, and 3) the ones that are compatible with commercial analysis programs require high amounts of communication data and therefore not applicable to large structural systems.

6. None of the above-mentioned studies specifically investigated the application of multi-platform analysis to reinforced concrete structures. Some of the advanced reinforced concrete

analysis tools use secant-based solution methods to avoid well-recognized numerical problems associated with most tangent-based methods. These numerical problems are mainly caused by zero stiffness values in the reinforcement response between the yielding and strain-hardening regions and negative stiffness values in the post-cracking and post-peak response of the concrete in tension and compression, respectively. Therefore, the integration of analysis tools with different solution schemes should be investigated.

In this study, a new multi-platform simulation framework is proposed which intends to address some of the deficiencies of the aforementioned studies, allowing for a more realistic experimental-analytical simulation of complex reinforced concrete structural systems. The integrated simulation procedure is applicable to both academic and commercial analysis programs. The mathematical basis for integration of analysis tools with different solution schemes is provided. The framework is enhanced with a newly developed standardized data exchange format facilitating communication with diverse numerical analysis tools and test specimens. In addition, it is compatible with a generalized interface program which provides a flexible physical module applicable to a wide range of laboratory equipment and testing configurations. The effectiveness of the proposed simulation framework is demonstrated by several application and verification examples.

2.3 Description of the Proposed Simulation Framework

2.3.1 Overview of the Framework

The proposed integrated framework, named Cyrus, is written in the C++ programming language using the Microsoft Foundation Classes and the Open Graphics Library. The architecture of the framework is based on an object-oriented methodology with two core classes: Document.cpp and View.cpp. The objects of the Document.cpp class provide applications to handle data for multi-platform simulations. Applications can be stored and retrieved for future simulations using the serialization technique. The objects of the View.cpp class provide mechanisms to display data stored in the Document.cpp class on the screen. The document/view structure of the framework contains six classes: ExpModule.cpp, NumModule.cpp, Com.cpp, Mapping.cpp, Solution.cpp, and Draw.cpp. The objects of the ExpModule.cpp and NumModule.cpp classes contain information on the experimental and numerical modules, respectively, including: substructure type, communication method, port number, number of interface DOFs, and local interface node numbers. These classes are written in a standard form making them suitable for adopting to other potential experimental facilities or analysis tools. The Com.cpp class provides two types of local communication methods (pipes and files) and a distributed communication method (TCP/IP sockets) through the Internet network. The Mapping.cpp class automatically finds the interface DOFs between substructure modules and maps them based on a global numbering scheme. The Solution.cpp class computes the displacements at the interface DOFs based on the equilibrium and compatibility conditions. The Draw.cpp class displays substructure modules on the screen and highlights their interface nodes using the Open Graphics Library. The framework is linked to two advanced C++ libraries, MKL (2012) and PARDISO (Schenk and Gartner, 2004), enabling high-performance memory-efficient sparse matrix calculations. The object-oriented structure of the framework is shown in Figure 2.9. A comprehensive description of each part of the framework is presented in the following subsections.

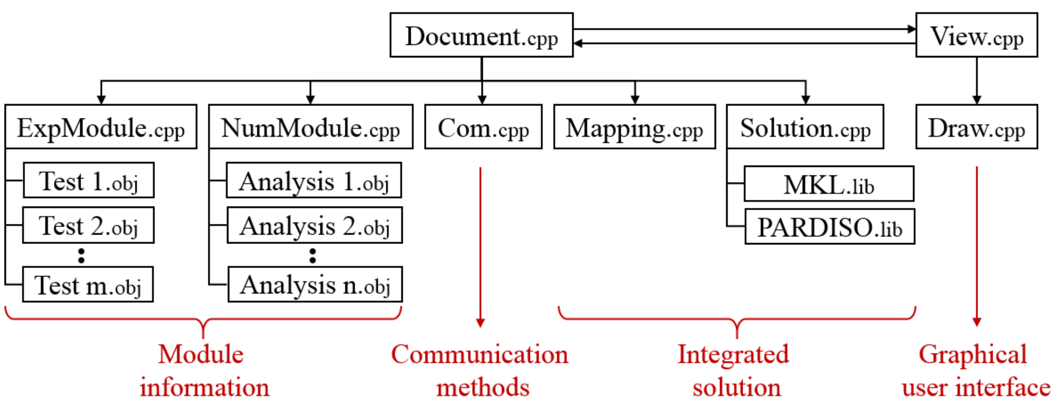

Figure 2.9 Object-oriented structure of the simulation framework

To date, eight different nonlinear analysis tools have been integrated into the simulation framework: Zeus-NL, OpenSees, ABAQUS, and the VecTor suite of software which includes VecTor2, VecTor3 (ElMohandes and Vecchio, 2013), VecTor4 (Hrynyk and Vecchio, 2015), VecTor5 (Guner and Vecchio, 2010a), and VecTor6 (Lulec, 2017). For the programs with accessible source codes (e.g., VecTor suite of software), the communication functions are implemented in the source code. For other programs, an interface program, NICA (Kwon et al., 2008), is used to provide network communication capability. NICA runs the analysis software as a child process and uses inter-process communication (files or named pipes) to exchange data with it. Also, to incorporate experimental specimens as substructure modules, the framework is connected to another interface program, NICON (Zhan and Kwon, 2015), which is compatible with various types of testing equipment and specimen configurations. NICON was developed based on the LabView programming software and uses the National Instrument hardware to connect to actuator controllers. A detailed description of the program is provided in Section 5.3.2 of Chapter 5. Figure 2.10 shows the different parts of the proposed multi-platform simulation framework and its application to a reinforced concrete frame structure with shear-critical beams.

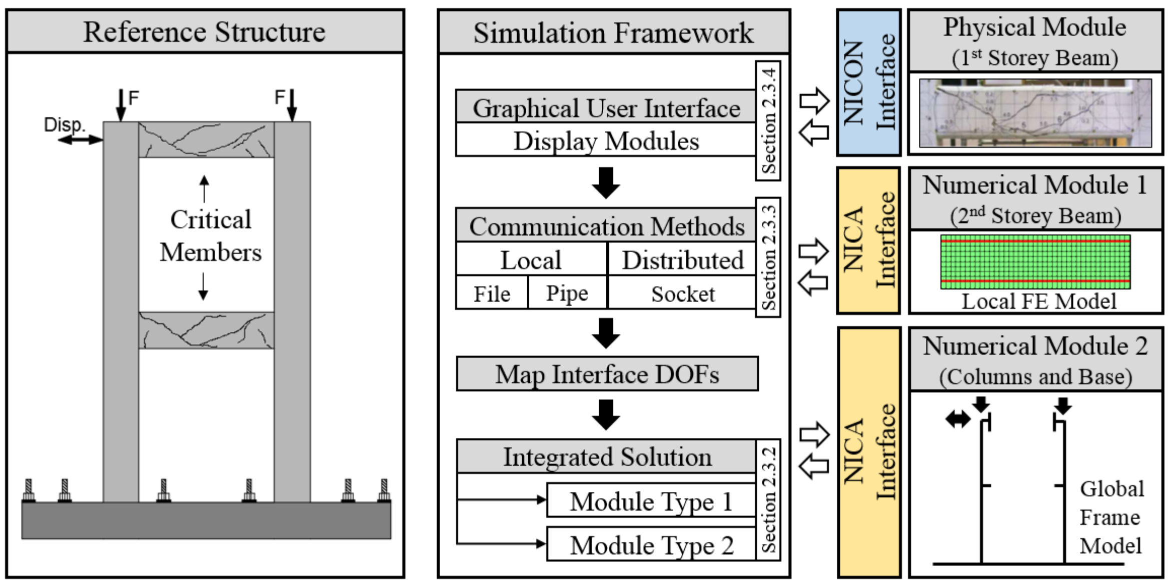

Figure 2.10 Overview of the multi-platform simulation configuration

For multi-platform simulation of a structural system, each complex or potentially critical member, based on its mechanical characteristics, is modelled using the most suitable NLFEA tool or is represented with a physical test specimen, while the rest of the structure is modelled with a computationally fast global analysis software. For example, for the reinforced concrete frame shown in Figure 2.10, the first and second storey beams have inadequate shear reinforcement and are the critical members of the structure. To accurately capture their behaviour, the first storey beam is represented with a test specimen and the second storey beam is modelled using a local finite element program capable of considering shear behaviour (e.g., VecTor2). The columns and foundation which are noncritical members of the structure are modelled with a computationally fast frame-type analysis software (e.g., VecTor5).

2.3.2 Solution Method

2.3.2.1 Combination of Different Nonlinear Solution Schemes

To consider the geometry and material nonlinearities of reinforced concrete structures, analysis programs use different types of iterative solution schemes. In a nonlinear finite element system, the general equation that should be solved to satisfy equilibrium requirements at each node can be written as:

$$\{\mathrm{R}(\mathrm{U}^*)\} = \{\mathrm{F}(\mathrm{U}^*)\} - \{\mathrm{f}(\mathrm{U}^*)\} = 0 \tag{2.1}$$

where $\{\mathrm{R}\}$ is the unbalanced force vector, $\{\mathrm{F}\}$ is the external load vector, $\{\mathrm{f}\}$ is the internal force vector computed based on the element stresses, and U^* are the displacement values that satisfy Eq. 2.1. Because $\{\mathrm{f}\}$ is a function of the nodal displacements at the current load step, an iterative solution scheme is required to solve Eq. 2.1. The existing solution methods can be mainly categorized into two groups: tangent stiffness-based methods and secant stiffness-based methods. Both groups can be represented either with incremental formulations or total formulations.

A generalized multi-platform simulation procedure should be capable of integrating analysis tools with different solution schemes. In this section, combining tangent stiffness-based methods and secant stiffness-based methods for both incremental and total formulations is investigated.

Incremental Formulations

The most commonly used nonlinear solution schemes are the incremental tangent stiffness-based methods (e.g., Bathe, 1982). With these methods, the unbalanced force vector is calculated using a Taylor series expansion based on the forces and displacements of the previous load stage:

$$\{\mathrm{R}(\mathrm{U}^*)\} = \{\mathrm{R}(\mathrm{U})\}^{\mathrm{i}-1} + \left[\frac{\partial \mathrm{R}}{\partial \mathrm{U}}\right]^{\mathrm{i}-1} \left(\{\mathrm{U}^*\} - \{\mathrm{U}\}^{\mathrm{i}-1}\right) + \alpha \tag{2.2}$$

where U^* is the converged displacement vector, U^{i-1} is the displacement vector at the previous load step, and α represents the higher-order terms in the Taylor series.

Substituting Eq. 2.1 into Eq. 2.2 and neglecting the higher-order terms yield the following equation:

$$0 = \left(\{\mathrm{F}\}^{\mathrm{i}-1} - \{\mathrm{f}\}^{\mathrm{i}-1}\right) + \left[\frac{\partial (\mathrm{F} - \mathrm{f})}{\partial \mathrm{U}}\right]^{\mathrm{i}-1} \left(\{\mathrm{U}^*\} - \{\mathrm{U}\}^{\mathrm{i}-1}\right) \tag{2.3}$$

Assuming the external loads are independent from the load step and displacements, Eq. 2.3 can be simplified as:

$$\{\mathrm{F}\} - \{\mathrm{f}\}^{\mathrm{i}-1} = \left[\frac{\partial \mathrm{f}}{\partial \mathrm{U}}\right]^{\mathrm{i}-1} \left(\{\mathrm{U}^*\} - \{\mathrm{U}\}^{\mathrm{i}-1}\right) \tag{2.4}$$

Eq. 2.4 can be written in an incremental form:

$$\{\mathrm{F}\} - \{\mathrm{f}\}^{\mathrm{i}-1} = [\mathrm{K}]_{\mathrm{t}}{}^{\mathrm{i}-1} \{\Delta \mathrm{U}\}^{\mathrm{i}} \tag{2.5}$$

where $[K]_t^{i-1}$ is the incremental tangent stiffness matrix which represents the slope of the load-deflection response at the previous load step:

$$[\mathrm{K}]_{\mathrm{t}}{}^{\mathrm{i}-1} = \left[\frac{\partial \mathrm{f}}{\partial \mathrm{U}}\right]^{\mathrm{i}-1} \tag{2.6}$$

and $\{\Delta U\}^i$ is the incremental displacement vector from which the improved displacement values at the current load step can be found:

$$\{\mathrm{U}\}^{\mathrm{i}} = \{\mathrm{U}\}^{\mathrm{i}-1} + \{\Delta \mathrm{U}\}^{\mathrm{i}} \tag{2.7}$$

As shown in Figure 2.11 (a), by updating the incremental tangent stiffness matrix at every load step of the solution scheme new values for the displacement vector can be computed. This procedure is repeated until the displacement values converge within a predefined error limit.

Unlike the incremental tangent stiffness-based methods, the incremental secant stiffness-based methods are less popular in the area of nonlinear finite element analysis (e.g., Onate, 1995). With these methods, the incremental secant stiffness is defined as the slope of the line which connects the previous iteration (u_{i-1}, f_{i-1}) and current iteration (u_i, f_i) points in the load-deflection response:

$$[K]_s^i = \frac{\{\Delta f\}^i}{\{\Delta U\}^i} = \frac{\{f\}^i - \{f\}^{i-1}}{\{U\}^i - \{U\}^{i-1}} \tag{2.8}$$

The nonlinear behaviour of the structure is taken into account by updating the incremental secant stiffness values in each iteration (see Figure 2.11 (b)).

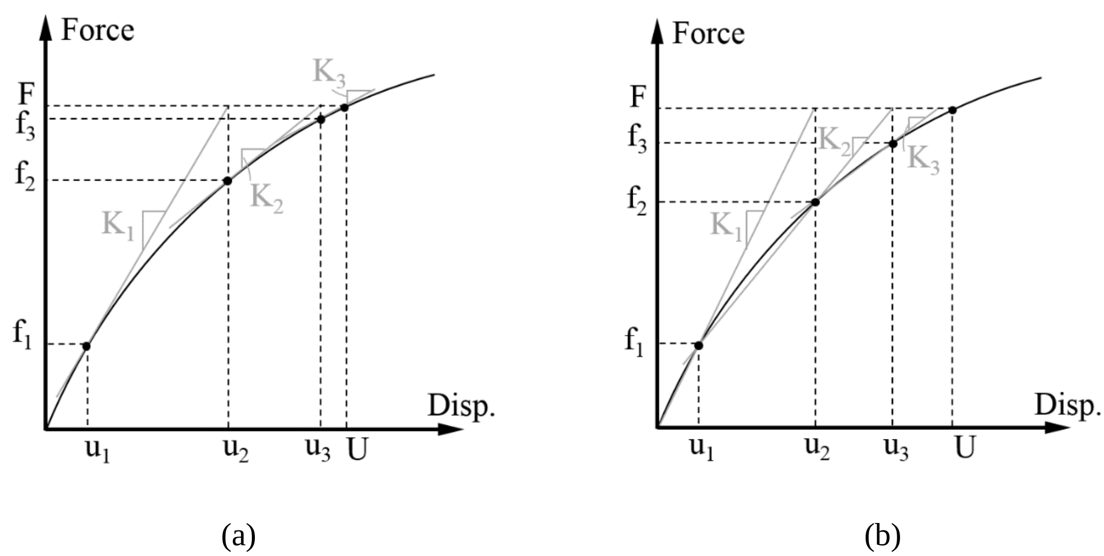

Figure 2.11 Incremental forms of nonlinear solution schemes: (a) tangent-based method; (b) secant-based method

For sufficiently small load steps, the incremental tangent stiffness can be approximated as being equal to the incremental secant stiffness:

$$[K]_t^i \approx \lim_{\Delta U \to 0} [K]_s^i \tag{2.9}$$

Figure 2.12 compares the incremental tangent stiffness at load step “i” (indicated with the red line) to the incremental secant stiffness values calculated using two different load step sizes (specified with blue and green lines). It can be seen that, by using reasonably small load steps, the incremental tangent and secant stiffness values are equivalent and therefore analysis tools with different types of solution techniques can be combined.

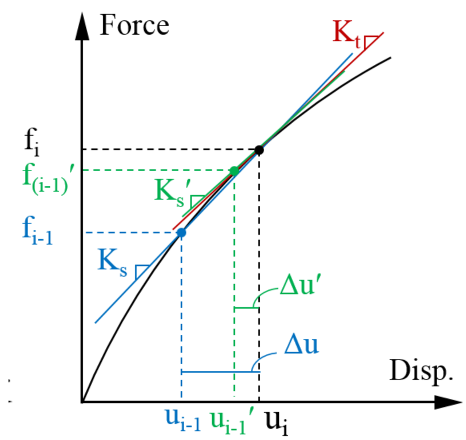

Figure 2.12 Comparison of incremental tangent and secant stiffness values using different load step sizes

Total Formulations

The integration of the tangent and secant stiffness-based methods can also be shown for the total forms of the methods. Figure 2.13 presents the total forms of the tangent and secant stiffness-based methods with red and blue lines, respectively, and the combination of the two methods using green lines. It should be noted that with the total form of the tangent stiffness-based method that is presented here, the stiffness matrix is constant throughout the iterations and load increments, and is equal to the initial stiffness matrix of the structure. The nonlinear behaviour of the structure is taken into account by updating the unbalanced force values in each iteration. As shown in Figure 2.13, combining the two methods results in the total stiffness values (K_c) that are not as high as the initial stiffness (K_i) and not as low as the total secant stiffness (K_s) of the system. Similarly, the total combined force values (f_c) are within the range of the total external force (F) and total unbalanced force values ($F+\Delta f_1$). Therefore, the displacements computed by the combined method (u_{2c}) are always between the values obtained from the tangent and secant stiffness-based methods (u_{2t} and u_{2s}, respectively). Assuming small load steps, it can be concluded that the solution of the combined method is equivalent to the solutions of the tangent and secant stiffness-based methods with total formulations. Also, the convergence rate of the combined method is within the range of the convergence rates of the tangent and secant stiffness-based methods.

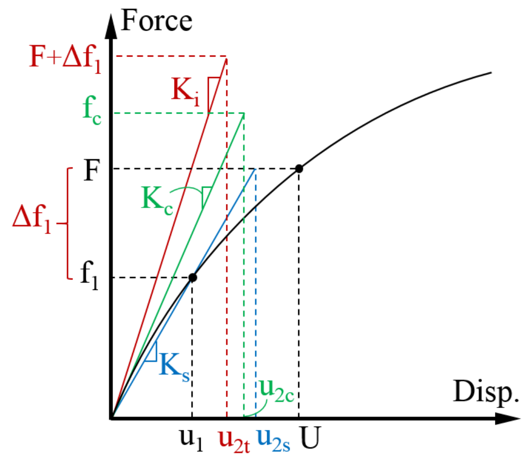

Figure 2.13 Combination of total forms of tangent and secant solution schemes

2.3.2.2 Formulation and Solution of the System Matrix

For each substructure module, the degrees of freedom can be partitioned into internal DOFs and interface DOFs, resulting in the following form of the equilibrium equation:

$$\begin{bmatrix} K_{mm} & K_{mn} \\ K_{nm} & K_{nn} \end{bmatrix} \begin{Bmatrix} U_m \\ U_n \end{Bmatrix} = \begin{Bmatrix} P_m \\ P_n \end{Bmatrix} \tag{2.10}$$

where [K] is the stiffness matrix, {U} is the displacement vector, {P} is the external force vector, and the subscripts “n” and “m” correspond to the internal and interface DOFs, respectively. Eliminating the internal displacements, $\{U_n\}$, from Eq. 2.10 leads to the following relation:

$$([K_{mm}] - [K_{mn}][K_{nn}]^{-1}[K_{nm}])\,\{U_m\} = \{P_m\} - [K_{mn}][K_{nn}]^{-1}\{P_n\} \tag{2.11}$$

This equation can be written in a format similar to that of the equilibrium equation by defining equivalent forms of the stiffness matrix, $[K_{mm}]_c$, and force vector, $\{P_m\}_c$:

$$[K_{mm}]_c\{U_m\} = \{P_m\}_c \tag{2.12}$$

Eq. 2.12 is the condensed form of the equilibrium equation at the interface DOFs and can be used to calculate related displacements. After determining the interface displacements, the internal displacements can be computed using the following equation:

$$\{U_n\} = [K_{nn}]^{-1}(\{P_n\} - [K_{nm}]\{U_m\}) \tag{2.13}$$

To perform multi-platform simulation, the proposed framework categorizes the analysis tools into two types:

1) Module Type 1: analysis programs with accessible source code in which the network communication and static condensation functions are implemented in their source code (e.g., some academic software).

2) Module Type 2: analysis tools whose source code cannot be modified and only the input and output files containing model information and analysis results are accessible (e.g., most commercial software).

In the following, details of integrating each type of module into the framework are presented using a simple FE model of a cantilever beam, shown in Figure 2.14. The FE model contains two rectangular elements with each node having a single degree of freedom in the horizontal direction.

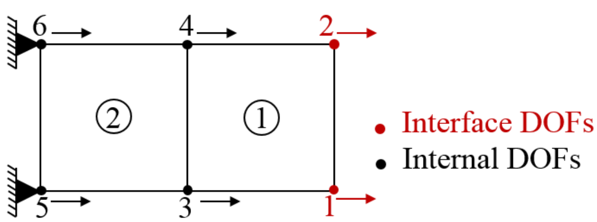

Figure 2.14 FE model of cantilever beam

The stiffness matrix of the elements can be written as:

$$[\mathrm{k}]_1 = \begin{bmatrix} \mathrm{k}_{11} & \mathrm{k}_{12} & \mathrm{k}_{13} & \mathrm{k}_{14} \\ \mathrm{k}_{21} & \mathrm{k}_{22} & \mathrm{k}_{23} & \mathrm{k}_{24} \\ \mathrm{k}_{31} & \mathrm{k}_{32} & \mathrm{k}_{33} & \mathrm{k}_{34} \\ \mathrm{k}_{41} & \mathrm{k}_{42} & \mathrm{k}_{43} & \mathrm{k}_{44} \end{bmatrix} \quad ; \quad [\mathrm{k}]_2 = \begin{bmatrix} \mathrm{k}_{33} & \mathrm{k}_{34} & \mathrm{k}_{35} & \mathrm{k}_{36} \\ \mathrm{k}_{43} & \mathrm{k}_{44} & \mathrm{k}_{45} & \mathrm{k}_{46} \\ \mathrm{k}_{53} & \mathrm{k}_{54} & \mathrm{k}_{55} & \mathrm{k}_{56} \\ \mathrm{k}_{63} & \mathrm{k}_{64} & \mathrm{k}_{65} & \mathrm{k}_{66} \end{bmatrix} \tag{2.14}$$

By assembling the two matrices and eliminating the restrained DOFs, the global stiffness matrix of the system can be found:

$$[\mathrm{K}] = [\mathrm{k}]_1 + [\mathrm{k}]_2 = \begin{bmatrix} \mathrm{k}_{11} & \mathrm{k}_{12} & \mathrm{k}_{13} & \mathrm{k}_{14} \\ \mathrm{k}_{21} & \mathrm{k}_{22} & \mathrm{k}_{23} & \mathrm{k}_{24} \\ \mathrm{k}_{31} & \mathrm{k}_{32} & 2\mathrm{k}_{33} & 2\mathrm{k}_{34} \\ \mathrm{k}_{41} & \mathrm{k}_{42} & 2\mathrm{k}_{43} & 2\mathrm{k}_{44} \end{bmatrix} \tag{2.15}$$

For simplicity, this equation is expressed with the following notation in the subsequent sections:

$$[\mathrm{K}] = \begin{bmatrix} \mathrm{a} & \mathrm{b} & \mathrm{c} & \mathrm{d} \\ \mathrm{e} & \mathrm{f} & \mathrm{g} & \mathrm{h} \\ \mathrm{i} & \mathrm{j} & \mathrm{k} & \mathrm{l} \\ \mathrm{m} & \mathrm{n} & \mathrm{o} & \mathrm{p} \end{bmatrix} \tag{2.16}$$

Module Type 1

For analysis tools with accessible source code, the communication and static condensation functions are implemented in the source code. In each step of the simulation, Cyrus collects the condensed forms of the stiffness matrix and force vector from each numerical module, maps them based on the connectivity of the substructures and a global numbering scheme, and solves for the interface displacements. The displacements of interface DOFs of two substructures are considered to be identical so that compatibility is satisfied in the system. The framework sends the interface displacements to the related modules so they can determine the internal displacements using Eq. 2.13. For high-performance matrix calculations including the static condensation procedure and solution of the equilibrium equation, numerical modules and Cyrus are linked to the PARDISO library.

As discussed in Section 2.3.2.1, numerical modules can be based on either the secant or tangent stiffness-based methods. The VecTor suite of programs are integrated into the simulation framework using the Module Type 1 integration format. VecTor2, VecTor3, VecTor4, and VecTor6 are based on the secant solution scheme; whereas VecTor5 uses a hybridized (tangent-secant) solution scheme.

The simulation procedure only requires transferring stiffness and force values of interface DOFs, minimizing the amount of communication. In addition, since the analysis procedure of each numerical module including solution of the internal displacements is performed in parallel, the simulation time can be significantly lower compared to that of the single-platform analysis. It should be noted that for each step of the simulation, the substructure modules need to find the condensed forms of the stiffness matrix and force vector which require matrix inversion. Without the use of high-performance matrix calculations libraries, the time required for the static condensation procedure can significantly influence the total analysis time.

With the cantilever beam example shown in Figure 2.14, considering DOF 1 and DOF 2 as the interface degrees of freedom, the condensed forms of the stiffness matrix and force vector can be computed using Eq. 2.12:

$$[\mathrm{K}]_c = \begin{bmatrix} a & b \\ e & f \end{bmatrix} - \begin{bmatrix} c & d \\ g & h \end{bmatrix} \begin{bmatrix} k & l \\ o & p \end{bmatrix}^{-1} \begin{bmatrix} i & j \\ m & n \end{bmatrix} \tag{2.17}$$

$$\begin{Bmatrix} P_1 \\ P_2 \end{Bmatrix}_c = \begin{Bmatrix} P_1 \\ P_2 \end{Bmatrix} - \begin{bmatrix} c & d \\ g & h \end{bmatrix} \begin{bmatrix} k & l \\ o & p \end{bmatrix}^{-1} \begin{Bmatrix} P_3 \\ P_4 \end{Bmatrix} \tag{2.18}$$

Performing matrix calculations results in the following equations:

$$[\mathrm{K}]_c = \begin{bmatrix} a & b \\ e & f \end{bmatrix} - \left(\frac{1}{lo - kp}\right) \begin{bmatrix} -dkm + clm + dio - cip & -dkn + cln + djo - cjp \\ -hkm + glm + hio - gip & -hkn + gln + hjo - gjp \end{bmatrix} \tag{2.19}$$

$$\begin{Bmatrix} P_1 \\ P_2 \end{Bmatrix}_c = \begin{Bmatrix} P_1 \\ P_2 \end{Bmatrix} - \left(\frac{1}{lo - kp}\right) \begin{bmatrix} do - cp & -dk + cl \\ ho - gp & -hk + gl \end{bmatrix} \begin{Bmatrix} P_3 \\ P_4 \end{Bmatrix} \tag{2.20}$$

Module Type 2

For analysis software that do not output the stiffness and unbalanced force values, the simulation framework employs the modified Newton Raphson procedure to integrate the module. The procedure consists of two steps: 1) stiffness evaluation and 2) integrated analysis, which are explained in the following.

To estimate the condensed form of the stiffness matrix ($[K]_c$), without having access to the global stiffness matrix ([K]), the simulation framework sends small displacements to each interface DOF, while restraining other interface DOFs, and collects the computed restoring forces. It can be shown that the stiffness matrix assembled from the restoring forces is equal to the condensed form of the stiffness matrix expressed in Eq. 2.12. For example, with the cantilever beam structure, the equilibrium equation can be written as:

$$\begin{Bmatrix} P_1 \\ P_2 \\ P_3 \\ P_4 \end{Bmatrix} = \begin{bmatrix} a & b & c & d \\ e & f & g & h \\ i & j & k & l \\ m & n & o & p \end{bmatrix} \begin{Bmatrix} U_1 \\ U_2 \\ U_3 \\ U_4 \end{Bmatrix} \tag{2.21}$$

Imposing a unit displacement at the interface DOF 1 ($U_1 = 1$), while restraining the displacement at the interface DOF 2 ($U_2 = 0$), yields the following equation:

$$\begin{Bmatrix} P_1 \\ P_2 \end{Bmatrix} = \begin{Bmatrix} a \\ e \end{Bmatrix} + \begin{bmatrix} c & d \\ g & h \end{bmatrix} \begin{Bmatrix} U_3 \\ U_4 \end{Bmatrix} \tag{2.22}$$

Also, by eliminating the rows and columns associated with the interface DOFs from Eq. 2.21, the equilibrium equation for the internal DOFs can be found as:

$$\begin{Bmatrix} P_3 \\ P_4 \end{Bmatrix} = \begin{Bmatrix} i \\ m \end{Bmatrix} + \begin{bmatrix} k & l \\ o & p \end{bmatrix} \begin{Bmatrix} U_3 \\ U_4 \end{Bmatrix} \tag{2.23}$$

Since during the stiffness evaluation the external forces are zero, U_3 and U_4 can be computed as:

$$\begin{Bmatrix} U_3 \\ U_4 \end{Bmatrix} = \left(\frac{1}{lo - kp}\right) \begin{Bmatrix} pi - ml \\ km - io \end{Bmatrix} \tag{2.24}$$

Substituting Eq. 2.24 into Eq. 2.22, the equivalent forces for the applied displacements can be found:

$$\begin{Bmatrix} P_1 \\ P_2 \end{Bmatrix} = \begin{Bmatrix} a \\ e \end{Bmatrix} + \left(\frac{1}{lo - kp}\right) \begin{Bmatrix} cip - clm + dkm - dio \\ gip - glm + hkm - hio \end{Bmatrix} \tag{2.25}$$

Comparing Eq. 2.25 and Eq. 2.19 demonstrates that P_1 and P_2 are equal to the K_{11} and K_{21} terms of $[K]_c$, respectively. By imposing the unit displacement at DOF 2, while restraining the displacement at DOF 1, the K_{22} and K_{12} terms can also be computed in a similar manner. Therefore, the stiffness matrix assembled from the restoring forces is equal to the condensed form of the stiffness matrix presented in Eq. 2.19.

To minimize the communication and analysis time, the simulation framework carries out the stiffness evaluation step only at the beginning of the analysis, estimating the condensed form of the initial stiffness matrix, $[K]_{i,c}$. This stiffness matrix will be used throughout the integrated analysis.

After determining $[K]_{i,c}$, the modified Newton Raphson procedure is employed to satisfy the equilibrium and compatibility requirements at the interface sections of the substructure modules. In each step of the simulation, the framework imposes displacements, determined from previous load stage, at the interface DOFs on each module ($\{D_m\}$) and receives the computed restoring forces ($\{P_m\}_r$). To satisfy equilibrium at each node, the summation of the restoring forces from connecting elements should be equal to the external forces applied at that node. Assuming the external forces at the internal DOFs are zero, based on Eq. 2.12, the restoring force vector at the interface DOFs be equal to its condensed form:

$$\{P_m\}_{r,c} = \{P_m\}_r - [K_{mn}][K_{nn}]^{-1}\{P_n\}_r = \{P_m\}_r \tag{2.26}$$

where subscripts “m” and “n” correspond to the interface and internal DOFs, respectively, and subscripts “r” and “c” indicate the restoring force and condensed form of the force vector, respectively. For the interface DOFs, using $\{P_m\}_{r,c}$ and the condensed form of the linear elastic force vector ($\{P_m\}_{e,c}$), calculated from the equilibrium equation (Eq. 2.27), the condensed form of the unbalanced force vector can be determined ($\{P_m\}_{u,c}$):

$$\{P_m\}_{e,c} = [K]_{i,c}\{D_m\} \tag{2.27}$$

$$\{P_m\}_{u,c} = \{P_m\}_{e,c} + \left(\{P_m\}_{e,c} - \{P_m\}_{r,c}\right) = 2\{P_m\}_{e,c} - \{P_m\}_{r,c} \tag{2.28}$$

Figure 2.15 provides a graphical illustration of the unbalanced force calculations using the modified Newton Raphson procedure.

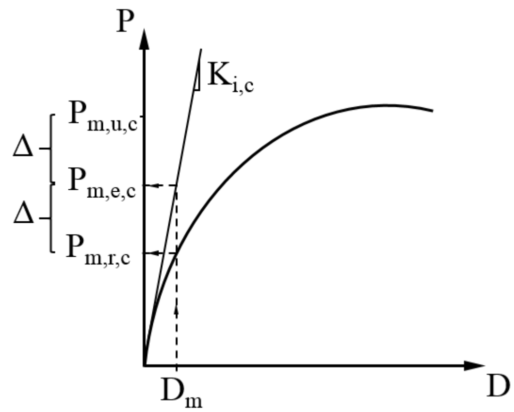

Figure 2.15 Modified Newton Raphson procedure used for Module Type 2

Knowing $[K]_{i,c}$ and $\{P_m\}_{u,c}$, a similar procedure to that described for the Module Type 1 can be used to integrate the module into the system and find the interface displacements of next step. The integrated analysis procedure is repeated until either the interface displacements converge within a predefined error limit, or a predefined maximum number of iterations are performed.

Figure 2.16 shows the algorithm of the solution scheme in the proposed multi-platform simulation framework for the Module Type 1 and Module Type 2. With Module Type 2, the network communication is provided by the NICA interface program. In each step of the simulation, the framework sends the following commands to NICA:

1) Update the load section of the input files based on the computed interface displacements.
2) Run the module to perform the analysis.
3) Read the related restoring forces from the analysis output files.

The Module Type 2 configuration is also used to integrate the physical test specimens into the simulation framework. A comprehensive discussion of physical module integration is provided in Section 5.3 of Chapter 5.

Although the Module Type 2 integration format eliminates modifications to the source code of the program, its iterative procedure at the interface sections can be computationally expensive and therefore its application to sophisticated analysis tools that require several iterations for computing the restoring forces may not be practical (e.g., VecTor suite of software). For this type of analysis tools, the Module Type 1 integration format should be used.

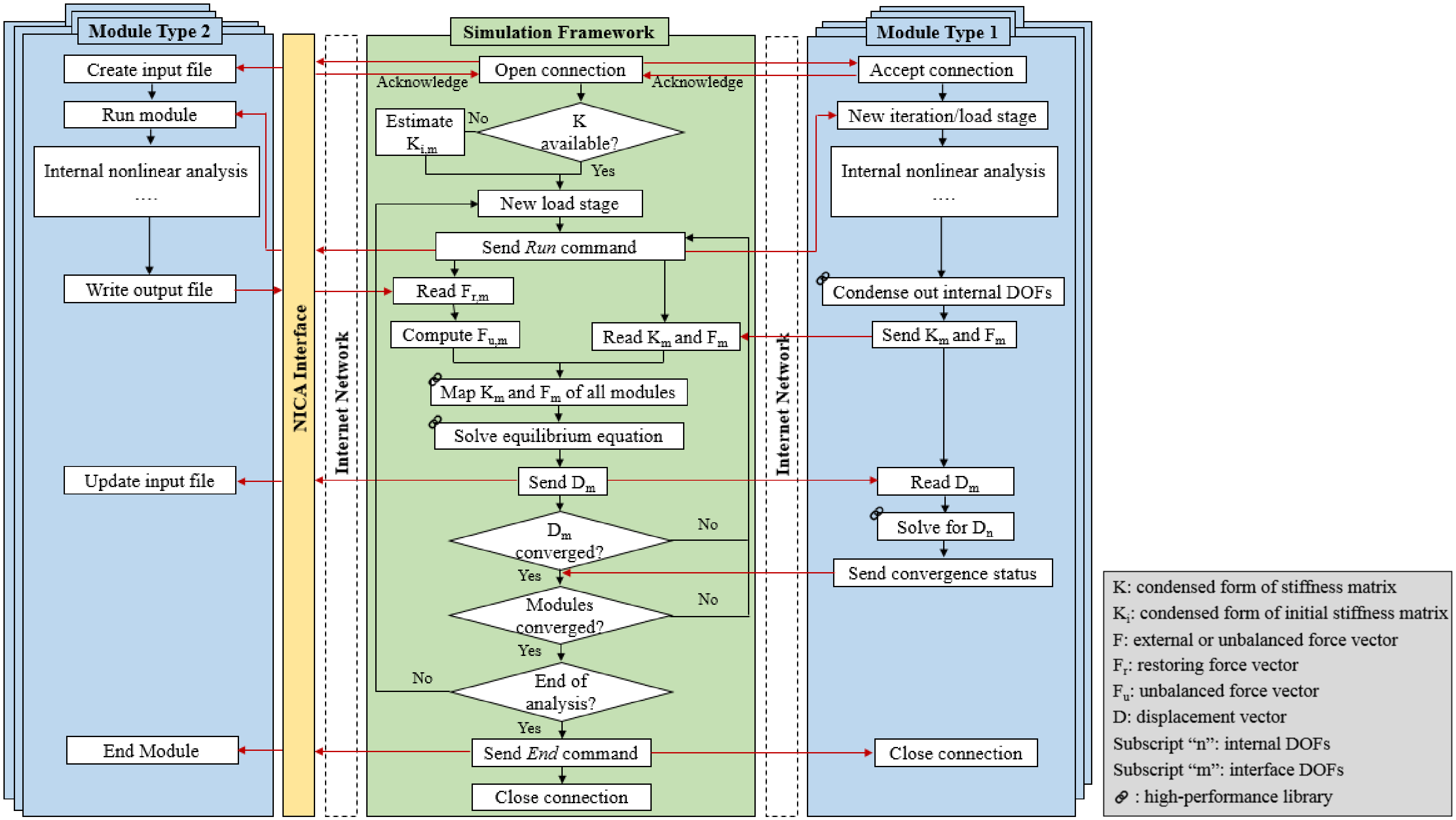

Figure 2.16 Algorithm of the proposed multi-platform framework

2.3.3 Communication Methods

To exchange data among substructures, Cyrus includes three types of communication methods: pipes, files (ASCII and binary formats), and TCP/IP sockets. The first two methods provide inter-process communication for transferring data between two or more instances of analysis software in a single computer. The last method enables distributed communication between multiple computers connected through the Internet network. A brief description of each communication method is provided in the following. Figure 2.17 shows the overall architecture of the methods.

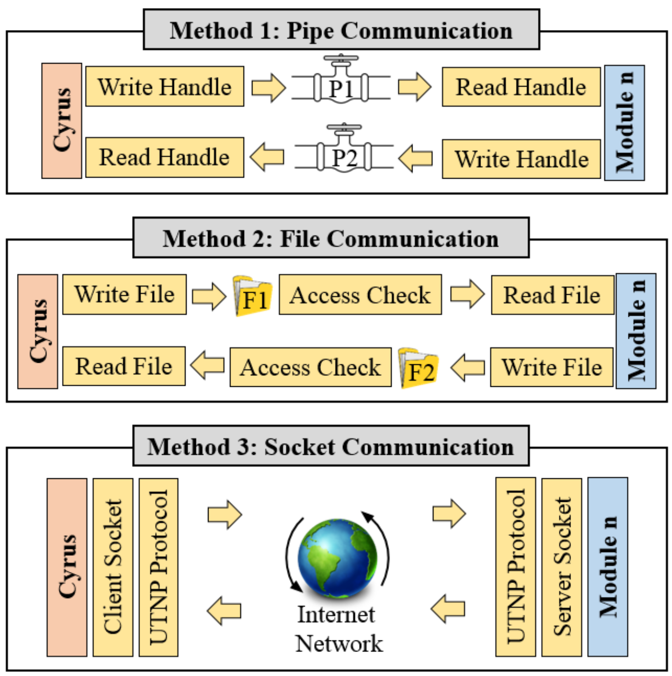

Figure 2.17 Communication methods implemented in the simulation framework

The pipe communication is used to redirect inputs and outputs of the proposed simulation framework (Cyrus) and substructure modules, and send them control commands (e.g., run and pause). To exchange data in both directions, the framework creates two anonymous pipes per module. It writes data to one pipe using its write handle, and the module reads the data from that pipe using its read handle. Similarly, the module writes data to the other pipe and the framework reads from it. The pipes have a limited buffer size that depends on the system properties. If the size of the data is larger than the buffer size, the program transfers the data in multiple byte blocks.

For large structural systems, using the pipe option to transfer data in multiple byte blocks can be time-consuming. To improve communication performance, binary format files are used in conjunction with the pipes. In this configuration, the pipes are responsible for sending control commands, whereas the binary files are used to transfer the restoring force, stiffness, and displacement values. Unlike the pipes, there is no size limitation for the files; therefore, all data can be transferred in a single file instead of multiple byte blocks. To facilitate the debugging process, ASCII format files are also incorporated into the system as a communication method.

Both the pipes and files are local communication methods and cannot be used over a network. To perform geographically distributed simulation or connect multiple distinct computing nodes to increase the computational performance and storage capacity of the system, a socket communication method is implemented in the framework. The type of socket used is a stream socket, also known as a connection-oriented socket, which uses TCP (Transmission Control Protocol) internet protocol for exchanging data. In this architecture, each substructure module acts as a server program and creates a socket at the beginning of the simulation. The sockets are placed in the listening state waiting for connection from the framework, which is the client program. Each socket is characterized by a socket address including an IP address and a port number.

To facilitate communication with diverse numerical analysis tools and test specimens, the framework is enhanced with a newly developed standardized data exchange format, known as the University of Toronto Networking Protocol (UTNP) (Huang et al., 2015). As shown in Figure 2.18, the UTNP data exchange format consists of two sections: a header section and its corresponding data section. The header section has the general information of communication and includes the following parts:

- *Version:* indicates the version of the data exchange format.
- *Command:* indicates the communication action (e.g., send target displacements to the substructure modules, and ask them for the restoring forces).

- *Test Type:* indicates whether the hybrid simulation is pseudo-dynamic or real-time.
- *Substructure Type:* specifies whether the type of the substructure is numerical or experimental.
- *Precision:* specifies the precision of data appended to the message header (single precision versus double precision).
- *Data Type:* indicates the type of the appended data which can be either displacement, force, velocity, acceleration, temperature, or any combination thereof.
- *Number of DOFs:* indicates number of DOFs for communication.

The size of the header section is fixed and equal to 16 bytes, whereas the size of the data section depends on the parameters defined in its message header. To facilitate the implementation of the UTNP data exchange format, it is incorporated into a series of network communication functions and compiled as a dynamic-link library (DLL). Any new physical or numerical substructure module can be linked to this library and use its standard functions to communicate with the simulation framework.

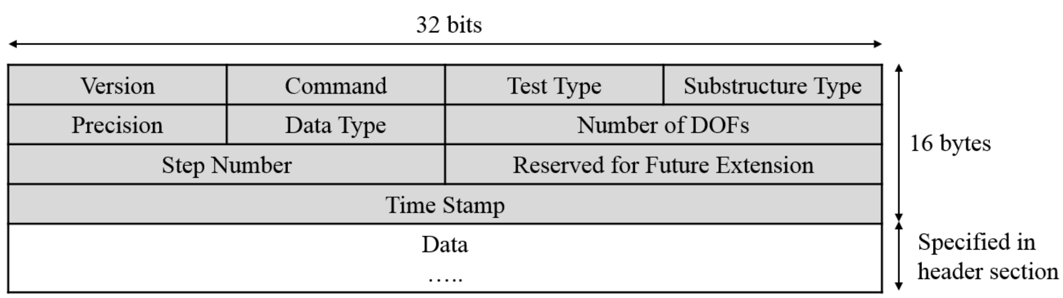

Figure 2.18 UTNP data exchange format (Huang et al., 2015)

2.3.4 Graphical User Interface

FormWorks-Plus (Sadeghian and Vecchio, 2015), the graphical user interface of VecTor suite of software, is further extended to accommodate multi-platform modelling. It allows using various types of modelling and analysis options available in different VecTor programs in a single finite element model. In particular, it can greatly simplify the integration of VecTor2, a membrane finite element program, and VecTor5, a frame-type analysis software. For this type of integration, first the entire structure is modelled using fibre beam elements and analyzed with VecTor5. Based on the analysis results, the user can select the critical frame elements and ask the program to convert them to an equivalent VecTor2 mesh with membrane elements. The geometry of the critical zone and mesh configuration are determined based on the connectivity and properties of the related frame elements, respectively. In addition, the program recognizes the interface sections between membrane and frame elements and automatically connects them using the newly developed F2M elements. A comprehensive discussion of the F2M interface element is provided in Chapter 3.

The simulation framework also includes a graphical user interface that enables adding substructure modules, displaying them on the screen, determining the interface DOFs based on the connectivity of the modules and their nodal coordinates, and selecting the communication method. These features make the multi-platform modelling process more transparent for engineers, contributing to the understanding and utilization of the simulation framework.

2.4 Verification and Application Examples

The proposed framework is verified through multi-platform simulation of two different experimental case studies reported in the literature using the VecTor suite of software. All the analyses were done according to the default material models and analysis parameters, summarized in Table 2.1. In addition, to demonstrate the application of the framework to other analysis tools, the response of a geotechnical-structural system is investigated by integrating the VecTor2 and OpenSees programs. Lastly, the computational performance of the framework is evaluated by three-dimensional analyses of a reinforced concrete column.

Table 2.1 Default material models and analysis options for VecTor suite of software

Concrete Models		Reinforcement Models	
Compression Pre-Peak	Hognestad	Hysteretic Response	Seckin
Compression Post-Peak	Modified Park-Kent	Dowel Action	Tassios (Crack Slip)
Compression Softening	Vecchio 1992-A	Buckling	Akkaya 2013
Tension Stiffening	Modified Bentz 2003		
Tension Softening	Bilinear	**Analysis Options**	
Confined Strength	Kupfer/Richart	Strain History	Considered
Dilation	Variable - Orthotropic	Geometric Nonlinearity	Considered
Cracking Criterion	Mohr-Coulomb (Stress)	Section Analysis**	Nonlinear
Crack Stress Calculation	Basic (DSFM/MCFT)	Shear Analysis**	Parabolic Shear Strain
Crack Width Check	Max Crack (Agg/2.5)		
Crack Slip Calculation	Walraven		
Hysteretic Response	Nonlinear-Plastic Offsets		
Bond*	Eligehausen		

* Available in VecTor2 and VecTor3

**Analysis options in VecTor4 and VecTor5

2.4.1 Wide Flange Shear Wall

Palermo and Vecchio (2002) tested a large-scale reinforced concrete shear wall (DP1) under lateral cyclic displacements and constant axial load, as shown in Figure 2.19. The displacement was applied at the mid-depth of the top slab with amplitude increments of 1 mm, with two repetitions at each displacement step. The self-weight of the top slab contributed an additional 260 kN load to the externally imposed axial force of 940 kN. The large overhanging flanges of the wall with an approximate width to height ratio of 0.75, 50% larger than design code specifications, was a significant challenge for the analysis. The material properties of the concrete and reinforcement obtained from compressive cylinder tests and tensile coupon tests, respectively, are presented in Table 2.2.

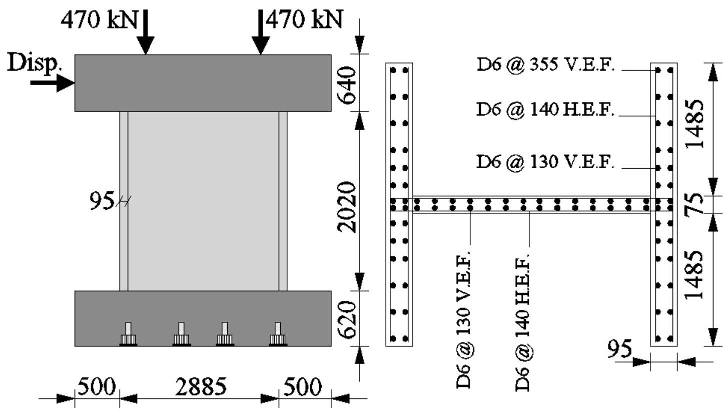

Figure 2.19 Details of the wide flange shear wall tested by Palermo and Vecchio (2002) (dimensions in millimeters)

Table 2.2 Material properties of shear wall

Concrete				
Zone	f'_c (MPa)	ε_o ($\times 10^{-3}$)	E_c (MPa)	Max Agg. Size (mm)
Wall	21.7	2.04	25,900	10
Top Slab	43.9	1.93	43,700	10
Bottom Slab	34.7	1.90	36,900	10

Reinforcement

Bar Size	Diameter (mm)	Area (mm^2)	f_y (MPa)	E_s (MPa)	f_u (MPa)	ε_u ($\times 10^{-3}$)
D6	7.0	38	605	190,250	652	47
30M	29.9	700	550	220,000	696	36

For two-dimensional analysis, modelling the full width of the flanges within a single layer of 2D elements can have some consequences on the stiffness and strength of the structure. Depending on the assumption made for the effective width of the flanges, the level of lateral confinement of the web and amount of shear force carried by the flanges can substantially change. In addition, the shear lag effect occurring in the out-of-plane direction and failure mechanisms such as flange punching cannot be captured in 2D models. To consider three-dimensional effects, a more advanced analysis of the wall is required. Due to the size of the structure and required level of mesh resolution, analyzing the entire structure as a stand-alone single 3D model in a detailed FE program would not be practical. Alternatively, a combination of 2D and 3D analysis tools, each suitable for specific part of the system, can be used to analyze the structure in a reasonable amount of time while considering three-dimensional effects. The proposed simulation framework is used to coordinate the multi-platform analysis. The modelling and analysis results of a 2D model with fully effective flange width assumption and two multi-platform models with different configurations are described here. For all the analysis cases presented in this section, taking advantage of the symmetry of the shear wall and test setup, only half of the structure was modelled.

Stand-Alone Two-Dimensional FE Model

For the 2D model, as shown in Figure 2.20, the structure was divided into four regions (web, flanges, top slab, and bottom slab) and meshed with 8-DOF rectangular elements. Regions varied in terms of material properties and mesh size. Since the top and bottom slabs were heavily reinforced, a larger mesh size was used for these regions. All the nodes located along the bottom row of the bottom slab were fully restrained in both the X and Y translational directions. The external axial load, as well as the self-weight of the top slab, were modelled as vertical loads distributed over all nodes located at the mid-height of the top slab. The lateral load was imposed by controlling the lateral displacement of the node located at the mid-height of the top slab, in 1 mm increments, in a reversed cyclic manner.

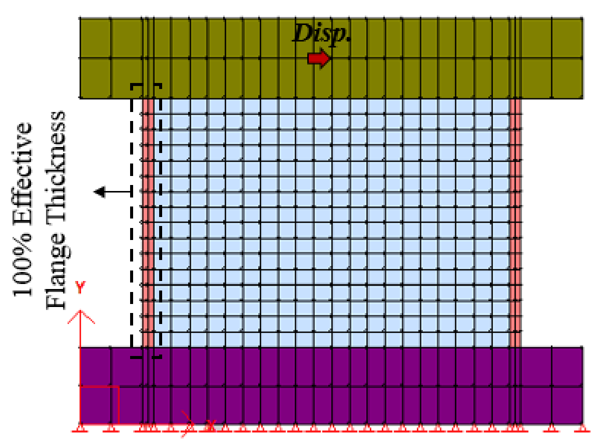

Figure 2.20 2D stand-alone finite element model of shear wall

Mixed-Type FE Models

The multi-platform models were created in two forms: Mixed-Type A and Mixed-Type B. In both model types, the web which experienced predominantly in-plane behaviour was modelled similar to the 2D model and analyzed with VecTor2. The rest of the structure was modelled with 3D programs to capture the out-of-plane effects. The top and bottom slabs were analyzed with VecTor3. For the Mixed-Type A model, the flanges were analyzed with VecTor3 using hexahedral elements while for the Mixed-Type B model they were analyzed with VecTor4 using layered shell elements.

With the Mixed-Type B model, the interface nodes between VecTor3 and VecTor4 were connected in the global X, Y, and Z translational directions. The interface nodes of VecTor4 located between the slabs and flanges were restrained against the rotational displacement around the global Z direction (M_Z). Also, the interface nodes between VecTor2 and VecTor4 were coupled in the global X and Y translational directions. The interface nodes of VecTor4 located between the web and flanges were restrained against the rotational displacement around the global Y direction (M_Y). Restraining rotational displacements of the VecTor4 sub-model were essential to provide stability for the structural system. Figure 2.21 shows different components of the Mixed-Type B model.

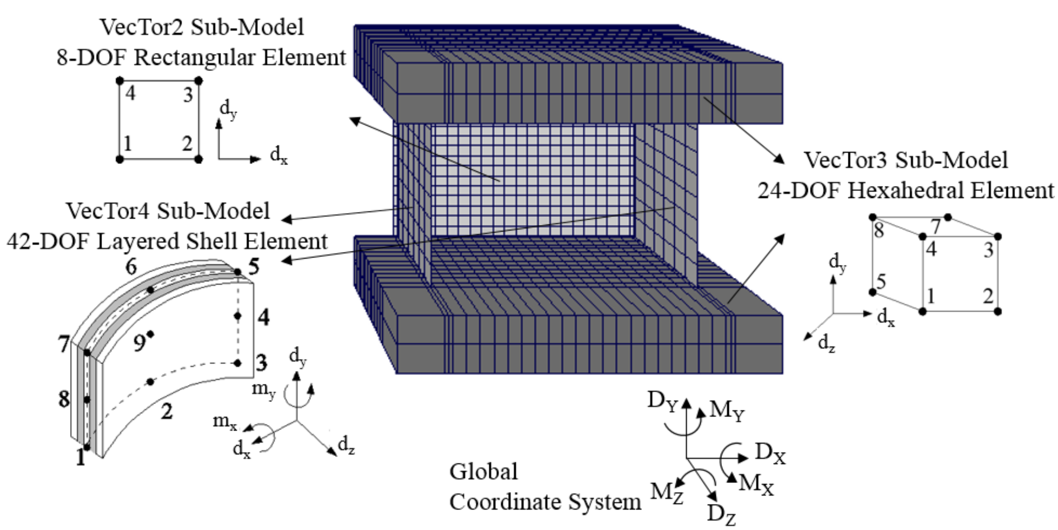

Figure 2.21 Mixed-Type B model of shear wall

The calculated push-over and reversed cyclic load-deflection responses for different analysis cases are compared to the experimental results in Figure 2.22 and Figure 2.23, respectively. The single-platform 2D analysis provided acceptable results; however, it overestimated the stiffness and strength. The multi-platform analyses calculated smaller lateral loads with increasing displacements, resulting in better agreements with the experimental data compared to the 2D analysis. With the Mixed-Type B model, the multi-layer nature of the shell elements enabled a more accurate analysis of the out-of-plane behaviour of the flanges than did the Mixed-Type A model. Compared to the experimentally observed response, all the analysis cases slightly underestimated the initial stiffness of the structure and resulted in a somewhat more dramatic softening effect in the post-peak region.

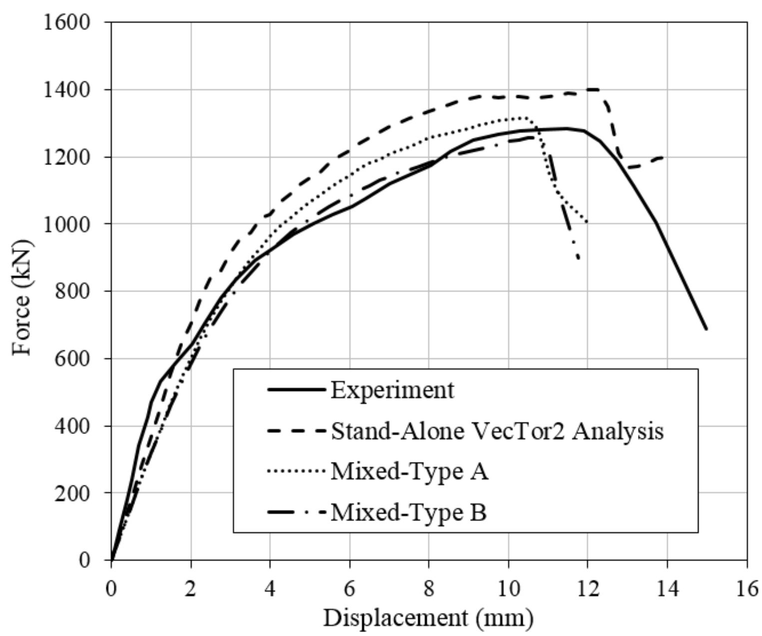

Figure 2.22 Load-deflection responses of push-over analyses versus envelopes of the experiment

The computed failure mode in the multi-platform analysis consisted of a shear failure of the web concrete in horizontal planes near the base and crushing of the concrete at the toe. This caused high shear stresses on the flange elements near the base at the interface section, resulting in punching of the flanges which also contributed to the failure. The failure mode correlated well with the experimental results. The results illustrated that, unlike the 2D analysis, the multi-platform analysis was able to take into account the three-dimensional effects and capture the observed damage to the flanges. The crack pattern and deflected shape of the multi-platform analysis for the Mixed-Type B model at ultimate load are shown in Figure 2.24.

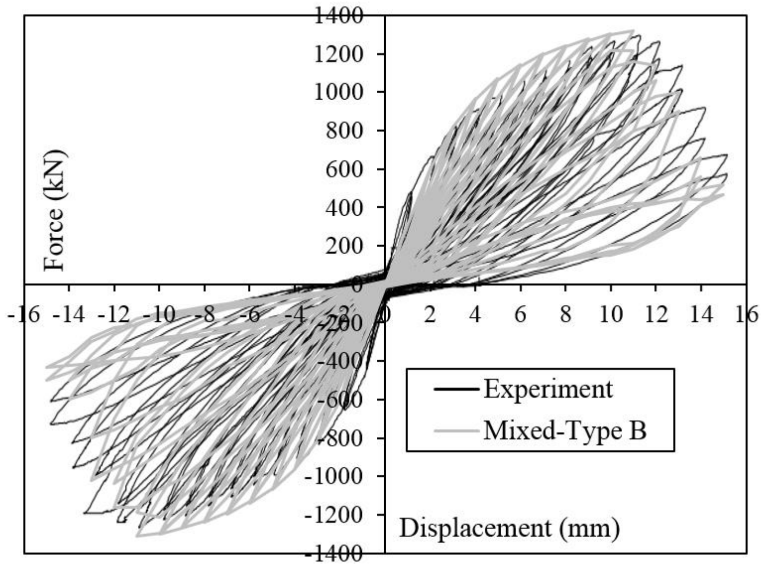

Figure 2.23 Load-deflection responses of shear wall under reversed cyclic loads

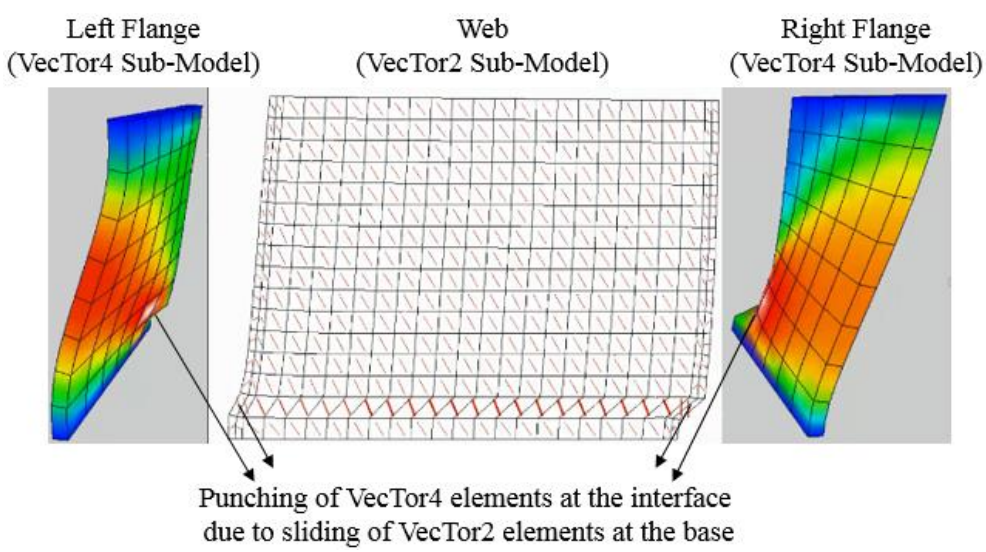

Figure 2.24 Deformed shape of multi-platform analysis for Mixed-Type B model

2.4.2 Three-Storey Frame

Calvi et al. (2002) performed quasi-static cyclic test on a three-story 2/3-scaled reinforced concrete building frame designed only for gravity loads based on typical Italian construction practice common between the 1950s and 1970s. To be consistent with the old design practice, smooth bars were used for the reinforcement and the joint regions were constructed without any transverse reinforcement. Also, instead of bending the longitudinal bars in the exterior joints and providing adequate anchorage length, they were anchored with short 180 degrees end-hooks. The lateral loads were applied in a hybrid force-displacement control manner; the displacement at the top floor was increased in a reversed cyclic regime while maintaining a linear force distribution along the height of the structure. The lateral force distribution was proportional to the mass and height of each storey, as presented in Eq. 2.29. In addition, a gravity load of 73 kN was applied on the first and second floors and 54.2 kN was imposed on the third floor. Figure 2.25 shows dimensions and reinforcement details of the frame structure.

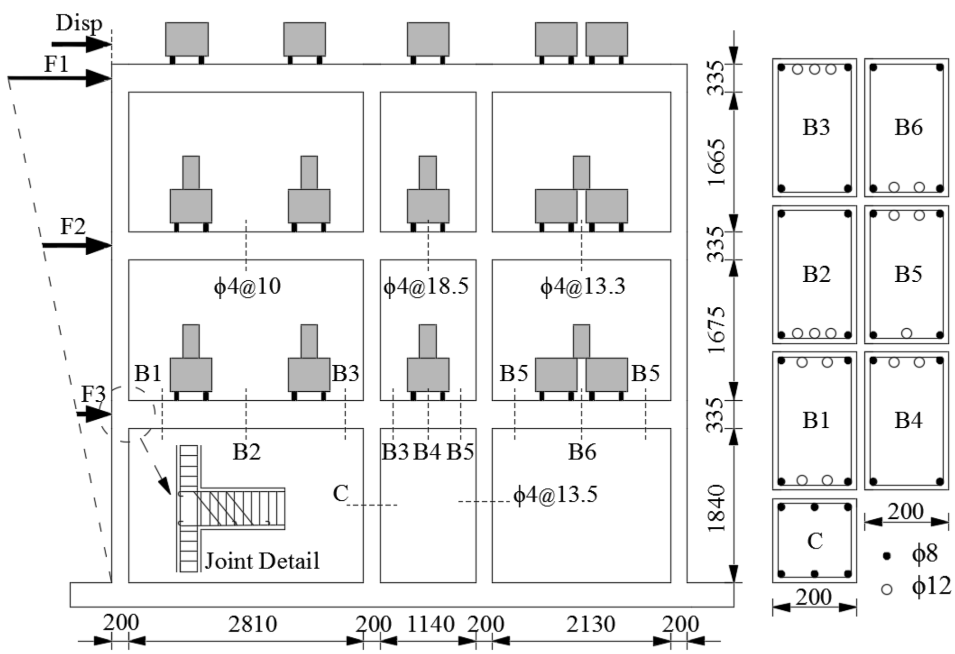

Figure 2.25 Details of RC frame tested by Calvi et al. (2002) (dimensions in millimeters)

$$\{F\} = \begin{Bmatrix} F_1 \\ F_2 \\ F_3 \end{Bmatrix} \rightarrow \frac{\{F\}}{F_1} = \begin{Bmatrix} 1 \\ \dfrac{F_2}{F_1} \\ \dfrac{F_3}{F_1} \end{Bmatrix} = \begin{Bmatrix} 1 \\ (\dfrac{m_2}{m_1})(\dfrac{h_2}{h_1}) \\ (\dfrac{m_3}{m_1})(\dfrac{h_3}{h_1}) \end{Bmatrix} = \begin{Bmatrix} 1.00 \\ 0.90 \\ 0.45 \end{Bmatrix} \tag{2.29}$$

The strength of the concrete obtained from compressive cube tests and the properties of the reinforcement measured from tensile coupon tests are presented in Table 2.3 and Table 2.4, respectively. The equivalent compressive strength of concrete from cylinder tests was found by dividing the values of Table 2.3 by a factor of 1.25. Other material properties of the concrete were determined based on the default material relationships available in the VecTor programs (Wong et al., 2013). Also, the modulus of elasticity and ultimate strain of the Φ8 and Φ12 reinforcing bars, which were not available in the test report, were assumed to be equal to those of the Φ4 reinforcement.

Table 2.3 Compressive strength of concrete cubes for RC frame

Storey	Member	f'_{ck} (MPa)
1st storey	Column	17.8
	Beam	13.3
2nd storey	Column	13.2
	Beam	13.8
3rd storey	Column	13.5
	Beam	12.7

Table 2.4 Reinforcement properties for RC frame

Reinforcement						
Bar Size	Diameter (mm)	Area (mm^2)	f_y (MPa)	E_s (MPa)	f_u (MPa)	ε_u ($\times 10^{-3}$)
Φ4	4	12	350	106,060	400	17
Φ8	8	50	386	N/A	451	N/A
Φ12	12	113	346	N/A	459	N/A

According to the test results, the poor detailing of the reinforcement led to a brittle failure mode with most of the damage concentrated in the exterior beam-column joint regions of the first floor. As shown in Figure 2.26, the failure mechanism consisted of shear cracks in the joint region along with the formation of a wide flexural crack at the interface of the beam due to slip of the smooth bars.

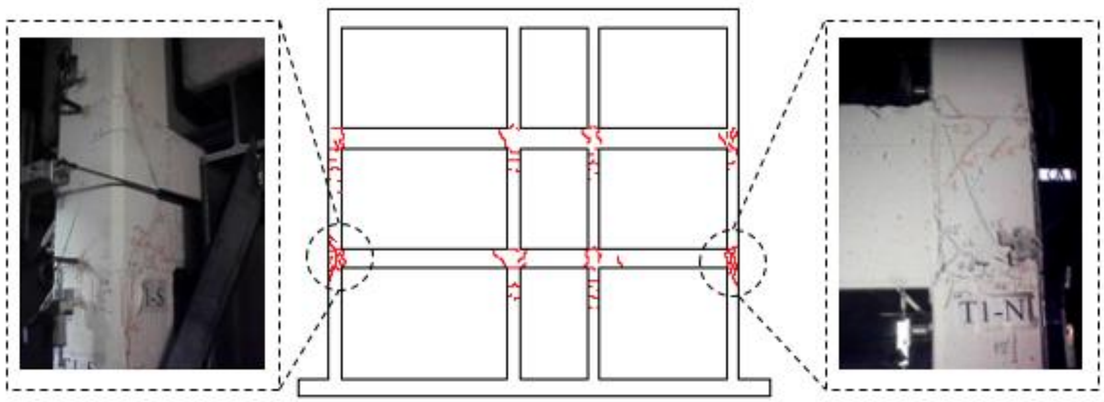

Figure 2.26 Experimentally obsereved crack pattern at ultimate load (Calvi et al., 2002)

A frame model of the entire structure was analyzed using VecTor5. A total of 338 layered elements with member lengths of about half of the cross section depth were used. Each element was divided into about 30 concrete layers, providing sufficient accuracy for the sectional analysis. Based on the configuration of the stirrups, the out-of-plane reinforcement ratio (ρ_z) and transverse reinforcement ratio (ρ_t) were determined and assigned to the outer layers and core layers of the cross section, respectively. Like other sectional analysis procedures, VecTor5 is unable to rigorously analyze disturbed regions; thus, as suggested by Guner and Vecchio (2010b), the amount of reinforcement in the beam-column joint regions was increased by a factor of two to avoid artificial damage. The gravity loads were modelled as nodal and element forces in the vertical direction representing the externally applied loads and self-weight of the structure, respectively. Because the hybrid force-displacement type of loading is not available in VecTor5, instead of applying the lateral loads in a reversed cyclic manner a push-over analysis was performed. The lateral loads were modelled with nodal forces and monotonically increased up to the failure point in increments of 0.5 kN.

The load-deflection response of the push-over analysis is compared to the experimentally observed behaviour in Figure 2.28. The stand-alone VecTor5 analysis response agreed reasonably well with the experimental results up to the point where the joints began to crack. However, beyond this point, the analysis began to overestimate the strength and stiffness, resulting in much higher failure load than the experiment. This is a consequence of the limitations associated with most frame analysis software, including VecTor5, which are: 1) the plane sections remain plane assumption in the sectional analysis procedure is not applicable to disturbed regions such as beam-column joints where the strain distribution is highly nonlinear, 2) the assumptions used for stiffening the joint regions can affect the stiffness of the system, and 3) the frame elements assume perfect bond between the concrete and reinforcement; however, high levels of slip can occur in the joint panels and at the beam interfaces, particularly if the reinforcement detailing is insufficient.

The proposed multi-platform analysis procedure can be used to address the deficiencies related to frame analysis methods and extend their application from a global analysis tool to include local behaviour of critical parts of the structure. Here, based on the stand-alone frame analysis results and experimental crack pattern presented in Figure 2.26, the external joints in the first floor and an extension of the connecting members in each direction (equal to the member height) were selected as critical components of the structure. These regions were modelled using a more detailed analysis software, VecTor2, while the rest of the structure was modelled using frame analysis software VecTor5. The newly developed beam-membrane interface element, the F2M element (discussed in Chapter 3), was used to connect the two finite element sub-models. Cyrus combined the two sub-models and coordinated the multi-platform analysis. For the VecTor2 sub-model, rectangular and truss elements were used to model the concrete and longitudinal reinforcement, respectively, while the transverse reinforcement was modelled as smeared. In addition, link elements were used between rectangular elements and truss elements to capture any possible bond-slip effects. Details of the multi-platform model and its VecTor2 sub-model are shown in Figure 2.27.

Based on the load-deflection responses presented in Figure 2.28, the multi-platform analysis computed the peak load and stiffness values with much better accuracy compared to the stand-alone analysis. The multi-platform analysis predicted multiple cracks in the joint panel zone as well as the formation of a wide flexural crack at the beam-column interface. Thereafter, a large amount of slip was computed in the longitudinal reinforcement of the beams at the interface section, resulting in a significant reduction in the stiffness of the system. As shown in Figure 2.29, the computed crack pattern agreed well with the experimentally observed behaviour. The analysis also showed post-peak decay in strength due to local failure in the joints. None of these mechanisms were captured in the stand-alone frame analysis, illustrating the effectiveness of the multi-platform simulation.

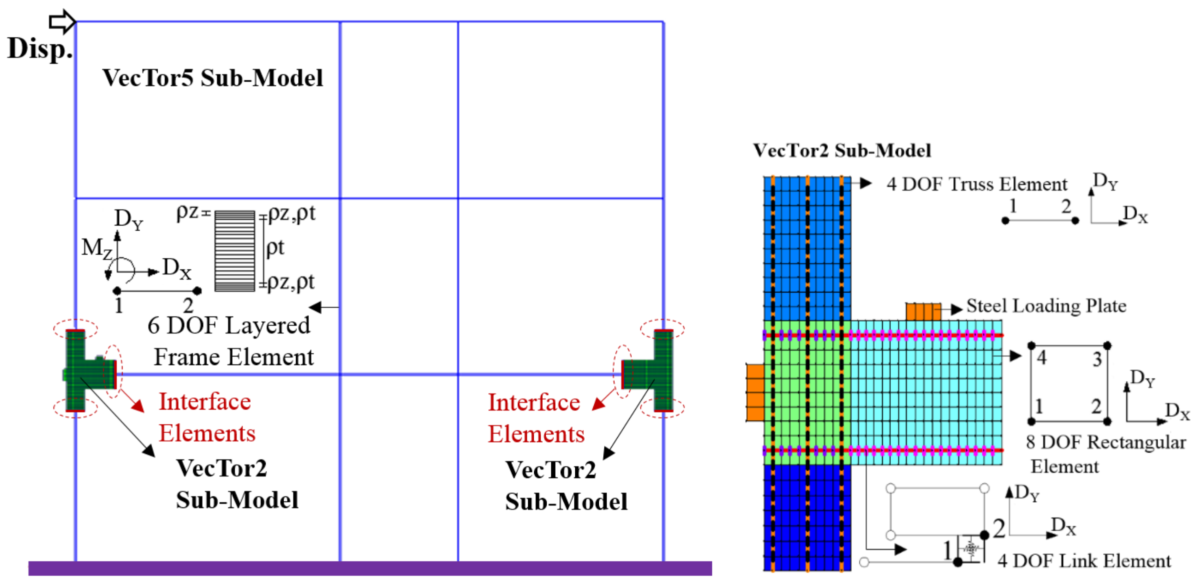

Figure 2.27 Multi-platform finite element model of RC frame

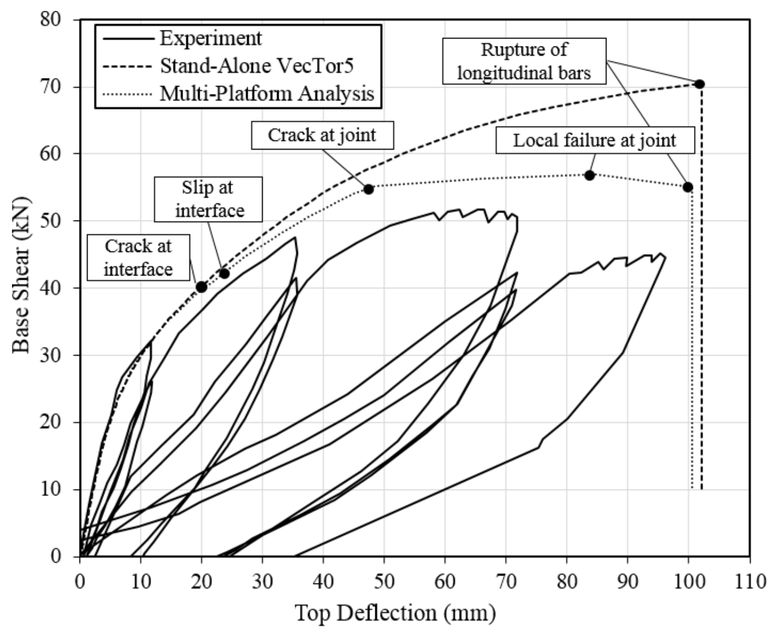

Figure 2.28 Analyitcal and experimental load-deflection responses for RC frame

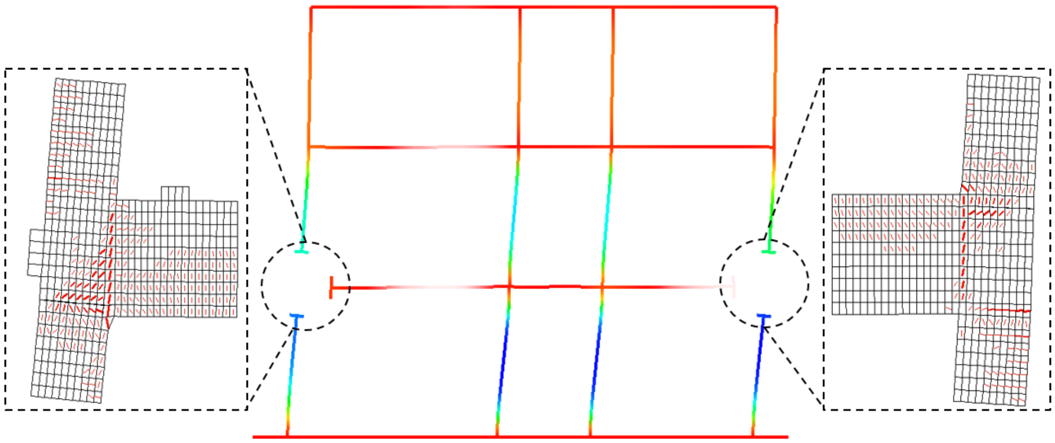

Figure 2.29 Crack pattern obtained from multi-platform analysis at peak load

2.4.3 Soil-Structure Interaction

To demonstrate the capability of the proposed simulation framework for integrating analysis tools whose source code is not accessible, a soil-structure interaction analysis was performed using the VecTor2 and OpenSees programs. To integrate the OpenSees module, only the input and output files containing model information and analysis results were used. The structural-geotechnical system was a one-storey one-bay reinforced concrete frame structure constructed on different types of clay soils. Details of the system are shown in Figure 2.30. The column clear height was 2.0 m and the beam clear span was 2.2 m. Each column was attached to a footing pad with dimensions of 1.2 m long, 0.8 m wide, and 0.4 m thick. The soil domain was extended from each side of the foundation by 4 m and had a depth and thickness of 5 m. An axial load of 420 kN was imposed on each column and maintained during the analysis in a force-controlled manner. The lateral load was applied in a displacement-controlled manner at the mid-depth of the beam. The expected failure mode of the frame was shear failure of the columns which had low amounts of transverse reinforcement (ρ_v = 0.1%). The influence of three types of clay soils with different stiffness values (stiff clay, medium clay, and soft clay) were evaluated.

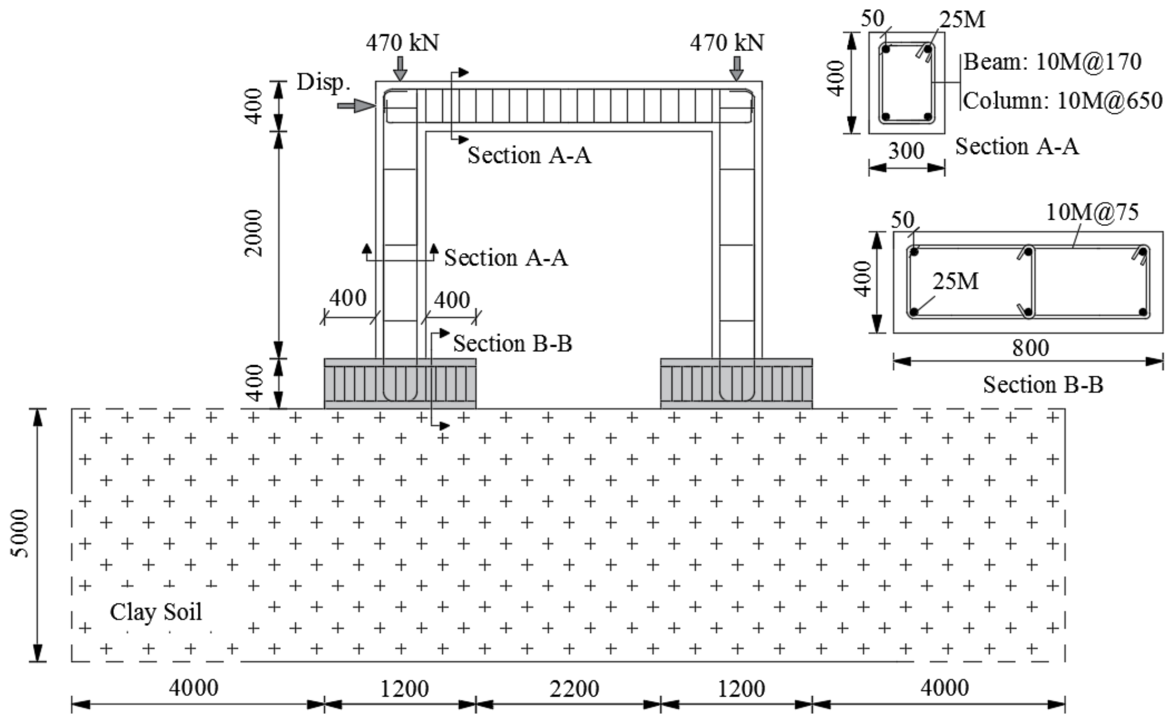

Figure 2.30 Details of frame and soil domain
(dimensions are in millimeters and not to scale)

The material properties of the frame structure and different types of clay soils, as suggested in the User's Manual of OpenSees (2012), are presented in Table 2.5 and Table 2.6, respectively.

Table 2.5 Material properties of RC frame

Concrete			
f'_c (MPa)	ε_o ($\times 10^{-3}$)	E_c (MPa)	Max Agg. Size (mm)
30.0	2.02	25,100	20

Reinforcement							
Bar Size	Diameter (mm)	Area (mm^2)	f_y (MPa)	E_s (MPa)	E_{sh} (MPa)	f_u (MPa)	ε_u ($\times 10^{-3}$)
10M	11.3	100	400	200,000	1430	600	150
25M	25.2	500	400	200,000	1430	600	150

Table 2.6 Material properties of different types of clay soils

Clay Type	ρ (ton/m^3)	G_r (kN/m^2)	B_r (kN/m^2)	c (kN/m^2)	γ_{max} (m/m)	Φ (degree)	P_r (kN/m^2)	d
Stiff	1.8	1.5×10^5	7.5×10^5	75	0.1	0	100	0
Medium	1.5	6.0×10^4	3.0×10^5	37	0.1	0	100	0
Soft	1.3	1.3×10^4	6.5×10^4	18	0.1	0	100	0

ρ: saturated soil mass density.

G_r: reference shear modulus, specified at P_r.

B_r: reference bulk modulus, specified at P_r.

c: apparent cohesion at zero effective confinement.

γ_{max}: an octahedral shear strain corresponding to the maximum shear strength, specified at P_r.

Φ: friction angle at peak shear strength.

P_r: reference mean effective confining pressure at which G_r, B_r, and γ_{max} are defined.

D: a positive constant defining variations of shear modulus and bulk modulus as a function of instantaneous effective confinement.

To investigate the influence of the soil on the behaviour of the structure, two types of analyses were performed:

1) A stand-alone analysis: the influence of the soil was neglected and only the structure was analyzed using VecTor2 assuming fully fixed foundation.
2) Multi-platform analyses: the structure and soil were modelled in VecTor2 and OpenSees, respectively, and analyses were performed in an integrated manner for three types of soils.

The following is a description of the model and computed results for each case study.

Stand-Alone Model

The frame structure was modelled using 2282 four-noded rectangular elements, representing the concrete, and 542 two-noded truss elements, representing the longitudinal reinforcement. The transverse reinforcement was added as a smeared component to the concrete elements. Since the influence of the soil was neglected, all the nodes located at the bottom row of the footings were fully restrained in both the X and Y translational directions, simulating the fixed end condition for the frame. A constant nodal force of 420 kN was imposed in the downward direction at the top of each column. The lateral load was applied by gradually increasing the lateral displacement of the left-end node of the beam located at mid-height of the cross section in increments of 0.5 mm. To avoid local failure under the loads, the nodal forces were applied on steel plates with dimensions of 300 mm × 160 mm × 40 mm. Figure 2.31 shows the stand-alone finite element model that was analyzed with VecTor2.

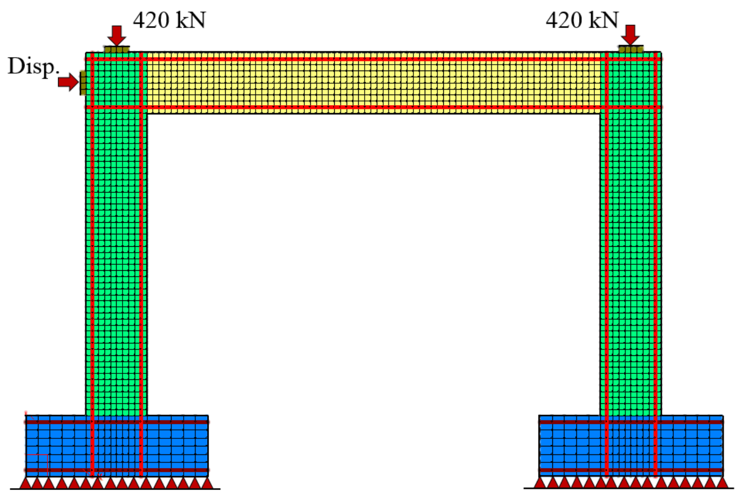

Figure 2.31 Stand-alone VecTor2 finite element model

Multi-Platform Model

For the frame structure, a similar model to that described for the stand-alone VecTor2 analysis was employed. The soil was modelled with OpenSees using 2025 four-noded quadrilateral elements assuming a plane strain behaviour. Beneath the footings the elements had a mesh size of 40 mm × 100 mm in the X and Y directions, respectively. Moving further from the footings, the mesh size gradually increased to 400 mm in both the X and Y directions. All the boundary nodes located at the left, right, and bottom sides of the soil domain were fully restrained in both the X and Y translational directions. A more realistic simulation of the boundary conditions can be achieved by using spring elements available in the literature (e.g., Mozos and Luco, 2011). For simplicity, the clay soil was represented as a linear elastic material model in which the shear behaviour is not influenced by confinement changes. At the interface section between the frame model and soil model, a total of 42 nodes were fully coupled in the X and Y translational directions. Cyrus simultaneously ran the VecTor2 and OpenSees modules and coordinated the analysis. At the beginning of the simulation, a stiffness evaluation procedure, as described in Section 2.3.2.2, was performed to estimate the condensed form of the initial stiffness of the soil sub-model at the interface DOFs. The multi-platform finite element model of the system is shown in Figure 2.32.

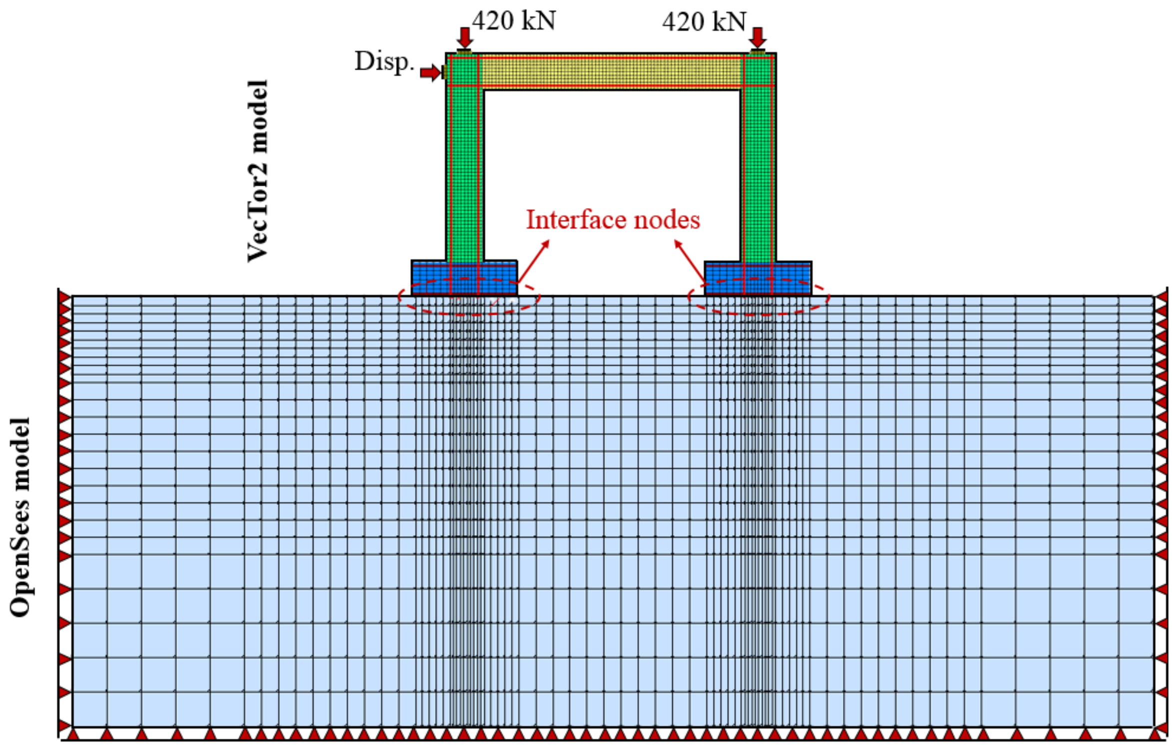

Figure 2.32 Multi-platform finite element model of RC frame and soil

The load-deflection responses of the stand-alone analysis and multi-platform analyses are compared in Figure 2.33. Also, the computed crack patterns are presented in Figure 2.34 and Figure 2.35. It can be seen that neglecting the influence of the soil on the structure resulted in a brittle shear failure in the columns. As shown in Figure 2.34, the damage mode consisted of large diagonal shear cracks at the bottom of the columns which continued as vertical cracks along the longitudinal reinforcement layers. In addition, a horizontal flexural crack was predicted at the interface between the column and foundation. The transverse and longitudinal reinforcements of the columns started to yield at applied lateral displacements of 9 mm and 14 mm, respectively. No major cracks or yielding of reinforcing bars were predicted in the beam and joint panels.

Taking into account the soil-structure interaction using a multi-platform analysis, enabling the consideration of the rotation of the foundations, resulted in more ductile load-deflection responses. As the stiffness of the soil reduced ($G_{r,\,Stiff} = 2.5\ G_{r,\,Medium} = 11.5\ G_{r,\,Soft}$), the amount of rotation and consequently the ductility (i.e., a level of deformation that a structure can undergo without losing a significant amount of strength) of the structure increased. Also, the rotation of the foundations led to higher stress values in the joint panels compared to the fully fixed base analysis case. For example, with the frame constructed on the soft clay soil analysis case, the transverse reinforcement in the joint panels and the longitudinal reinforcement at the interface between the beam and joint panels yielded at the applied lateral displacements of 18 mm and 32 mm, respectively. For the columns, the transverse reinforcement did not yield until a lateral displacement of 53 mm had been applied, and the longitudinal reinforcement did not yield at all. In terms of the damage mode, the first major cracks developed at the left side joint which were followed by a vertical crack in the upper portion of the column. Then, vertical cracks formed at the interface between the beam and the joints with a maximum crack width of 14 mm near the peak load. Finally, similar to the fixed foundation analysis case, diagonal shear cracks started to develop at the bottom of the columns. The final failure was due to excessive crack widths at the interface between the beam and joints and lower portion of the columns leading to a shear failure.

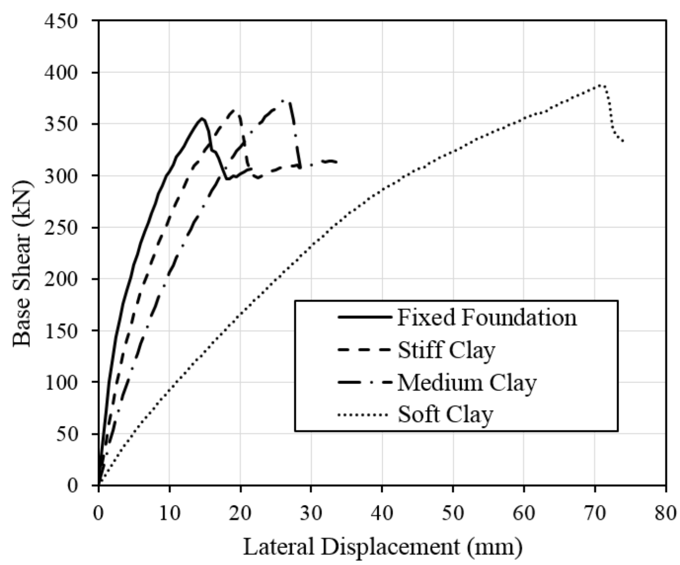

Figure 2.33 Load-deflection responses of RC frame

From the above-mentioned discussion it can be concluded that the soil-structure interaction can affect the stress distribution in the structure and alter the critical regions. With the demonstration example, the multi-platform analysis computed significant damage and yielding of reinforcing bars in the beam, joint panels, and upper portion of the columns, which were not accurately captured by the single-platform analysis assuming fully fixed foundation. Therefore, the influence of soil on the behaviour of the structure should be considered, particularly if the structure is constructed on a soft soil. It should be noted that this was an illustration example in which the response of the soil at the material-level was greatly simplified and the potential sliding at the interface between the soil and the structure was neglected. For the analysis of real-world systems, advanced nonlinear soil models with more realistic representation of the interface section should be employed.

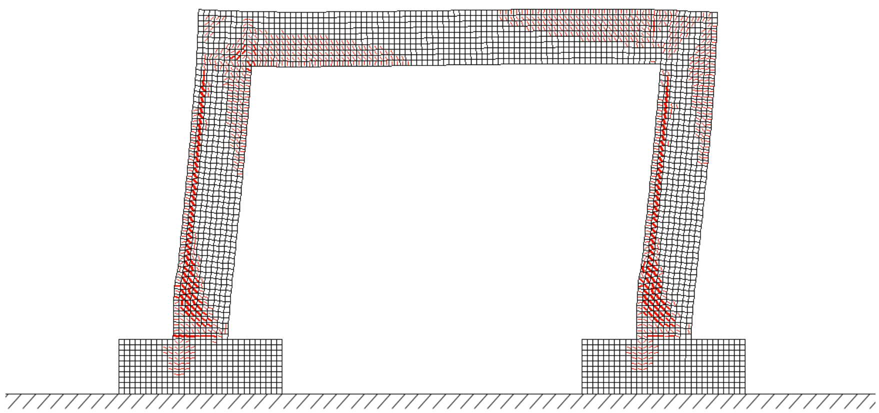

Figure 2.34 Stand-alone analysis crack pattern (displacement maginifcation factor = 10)

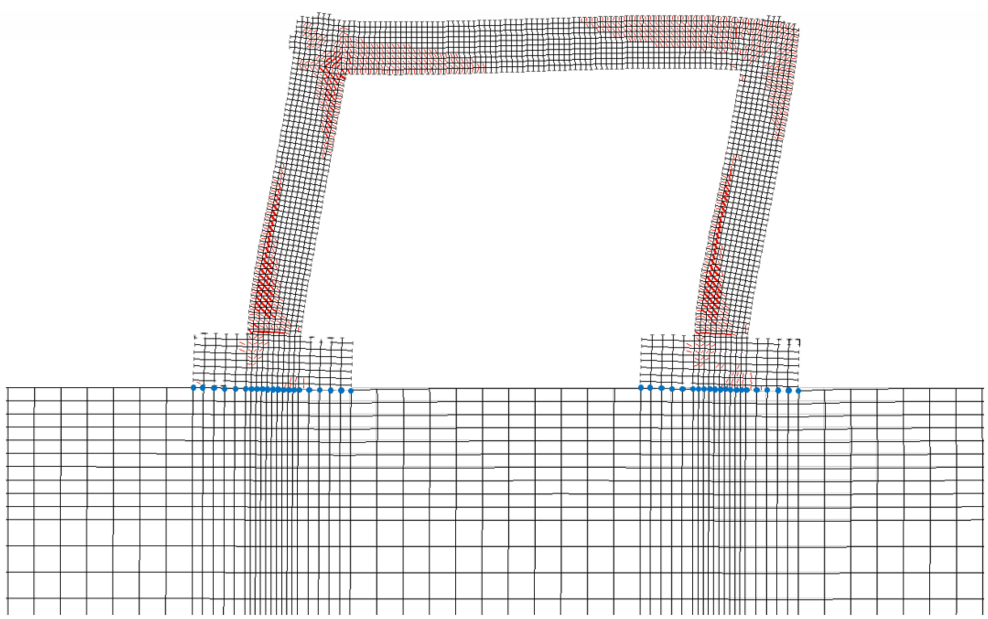

(a) RC frame located on stiff clay soil

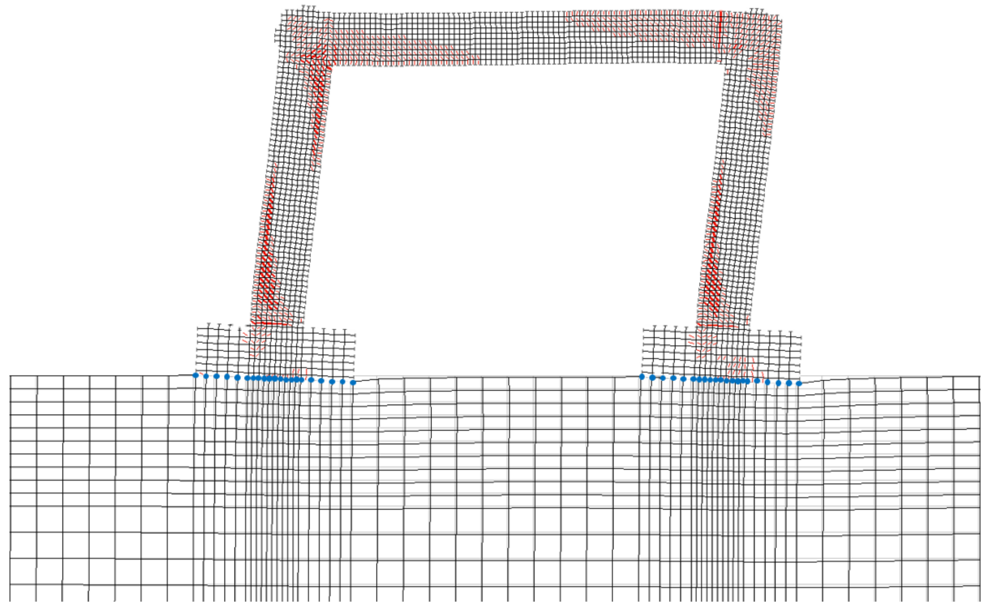

(b) RC frame located on medium clay soil

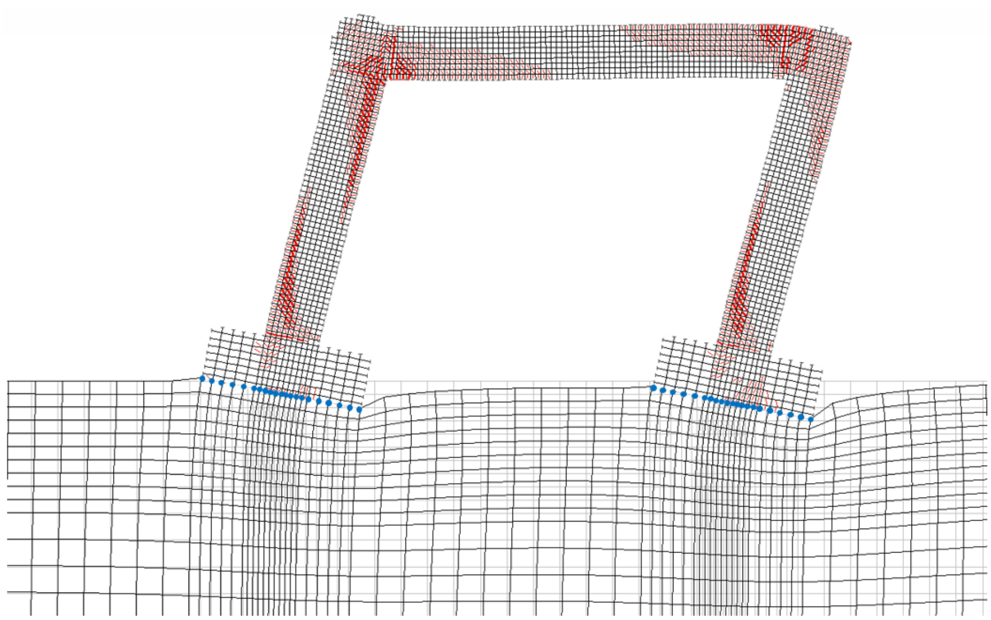

(c) RC frame located on soft clay soil

Figure 2.35 Multi-platform analysis crack patterns (displacement maginifcation factor = 10)

2.4.4 Computational Performance Evaluation

The complex analysis procedure of nonlinear FE programs requires high computational power and storage capacity. In addition, because of the increasing demand for accurately capturing the true behaviour of structures, more complex FE models with finer meshes are required. However, computational resource limitations lead to questions regarding the practical use of nonlinear tools, especially for large structures. The substructuring concept used in the proposed integrated framework enables one to reduce the required computational time and memory storage by distributing the analysis to multiple processors. Parallel computations can be performed on a single computer with multiple processors or on several computers linked together by a network.

The performance of the proposed simulation framework was evaluated through the nonlinear three-dimensional analysis of a reinforced concrete column using the VecTor3 software. As shown in Figure 2.36, to investigate the influence of substructuring, three identical finite element models with varying numbers of substructures (one, two, and three) were created. The configuration of substructure modules was also evaluated by using different numbers of computing nodes each had an Intel Core i7 processor (one, two, and three computers). All the models were identical in terms of number of elements (10,000 elements), element type (hexahedral element), analysis options, and material models. The interface DOFs between substructures were fully connected to produce the exact same system behaviour as that of the stand-alone model. It must be noted that this is an illustration example with the number of computing nodes and substructures limited to three. For a realistic application of parallel computing, a much larger structural system with substantially higher numbers of computing nodes are required.

To evaluate the performance of the system, the multi-platform simulation time was measured in three separate stages: the analysis stage, which included the material nonlinearity computations performed by each module; the solver stage, which consisted of the static condensation phase and solution of the equilibrium equation; and the data transfer stage. Based on the measured total simulation time, a speed-up factor and an efficiency factor were computed for each case. The speed-up factor indicates the relative performance improvement obtained compared to the stand-alone analysis. The efficiency factor is the ratio of the speed-up factor to the ideal speed-up (i.e., linear speed up), describing how well-utilized the processors are.

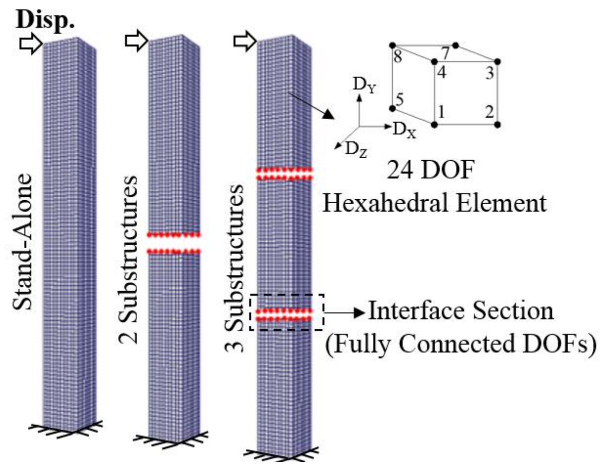

Figure 2.36 Finite element models of RC columns

As shown in Table 2.7, using the multi-platform analysis improved the performance of the system by factors of 1.96 and 2.39 for the two-substructure and three-substructure cases, respectively. Due to the communication time, the relation between the speed-up factor and the number of processors was not linear. As the number of substructures increases, the time required for transferring data increases, reducing the benefit of parallel computing. In addition, based on the comparison of the efficiency factors, the optimum performance is achieved when the number of computing nodes is equal to or greater than the number of substructures. The reason is that, by default, the local analysis in each module is performed in parallel. By changing the local analysis from parallel to sequential, the amount of computing resources required should be reduced. Additionally, it should be noted that using larger sample FE models can produce better speed-up results, making the value of substructuring more apparent. For larger FE models, typically the ratio of internal DOFs to interface DOFs is much higher; therefore, the influence of the communication time on the total simulation time is lower.

Table 2.7 Performance test results for RC column

Model Type	# of Comp. Nodes*	Time Per Load Stage (seconds)				**Speed Up Factor**	**Efficiency Factor**
		Analysis	Data Transfer	Solver	Total		
Stand-Alone	1	40 (17%)	---	197 (83%)	237	1	1
2 Substructure	1	39 (21%)	10 (6%)	133 (73%)	182	1.3	0.65
	2	36 (30%)	11 (9%)	75 (61%)	122	1.94	0.97
	3	41 (34%)	9 (7%)	71 (59%)	121	1.96	0.98
3 Substructure	1	38 (19%)	28 (14%)	134 (67%)	200	1.19	0.40
	2	32 (20%)	28 (18%)	97 (62%)	157	1.51	0.50
	3	22 (22%)	28 (28%)	49 (50%)	99	2.39	0.80

* Each computing node had an Intel Core i7 processor

2.5 Summary and Conclusions

This chapter presented a newly developed multi-platform simulation framework that can integrate different finite element analysis software and test specimens, enabling the accurate simulation of complex reinforced concrete systems. Different parts of the framework including the solution algorithm, communication methods, and graphical user interface were discussed. The combined tangent-secant solution method was verified, demonstrating that analysis tools with different solution algorithms can be integrated. A recently developed standardized data exchange format was implemented into the framework, facilitating communication with diverse numerical analysis tools and test specimens. To verify the framework and demonstrate its capabilities, four case studies were investigated:

1) Multi-platform analysis of a wide flange shear wall structure.
2) Multi-platform analysis of a three-storey frame structure.
3) Multi-platform analysis of a structural-geotechnical system.
4) Computational performance evaluation of three-dimensional analyses of a column structure using different numbers of substructures.

The following conclusions can be drawn from the conducted studies:

- The multi-platform analysis computed the behaviour of the structures with a level of accuracy that was previously difficult to achieve with most single-platform analysis software. For the wide flange shear wall structure, integrating a 2D FE software with 3D FE programs allowed considering the out-of-plane behaviour of critical components in a practical manner. For the three-storey frame structure, the global frame-type analysis was enhanced with an effective solution technique for the detailed analysis of disturbed regions, such as beam-column joints, and bond effects between the reinforcement and concrete. The multi-platform analysis results of both structures agreed well with the experimentally reported responses.

- The one-storey frame example demonstrated that taking into account the soil-structure interaction can influence the behaviour of the structure and result in new damage zones, especially if the structure is located on a soft soil. Multi-platform simulation can be a reliable analysis procedure to consider soil effects, providing a more realistic behaviour of the structure.

- The multi-platform analysis allows dividing the system into several substructures and performing parallel computing which can substantially reduce the overall simulation time. Based on the performance evaluation tests of the three-dimensional column model, for systems with large number of substructures, the communication time between the substructure modules and the framework can be significant. However, for larger finite element models, typically the ratio of internal DOFs to interface DOFs is much higher, which should reduce the influence of the communication time on the total simulation time.

Through the development and verification of the framework, there were several issues identified that could benefit from some level of further development or study:

- The current version of the simulation framework can integrate different VecTor programs for dynamic analysis. The dynamic analysis procedure implemented in the VecTor programs formulates the equation of motion in a similar format as the equilibrium equation with equivalent stiffness matrix and force vector containing the dynamic effects (i.e., inertia, damping, and mass). Therefore, a similar multi-platform analysis procedure to that described in Section 2.3.2 can be employed for structures subjected to dynamic loads. At the beginning of the simulation, the framework collects mass and stiffness values of all the degrees of freedom and finds the eigenvalues of the structural system. The eigenvalues are sent to the substructure modules where they are used in the equation of motion for computing the equivalent stiffness and force values. Although the multi-platform dynamic analysis for the VecTor programs was successfully tested using simple linear elastic examples, a more comprehensive verification study is required to assess the performance of the analysis procedure and identify its capabilities and limitations.

- To integrate other structural software or test specimens for dynamic analysis, a time integration scheme should be implemented in the simulation framework. The time integration scheme enables the framework to account for the dynamic characteristics of the structure including the mass and damping. The measured and computed restoring forces are collected by the framework and incorporated into the equation of motion.

- The interface program (NICA) used in the simulation framework is compatible with Zeus-NL, OpenSees, ABAQUS, and the VecTor suite of software. The integration of the different types of VecTor programs with each other and with OpenSees was verified in this study. The application of the framework to the remainder of the analysis tools should also be verified.

- Although the soil-structure interaction example and computational performance evaluation study demonstrated the capabilities of the simulation framework to some extent, they were limited to simplified systems. To fully illustrate the value of the multi-platform simulation in the areas of multi-disciplinary modelling and parallel computing, more realistic systems should be investigated. Particularly, the performance evaluation tests should be performed on larger structural systems. Also, for structural-geotechnical systems, the behaviour of the soil at the material-level and the mechanisms at the soil interface with the structure (e.g., friction effects) should be studied in detail.

CHAPTER 3

MODELLING BEAM-MEMBRANE INTERFACE IN REINFORCED CONCRETE MEMBERS

3.1 Introduction

In multi-platform simulation, each of the finite element (FE) programs used in combination may have a different element library and different types and numbers of degrees of freedom (DOFs). One of the main challenges in mixed-dimensional analysis is the modelling of the interface between two different types of elements. One common instance is the connection between beam elements of one sub-model to membrane elements of another sub-model. The rotation at the interface nodes of beam elements must be transferred to the equivalent displacements of membrane elements which typically only support translational DOFs. The procedure must satisfy compatibility and equilibrium at the interface section. In addition, it must compute realistic stress distributions at the connecting section between the two sub-models. According to Saint-Venant's principle, the disturbance in stress and strain distributions will be negligible at sufficiently large distance from the connecting section. However, there is a need to accurately model the stress and strain distributions at the interface between membrane and frame elements because of the following reasons: 1) the distance which is influenced by the interface section is not known prior to the analysis and 2) the detailed sub-model might not have an adequate length and the connecting section might be located in the critical part of the structure.

In this chapter, an overview of previous studies on the coupling of two-dimensional beam elements with membrane elements is first described. Then, the strengths and weaknesses of current methods when applied to nonlinear analysis of reinforced concrete (RC) structures are discussed. This is followed by a comprehensive description of a newly developed beam-membrane interface element which improves the mixed-dimensional analysis of RC structures. Lastly, the accuracy of the proposed interface element is compared against a stand-alone membrane model and against two commonly used coupling methods presented in the literature.

3.2 Literature Review

The current commonly used coupling methods can be categorized into three main types: Rigid Links, Multi-Point Constraints (MPC) and Transition Elements. A brief description of each method, along with several examples from the literature, are presented in this section. Emphasis is given to coupling methods between two-dimensional beam elements and membrane elements. The coupling of other types of elements is beyond the scope of this study.

Rigid Links are the simplest type of coupling method in which extremely high stiffness members connect beam and membrane elements (Adams and Askenazi, 1999). The Rigid Links enable transferring the rotation from the beam element to the equivalent translational displacements in the membrane elements at the interface section based on the assumption that "plane sections remain plane". Figure 3.1 shows a beam-membrane connection using the Rigid Links method. Mata et al. (2008) used a similar approach to perform a mixed-dimensional analysis of an RC frame structure. The beams and columns were modelled using frame elements while the joint panels were modelled using solid elements. Rigid body displacements were assumed at the interface surface between the beam elements and solid elements. However, the analysis did not consider second-order material effects such as tension stiffening nor mechanisms influencing beam-column joint behaviour such as bond-slip effects. Also, the mixed-dimensional analysis results were only verified against the analysis results of the full-frame model.

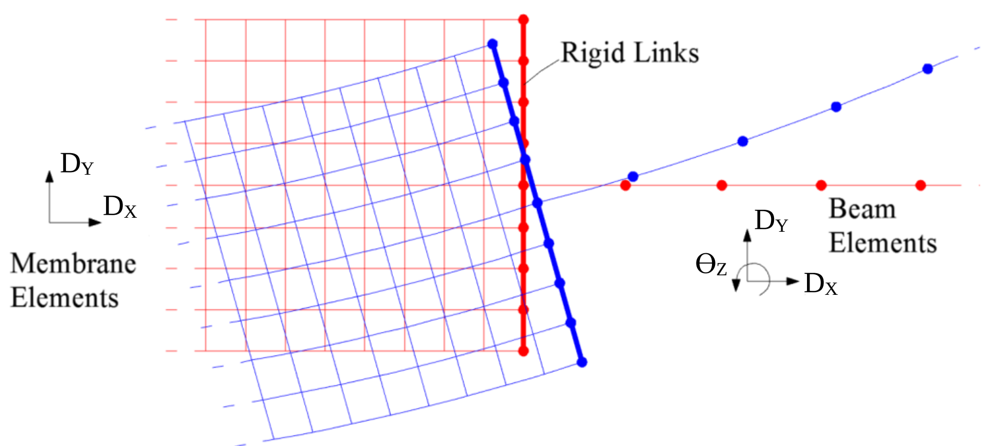

Figure 3.1 Beam-membrane connection using Rigid Links

Although the Rigid Links method satisfies compatibility and equilibrium requirements, it does not provide a realistic stress distribution at the interface section. In addition, a set of transverse rigid members at the connection acts as a strong ‘stirrup’ that does not allow transverse expansion at the interface, adding additional stiffness to the structure which may affect the response of the system.

In the MPC methods, constraint equations define the relationship between the displacements at interface DOFs of the membrane and beam elements. The most basic type of MPC methods is based on the constraint equations that represent a similar behaviour at the interface section as the Rigid Links method. As shown in Figure 3.2 in the X direction, displacements of the interface membrane nodes are formulated as a function of the displacements and rotations of the interface beam node and the distance between the interface membrane nodes and the centroid of the cross section. This is based on the combined assumptions of “plane sections remain plane” and “small angular displacements”. In the Y direction, the method assumes that the displacements of the membrane nodes and the beam node at the interface section are equal. For instance, for a connection case represented in Figure 3.2 with eight membrane elements at the interface section, the constraint equations can be written as the following:

$$\begin{cases} x_1 = x_{10} + \theta(\frac{h}{2}) \\ x_2 = x_{10} + \theta(\frac{3h}{8}) \\ \quad \cdots \\ x_5 = x_{10} \\ \quad \cdots \\ x_8 = x_{10} - \theta(\frac{3h}{8}) \\ x_9 = x_{10} - \theta(\frac{h}{2}) \end{cases} \tag{3.1}$$

$$y_1 = y_2 = \cdots = y_9 = y_{10} \tag{3.2}$$

where ϴ is the rotation at the interface node of the beam element and h is the height of the cross section.

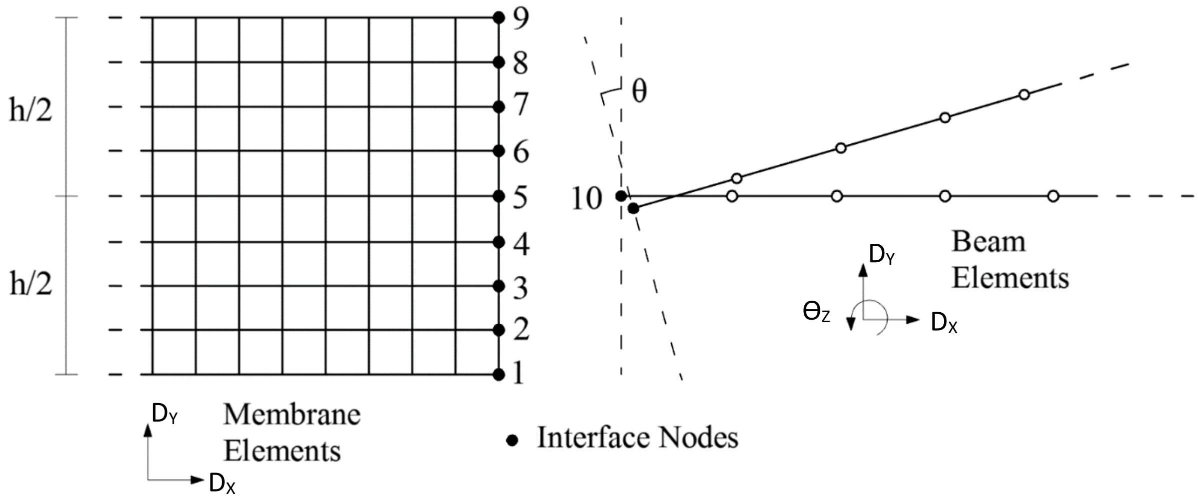

Figure 3.2 Beam-membrane connection using MPC

The basic type of MPC method is subject to the same limitations as the ones described for the Rigid Links method. Jialin et al. (1996) improved the basic MPC method and proposed a set of constraint equations for a solid-shell connection which allowed for transverse expansion at the interface section by introducing two additional DOFs. One of the most widely used MPC methods is the one proposed by McCune et al. (2000). In this method, the constraint equations were derived based on equating the work done by the stresses in each element type at the interface and the assumed stress distribution along the cross section. The work done by the frame sub-model (W_f) and the membrane sub-model (W_m) can be expressed in Eq. 3.3 and Eq. 3.4, respectively.

$$W_f = Pu + Qv + M\theta \tag{3.3}$$

$$W_m = \int \left(\sigma_x U + \tau_{xy} V\right) dA \tag{3.4}$$

In Eq. 3.3, P, Q, and M are the axial force, shear force, and bending moment in the beam element at the interface section, respectively, and u, v, and Θ are the corresponding translational and rotational displacements. In Eq. 3.4, σ_x and τ_{xy} are the axial and shear stresses in the membrane element at the interface section and U and V are the corresponding translational displacements. The authors used the well-established linear axial stress distribution and parabolic shear stress distribution relationships for linear elastic materials

(Jourawski, 1856; Goodier, 1938) to define the stress conditions at the interface section of the membrane sub-model for a rectangular cross section:

$$\sigma_x = \frac{P}{A} + \frac{My}{I} \tag{3.5}$$

$$\tau_{xy} = \frac{3}{2}\frac{Q}{A}\left(1 - \frac{4y^2}{h^2}\right) \tag{3.6}$$

The stress distributions are illustrated in Figure 3.3.

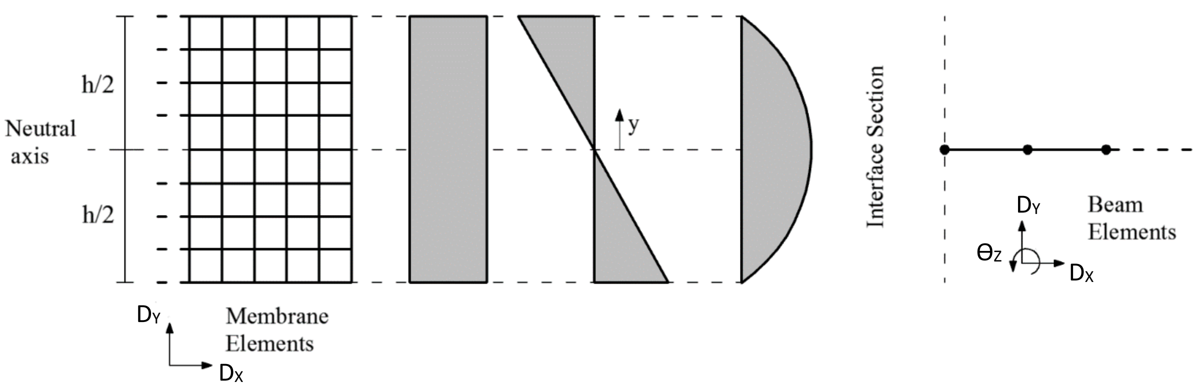

Figure 3.3 Axial and shear stress distributions of membrane elements at the interface section

By equating the work done by the two sub-models, the following equation can be written:

$$Pu + Qv + M\theta = \int \left\{\left(\frac{P}{A} + \frac{My}{I}\right)U + \frac{3}{2}\frac{Q}{A}\left(1 - \frac{4y^2}{h^2}\right)V\right\} dA \tag{3.7}$$

where A and I are the area and moment of inertia of the section and y is the distance from the neutral axis to the layer of the cross section for which the stress is being computed.

Based on Eq. 3.7, McCune et al. (2000) derived the following relationships (Eq. 3.8) between the translational and rotational DOFs of the beam element and the translational DOFs of the membrane elements for a rectangular cross section. The continuum displacements of the membrane elements are represented by the nodal displacements and the shape functions (N_iU_i, N_iV_i). The authors presented the constraint equations for the connection between a beam element and ten eight-noded membrane elements with quadratic shape functions. The method was claimed to be a general approach for linear elastic analysis as long as the stress distributions were known at the interface section.

$$\begin{Bmatrix} u \\ v \\ \theta \end{Bmatrix} = \int_{-\frac{h}{2}}^{\frac{h}{2}} \begin{Bmatrix} \frac{1}{h} N_i U_i \\ \frac{3}{2h} N_i V_i \left[1 - \left(\frac{2y}{h}\right)^2\right] \\ \frac{6}{h^2} N_i U_i \left(\frac{2y}{h}\right) \end{Bmatrix} dy \tag{3.8}$$

Ho et al. (2010) proposed constraint formulations based on defining equivalent forces and moment for the beam element at the connection section. The method was implemented in an explicit FE solver and verified through static and dynamic analyses of a cantilever beam structure. Although using the concept of equivalent forces and moment resulted in a uniform and unperturbed stress distribution between the two types of elements, the procedure assumed rigid displacements which did not allow transverse expansion at the interface section. In addition, no discussion on the accuracy of the stress distributions through the cross section at the interface was provided.

Wang et al. (2014) used the virtual work concept to demonstrate that the coefficient matrix (C) of the displacement constraint equation is equal to the negative transpose of the coefficient matrix of the force constraint equation:

$$U_m = CU_f \tag{3.9}$$

$$F_m = -C^T F_f \tag{3.10}$$

where (U_m, F_m) and (U_f, , F_f) are the displacements and forces in the membrane and beam elements at the interface section. The coefficient matrix (C) was computed from the nodal forces of the membrane sub-model at the interface section when unit forces and moment were applied on the beam sub-model. The authors developed an iterative method to compute the coefficient matrix and consequently formulated the constraint equations. As shown in Figure 3.4, an interface substructure was used to reduce the end effects on the computed nodal forces. The method eliminated the stress distribution assumptions made in previous MPC methods.

While the procedure was extended to nonlinear analysis, the expensive computations required to obtain the coefficient matrix prohibited its practical application.

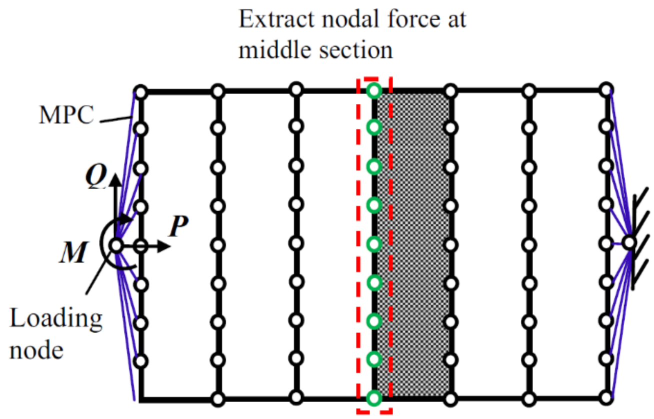

Figure 3.4 Interface substructure to compute nodal forces (taken from Wang et al., 2014)

With respect to the implementation of MPC methods in analysis software, three different approaches have been developed: Master-Slave, Lagrange Multiplier, and Penalty Function. Each type of method has its own relative merits. The Master-Slave method, also known as transformation approach, requires expensive matrix operations to eliminate the dependent DOFs. Curiskis and Valliapan (1978) presented a general approach based on the Gauss elimination method to incorporate the constraint equations into the global stiffness matrix of the structure. Shephard (1984) developed a term-by-term stiffness matrix assembly procedure to apply the constraint equations and to reduce expensive matrix operations. Chang and Lin (1988) presented a method in which the constraint equations were applied at the element-level rather than at the global-level stiffness matrix. Unlike the previous techniques, no modifications were required to the global stiffness matrix which resulted in a more efficient implementation of constraint equations. The Lagrange Multiplier method requires defining additional unknowns in the system which can destroy the banded and positive definite nature of stiffness matrix. Narayanaswamy (1985) evaluated different forms of the Lagrange Multiplier method and provided guidelines to reduce the computational time and preserve the positive definite and symmetry of the stiffness matrix. Park et al. (2000) developed a localized type of the Lagrange Multiplier method to address the aforementioned numerical issues. Unlike the Master-Slave and the Lagrange Multiplier methods which enforce the constraint equations in exact form, the Penalty Function method is an approximate approach in which the accuracy depends on the selected penalty parameters. Some researchers proposed iterative procedures to improve the accuracy of the Penalty Function method (e.g., Felippa, 1978).

Although MPC methods have been widely implemented in analysis tools and successfully employed by several researchers (Houlsby et al., 2000; Narayanaswamy, 1985), inaccurate results have been reported in cases which had complex connections or complicated stress behaviour (Surana, 1980).

Another effective coupling method is to use transition elements. Most of the research in this area has been focused on shell-solid connections. For the beam-membrane coupling problem, Bathe (1982) proposed a transition element based on isoparametric FE formulation of a one-dimensional beam element. Kim and Hong (1994) introduced a two-dimensional transition element for analysis of coupled frame-shear wall structures. As shown in Figure 3.5, their transition element consisted of three types depending on the connection configuration. The stiffness matrix of the transition element was formulated based on constraint equations which assumed linear and constant displacement distributions in the axial and vertical directions, respectively.

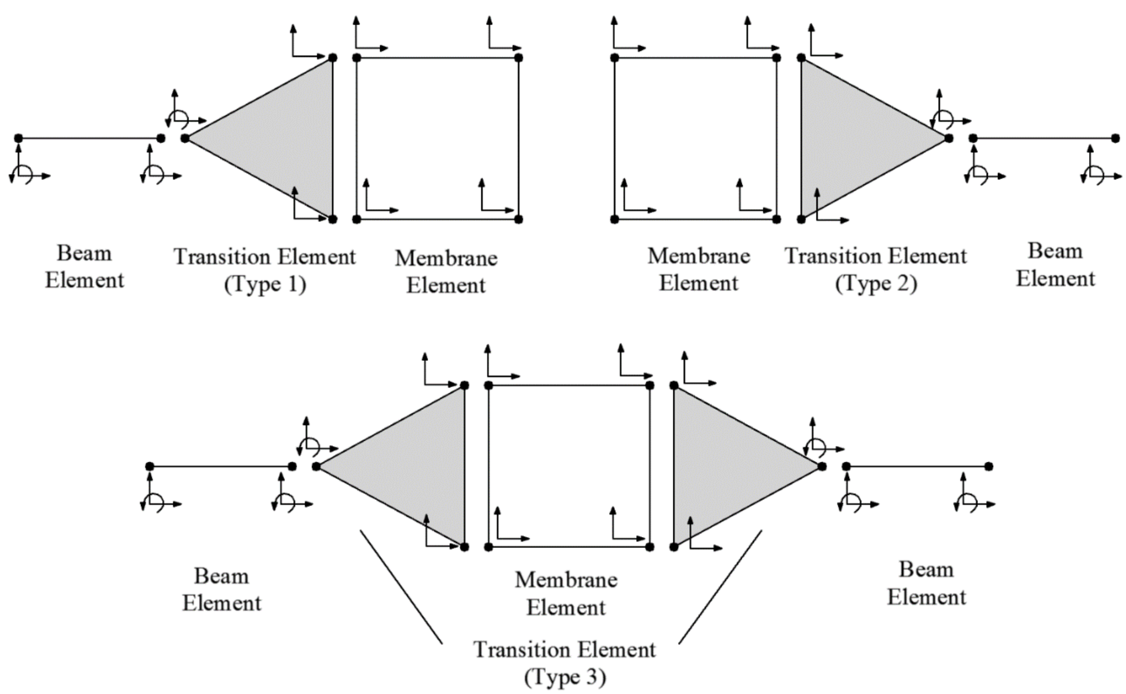

Figure 3.5 Beam-membrane transition elements (taken from Kim and Hong, 1994)

Garusi and Tralli (2002) proposed a hybrid set of stress-assumed transition elements for beam-solid and beam-shell connections. Instead of formulating the stiffness matrix using relationships between displacements of DOFs, the method derived stiffness properties by assuming a stress field based on the Saint-Venant theory. However, these transition elements were prone to “spurious kinematic modes” which had to be suppressed through the introduction of a penalty strain energy term. Figure 3.6 shows the connection between the five-noded transition element and the shell element.

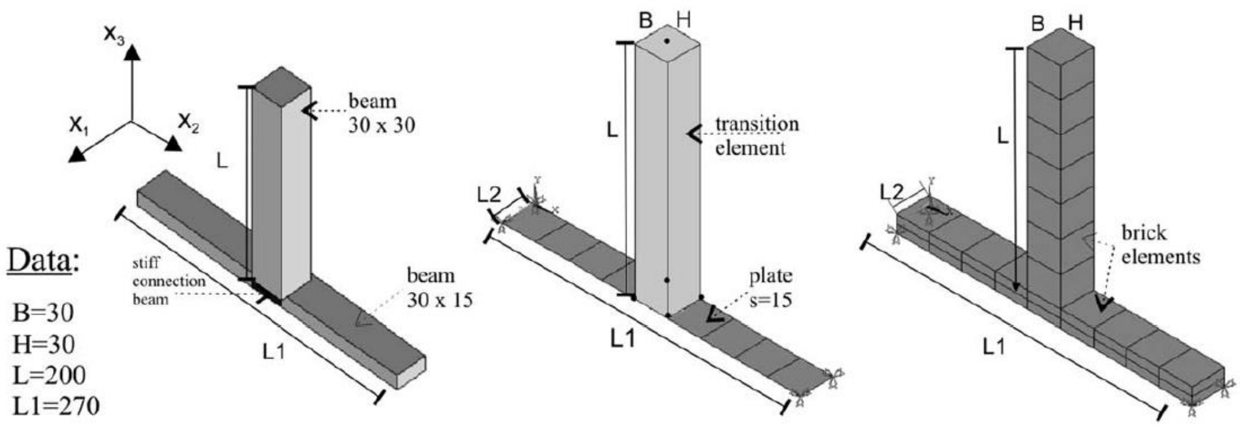

Figure 3.6 Shell-beam transition element (taken from Garusi and Tralli, 2002)

Compared to MPC methods, the implementation of transition elements in FE software is difficult because each type of connection requires a different formulations. For instance, Surana (1980) developed ten transition elements for different types of shell-solid connections. Guzelbey and Kanber (2000) attempted to provide a practical general rule to formulate shape functions for transition elements. Transition elements are also prone to the shear locking numerical problem. Gmur and Kauten (1993) developed a solid-beam transition element which avoided shear locking for dynamic analysis. Furthermore, the behaviour of the structure at the transition zone must change smoothly from one type of element to another type of element. This depends on the length of the transition zone and constitutive relationships used to formulate the stiffness matrix of the transition element. Schorderet and Gmur (1991) investigated shell-solid connections and concluded that the constitutive relationships must be formulated depending on the location of the transition element in the FE model and whether the behaviour at the transition zone is more like the shell elements or the solid elements. These issues demonstrate the difficulties of properly formulating the transition elements.

While the above-mentioned beam-membrane coupling methods are able to satisfy the compatibility and equilibrium requirements at the interface section, they have some major limitations when applied to nonlinear analysis of reinforced concrete structures. Some of the methods impose a constant vertical displacement distribution which does not allow for transverse expansion and accurate calculation of Poisson's effects. Some of the methods do not consider stress distribution at the interface, and the ones that do so analyze the effects of axial stresses and shear stresses separately. However, in reinforced concrete structures, the axial and shear stresses are closely related to each other (e.g., stress condition at the crack). Also, for detailed modelling of reinforced concrete, which is a composite material, truss elements must be used in conjunction with membrane elements to model the reinforcing bars and the concrete. Having truss elements at the interface section requires special consideration for the stress and strain distributions. Furthermore, almost all of the previous studies have been focused on linear elastic analysis. But the behaviour of reinforced concrete structures is highly nonlinear due to the low cracking stress of the concrete, nonlinear compression response of the concrete, and yielding of the reinforcement.

In this study, a new beam-membrane interface element, the F2M element, is developed particularly for the analysis of reinforced concrete structures which attempts to address some of the aforementioned limitations. The procedure is capable of computing linear and nonlinear stress distributions including shear stresses at the interface section reasonably well. The accuracy of the proposed interface element is compared against the stand-alone membrane model and two other commonly used coupling methods.

3.3 Proposed Interface Element

3.3.1 Element Description

The F2M interface element is a two-noded semi-deformable element which has to be used as a group of elements oriented perpendicular to the beam element and along the membrane elements at the connecting section (see Figure 3.7). The number of required F2M elements is equal to the number of membrane elements at the interface section. As shown in Figure 3.7, the stiffness matrix of the F2M element is set such that it has high stiffness values in the transverse and rotational directions (K_{22} and K_{33}, respectively) and zero stiffness in the axial direction (K_{11}). This enables the analysis to transfer the rotation from the frame sub-model to the equivalent translational displacements in the membrane sub-model based on the assumption that "plane sections remain plane" which is consistent with the layered frame analysis procedure. In addition, having zero stiffness in the axial direction avoids the addition of extra stiffness to the system and allows lateral expansion at the connecting section.

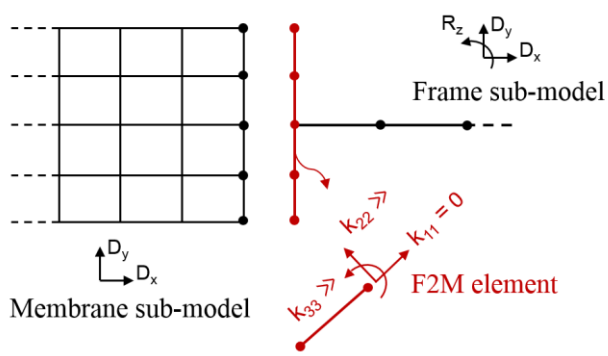

Figure 3.7 Overview of F2M interface element

3.3.2 Stress Distributions

An iterative procedure is used to transfer shear between the two sub-models. The procedure is adopted from frame analysis software developed by Guner and Vecchio (2010a). In the first iteration of the analysis, the solution of the structural system is calculated assuming high stiffness in the axial direction for the F2M elements (i.e., F2M elements initially act similar to the Rigid Links method). In the subsequent iterations, the axial stiffness of the F2M elements is set to zero. Using a layered analysis approach which assumes "plane sections remain plane", the longitudinal strains at each layer of the cross section can be calculated from the change in the length and curvature of the connecting beam element.

$$\varepsilon_{c,p} = \frac{L_p - L_o}{L_o} \tag{3.11}$$

$$\phi_p = \frac{\Theta_{1,p} + \Theta_{2,p}}{L_p} \tag{3.12}$$

$$\varepsilon_{i,p} = \varepsilon_{c,p} + \phi_p \left(\frac{d}{2} - d_i\right) \tag{3.13}$$

where Θ_1 and Θ_2 are the rotations at the two ends of the connecting beam element, d and d_i are the heights of the cross section and i^{th} layer, L_o is the initial length of the element, L_p and ϕ_p are the length and curvature of the element at iteration "p", and ε_c and ε_i are the axial strains at mid-depth and i^{th} layer of the cross section. Using the computed shear force from the structural system solution, the shear strain at the mid-depth of the element ($\gamma_{c,p}$) can be estimated for elastic members (e.g., uncracked concrete sections) as:

$$\gamma_{c,p} = SF \frac{V}{G_c . A_t} \tag{3.14}$$

where V is the shear force, G_c is the elastic shear modulus as given by Eq. 3.15, A_t is the transformed cross-sectional area, and SF is the shear area factor for elastic members which depends on the cross-sectional shape. In this study, as suggested by Gere and Timoshenko (1991), shear area factors of 1.20 and 1.11 were used for rectangular sections and circular sections, respectively.

$$G_c = \frac{E_c}{2(1+\nu)} \tag{3.15}$$

In Eq. 3.15, E_c and ν are the modulus of elasticity and the Poisson's ratio of the concrete, respectively. Knowing the shear strain at the mid-depth of the cross section and assuming a parabolic shear strain distribution, the shear strain of each layer at iteration "p" of the analysis can be determined as:

$$\gamma_{i,p} = \frac{4\gamma_{c,p}}{d^2}(dd_i - d_i^2) \tag{3.16}$$

Figure 3.8 shows the axial and shear strain distributions through the cross section between the two sub-models.

The stress-strain constitutive relationship at the interface section can be written as:

$$\begin{Bmatrix} \sigma_x \\ \sigma_y \\ \tau_{xy} \end{Bmatrix} = \begin{bmatrix} D_{11} & D_{12} & D_{13} \\ D_{21} & D_{22} & D_{23} \\ D_{31} & D_{32} & D_{33} \end{bmatrix} \times \begin{Bmatrix} \varepsilon_x \\ \varepsilon_y \\ \gamma_{xy} \end{Bmatrix} - \begin{Bmatrix} {\sigma_x}^o \\ {\sigma_y}^o \\ {\tau_{xy}}^o \end{Bmatrix} \tag{3.17}$$

where $\{\sigma\}$ and $\{\varepsilon\}$ are the total stress and strain vectors, [D] is the composite material stiffness matrix, and $\{\sigma^o\}$ is the pseudo-stress vector corresponding to the strain offsets as per the Disturbed Stress Field Model (DSFM) (Vecchio, 2000).

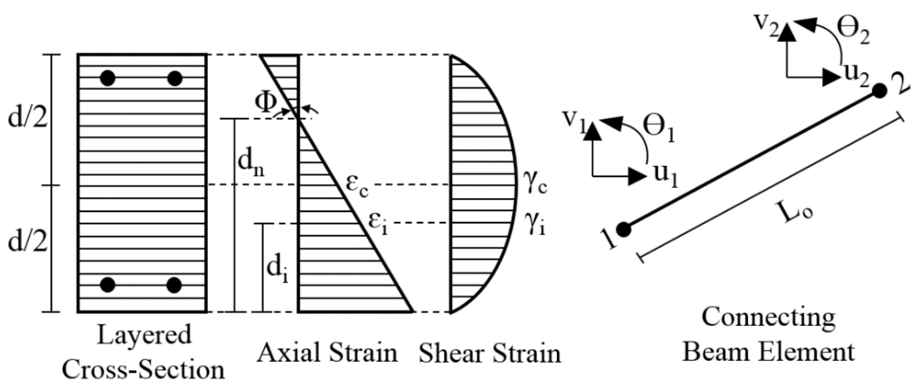

Figure 3.8 Strain distributions through the cross section at the interface section

The total strains in concrete can be expressed as a composition of: 1) net strains, $\{\varepsilon_c\}$, which are used for calculations of stresses and stiffness moduli in the concrete, 2) elastic offset strains, $\{\varepsilon_c{}^o\}$, due to lateral expansion, thermal, shrinkage, and prestrain effects, 3) plastic offset strains, $\{\varepsilon_c{}^p\}$, due to permanent deformation resulting from cyclic loading, and 4) crack slip offset strains, $\{\varepsilon_c{}^s\}$, due to shear slip on the crack. The total concrete strains can be represented as:

$$\{\varepsilon\} = \{\varepsilon_c\} + \{\varepsilon_c^o\} + \{\varepsilon_c^p\} + \{\varepsilon_c^s\} \tag{3.18}$$

Assuming perfect bond between the reinforcement and the concrete, the total strains developed in the i^{th} reinforcement component are equal to the total strains of the concrete at the same location. Therefore, in a similar manner, the total strains in the reinforcement can be expressed as a summation of: 1) net strains, $\{\varepsilon_s\}$, which are used for calculations of the stress and stiffness modulus in the reinforcement, 2) elastic offset strains, $\{\varepsilon_s^o\}$, due to thermal and prestrain effects, and 3) plastic offset strains, $\{\varepsilon_s^p\}$, due to steel yielding and damage resulted from cyclic loading. The total reinforcement strains can be written as:

$$\{\varepsilon\}_i = \{\varepsilon_s\}_i + \{\varepsilon_s^o\}_i + \{\varepsilon_s^p\}_i \tag{3.19}$$

The pseudo-stress vector, $\{\sigma^o\}$, is computed from the summation of the pseudo-stress vector arising from strain offsets of the concrete, $\{\sigma_c^o\}$, and the pseudo-stress vectors resulting from strain offsets of all the reinforcement components, $\{\sigma_s^o\}$:

$$\{\sigma^o\} = \{\sigma_c^o\} + \sum_{i=1}^{n} \{\sigma_s^o\}_i \tag{3.20}$$

$$\{\sigma_c^o\} = [D_c] \times \left(\{\varepsilon_c^o\} + \{\varepsilon_c^p\} + \{\varepsilon_c^s\}\right) \tag{3.21}$$

$$\{\sigma_s^o\}_i = [D_s]_i \times \left(\{\varepsilon_s^o\}_i + \{\varepsilon_s^p\}_i\right) \tag{3.22}$$

where $[D_c]$ and $[D_s]_i$ are the material stiffness matrices for the concrete and the i^{th} reinforcement component, respectively.

Assuming zero clamping stress at the interface section ($\sigma_y = 0$) an iterative procedure can be used to calculate the axial stress (σ_x) and shear stress (τ_{xy}) at each layer of the cross section without decoupling the effects of stresses. First, the axial strain (ε_x) and shear strain (γ_{xy}) are determined from Eq. 3.13 and Eq. 3.16, respectively. Assuming $[D_c]$ and $[D_s]_i$ are known matrices (developments presented in Section 3.3.3), $\{\sigma^o\}$ can be computed from Eq. 3.20 to Eq. 3.22 using the strain offsets. Thus, the constitutive relationship, Eq. 3.17, can be simplified to three equations and three unknowns in which the unknowns are the axial stress (σ_x), shear stress (τ_{xy}), and transverse strain (ε_y). Solving Eq. 3.17 provides the axial and shear stress distributions at the beam side of the interface section. Using the computed shear stress distribution and the tributary area concept, the equivalent axial forces at the F2M element nodes are computed. To transfer shear between the two sub-models, the computed equivalent forces are applied in the opposite direction on the corresponding nodes of the connecting membrane elements.

To satisfy equilibrium at the interface section, the computed force of the membrane node located at the cross-sectional mid-depth must be modified to account for the total shear force carried by the corresponding node in the frame sub-model. As presented in Figure 3.9 and Eq. 3.23, this modified force (P_*) is equal to the difference between the total shear force (P_f) and the equivalent force of the membrane node at the cross-sectional mid-depth (P_c) and must be applied in the opposite direction of the equivalent force:

$$P_* = P_f - P_c \tag{3.23}$$

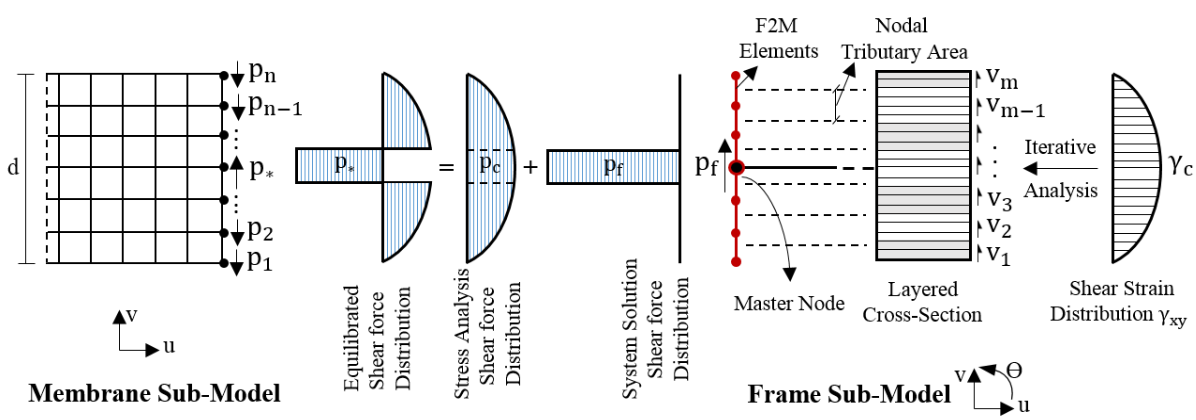

Figure 3.9 Transferring shear forces between beam and membrane elements

Without the above-mentioned force modification, the shear force at the interface section equals the summation of the externally applied forces to the membrane sub-model along the cross section and a concentrated force applied at the mid-depth node of the membrane sub-model. The concentrated force is computed from the system-level solution and is equal to the total shear force. This results in a final sectional shear force which is twice the correct value.

3.3.3 Material Matrix Formulation

A smeared crack approach is used to compute the behaviour of cracked concrete at the interface section. In this approach, concrete is assumed to remain a continuum after cracking. The cracks are considered as an average deformation spread out over the area of the FE elements. To compute the principal stresses and strains in the concrete, the smeared crack approach can be characterized into two types according to assumptions made regarding the subsequent direction of cracks: 1) rotating crack model and 2) fixed crack model. In the rotating crack model, as the material state changes (e.g., reinforcement yielding) or as loading conditions change (e.g., change in the direction of the load in a cyclic loading condition), the crack direction effectively “rotates”. Conversely, in the fixed crack model, once the cracks forms, the direction of the crack is set and remains constant during the analysis. Each approach has its own strengths and weaknesses. In the following, to extend the application of the proposed interface element, the formulations are presented according to both the rotating crack model (e.g., Vecchio and Collins, 1986; Vecchio, 2000) and the fixed crack model (e.g., Okamura and Maekawa, 1991; Kaufmann and Marti, 1998).

In the stress-strain constitutive relation (Eq. 3.17), the matrix [D] is a function of strains and the transverse strain (ε_y) is the unknown. An iterative procedure is used to determine the matrix [D]. The procedure is presented in a general form so it can be applied to other secant-based or tangent-based analysis formulations. First, an arbitrary value is assumed for the transverse strain (ε_y). Knowing all three strain components in the X and Y coordinate system, the concrete principal strains (ε_{c1} and ε_{c2}) can be calculated according to the relationships provided by the rotating crack model, Eq. 3.24, or the fixed crack model, Eq. 3.26 and Eq. 3.27. In the rotating crack model, the inclination of the principal tensile net strain (i.e., normal to the crack), Θ, is computed using Eq. 3.25. In the fixed crack model, Θ is constant and equal to (Θ_{ic} - 90), where Θ_{ic} is defined as the initial direction of the crack.

Figure 3.10 and Figure 3.11 show the crack formation and Mohr’s circle of strains for the rotating crack model and the fixed crack model, respectively. In Figure 3.10, the subscripts “p” and “c” correspond to the principal directions in the previous load stage and the current load stage, respectively. It must be noted that in the rotating model, cracks are not erased and redeveloped at new orientation; rather, new cracking and crack extensions result in a change in the direction of total crack condition.

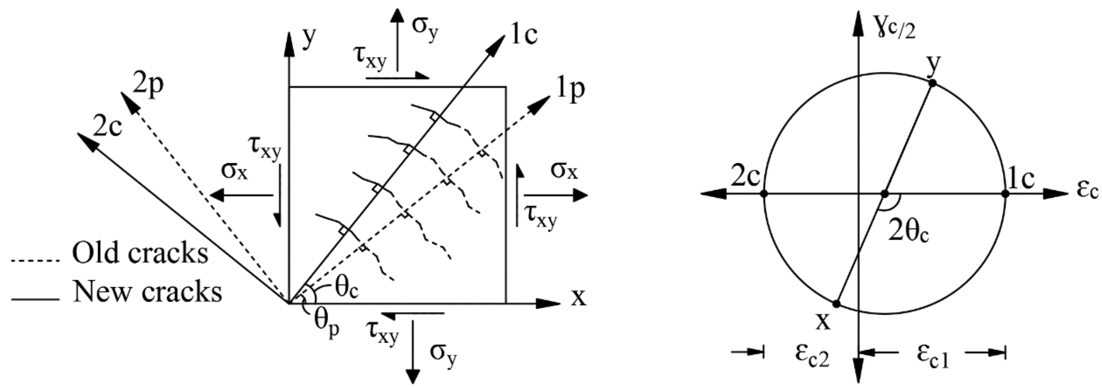

Figure 3.10 Crack direction and Mohr's circle of strains for the rotating crack model

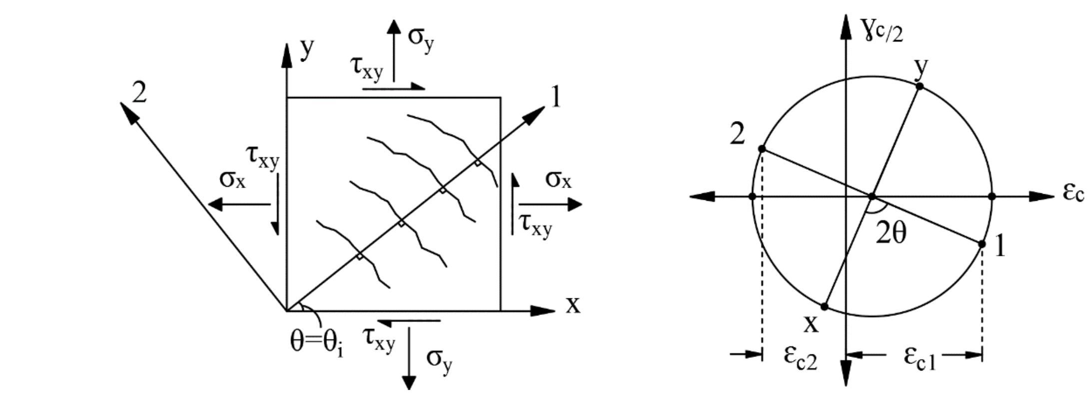

Figure 3.11 Crack direction and Mohr's circle of strains for the fixed crack model

The rotating crack model strain transformation relationships are:

$$\varepsilon_{c1}, \varepsilon_{c2} = \frac{(\varepsilon_{cx} + \varepsilon_{cy})}{2} \pm \frac{1}{2}\sqrt{(\varepsilon_{cx} - \varepsilon_{cy})^2 + \gamma_{cxy}^2} \tag{3.24}$$

$$\theta = \frac{1}{2}\tan^{-1}\left(\frac{\gamma_{cxy}}{\varepsilon_{cx} - \varepsilon_{cy}}\right) \tag{3.25}$$

The fixed crack model strain transformation relationships are:

$$\varepsilon_{c1} = \varepsilon_{cx}\cos^2\theta + \varepsilon_{cy}\sin^2\theta + \gamma_{cxy}\sin\theta\cos\theta \tag{3.26}$$

$$\varepsilon_{c2} = \varepsilon_{cx}\cos^2(\Theta + 90) + \varepsilon_{cy}\sin^2(\Theta + 90) + \gamma_{cxy}\sin(\Theta + 90)\cos(\Theta + 90) \tag{3.27}$$

Using available stress-strain relationships for concrete and steel, the concrete stresses in the principal directions (f_{c1} and f_{c2}) and the steel stress in the direction of each reinforcing bar component (f_{si}) can be computed. In this study, the constitutive formulations presented in the DSFM (Vecchio, 2000) are applied.

Based on the computed stresses and strains in the principal directions, the composite RC material stiffness matrix, [D], can be constructed by superposition of the material stiffness matrices of the concrete and all the reinforcement components:

$$[D] = [D_c] + \sum_{i=1}^{n}[D_s]_i \tag{3.28}$$

Prior to cracking, concrete has a linear elastic isotropic behaviour. Therefore:

$$[D_c] = \frac{E_c}{1-\nu^2}\begin{bmatrix} 1 & \nu & 0 \\ \nu & 1 & 0 \\ 0 & 0 & \dfrac{1-\nu}{2} \end{bmatrix} \tag{3.29}$$

After cracking, the concrete material stiffness matrix is calculated using effective moduli defined with respect to the principal directions:

$$[D_c]' = \begin{bmatrix} E_{c1} & 0 & 0 \\ 0 & E_{c2} & 0 \\ 0 & 0 & G_c \end{bmatrix} \tag{3.30}$$

The $[D_c]$' matrix can be transformed back to the X and Y axes using the following transformation matrix, $[T_c]$ (Cook et al., 1989):

$$[D_c] = [T_c]^T[D_c]'[T_c] \tag{3.31}$$

$$[T_c] = \begin{bmatrix} \cos^2\psi & \sin^2\psi & \cos\psi \times \sin\psi \\ \sin^2\psi & \cos^2\psi & -\cos\psi \times \sin\psi \\ -2 \times \cos\psi \times \sin\psi & 2 \times \cos\psi \times \sin\psi & \cos^2\psi - \sin^2\psi \end{bmatrix} \tag{3.32}$$

where ψ is equal to the inclination of the principal tensile stress direction (Θ_σ).

The contribution from the i^{th} reinforcement component to the material stiffness matrix is defined as:

$$[D_s]'_i = \begin{bmatrix} \rho_{si}E_{si} & 0 & 0 \\ 0 & 0 & 0 \\ 0 & 0 & 0 \end{bmatrix} \tag{3.33}$$

where ρ_{si} is the reinforcement ratio and E_{si} is the effective steel modulus for i^{th} reinforcement component. Using a similar transformation matrix applied for the concrete material stiffness, $[D_s]_i$' can be transferred from the longitudinal axis of the reinforcing bar to the X and Y reference axes:

$$[D_s]_i = [T_s]_i{}^T[D_s]'_i[T_s]_i \tag{3.34}$$

In the $[T_s]_i$ transformation matrix, ψ_i is equal to the inclination of the i^{th} reinforcing bar.

Depending on the selected analysis procedure for the structural system, the effective moduli for concrete and steel can be defined according to either secant $(\overline{E})$ or tangent $(\dot{E})$ formulations. In the secant formulation, the effective stiffness moduli are:

$$\overline{E}_{c1} = \frac{f_{c1}}{\varepsilon_{c1}} \quad ; \quad \overline{E}_{c2} = \frac{f_{c2}}{\varepsilon_{c2}} \tag{3.35}$$

$$\overline{G}_c = \frac{\overline{E}_{c1} \times \overline{E}_{c2}}{\overline{E}_{c1} + \overline{E}_{c2}} \tag{3.36}$$

$$\overline{E}_{si} = \frac{f_{si}}{\varepsilon_{si}} \tag{3.37}$$

While in the tangent formulation, the effective stiffness moduli are:

$$\dot{E}_{c1} = \begin{cases} E_{el,c} & \text{for} \quad \varepsilon_c < \varepsilon_{cr} \\ 0 & \text{for} \quad \varepsilon_c \geq \varepsilon_{cr} \end{cases} \quad ; \quad \dot{E}_{c2} = \frac{df_{c2}}{d\varepsilon_{c2}} \tag{3.38}$$

$$\dot{G}_c = \frac{f_{c2} - f_{c1}}{2(\varepsilon_{c2} - \varepsilon_{c1})} \tag{3.39}$$

$$\dot{E}_{si} = \begin{cases} E_{el,si} & \text{for} \quad \varepsilon_{si} < \varepsilon_{yi} \\ 0 & \text{for} \quad \varepsilon_{yi} \le \varepsilon_{si} < \varepsilon_{shi} \\ E_{sh,si} & \text{for} \quad \varepsilon_{shi} \le \varepsilon_{si} < \varepsilon_{ui} \end{cases} \tag{3.40}$$

where $E_{el,c}$ and ε_{cr} are the elastic stiffness modulus and the cracking strain of the concrete, $E_{el,si}$ and $E_{sh,si}$ are the elastic stiffness modulus and the strain hardening stiffness modulus of the ith reinforcing bar, and ε_{yi} and ε_{shi} are the yielding strain and the strain hardening strain of the ith reinforcing bar.

Figure 3.12 and Figure 3.13 present the definition of the tangent and the secant stiffness moduli in the concrete and the reinforcement responses, respectively.

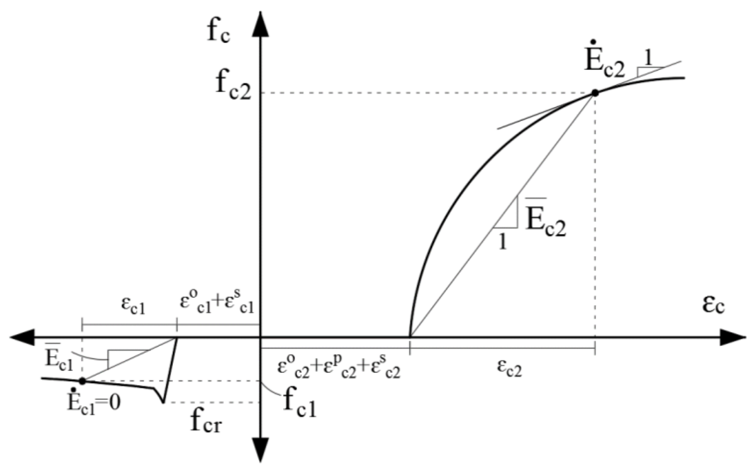

Figure 3.12 Determination of secant and tangent stiffness moduli in concrete response

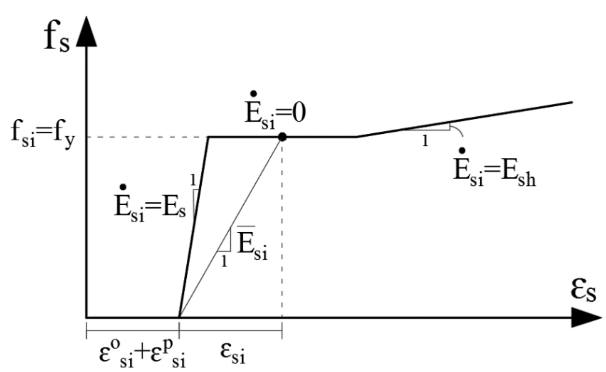

Figure 3.13 Determination of secant and tangent stiffness moduli in reinforcement response

In the fixed crack model, it is common to assume a fixed value for the tangent and the secant shear stiffness moduli to represent the effects of aggregate interlock in cracked concrete (Gambarova, 1981) :

$$\overline{G}_c \approx \dot{G}_c \approx \beta G_c \tag{3.41}$$

where β is the "shear retention factor" ranging from 0.01 to 0.20.

It should be noted that the F2M interface element is based on the rotating crack model. The fixed crack model is presented for demonstration purposes only. Formulating the F2M element using the fixed crack model requires addressing several numerical challenges which was beyond the scope of this study (e.g., negative tangent stiffness of the post-peak response of the concrete in compression, zero tangent stiffness of the post-cracking response of the concrete in tension, and zero tangent stiffness in the yielding zone of the reinforcing bar response).

Using the calculated secant or tangent effective moduli, the concrete and steel material stiffness matrices, [D_c] and [D_s], and consequently the composite material stiffness matrix, [D], at the interface section can be constructed according to Eq. 3.28 to Eq. 3.34. The computed [D] matrix can be used in Eq. 3.17 to determine shear stress distribution at the connecting section. Figure 3.14 indicates the main steps of the proposed beam-membrane coupling method.

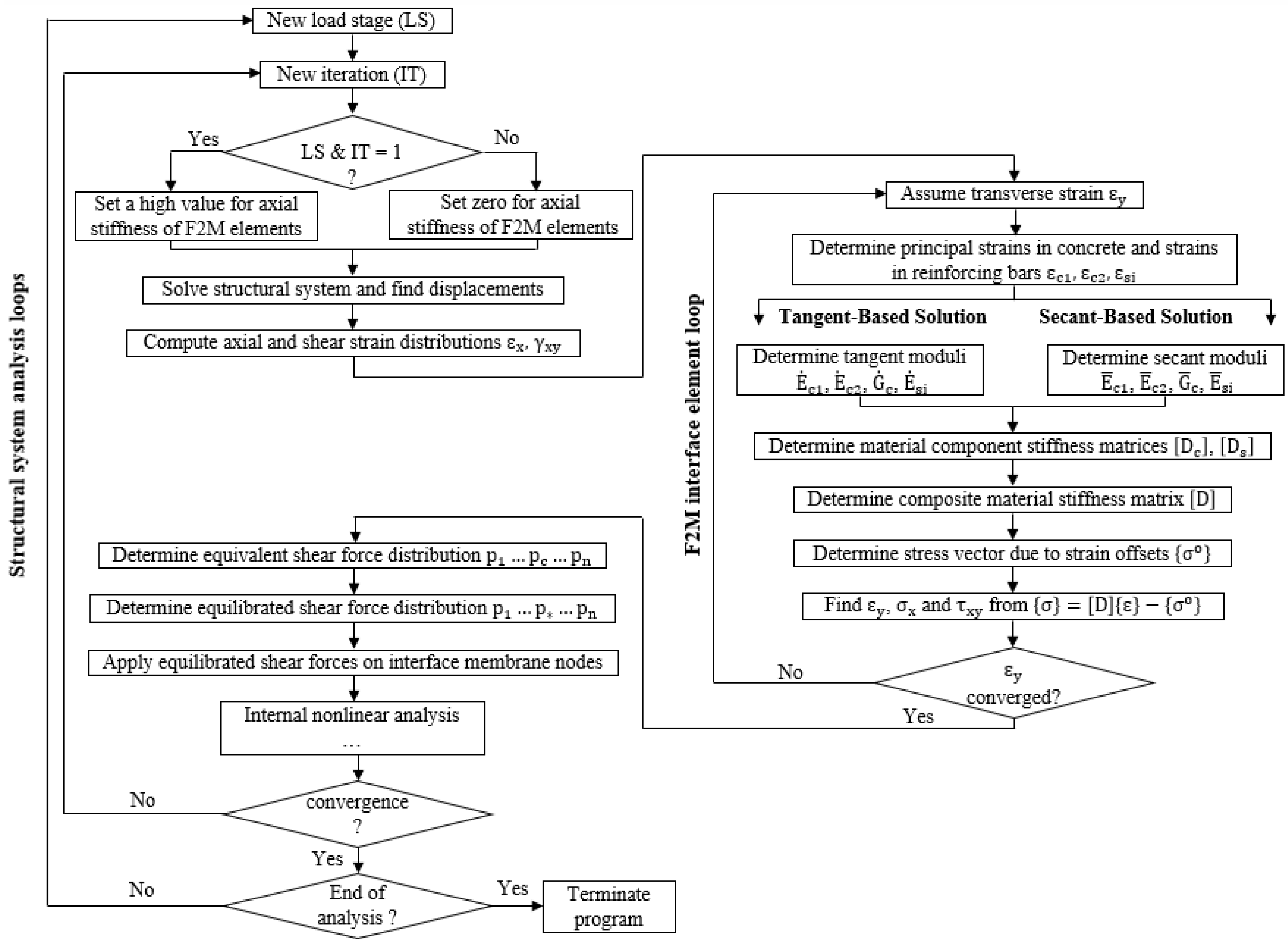

Figure 3.14 Algorithm of the proposed beam-membrane interface element

3.4 Verification Example: Shear-Critical Beams

A series of shear-critical reinforced concrete beams tested by Bresler and Scordelis (1963) is commonly used as a benchmark to verify the accuracy of finite element programs and analytical procedures, particularly in capturing the shear behaviour. The high recognition of the Bresler-Scordelis beams for verification purposes has been attributed to the well-documented testing program and the fact that computing the experimentally observed behaviour of the beams has proven to be a difficult challenge for many existing nonlinear analysis formulations.

In 2004, Vecchio and Shim performed an experimental study at the University of Toronto in an effort to recreate, as much as possible, the classic Bresler-Scordelis test series conducted in 1960s. The primary objectives of the study were to assess the repeatability of the results obtained from the Bresler-Scordelis tests and to provide additional information regarding the failure mechanisms and post-peak responses of the beams. The Bresler-Scordelis tests terminated at the peak loads due to their force-controlled loading procedure. In the Vecchio-Shim (VS) tests, a combination of force-controlled and displacement-controlled loading procedures was used enabling continuation of the tests into the post-peak regimes.

The experimental program conducted by Vecchio and Shim (2004) consisted of twelve simply supported beams tested under monotonically increasing point load. The specimens varied in span, width, concrete compressive strength, and reinforcement ratio. The beams were categorized into three series of tests (Series 1, 2 and 3) according to their clear span length (3.66 m, 4.57 m, and 6.40 m, respectively). Each series of tests comprised four beam specimens and each had a different cross-sectional width and reinforcement configuration (Beam OA, A, B, and C). All the beams were designed to be critical in shear with light amounts of transverse reinforcements ranging from 0.0% to 0.2%. The cross section and elevation details of the beams are presented in Figure 3.15 and Figure 3.16, respectively.

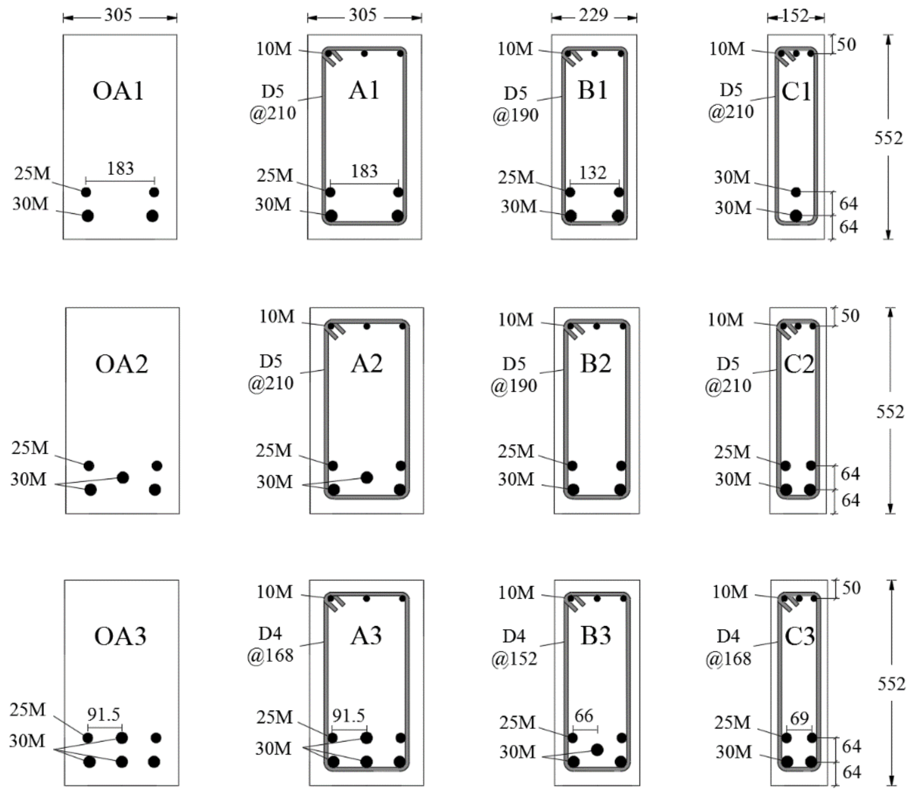

Figure 3.15 Cross section details of Vecchio-Shim beams (dimensions in millimeters)

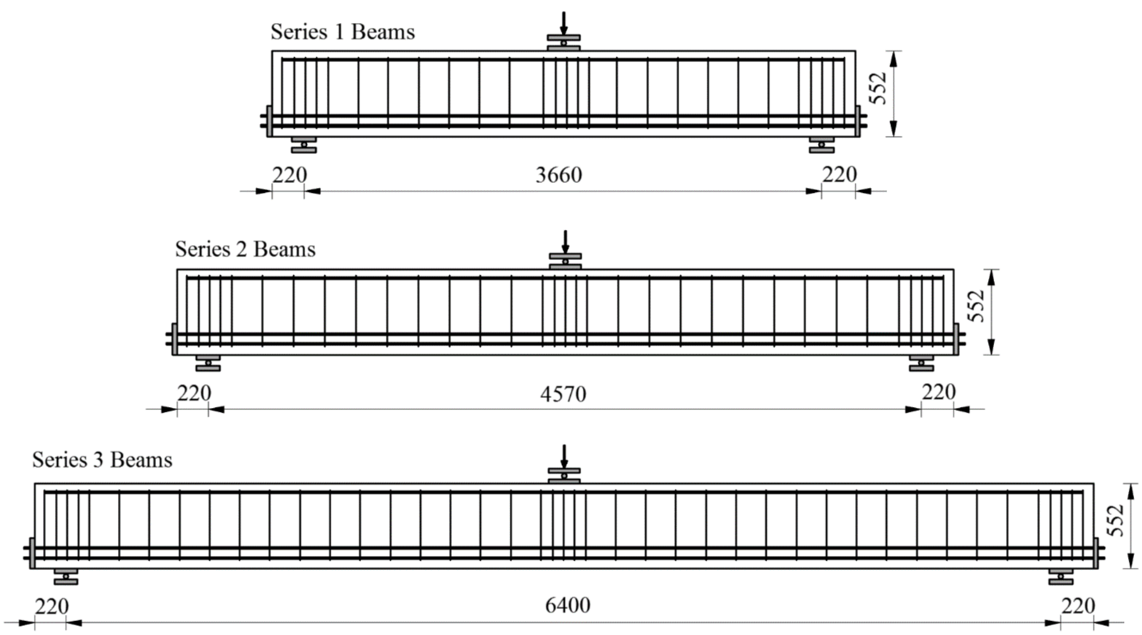

Figure 3.16 Elevation details of Vecchio-Shim beams (dimensions in millimeters)

The material properties of the concrete were obtained from compressive tests and tensile splitting tests of standard six-inch diameter cylinder specimens, and the properties of the reinforcement were determined from tensile coupon tests. The material properties are summarized in Table 3.1.

Table 3.1 Material properties of Vecchio-Shim beams

Concrete					
Beam Series	f'_c (MPa)	ε_o ($\times 10^{-3}$)	E_c (MPa)	f_{sp} (MPa)	Max Agg. Size (mm)
Series 1	22.6	1.6	36,500	2.37	20
Series 2	25.9	2.1	32,900	3.37	20
Series 3	43.5	1.9	34,300	3.13	20

Reinforcement							
Bar Size	Diameter (mm)	Area (mm^2)	f_y (MPa)	f_u (MPa)	E_s (MPa)	ε_{sh} ($\times 10^{-3}$)	ε_u ($\times 10^{-3}$)
10M	11.3	100	315	460	200,000	7.7	207
25M[a]	25.2	500	440	615	210,000	7.5	200
25M[b]	25.2	500	445	680	220,000	8.5	216
30M	29.9	700	436	700	200,000	11.4	175
D4	5.7	25.7	600	651	200,000	3.0	38
D5	6.4	32.2	600	649	200,000	3.0	35

[a] Series 2
[b] Series 1 and 3

3.4.1 Analytical Modelling

To assess the performance of the proposed beam-membrane interface element, two types of analysis were conducted and are described in this section:

1) Stand-alone analyses using a frame-type program, VecTor5, and a detailed FE-type program, VecTor2.
2) Mixed-Type analyses by integrating VecTor2 and VecTor5 programs using different configurations of substructuring.

The mixed-type analysis results were compared against the experimentally reported behaviours and the stand-alone analysis responses. A complete description of the model and computed results for each case study is presented in the following subsections.

In all analysis cases reported herein, the default material models and analysis parameters defined in all VecTor software programs were used. These material models and analysis options are summarized in Table 3.2.

Table 3.2 Default material models and analysis options utilized in verification studies

Concrete Models		Reinforcement Models	
Compression Pre-Peak	Hognestad	Hysteretic Response	Seckin
Compression Post-Peak	Modified Park-Kent	Dowel Action	Tassios (Crack Slip)
Compression Softening	Vecchio 1992-A		
Tension Stiffening	Modified Bentz 2003		
Tension Softening	Bilinear	**Analysis Options**	
Confined Strength	Kupfer/Richart	Strain History	Considered
Dilation	Variable - Orthotropic	Geometric Nonlinearity	Considered
Cracking Criterion	Mohr-Coulomb (Stress)	Section Analysis*	Nonlinear
Crack Stress	Basic (DSFM/MCFT)	Shear Analysis*	Parabolic Shear Strain
Crack Width Check	Max Crack (Agg/2.5)		
Crack Slip Calculation	Walraven		
Hysteretic Response	Nonlinear-Plastic Offsets		

* Analysis options in VecTor5

Stand-Alone Models

Two types of stand-alone analyses were performed for each beam: a frame-type analysis (VecTor5 program) and a detailed FE-type analysis (VecTor2 program). Taking advantage of the symmetry of the beams and test setup, only half of the beam span was modelled. In the stand-alone frame analysis, 6-DOF layered frame elements with element lengths ranging from 200 mm to 300 mm were used to model the beams. As a result, a total of 9, 10, and 12 elements were utilized to model the Series 1, 2, and 3 beams, respectively. Each frame element was divided into 50 concrete layers, providing sufficient accuracy for the sectional analysis. Based on the configuration of the stirrups, the out-of-plane reinforcement ratio (ρ_z) and transverse reinforcement ratio (ρ_t) were determined and assigned to the outer layers and core layers of the cross section, respectively. The out-of-plane reinforcement ratio represented the legs of the stirrups extended in the out-of-plane direction which provided strength and ductility enhancement for the corresponding concrete layers. This ratio was computed according to a tributary area enclosed by 5.5 times the bar diameter, as suggested by Guner and Vecchio (2010b). The loading was applied as an imposed displacement with increments of 0.25 mm at the mid-span of the beam. To model the support conditions, a roller support was defined at the left end of the beam by restraining the vertical DOF. In addition, to satisfy the condition of symmetry, both the horizontal and rotational DOFs were restrained at the mid-span nodes of the beam.

The stand-alone detailed FE model was created using 8-DOF reinforced concrete rectangular elements with an approximate mesh size of 45 mm × 37 mm in the X and Y directions, respectively. The selected mesh size provided an adequate number of elements through the height and along the length of the beam to sufficiently capture the stiffness degradation and damage mechanisms. Longitudinal reinforcing bars were modelled as discrete using 4-DOF truss bar elements; transverse reinforcement was modelled as smeared. As a result, the Series 1 beams were modelled with a total of 901 elements (760 rectangular elements and 141 truss elements); beams within Series 2 were modelled using a total of 1128 elements (920 rectangular elements and 228 truss elements); and a total of 1471 elements (1240 rectangular elements and 231 truss elements) were used to model the Series 3 beams. To accurately capture any possible damage due to the high compression forces under the loading plate, special considerations were given in modelling this critical region. The loading plate was modelled using structural steel rectangular elements. Between the steel and concrete elements a layer of unidirectional bearing elements was used to allow strain in the horizontal direction, providing a more realistic representation of the force distribution and crack pattern under the load. For the inclusion of confinement effects due to the steel plate in the out-of-plane direction, an out-of-plane smeared reinforcement (ρ_z) was added to the adjacent concrete elements; for the elements directly beneath the loading plate ρ_z was selected as 5% and for other six neighboring elements ρ_z of 2.5% was used. A sensitivity analysis was performed to investigate the influence of the out-of-plane reinforcement. Detailed modelling of the loading plate and neighboring elements are shown in Figure 3.17 and Figure 3.18.

Mixed-Type Models

Creating a proper mixed-type model, wherein the critical regions are modelled using high-dimensional elements (e.g., membrane elements) and the rest of the structure is modelled with low-dimensional elements (e.g., layered frame elements), requires having a good understanding of the behaviour of the structure and of the locations of potentially critical regions prior to the analysis. For a single member structure (e.g., beams and columns), this can be difficult; for a multi-member structure, the locations of potentially critical members is typically more intuitive.

For the Vecchio-Shim beams, three different failure modes were observed during the experiment: diagonal-tension, shear-compression, and flexural-compression. In this section, two sets of mixed-type models were used to assess the performance of the F2M interface elements and also to demonstrate the importance of using a proper mixed-type configuration. The following is a description of each set of the mixed-type models.

For the beams without shear reinforcement (OA1, OA2, and OA3), the behaviour was dominated by a diagonal-tension crack which continued as a sliding crack in the horizontal direction along the longitudinal reinforcement extending to the support. To accurately capture the failure mechanism, the membrane sub-model was created on the support side of the beam and the frame sub-model was created on the mid-span side of the structure. Two types of mixed-type models were used to investigate the influence of the length of the membrane sub-model: Mixed-Type 1 (0.65L in VecTor2 and 0.35L in VecTor5), and Mixed-Type 2 (0.90L in VecTor2 and 0.10L in VecTor5), where L is the half-span length of the beam.

With the other types of the beams (A, B, and C), which contained transverse reinforcement, the failure was initiated by crushing of the concrete in the compression zone under the loading plate. In the intermediate length beams (A1, A2, B1, B2, C1, and C2), the crushing failure was followed by a diagonal shear crack and some minor flexural cracks at the mid-span while in the long-span beams (A3, B3, and C3) the flexural cracks were much more pronounced and the diagonal shear crack was either insignificant or not observed at all. Therefore, unlike the beams without shear reinforcement, the beams containing shear reinforcement had more than one mechanism contributing to the final failure and the location of the critical zones varied from one beam to another. As a result, two types of mixed-type models with opposite substructuring configurations were created (Mixed-Type 1 and Mixed-Type 2). In the Mixed-Type 1 configuration, the membrane sub-model was located close to the support end of the beam, while in the Mixed-Type 2 configuration, the membrane sub-model was located near the loading plate. In both mixed-type models, 65% of the structure was modelled in the VecTor2 program and 35% of the structure was modelled in the VecTor5 program.

According to CSA A23.3 (2014) the critical section for checking the shear capacity of a beam is located d_v from the support or loading plate. d_v is defined as the effective shear depth which is taken as the greater of 0.72h or 0.90d where h is the cross section height and d is the distance from the extreme compression layer to centroid of the longitudinal reinforcement in the tension zone. It is worth noting that, regardless of the beam type, for the Mixed-Type 1 configuration the critical section as specified by CSA A23.3 is located in the VecTor5 sub-model while in the Mixed-Type 2 configuration the critical section is located in the VecTor2 sub-model.

For all the mixed-type models, the frame sub-model and membrane sub-model were defined in a similar fashion as explained for the stand-alone frame model and stand-alone membrane model, respectively. The two sub-models were connected using F2M interface elements. The multi-platform framework, Cyrus, was used to coordinate the mixed-type analysis. Figure 3.17 and Figure 3.18 provide details of the finite element models for beams without shear reinforcement and beams with shear reinforcement, respectively.

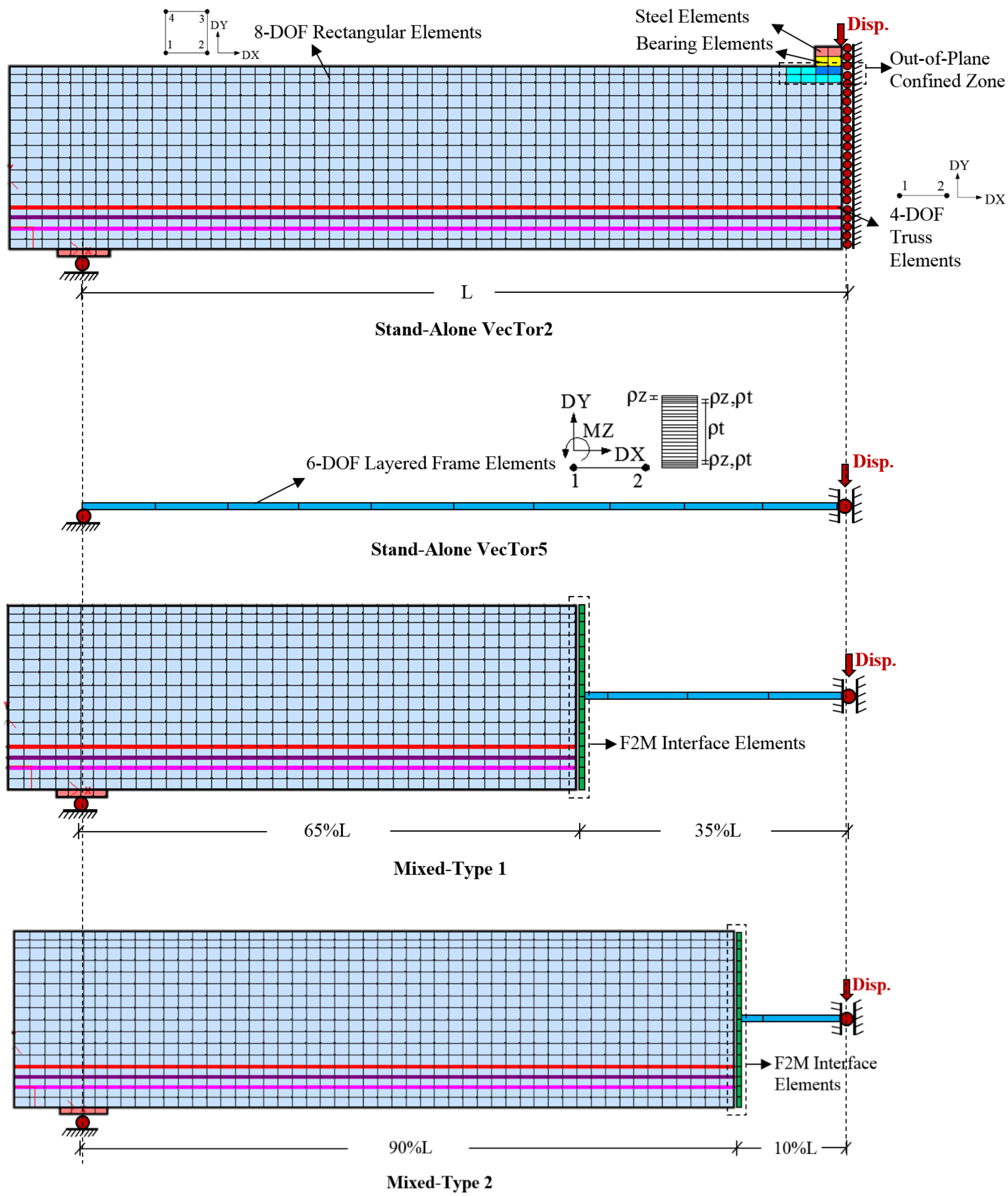

Figure 3.17 FE mesh for stand-alone and mixed-type analyses of OA type of beams

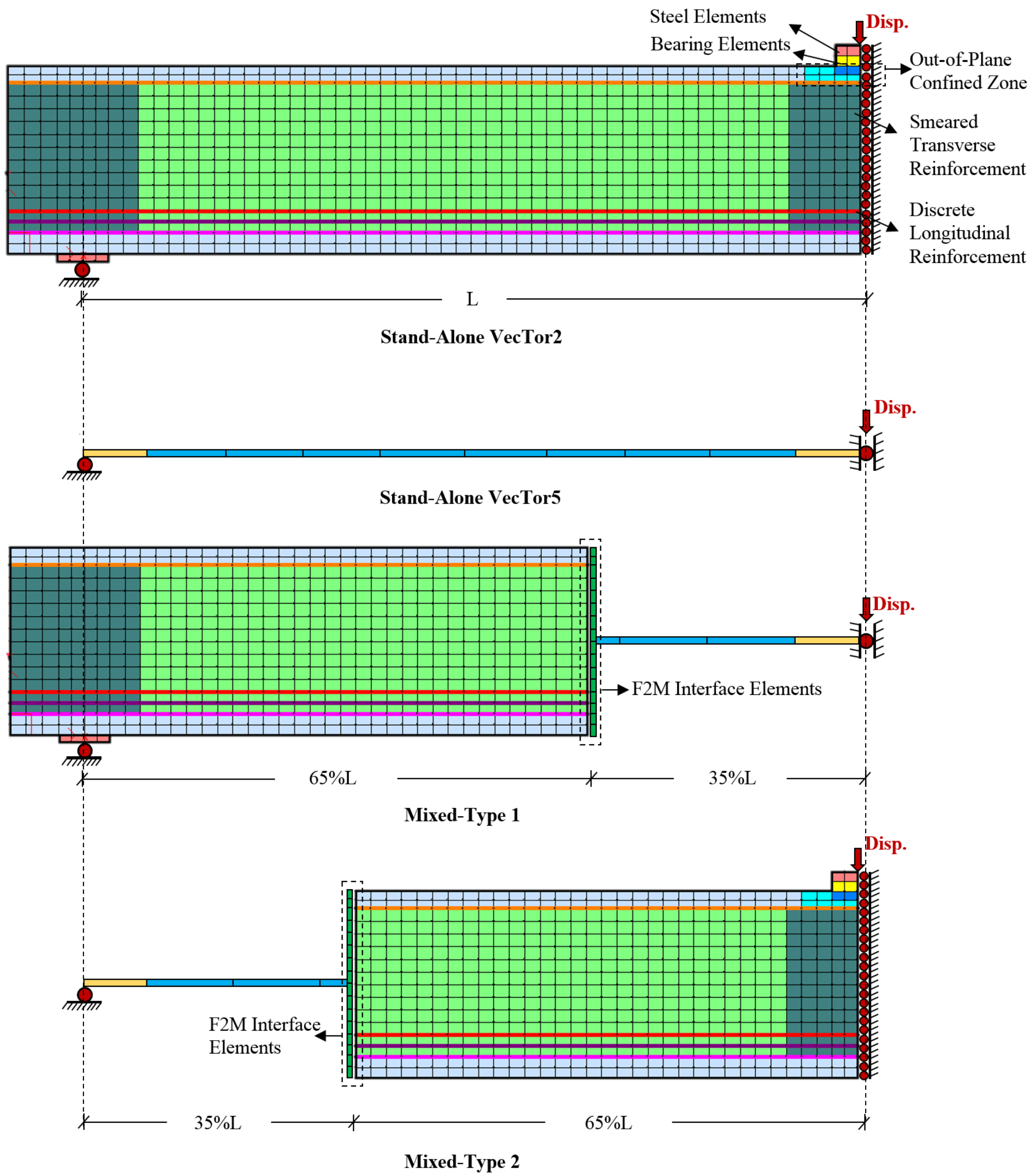

Figure 3.18 FE mesh for stand-alone and mixed-type analyses of A, B, and C types of beams

3.4.2 Comparison of the Results

Comparison against Stand-Alone Analyses

The load-deflection responses and crack patterns of the mixed-type analyses are compared against the stand-alone analysis results and experimentally observed behaviours in Figure 3.19 and Figure 3.20, respectively.

A summary of the stand-alone analysis results is presented in Table 3.3. It can be seen that both VecTor2 and VecTor5 were capable of computing the peak load capacity of the beams with a high level of accuracy, resulting in mean calculated to measured ratios of 1.05 and 1.07 with coefficient of variations of 4.8% and 10.4%, respectively. With regard to the displacements at ultimate load, VecTor2 had a mean analytical to experimental value of 0.99 with a coefficient of variation of 16.4% while VecTor5 resulted in a mean of 0.81 with a coefficient of variation of 21.5%. It is worth noting that most other frame-type analysis tools, unlike the VecTor5 program, do not consider shear-related mechanisms, which can result in significant overestimation of the load capacity and ductility. Although VecTor5 was capable of considering shear behaviour relatively well, because of the limitations associated with its frame-type analysis nature, it underestimated the ductility and was unable to accurately capture the post-peak response. These facets were computed with much better accuracy by VecTor2, which is expected for a detailed FE-type program.

For all types of mixed-type analyses, except the Mixed-Type 2 configuration of the A beams, the load-deflection responses fell between the stand-alone analysis results of VecTor2 and VecTor5 or were sufficiently close to them, resulting in a high level of accuracy in capturing the behaviour of the beams. With the Mixed-Type 1 configuration, the computed peak load capacity and ductility had mean analytical to experimental values of 1.04 and 0.79 with coefficients of variation of 9.7% and 20.2%, respectively. With the Mixed-Type 2 configuration, mean analytical to experimental values of 1.08 and 1.02 with coefficients of variation of 5.7% and 19.1 % were obtained for the peak load capacity and ductility, respectively. A summary of the mixed-type analysis results is presented in Table 3.4. A more detailed description of the analysis results for each type of cross section is provided in the following discussion.

Table 3.3 Summary of the stand-alone analysis results for VS beams

Beam	Peak Load (kN)					Displacement at Peak Load (mm)				
	Test	VT2	VT5	VT2/Test	VT5/Test	Test	VT2	VT5	VT2/Test	VT5/Test
OA1	331	325	376	0.98	1.14	9.1	8.5	7.5	0.93	0.82
OA2	320	371	441	1.16	1.38	13.2	13.2	16.5	1.00	1.25
OA3	385	374	415	0.97	1.08	32.4	24.7	28.7	0.76	0.89
A1	459	497	478	1.08	1.04	18.8	23.5	17.8	1.25	0.94
A2	439	458	474	1.04	1.08	29.1	30.2	22.8	1.04	0.78
A3	420	444	425	1.06	1.01	51.0	41.5	33.5	0.81	0.66
B1	434	462	455	1.06	1.05	22.0	23.7	16.8	1.08	0.76
B2	365	374	365	1.02	1.00	31.6	30.7	21.5	0.97	0.68
B3	342	357	344	1.04	1.01	59.6	50.2	34.3	0.84	0.57
C1	282	283	269	1.00	0.95	21.0	26.2	15.0	1.25	0.71
C2	290	311	332	1.07	1.14	25.7	29.0	23.5	1.13	0.91
C3	265	276	263	1.04	0.99	44.3	37.7	34.3	0.85	0.77
	Mean			1.05	1.07	Mean			0.99	0.81
	COV (%)			4.8	10.4	COV (%)			16.4	21.5

Table 3.4 Summary of the mixed-type analysis results for VS beams

Beam	Peak Load (kN)					Displacement at Peak Load (mm)				
	Test	MT1	MT2	MT1/Test	MT2/Test	Test	MT1	MT2	MT1/Test	MT2/Test
OA1	331	339	324	1.02	0.98	9.1	7.0	6.5	0.77	0.71
OA2	320	429	389	1.34	1.22	13.2	16.0	13.7	1.21	1.04
OA3	385	413	387	1.07	1.01	32.4	29.0	25.8	0.90	0.79
A1	459	460	522	1.00	1.14	18.8	16.0	23.7	0.85	1.26
A2	439	459	495	1.05	1.13	29.1	21.8	35.3	0.75	1.21
A3	420	421	450	1.00	1.07	51.0	34.8	42.3	0.68	0.83
B1	434	435	478	1.00	1.10	22.0	14.3	25.2	0.65	1.15
B2	365	358	380	0.98	1.04	31.6	22.0	32.5	0.70	1.03
B3	342	340	371	0.99	1.08	59.6	34.3	51.0	0.57	0.86
C1	282	263	290	0.93	1.03	21.0	14.5	27.5	0.69	1.31
C2	290	322	318	1.11	1.10	25.7	23.0	30.5	0.89	1.19
C3	265	260	279	0.98	1.05	44.3	34.8	38.3	0.78	0.86
	Mean			1.04	1.08	Mean			0.79	1.02
	COV (%)			9.7	5.7	COV (%)			20.2	19.1

For the OA beams containing no shear reinforcement, the F2M interface element was able to compute the diagonal shear crack at the connection section (see Figure 3.20). In addition, having the membrane sub-model on the support side of the beam enabled the mixed-type analysis to capture the sliding crack in the horizontal direction along the longitudinal reinforcement. In the Mixed-Type 1 configuration (0.65L in VecTor2 and 0.35L in VecTor5), the shear failure occurred in the VecTor5 sub-model resulting in a response which was closer to the stand-alone VecTor5 analysis. In the Mixed-Type 2 configuration, in which a greater portion of the structure was modelled in the VecTor2 program (0.90L in VecTor2 and 0.10L in VecTor5), the shear failure occurred in the VecTor2 sub-model and therefore the response leaned towards the stand-alone VecTor2 analysis.

The A beams, having the lowest amount of shear reinforcement among the beams containing stirrups (ρ_t equal to 0.1%), exhibited the most challenging behaviour to capture using the mixed-type analysis. In these beams, three types of mechanisms contributed to the final failure: horizontal sliding crack near the support, diagonal shear crack, and crushing of the concrete under the loading plate. In the Mixed-Type 1 configuration (0.65L in VecTor2 and 0.35L in VecTor5), the failure was governed by crushing of the top layers of frame elements in the compression zone, resulting in a response which was closer to the stand-alone VecTor5 analysis. For A1 and A2 beams, the peak loads were slightly lower than the VecTor5 stand-alone analysis results due to the damage in the VecTor2 sub-model attributed to the formation of a diagonal shear crack and a horizontal sliding crack. In the Mixed-Type 2 configuration (0.35L in VecTor5 and 0.65L in VecTor2), having the frame sub-model on the support side of the beams, compromised the ability of the mixed-type analysis to fully capture the horizontal sliding crack along the longitudinal reinforcement, resulting in overestimations of peak load by 14% and 13% and ductility by 26% and 21% for A1 and A2 beams, respectively. With the A3 beam, because the failure mode was flexural-compression and horizontal sliding crack had a minor effect, the computed peak load was similar to the stand-alone VecTor2 response and only ductility was adversely influenced. For all three beams (A1, A2, and A3), the mixed-type analysis was able to fully capture the diagonal shear crack and cracking near the loading plate due to high compressive stresses. However, the mixed-type analysis computed more flexural cracks at the mid-span compared to the stand-alone analysis due to its more ductile response (see Figure 3.20).

With the B and C beams, having higher amounts of shear reinforcement (ρ_t equal to 0.15% and 0.2%, respectively) compared to the OA and A beams, the failure was initiated by crushing of the concrete near the loading plate and followed by either a diagonal shear crack (intermediate-span beams) or a series of flexural cracks at the mid-span (long-span beams). In these beams, the influence of the horizontal sliding crack on the response of the structure was insignificant. Consequently, the analysis results computed by both the Mixed-Type 1 and Mixed-Type 2 configurations had excellent agreement with the stand-alone analysis responses and correlated reasonably well with the experimentally observed behaviour. Depending on whether the critical region of the beam was located in the detailed FE sub-model or the frame sub-model, the mixed-type analysis response followed a similar path as the stand-alone analysis response obtained from either VecTor2 or VecTor5.

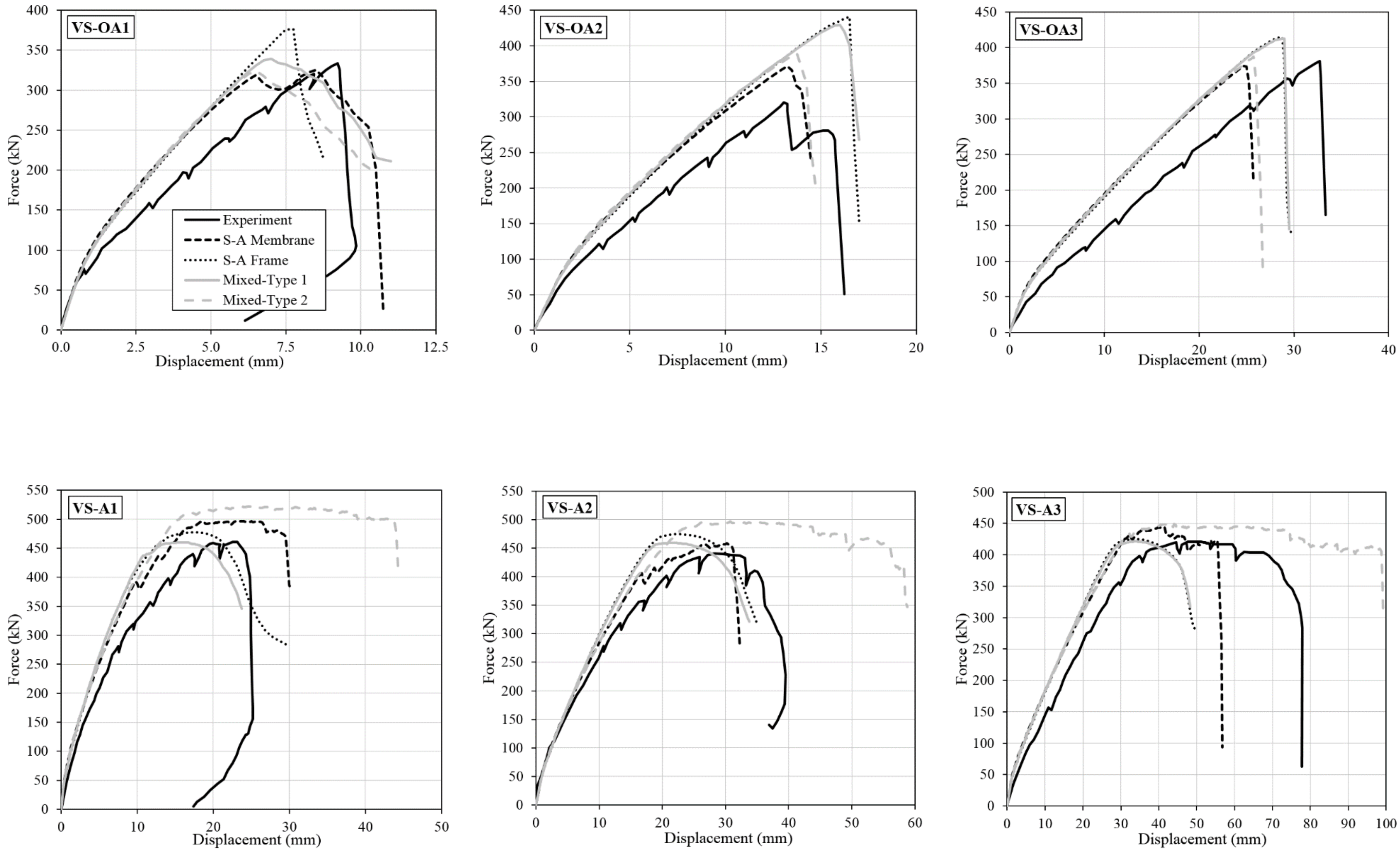

Figure 3.19 Comparison of the mid-span load-defection response for Vecchio-Shim beams

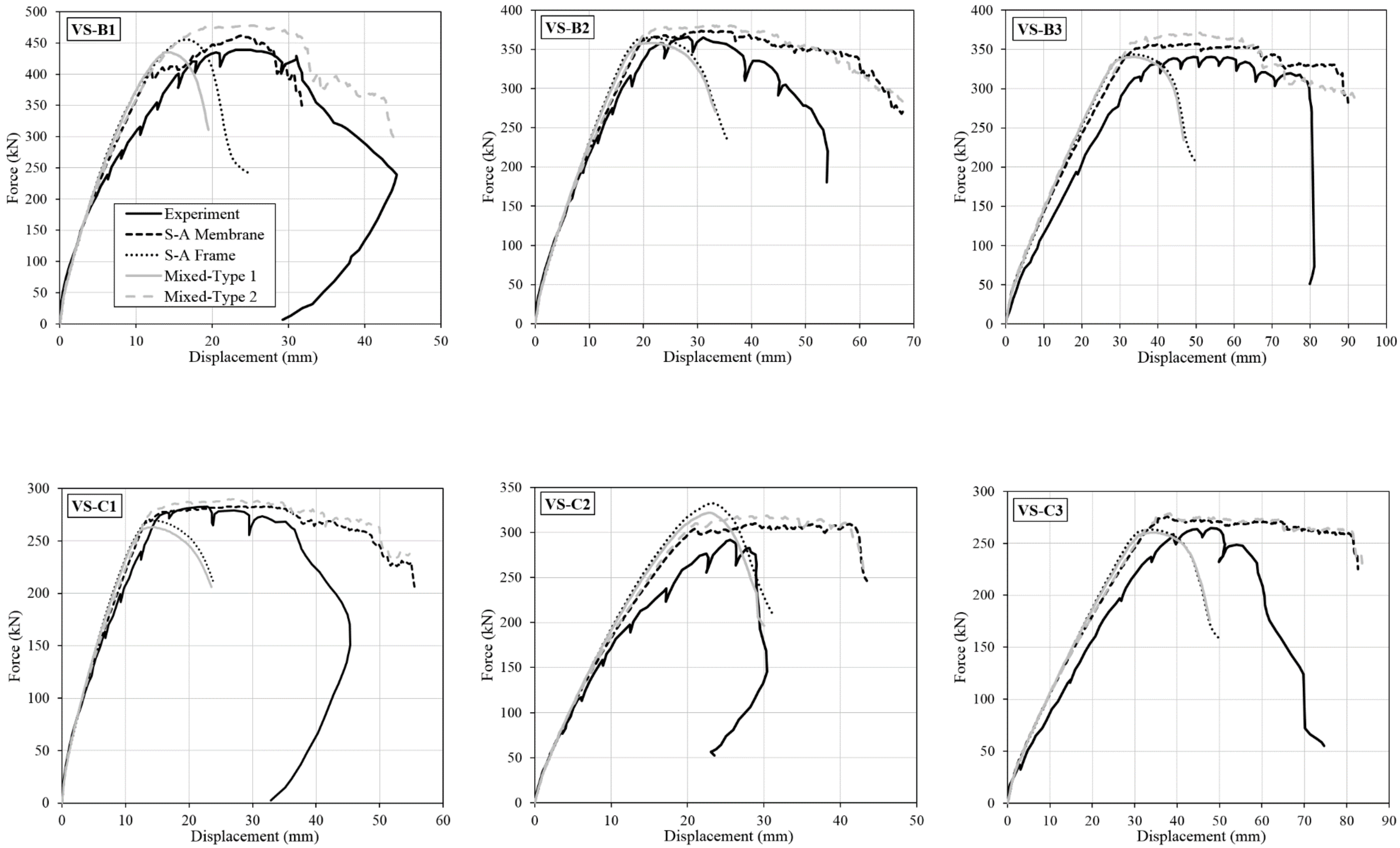

Figure 3.19 Comparison of the mid-span load-defection response for Vecchio-Shim beams (continued)

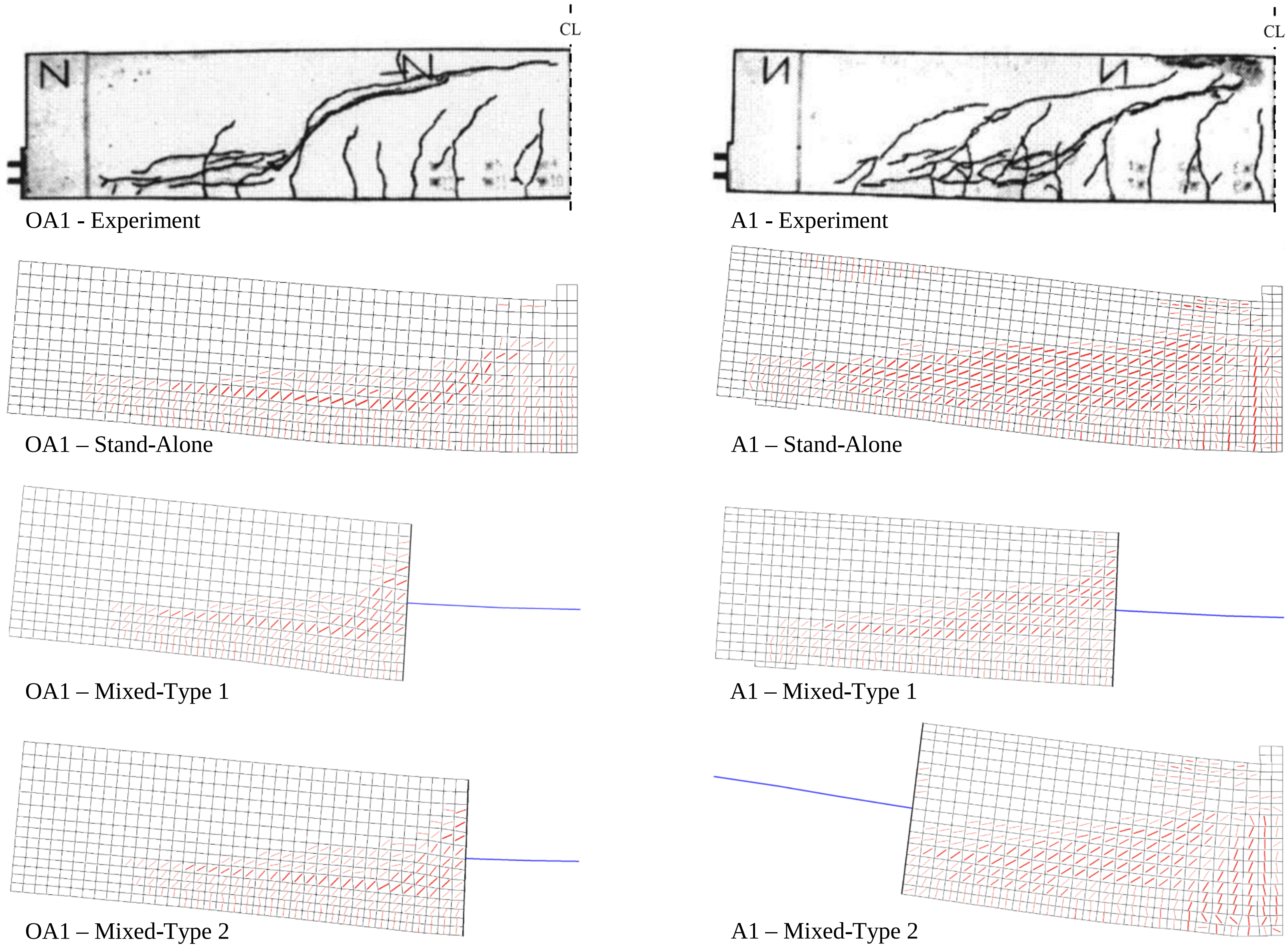

Figure 3.20 Comparison of the analytical and experimental crack patterns for Vecchio-Shim beams

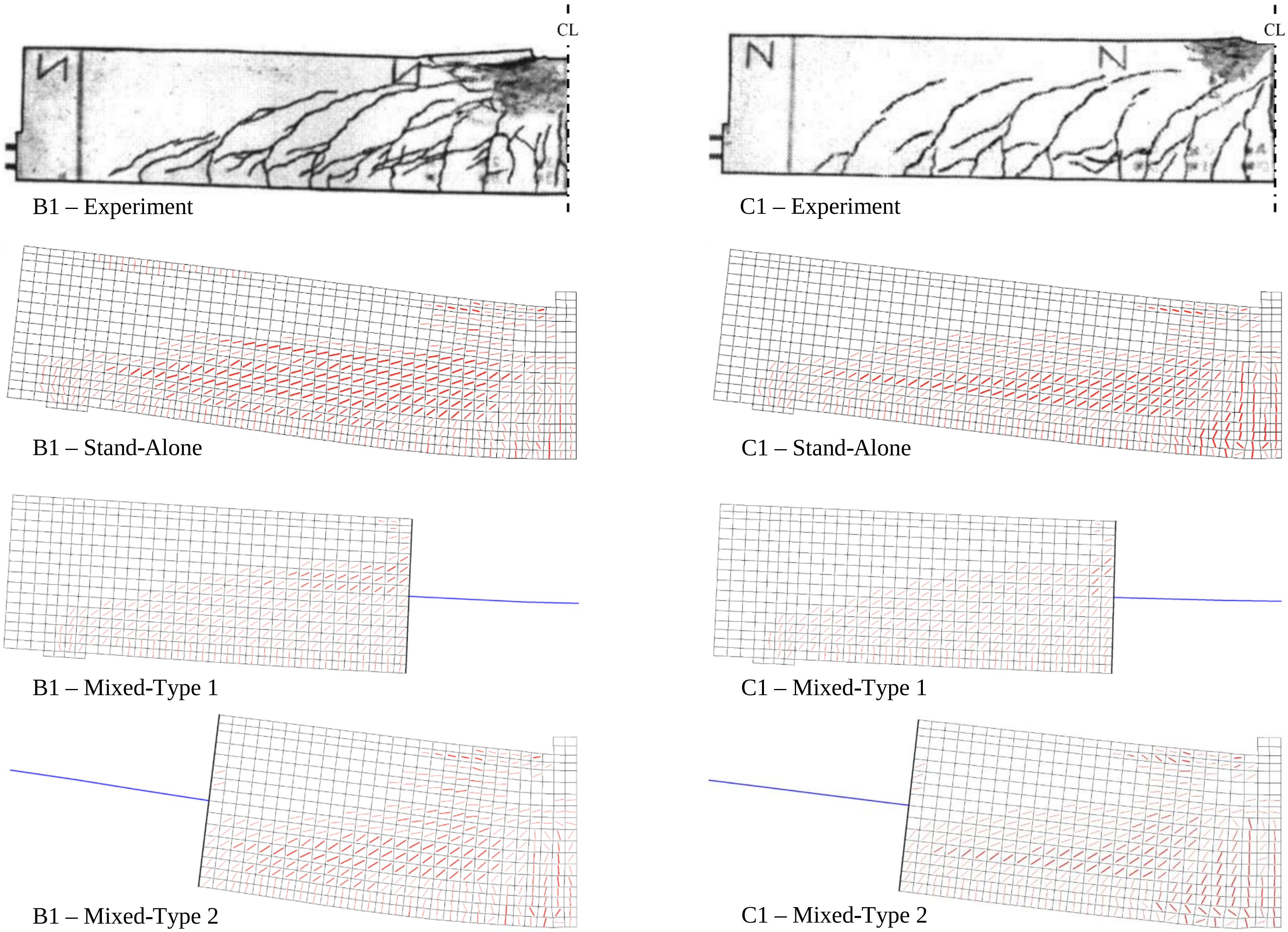

Figure 3.20 Comparison of the analytical and experimental crack patterns for Vecchio-Shim beams (continued)

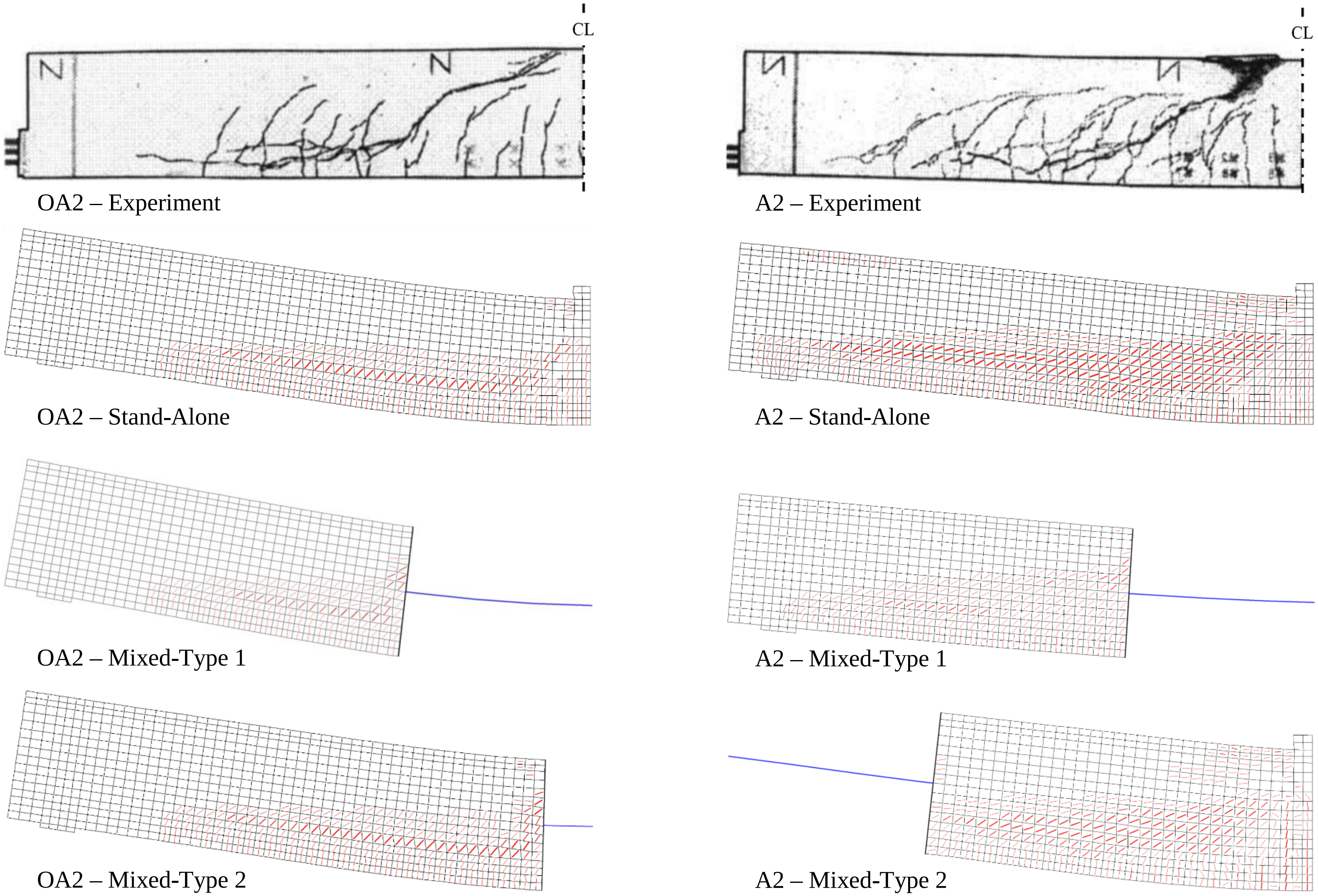

Figure 3.20 Comparison of the analytical and experimental crack patterns for Vecchio-Shim beams (continued)

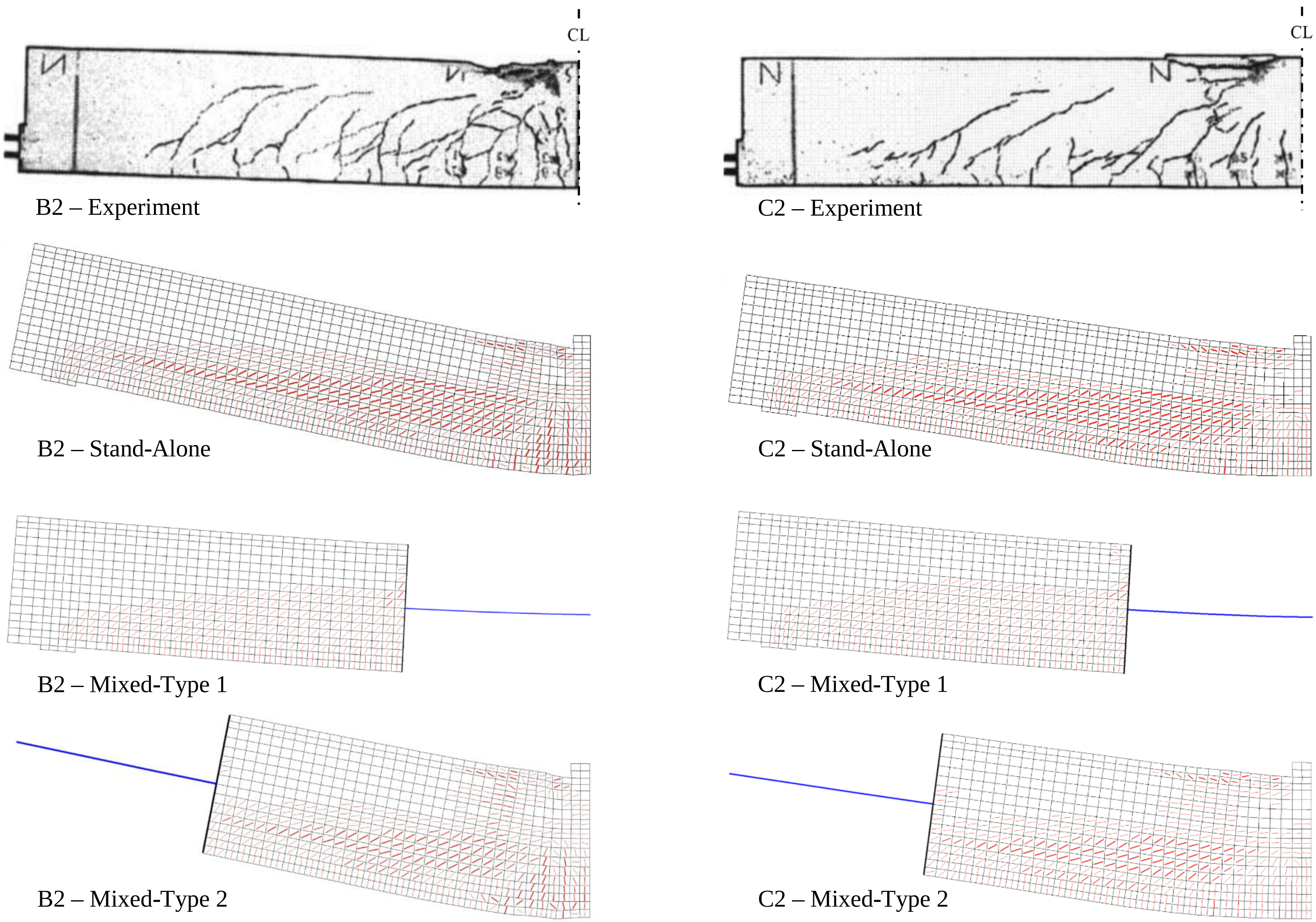

Figure 3.20 Comparison of the analytical and experimental crack patterns for Vecchio-Shim beams (continued)

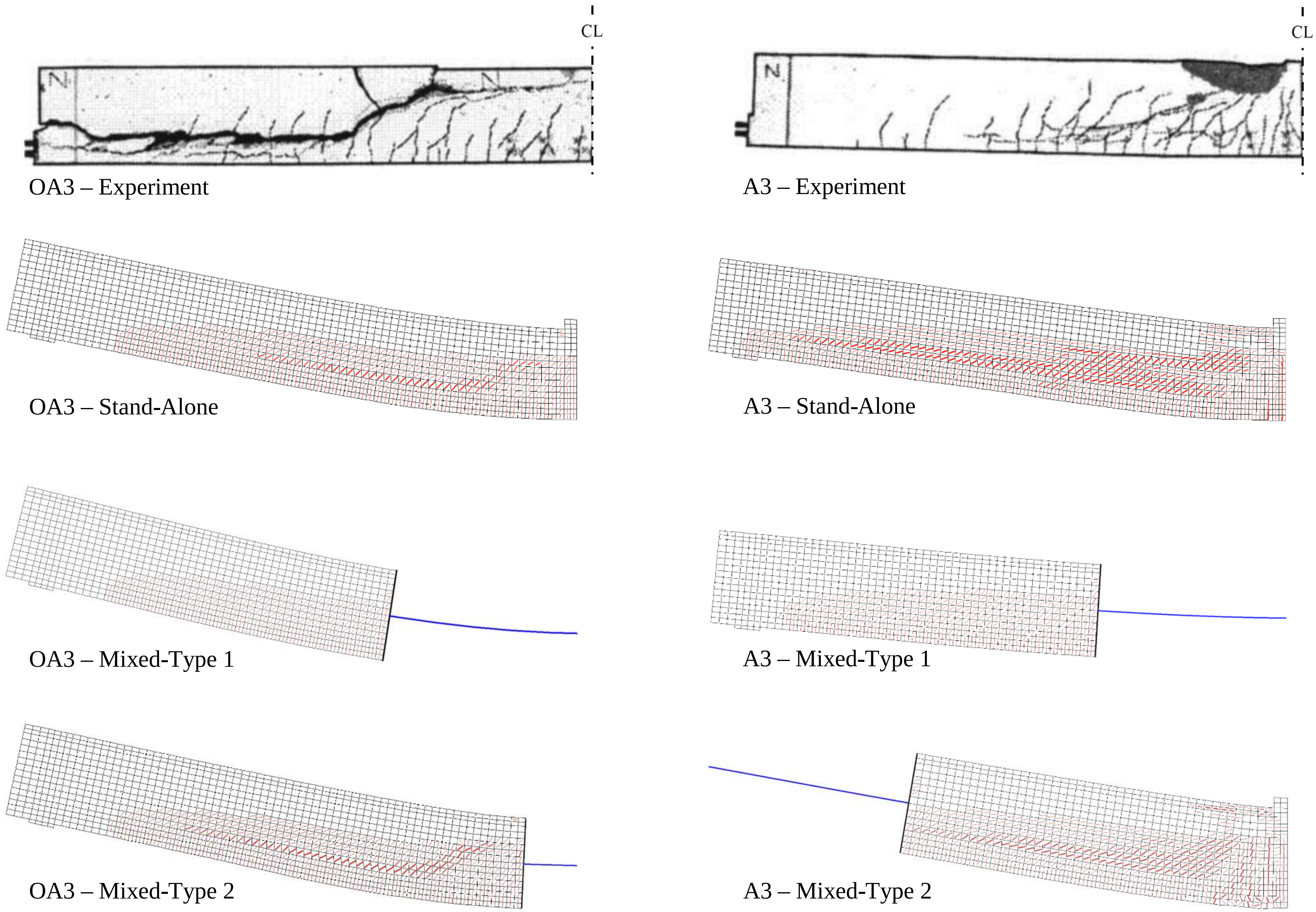

Figure 3.20 Comparison of the analytical and experimental crack patterns for Vecchio-Shim beams (continued)

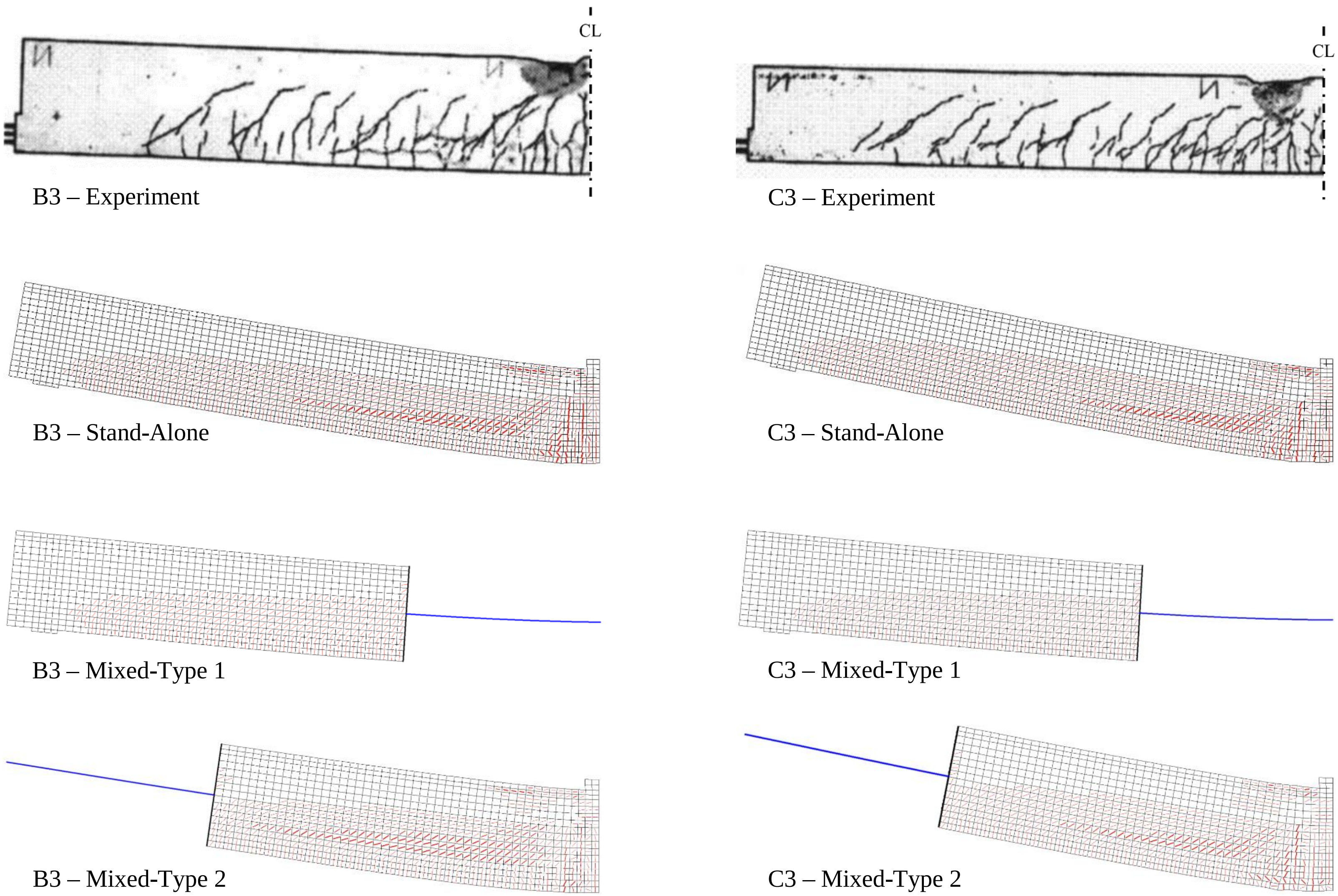

Figure 3.20 Comparison of the analytical and experimental crack patterns for Vecchio-Shim beams (continued)

It should be noted that for any of the aforementioned beam specimens, if all the critical regions of the structure were modelled in a detailed FE sub-model, which is common in a typical multi-platform simulation, the analysis response would be similar to that computed by the stand-alone detailed FE program. For example, considering a new type of mixed-type configuration (Mixed-Type 3) for A1 beam in which 75% of the full span length was modelled in VecTor2, the results of the mixed-type analysis were almost identical to that obtained by the stand-alone VecTor2 analysis. The finite element mesh and computed load-deflection response of the Mixed-Type 3 configuration for the A1 beam are presented in Figure 3.21 and Figure 3.22.

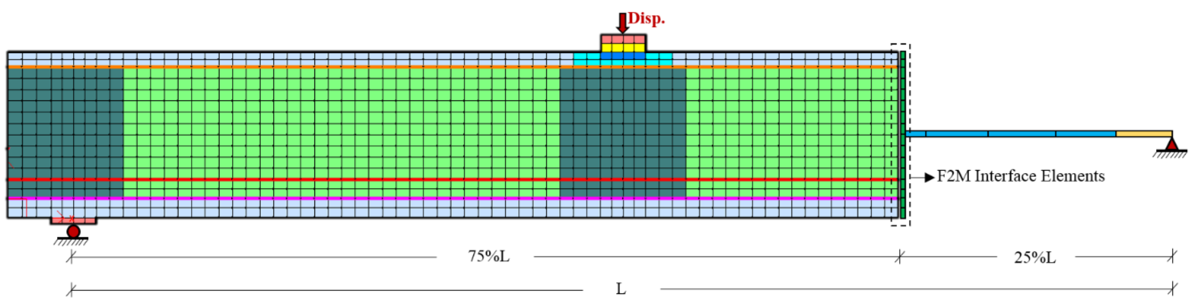

Figure 3.21 Finite element mesh of Mixed-Type 3 configuration for A1 beam

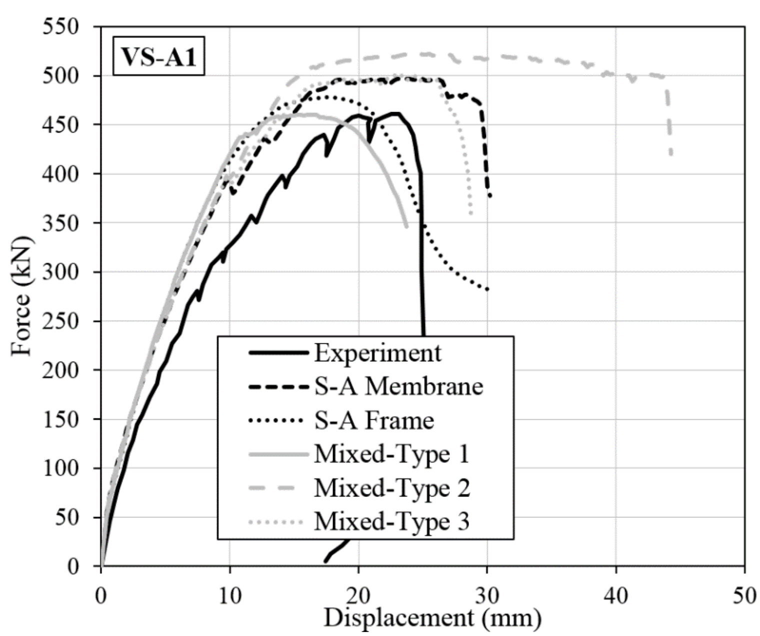

Figure 3.22 Load-defection response of A1 beam using different mixed-type configurations

To investigate the influence of confinement effects due to the steel plate in the out-of-plane direction, the out-of-plane smeared reinforcement ratios of elements beneath the loading plate (ρ_{z1}) and other six neighboring elements (ρ_{z2}) were set to zero and the stand-alone membrane analyses for A1 and B3 beams were repeated. The A1 beam had a shear-compression type of failure while the failure mode of the B3 beam was flexural-compression. The sensitivity analysis results are shown in Figure 3.23. It can be seen that the out-of-plane reinforcement had almost no effect on the peak strength and minor influence on the ductility of the beams. This was mainly attributed to modelling the bearing elements between the steel plate and the concrete elements which allowed horizontal expansions in elements located under the loading plate, preventing local failure.

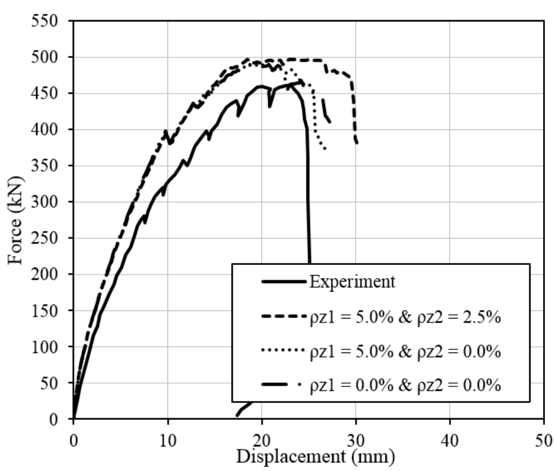

(a)

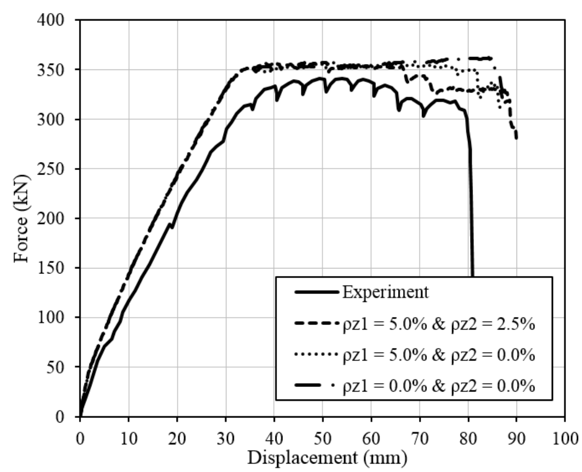

(b)

Figure 3.23 Influence of confinement effects in the out-of-plane direction due to the steel loading plate: (a) A1 beam; (b) B3 beam

The minor influence of the out-of-plane reinforcement on the ductility can be explained as the following. For the A1 beam, the compression failure happened in the neighboring elements of the loading plate with out-of-plane reinforcement. Neglecting the out-of-plane confinement reduced the maximum compressive strength of these elements, resulting in a small reduction in the ductility of the beam. For the B3 beam, the compression failure was caused by the concrete elements without out-of-plane reinforcement located further from the loading plate in the cover region. Neglecting the out-of-plane confinement reduced the compressive stress concentration at the top of the cross section and delayed the compression failure of these elements, slightly increasing the ductility of the beam.

Comparison against Other Mixed-Type Methods

To further assess the performance of the F2M interface element, the analysis results were compared against two other existing coupling methods which have been widely used in previous studies: the Rigid Links method (Adams and Askenazi, 1999) and the McCune et al. (2000) method. As discussed in Section 3.2, the McCune et al. (2000) method was originally presented for coupling a beam element with ten eight-noded membrane elements with quadratic shape functions. Here, using a similar procedure to that employed by McCune et al. (2000), the constraint equations were derived for coupling a beam element and (n-1) four-noded membrane elements with linear shape functions:

$$u_f = \frac{1}{2(n-1)} \sum_{p=1}^{n-1} \left(u_p + u_{p+1}\right) \tag{3.42}$$

$$\begin{aligned} v_f = \frac{3}{4(n-1)^3} \sum_{p=1}^{n-1} \Bigg\{ & v_p \left[(n-1)^2 - (2p-n)^2 - \frac{1}{3} + \frac{2}{3}(2p-n) \right] \\ & + v_{p+1} \left[(n-1)^2 - (2p-n)^2 - \frac{1}{3} - \frac{2}{3}(2p-n) \right] \Bigg\} \end{aligned} \tag{3.43}$$

$$\theta_f = \frac{-3}{h(n-1)^2} \sum_{p=1}^{n-1} \left[u_p (2p - n - \frac{1}{3}) + u_{p+1} (2p - n + \frac{1}{3}) \right] \tag{3.44}$$

where u_f, v_f, and Θ_f are the translational and rotational displacements at the interface node of the frame element, u_p and v_p are the translational displacements at the interface node of the p^{th} membrane element, and h is the height of the interface section.

The constraint relations were incorporated into the equilibrium equation of the system based on the master-slave method. First, a static condensation procedure was employed to find the condensed form of the force vector, {F}, displacement vector, {D}, and stiffness matrix, [K], of the system at the interface section. Then, the interface DOFs of the membrane and frame sub-models were considered as master and slave DOFs, respectively. The relation between the interface DOFs displacement vector, $\{\mathrm{D}\}$, and master DOFs displacement vector, $\{\bar{\mathrm{D}}\}$, can be expressed by defining a transformation matrix, [T], based on the constraint equations:

$$\{\mathrm{D}\}_{\mathrm{i}} = [\mathrm{T}]_{\mathrm{i,m}}\{\bar{\mathrm{D}}\}_{\mathrm{m}} \tag{3.45}$$

where i and m are the number of interface and master DOFs, respectively. By using the transformation matrix, a new force vector, $\{\bar{\mathrm{F}}\}$, and stiffness matrix, $[\bar{\mathrm{K}}]$, for the master DOFs can be computed:

$$\{\bar{\mathrm{F}}\}_{\mathrm{m}} = [\mathrm{T}]^{\mathrm{T}}{}_{\mathrm{m,i}}\{\mathrm{F}\}_{\mathrm{i}} \tag{3.46}$$

$$[\bar{\mathrm{K}}]_{\mathrm{m,m}} = [\mathrm{T}]^{\mathrm{T}}{}_{\mathrm{m,i}}[\mathrm{K}]_{\mathrm{i,i}}[\mathrm{T}]_{\mathrm{i,m}} \tag{3.47}$$

Thus, a new equilibrium equation at the interface section can be assembled which only contained the information of the master DOFs:

$$\{\bar{\mathrm{F}}\}_{\mathrm{m}} = [\bar{\mathrm{K}}]_{\mathrm{m,m}}\{\bar{\mathrm{D}}\}_{\mathrm{m}} \tag{3.48}$$

From the equilibrium equation, the displacements of the master DOFs can be found. Substituting these displacements in Eq. 3.45, the displacements of the slave DOFs can be calculated. Using the displacements at the interface section and static condensation equations, one can compute the internal displacements of the system.

The investigation was conducted on the Mixed-Type 1 model of Beam OA1 which exhibited a dominant shear behaviour in both the stand-alone analysis and in the experiment. In the frame sub-model (VecTor5 program), a shear protection mechanism developed by Guner and Vecchio (2010a) was used to ensure that failure occurred in the detailed FE sub-model (VecTor2 program). The mid-span load-deflection responses and crack patterns computed by different types of mixed-type methods are presented in Figure 3.24 and Figure 3.25, respectively.

The Rigid Links method greatly overestimated the peak load and ductility of the beam due to the use of high stiffness elements at the connection section between the two sub-models. A set of high stiffness elements located along the height of the section performed as a strong ‘stirrup’ which suppressed the formation of a diagonal shear crack at the interface section. This can be seen in the crack pattern of the beam in Figure 3.25.

The McCune et al. (2000) method computed the linear response of the structure well, however as expected, after cracking of the concrete it failed to capture the behaviour of the beam, resulting in a significant stress concentration at the longitudinal reinforcement layer and consequently a premature local failure. This method was developed for connections between beam elements and membrane elements for linear elastic analysis, and the constraint equations were not formulated to take into account the influence of truss elements representing longitudinal reinforcement at the interface section. To investigate the McCune et al. (2000) method in more detail, another mixed-type model was created in which the longitudinal reinforcement was modelled as smeared in a tributary area of approximately 7.5 times the bar diameter as recommended by CEB-FIP (1990). Although this prevented the local failure at the longitudinal reinforcement layer, the analysis response underestimated the stiffness and peak load compared to the stand-alone analysis results. In addition, the analysis was not able to capture the diagonal shear crack and computed a horizontal crack located at approximately the mid-depth of the elements containing smeared longitudinal reinforcement. It is worth reiterating that the McCune et al. (2000) method was developed for linear elastic problems and was not intended to be applicable to nonlinear analysis of reinforced concrete structures.

Unlike the other two mixed-type methods, the F2M interface element computed a load-deflection response which was between the stand-alone detailed FE analysis and the stand-alone frame analysis results and also correlated reasonably well with the experimentally reported behaviour. With respect to the crack pattern, the F2M element was able to capture the diagonal shear crack at the connection section and also the horizontal sliding crack along the longitudinal reinforcement layer.

The computed stress distributions at the interface section of the membrane sub-model (section A-A) for pre- and post-cracking conditions are presented in Figure 3.26 and Figure 3.27, respectively. For the proposed F2M element, prior to cracking, the computed axial and shear stresses are almost identical to the stand-alone detailed FE analysis results. After cracking of the concrete, the F2M element was able to accurately capture the stress reduction in the cracked elements located at the bottom of the cross section and the increase in stresses of the uncracked elements at the top of the cross section. Compared to the stand-alone detailed FE analysis, the axial stresses correlated very well and the shear stresses were reasonably accurate. There was a tendency to overestimate the vertical stresses in both pre- and post-cracking conditions.

The other two coupling methods showed major limitations in determining the interface stresses. Although the Rigid Links method accurately captured the axial stresses in both pre- and post-cracking conditions, the computed shear and vertical stresses appeared to have random distributions. Prior to cracking, the McCune et al. (2000) method was unable to capture the shear stresses of concrete membrane elements which were connected to truss elements representing reinforcing bars (i.e., discrete modelling). Alternatively, the longitudinal reinforcing bars were modelled as a component of membrane elements (i.e., smeared modelling). While the smeared modelling approach produced a correct shear stress distribution, it limited considering some RC mechanisms such as bond-slip effects which can be critical in other types of structures. After cracking of the concrete, both the smeared and discrete models of the McCune et al. (2000) method were unable to accurately capture the shear stress distribution which was expected since the method was developed for linear elastic modelling problems.

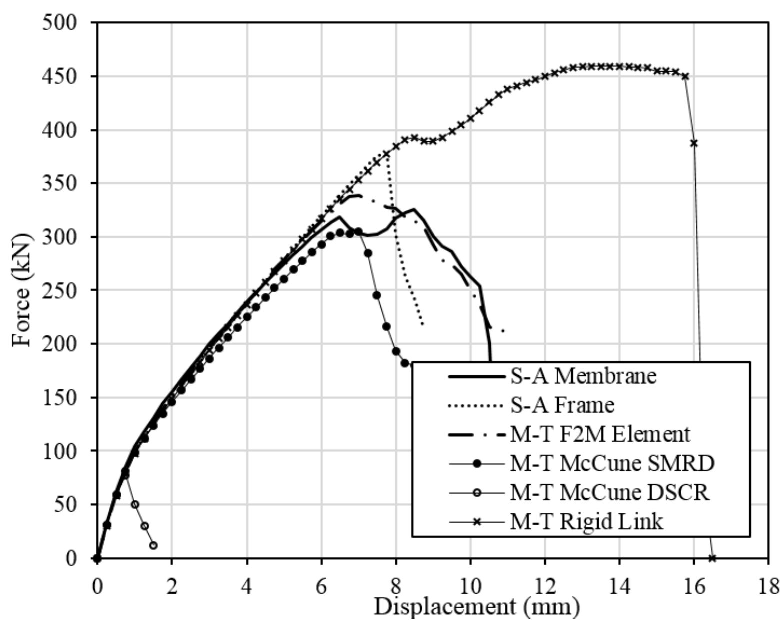

Figure 3.24 Load-deflection responses of OA1 beam based on different mixed-type methods

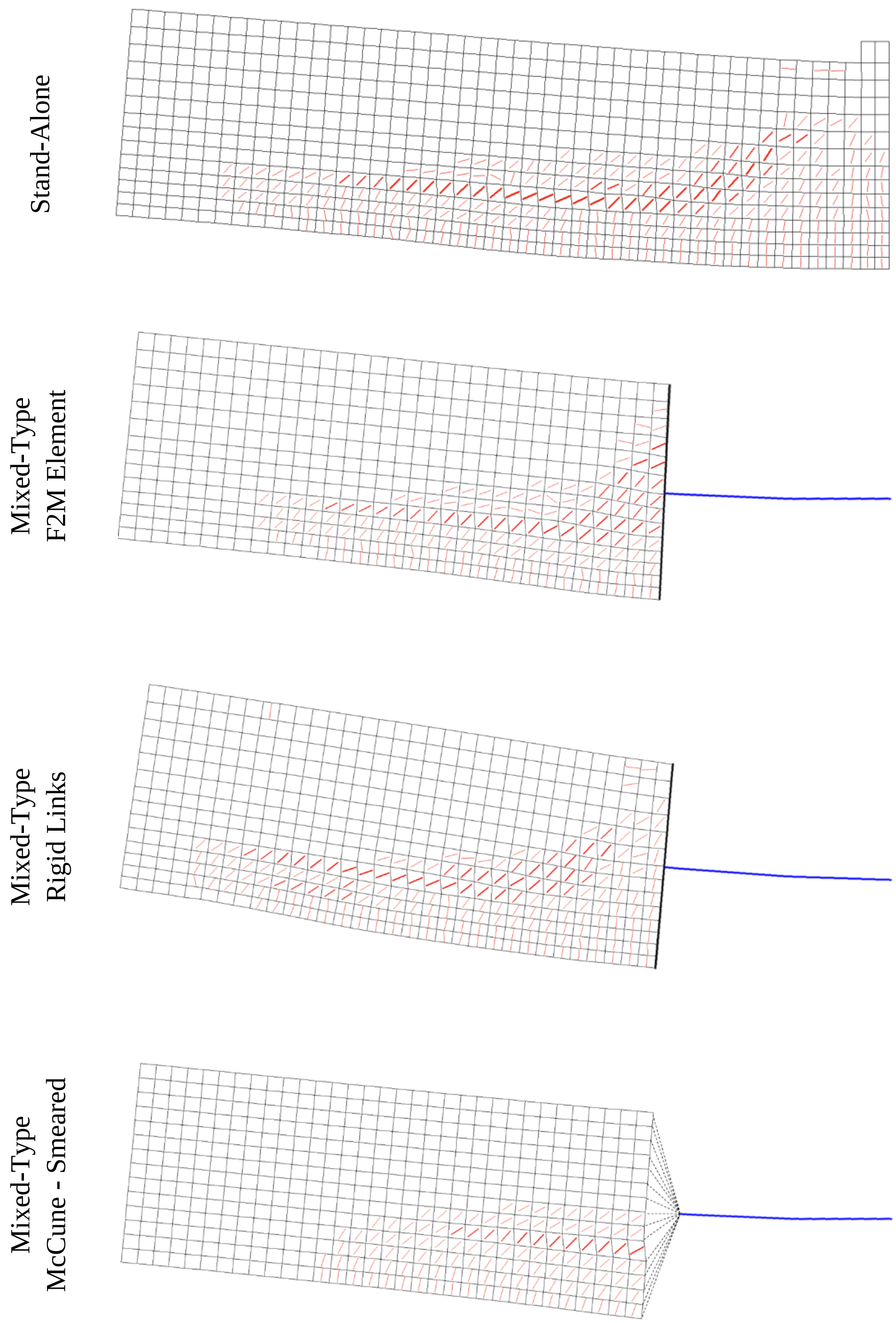

Figure 3.25 Comparison of crack patterns of OA1 beam based on different mixed-type methods

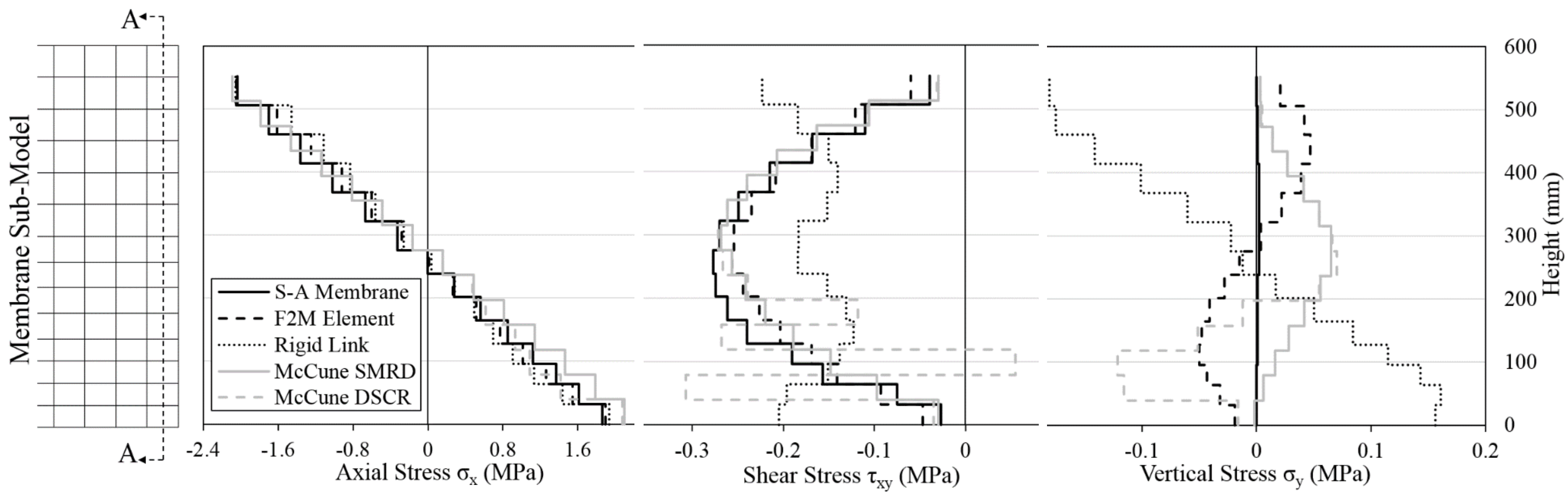

Figure 3.26 Stress distributions through the section prior to cracking (applied displacement = 0.5 mm)

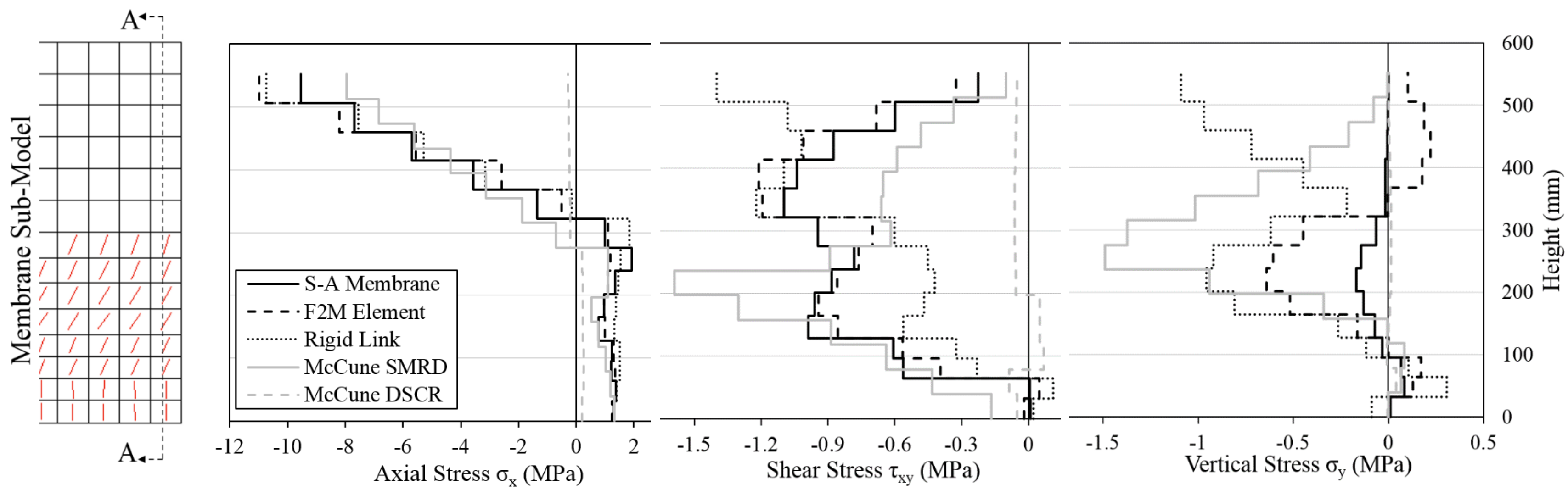

Figure 3.27 Stress distributions through the section after cracking (applied displacement = 4.0 mm)

3.5 Summary and Conclusions

In this chapter, a new beam-membrane interface element, the F2M element, which was specifically formulated for mixed-type analysis of reinforced concrete structures, was presented and verified. The procedure satisfies equilibrium and compatibility requirements at the connection section. The main contributions of the proposed interface method, not available in other known mixed-type methods, can be summarized as: 1) computing linear and nonlinear axial and shear stress distributions at the interface section with a high level of accuracy without decoupling the axial, flexural, and shear effects, 2) allowing for transverse expansion and accurate calculation of Poisson's effects at the interface section using offset strains, 3) considering reinforced concrete as a composite material enabling the use of truss elements (representing discrete reinforcement) in addition to the membrane elements (representing plain concrete) at the interface section.

The performance of the F2M element was verified through mixed-type modelling of a series of twelve shear-critical beam specimens which exhibited different types of failure modes. Two types of mixed-type models with different substructuring configurations were used for each beam. The mixed-type analysis results were compared against the experimentally observed behaviour, stand-alone frame-type analysis, stand-alone detailed FE-type analysis, and two other commonly used mixed-type methods. The following conclusions can be drawn from the verification study:

- Overall, the mixed-type analysis based on the F2M element provided reliable and consistently accurate calculations of initial stiffness, peak load, and ductility of the beams. For all beams considered, using a proper substructuring configuration, the mixed-type analysis results were sufficiently close to the stand-alone analysis results and consequently the experimentally reported values. The total analytical to experimental strength and ductility ratios of the 24 mixed-type analyses (i.e., two analyses per beam) were 1.06 with a coefficient of variation of 8.2% and 0.90 with a coefficient of variation of 24.1 %, respectively.

- The mixed-type analysis results demonstrated that modelling a critical region of the structure which contributes to the final failure in the frame sub-model instead of the detailed FE sub-model can significantly influence the response of the entire structural system. This was seen in the Mixed-Type 1 configuration of the C1 and B3 beams where crushing of the concrete in the top layers of the beam elements in the frame sub-model governed the failure and resulted in an underestimation of the ductility of the beams. In other cases, the effects of using an improper substructuring configuration on the analysis results can be much more substantial. For example, with the Mixed-Type 2 configuration of the A1 and A2 beams, the frame sub-models were unable to capture a horizontal sliding crack along the longitudinal reinforcement near the support, resulting in significant overestimations of the peak loads and ductilities of the beams. Also, the crack patterns and failure modes of the structures were influenced. Therefore, caution must be taken in using a mixed-type simulation method. Creating a proper mixed-type model requires having a good understanding of the expected behaviour of the structure and an anticipation of the location of critical regions prior to the analysis. For a single member structure, this can be difficult; for a multi-member structure, the location of potentially critical member(s) is typically more intuitive.

- The F2M element was able to capture the shear failure at the interface section and accurately compute the reduction in stress levels of the cracked concrete elements and, consequently, the increase in the stress values of uncracked elements. This resulted in axial and shear stress distributions which correlated reasonably well with the stand-alone detailed FE analysis results. Contrary to the F2M element, the Rigid Links method and the McCune et al. (2000) method had major limitations in capturing both the global and local behaviour of cracked reinforced concrete members.

CHAPTER 4

APPLICATION OF MULTI-PLATFORM ANALYSIS TO RC STRUCTURAL SYSTEMS REPAIRED WITH FRP SHEETS

4.1 Introduction

As reinforced concrete (RC) infrastructure around the world ages, many structures are reaching their design lifespan and are becoming in dire need of repair. In addition, environmental effects such as corrosion of steel, variation in temperature, and exposure to chemical substances can adversely affect the durability and safety of structures, resulting in severe damage and premature failures. For example in the US in 2014, almost 146,000 bridges, or 25% of the total, were rated as structurally deficient or functionally obsolete. In 10 years, one in four bridges will be 65 years or older while the average design lifespan is 50 years. Approximately two-thirds of these bridges are constructed with RC or prestressed concrete (FHWA, 2014). The infrastructure of most other developed countries is experiencing the same problems. This highlights the importance of proper maintenance and repair of RC structures.

Use of fibre-reinforced polymer (FRP) in the strengthening of deficient RC members is becoming increasingly common; however, the nonlinear analysis of structures containing such members poses several challenges. At the component-level, analyzing damage effects, confinement enhancement, buckling of longitudinal bars, bond-slip effects at the interface of concrete and FRP sheets, and other second-order material mechanisms requires finely detailed finite element (FE) models. At the system-level, force redistribution due to stiffness changes between different components can affect the response of the repaired member, especially when the structure experienced damage prior to retrofitting. According to the literature, almost all of the existing studies are only conducted at the component-level due to the computational time and memory storage limitations associated with detailed FE tools.

In this chapter, the application of the proposed multi-platform modelling approach to RC structural systems strengthened with FRP sheets is investigated by modelling and analyzing several test specimens including an RC frame with shear-critical beams and a series of RC columns. The influence of damage effects, FRP-related mechanisms, and buckling of longitudinal bars are investigated in detail. The procedure is found to simulate the experimental behaviour of the specimens examined with a high level of accuracy at both the component-level and global-level. In addition, as a demonstration example, the influence of repairing RC members and force redistribution on the system-level response of the structure is investigated through multi-platform modelling of a bridge structure.

4.2 Literature Review

In recent years, several repair strategies have been developed for damaged RC structures. Among them, FRP composites have proven to be an effective, convenient, and practical method of improving the performance of deficient structures, borne out in many experimental programs (Saadatmanesh and Ehsani, 1991; Lombard et al., 2000) and real-world structures (Sheikh and Homam, 2004). The advantages of FRP composites compared to other repair methods such as infill walls, steel jacketing, and concrete caging include high strength-to-weight ratio, high corrosion resistance, improved fire resistance (if proper insulation is provided), versatile design, and easy installation. Figure 4.1 demonstrates some applications of the FRP repair method to existing structures. In this section, an overview of existing studies on analysis of reinforced concrete structures repaired with FRP sheets is presented.

(a) Columns of a pre-heater unit repaired with glass FRP layers

(b) Transfer beam of a high-rise building repaired with carbon FRP layers

(c) Columns of a highway bridge repaired with glass FRP

Figure 4.1 RC structures repaired with FRP sheets (taken from Shaikh and Homam, 2004)

Modelling Shear Behaviour

Although a significant amount of research has been carried out on analyzing the behaviour of RC structures repaired with FRP composites, most have focused on the flexural response of the structure. However, the brittle nature of a shear failure which happens with little or no forewarning requires proper consideration, particularly when FRP sheets are used for shear strengthening. Al-Mahaidi et al. (2001) performed two-dimensional FE analysis to investigate the behaviour of shear deficient T-beams strengthened with web-bonded carbon FRP (CFRP) strips. The analysis assumed perfect bond between concrete and CFRP strips. The numerical response underestimated the peak load compared to the experimental results. Godat et al. (2007) developed a three-dimensional FE model using ADINA (Bathe et al., 1974) to simulate the behaviour of FRP shear-strengthened RC beams (see Figure 4.2). The model considered bond-slip effects between concrete and FRP using nonlinear link elements. The analysis showed good agreement with the experimental results. Sayed et al. (2013) conducted a parametric study using a three-dimensional FE model in ANSYS (Kohnke, 1994) to identify the variables influencing the shear capacity of RC beams strengthened with FRP sheets. The interface between FRP and concrete sheets was modelled using contact elements. The computed peak load values agreed well with the experimental results. However, the load-deflection responses were not reported.

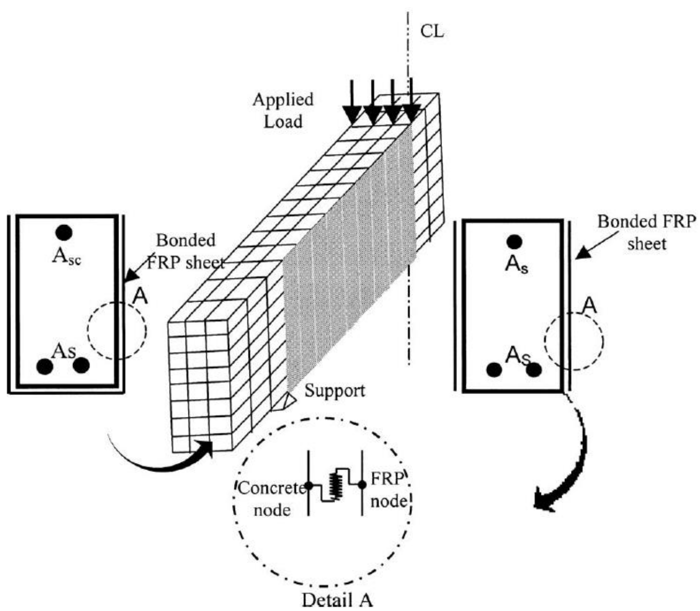

Figure 4.2 FE model of an RC beam with FRP sheets (taken from Godat et al., 2007)

The aforementioned shear models were developed for monotonic loading conditions. To investigate the response of structures under seismic loads, more comprehensive models with cyclic loading capabilities are needed. Li et al. (2005) attempted to capture the cyclic behaviour of shear walls strengthened with FRP sheets using ABAQUS (2012). Spring elements were used to simulate the constraint on deformation provided by FRP sheets. Although the analysis was able to capture the failure mode and shape of the hysteresis response reasonably well, it significantly underestimated the peak load.

Modelling Bond-Slip Behaviour

Several different bond constitutive relationships have been proposed to model the interface of concrete and FRP sheets. As shown in Figure 4.3, the bond models can be categorized into three types: elastic models with cut-off (e.g., Neubauer and Rostasy, 1999), elastic-plastic models (e.g., De Lorezis et al., 2001), and elastic models with softening (e.g., Lu et al., 2005; Nakaba et al., 2001; Ko et al., 2014). In each model type, the ascending and descending branches can be linear or nonlinear depending on the model. Apart from the model shape, the bond behaviour is defined mainly with three parameters: maximum bond stress (τ_m), slip corresponding to the maximum bond stress (s_m), and ultimate slip (s_u). Lu et al. (2005) assessed the accuracy of existing bond-slip models using the experimental data of 253 FRP plate pull-out tests. The large majority of the reviewed tests experienced a debonding type of failure which was initiated by cracking of the concrete layer adjacent to the adhesive layer. The reported fracture plane in concrete was generally slightly wider than the width of the FRP plate. Figure 4.4 shows different parts of a pull-out test and the fracture plane. The factors that influenced the bond-slip behaviour were summarized as: 1) concrete strength, 2) bond length (L), 3) FRP axial stiffness, 4) FRP-to-concrete width ratio (b_f/b_c), and 5) adhesive material properties. Comparison of the experimental data with existing models demonstrated that the level of accuracy of linear models is similar to that of nonlinear models. Therefore, because of their simplicity, the linear models are more preferable for implementation in FE programs. The study also concluded that the elastic models with softening branch provide the best correlation with the experimental results.

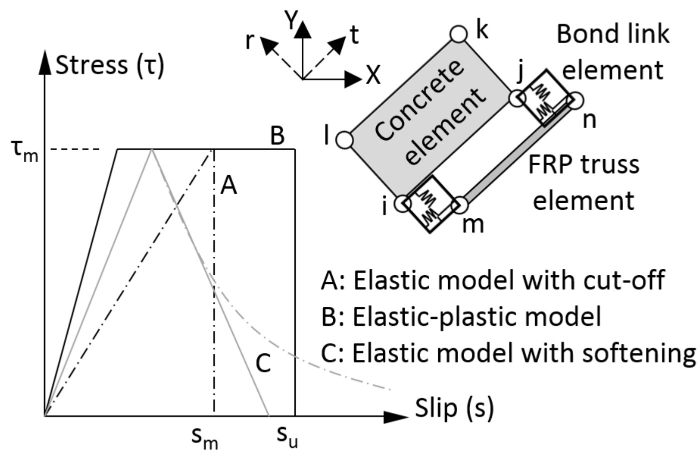

Figure 4.3 FRP link element and different types of stress-strain relationship for bond

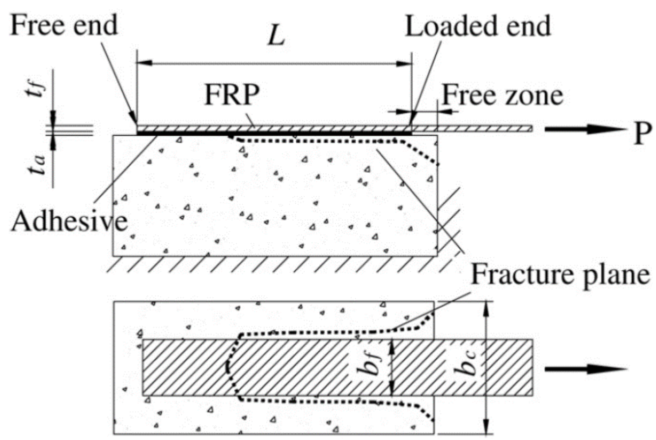

Figure 4.4 Typical fracture plane in FRP plate pull-out test (taken from Lu et al. 2005)

Modelling Confinement Enhancement

In recent years, many studies have shown the effectiveness of FRP composites in improving the ductility and hence the energy dissipation capacity of damaged or seismically deficient RC columns. Based on the experimental studies, different uniaxial stress-strain relationships have been proposed for the confinement enhancement of concrete due to FRP wraps. Figure 4.5 demonstrates stresses induced by FRP confinement effects and stress-strain response of confined concrete in compression. Lam and Teng (2002) provided an extensive review of previous test results on the axial compressive strength of circular FRP-confined concrete specimens and compared them with the available models. The test data were categorized into three groups according to the method used to determined FRP material properties: 1) flat coupon tensile tests (Data Set 1), 2) splitting tests on ring specimens (Data Set 2), and 3) other types of tests (Data Set 3). They found that there was a large scatter in terms of level of effectiveness of FRP confinement which was mainly associated with inaccuracy in the reported FRP material properties. As shown in Figure 4.6 and Table 4.1, parameters such as the unconfined concrete strength, size, and length-to-diameter ratio of the test specimens and fibre type had minor influence on the confinement effectiveness of FRP. The study also concluded that while some complicated models (e.g., Karbhari and Gao, 1997; Saafi et al., 1999) can predict the confinement behaviour with a high level of accuracy, the relationship between the strength of confined concrete and FRP lateral confining pressure can be closely approximated with simple linear equations.

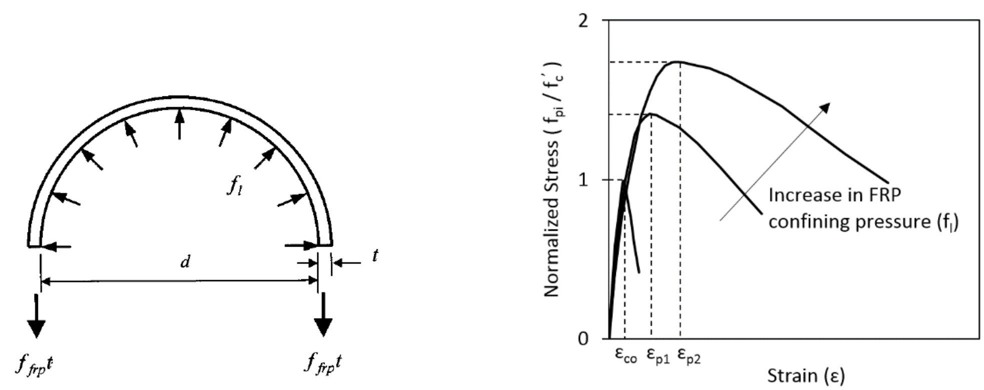

(a) (b)

Figure 4.5 Confinement enhancement of concrete due to FRP wraps: (a) FRP wrap stress diagram; (b) Schematic stress-strain response of concrete in compression

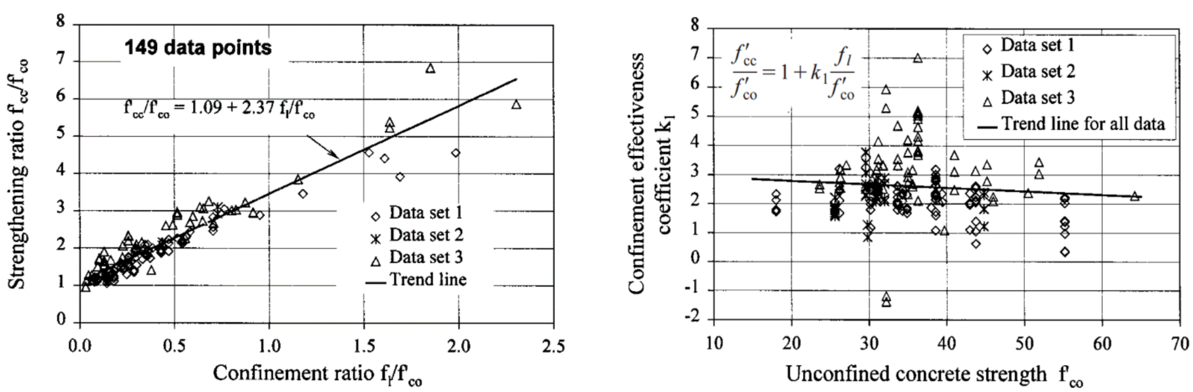

(a) (b)

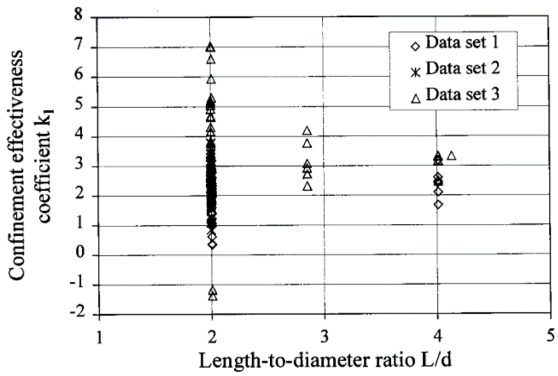

(c)

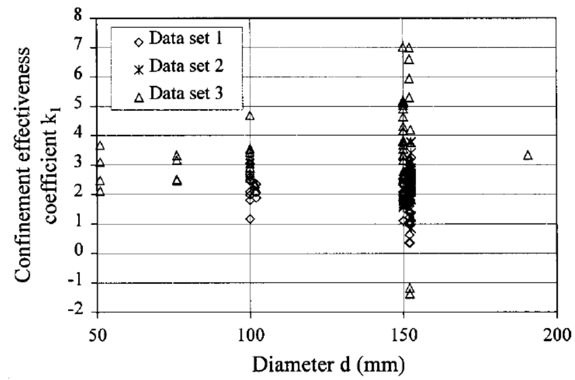

(d)

Figure 4.6 Influence of various parameters on confined-FRP concrete cylinders: (a) FRP confining pressure; (b) unconfined concrete strength; (c) length-to-diameter ratio; (d) diameter (taken from Lam and Teng, 2002)

Table 4.1 Effect of fibre type on confinement effectiveness of FRP (Lam and Teng, 2002)

Data	Fibre Type	Number of Data Points	Confinement Effectiveness Coefficient $k_1 = (f'_{cc} - f'_{co})/f_l$ Average	Standard Deviation
Set 1	Aramid	7	1.8	0.78
	Carbon	64	2.1	0.63
	E Glass	9	2.2	0.29
	Glass*	1	1.8	Not Reported
	Glass and Carbon	2	2.11	Not Reported
Set 2	E Glass	37	2.32	0.58
	S Glass	10	2.28	0.67

* Type of glass fibre was not reported

Although uniaxial compression models have enabled researchers to compute the response of plain concrete confined with FRP at the material-level, they do not fully represent the behaviour of retrofitted RC columns at the structural element-level which is influenced by the interaction between cracked concrete, reinforcing bars, and FRP wraps under combined axial, shear, and bending forces. Some experimental studies have investigated the structural element-level response of repaired RC columns under general loading conditions (e.g., Memon and Sheikh, 2005). However, there is limited research on composite modelling and analysis approaches. Zhu et al. (2006) modelled concrete-filled FRP tube columns in OpenSees software (Mazzoni et al., 2007) using nonlinear layered beam elements (see Figure 4.7). The confinement model of Samaan et al. (1998) was incorporated into a simplified concrete hysteresis model by Taucer et al. (1991) which could not consider cyclic damage of concrete. Teng et al. (2016) used a similar modelling approach while considering cyclic stress deterioration of concrete using the Lam and Teng model (2009). The effect of fixed-end rotations due to strain penetration of longitudinal bars in the foundation was taken into account by adding a rotational spring element at the base of the structure. Both studies had limitations such as assuming plane sections normal to the element axis remain plane during bending and neglecting bond-slip effects between FRP and concrete. Rougier and Luccioni (2007) analyzed circular RC columns confined with CFRP under concentric axial loads. The behaviour of concrete under triaxial compression was captured using a modified plastic damage model. The model was derived based on a calibration process and required a large number of input parameters. In addition, the analysis was performed in a monotonic loading manner and the accuracy of the model in capturing cyclic damage effects was not verified.

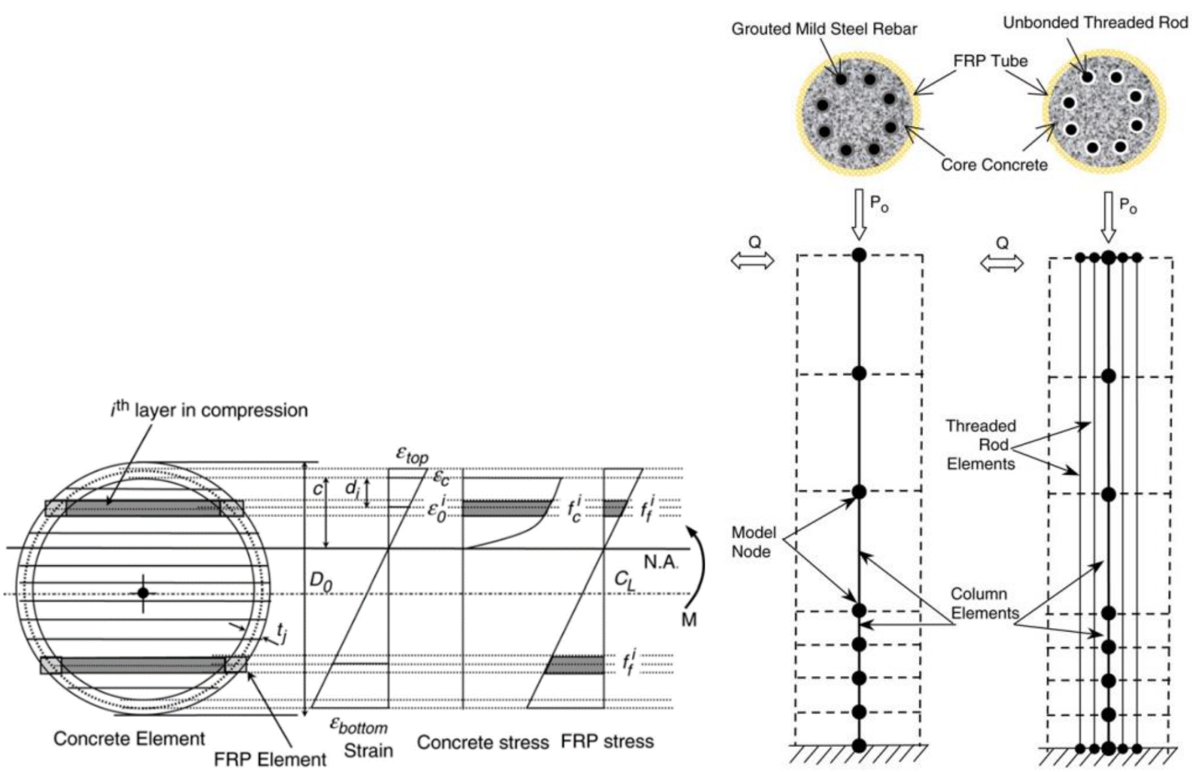

Figure 4.7 Fibre beam model of concrete-filled FRP columns (taken from Zhu et al., 2006)

Furthermore, the majority of numerical studies have considered crushing of concrete and rupture of steel bars or FRP as possible failure modes and have neglected the shear behaviour. Montoya et al. (2004) implemented a confined concrete model into VecTor3 software (ElMohandes and Vecchio, 2013) which was capable of considering shear behaviour in detail. However, the study was limited to monotonic concentric axial loading condition and did not consider slippage of FRP or buckling of steel bars.

Modelling Bar Buckling

Some experimental studies have reported bar buckling as a critical mechanism in the response of retrofitted RC columns (e.g., Memon and Sheikh, 2005). However, most analysis procedures including the abovementioned studies neglected this effect. Karabinis et al. (2008) performed a numerical study on the effectiveness of CFRP confinement in preventing buckling of longitudinal bars in concrete columns subjected to concentric axial loads using the ABAQUS software. A modified Drucker-Prager type model was used to represent the triaxial compression behaviour of concrete and define the failure criterion. The model required estimation of a friction value and a plastic dilatation parameter for concrete. Although the analysis procedure was able to accurately capture the monotonic response of heavily confined RC columns (e.g., four layers of FRP), it significantly underestimated the ductility of columns with lower levels of confinement (e.g., one layer of FRP) due to premature buckling failure of the steel bars. The buckling behaviour of steel bars was taken into account according to the Yalcin and Saatcioglou model (2000). In this model, the stress-strain response of steel in compression was formulated as a function of the reinforcing bar aspect ratio (L/D) using existing experimental data. The aspect ratio was defined as the ratio of unsupported bar length between two ties (L) to its diameter (D). The authors concluded that when the aspect ratio was greater than 8, reinforcing bars became unstable after reaching the yielding point. This was followed by a linear reduction in stress as strain increased. When the aspect ratio was less than 8, reinforcing bar specimens started to exhibit strain hardening behaviour. When the aspect ratio was less than 3.5, a completely developed strain hardening behaviour was observed and the stress-strain relationship in compression became identical to that in tension. Figure 4.8 shows the stress-strain response of steel in compression for reinforcing bars with different aspect ratios.

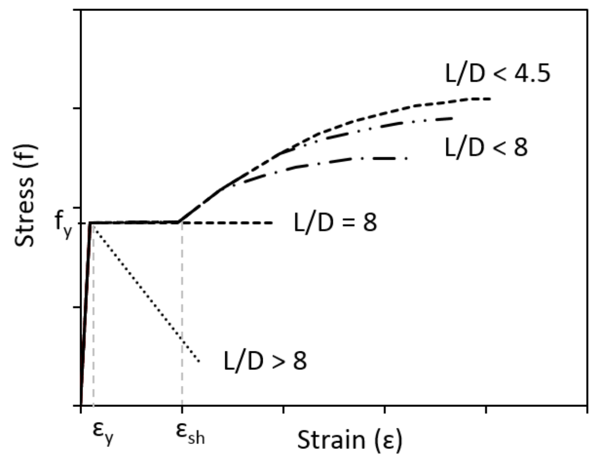

Figure 4.8 Schematic compressive stress-strain response of steel (Yalcin and Saatcioglou, 2000)

Modelling System-Level Behaviour

Most importantly, almost all previous studies have been performed at the component-level. There are a few studies which attempted to model the entire structural system while considering the RC components confined with FRP. However, they neglected shear behaviour and over-simplified the FRP-related mechanisms (e.g., Eslami and Ronagh, 2013), required the user to input force-displacement relationships for each member (e.g., Galal and El-Sokkary, 2008), or introduced a calibrated stiffness degradation factor to capture damage accumulation (e.g., Garcia et al., 2010). Such procedures raise questions about the applicability of the method to other structural systems. A brief description of some of these studies is presented in the following.

Eslami and Ronagh (2013) conducted a numerical study on an eight-storey RC building strengthened with glass FRP (GFRP) using SAP2000 (CSI, 2015). The analysis considered nonlinear behaviour using flexural plastic hinges and neglected shear-related effects. Galal and El-Sokkary (2008) conducted a similar study in which each member was modelled as a linear elastic element with inelastic flexure-shear rotation springs located at the ends. With this approach, the force-displacement relationship for each member has to be input manually which requires expert users and significant amounts of time and effort. Garcia et al. (2010) performed a two-dimensional FE analysis to evaluate the seismic behaviour of a two-storey RC building strengthened with CFRP. The beams and columns were modelled with nonlinear layered frame elements. Although the model considered confinement enhancements due to FRP sheets, it neglected any possible debonding effects. In addition, to capture the damage accumulation, a calibrated stiffness degradation factor was introduced to the model which raises questions about the general performance of the method.

Conclusions

In summary, the available numerical procedures have been shown to be capable of capturing the response of RC structures strengthened with FRP under monotonic concentric axial loads or bending forces. However, they have limitations in modelling and analyzing in respect to one or more of the following four areas: 1) general loading condition: combined axial, shear, and bending forces in a cyclic or reversed cyclic manner; 2) FRP-related mechanisms: slippage between FRP and concrete and tension stiffening effects; 3) RC-related mechanisms: damage effects prior to repair and buckling of reinforcing bars; 4) influence of component-level behaviour on the system-level response and vice versa.

In this chapter, first a brief overview of the various modules used for multi-platform analysis of repaired RC structures is presented. Then, the mechanisms influencing the component-level behaviour of FRP-confined RC members are described in detail in two separate sections: RC-related mechanisms and FRP-related mechanisms. Appropriate constitutive relationships are adopted to accurately model each material component and address the above-mentioned deficiencies in terms of their interactions. The capabilities of the proposed analysis procedure under general static loading conditions are investigated by modelling specimens from two different experimental studies reported in the literature: 1) a shear-critical frame specimen repaired with FRP wraps, and 2) a series of RC columns retrofitted (i.e., initially undamaged) or repaired (i.e., initially damaged) with FRP. Also as a demonstration example, a bridge structure is analyzed using a multi-platform approach to indicate the interaction between the sub-models and force redistribution effects. Lastly, strengths and limitations of the simulation method are summarized and recommendations for future studies are presented.

4.3 Analysis Framework

The proposed multi-platform analysis procedure consists of three main components: an integration module, substructure modules, and an interface module. A brief description of each part is provided in this section. Detailed explanations of the integration module and substructure modules are presented in Chapter 2 and a comprehensive discussion on the interface module is provided in Chapter 3.

4.3.1 Integration Module

Typically, modelling an entire structural system including the FRP repaired components in a detailed FE program is not practical due to the complicated analysis procedure and high computational demand. On the other hand, system-level analysis tools are not able to capture the detailed behaviour of RC members confined with FRP. The proposed integration module, Cyrus, enables combining different analysis tools while fully taking into account the interaction between the substructures. The repaired members along with other potentially critical components of the structure are modelled in detailed FE programs while the rest of the structure is modelled in a computationally fast frame-type analysis program using layered beam elements. The coupled formulation of the analysis allows the consideration of force redistribution due to stiffness changes between different components. Moreover, the integration module enables the use of the parallel processing technique to reduce computational time and memory storage limitations associated with sequential single-platform analyses. A complete discussion on the integration module is provided in Chapter 2.

4.3.2 Substructure Modules

In this study, FRP-confined RC members were modelled and analyzed using the VecTor2 program, a two-dimensional nonlinear FE software for reinforced concrete structures. The program uses a smeared, rotating crack formulation according to the Modified Compression Field Theory (MCFT) (Vecchio and Collins, 1986) and the Disturbed Stress Field Model (DSFM) (Vecchio, 2000). The MCFT and DSFM have been shown to be capable of accurately representing the behaviour of cracked reinforced concrete members particularly under shear (e.g., Collins et al., 1997; Vecchio, 2002). For analysis of RC members repaired with FRP wraps, appropriate models were used to take into account concrete confinement enhancement, tension stiffening effects, bond-slip effects at the interface, and buckling of reinforcing bars (for axially loaded members). In addition, damage effects and spalling of concrete cover prior to repair of structural members were considered. The modelling procedure for aforementioned mechanical effects is presented in the subsequent sections.

While the critical components were modelled in a detailed FE program, the rest of the structure was modelled in a frame analysis program using lower-dimensional elements. The integration framework is compatible with two different analysis programs which provide computational and memory efficient frame-type elements: VecTor5 (Guner and Vecchio, 2010a) and OpenSees (Mazzoni et al., 2007). OpenSees provides two types of beam elements, suitable for analysis of flexure-critical frame structures: 1) linear elastic beam elements with nonlinear rotational springs at each end, and 2) nonlinear layered beam elements. VecTor5 is a nonlinear frame analysis program based on a combination of the tangent and secant solution schemes which can consider shear-related effects. In this chapter, VecTor5 was chosen for modelling the non-critical members. An example of a VecTor2-OpenSees integration was provided in Chapter 2.

The VecTor programs analysis procedure employs a nonlinear elasticity approach, with the material strengths and post-peak responses dictated by the constitutive models; it does not rely on any plasticity-based failure hypotheses. The analysis continues until the secant moduli, displacements, or forces no longer reach convergence, after a certain number of iterations, as a result of structural capacity having been exceeded. The failure can be ascertained by examining several factors including computed load-deflection response, crack pattern, crack width, and stresses and strains in each component.

4.3.3 Interface Module

As discussed in detail in Chapter 3, one of the main challenges in a multi-platform simulation is the modelling of mixed-dimensional interfaces between the sub-models. In this study, the newly developed interface element, the F2M element, was used for membrane-beam mixed-dimensional connection. The F2M element is a two-noded semi-deformable element that can fully transfer translational and rotational displacements at the interface. The stiffness matrix of the element was formulated such that it has high stiffness values in the transverse and rotational directions and zero stiffness in the axial direction (i.e., direction perpendicular to the interface frame element). To transfer shear between the two sub-models, the F2M element computes the shear stress distribution at the interface of frame sub-model based on an MCFT model, and applies the equivalent forces in the opposite direction on the connecting membrane elements. Compared to the traditional rigid interface method, the F2M interface element does not add any additional stiffness to the system and allows lateral expansion. Compared to other common types of interface methods such as the multi-point-constraints (MPCs) approach and transition elements, the proposed method takes into account the nonlinear behaviour of the structure at the interface and provides a much more accurate shear stress distribution at the connection section.

Figure 4.9 demonstrates schematic application of the proposed multi-platform modelling procedure on an RC bridge structure with repaired and damaged columns.

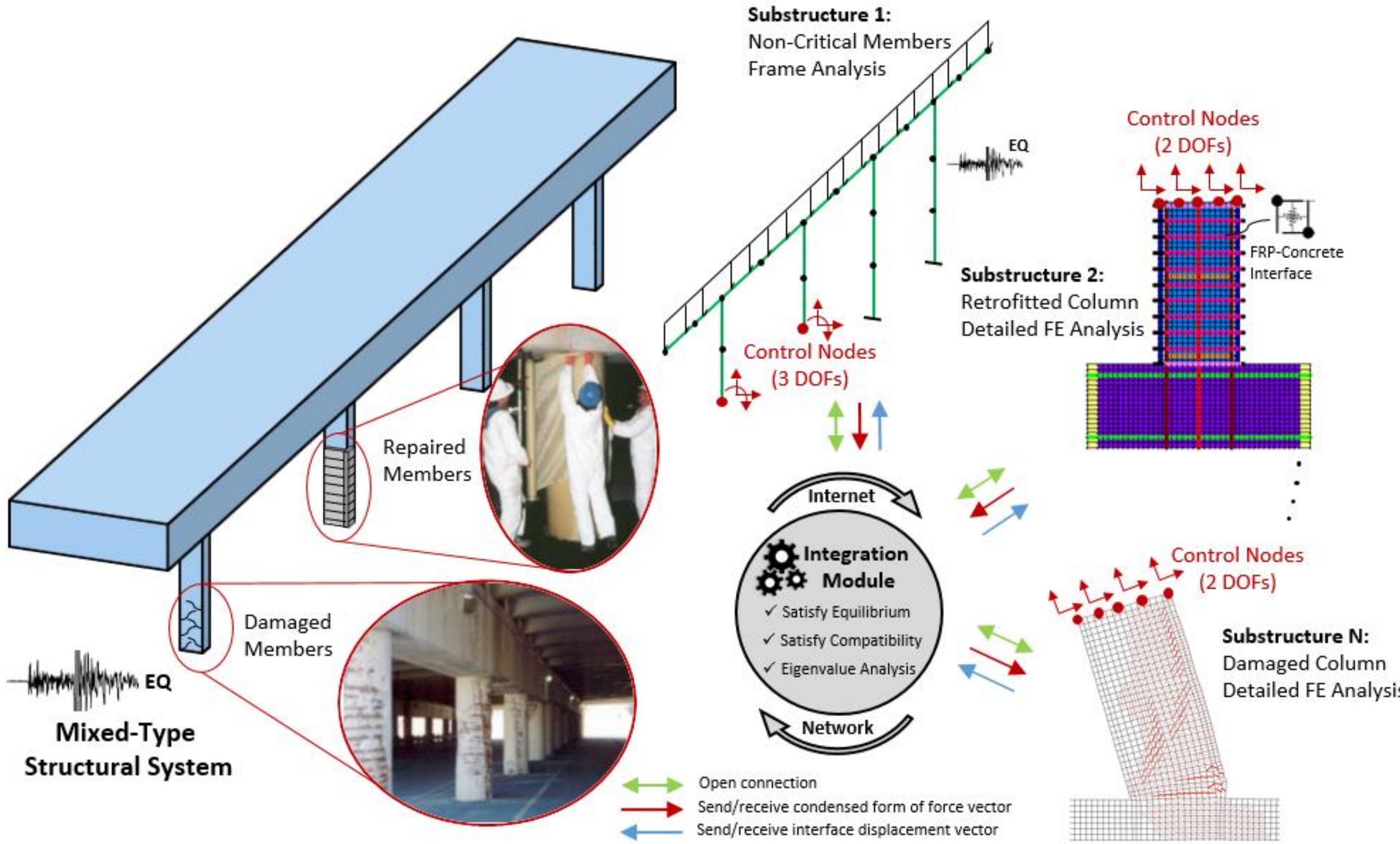

Figure 4.9 Schematic application of the multi-platform analysis on a bridge structure with repaired and damaged columns

4.4 Modelling RC-Related Mechanisms

In this section, material constitutive models for analyzing concrete and reinforcement are briefly described and RC-related mechanisms which have not been fully considered in the previous studies, including reinforcing bar buckling, concrete cover spalling, and damaged effects prior to repair, are presented in detail. For more information on the material constitutive models and second-order material effects, refer to the description of default models in the VecTor2 User's Manual (Wong et al., 2013).

The concrete compression pre-peak response was modelled using the Hognestad parabola. To account for the enhancement of strength and ductility due to confinement, a modified Park-Kent model (Scott et al., 1982) was used for the compression post-peak response of concrete. The hysteretic response of concrete was considered through use of the plastic offsets model proposed by Vecchio (1999). The resulting plastic offset strains, along with the area delineated by the hysteretic loops, are indicative of the internal damage and energy dissipation under cyclic loading. Four-noded rectangular membrane elements and two-noded layered beam elements were used to model concrete in the VecTor2 and VecTor5 programs, respectively.

In the VecTor2 program, two options are available for modelling reinforcing bars: the smeared option and the discrete option. Smeared reinforcement is modelled as a component of the concrete material within elements which can be four-noded rectangular or quadrilateral elements or three-noded triangular elements depending on the geometry of the structure and required mesh. This option is suitable if the reinforcement is uniformly distributed over a large area (e.g., shear reinforcement over a length of the beam). If the reinforcement is concentrated (e.g., longitudinal reinforcement of a beam), then it is best to model the bars discretely using two-noded truss elements. The discrete modelling of reinforcing bars enables the consideration of bond-slip effects between the reinforcement and concrete. Two-noded link elements can be used between truss elements and concrete elements to capture mechanisms related to bar slip. The hysteretic response of the reinforcement was represented using the Seckin model (1981). This model includes a linear elastic region followed by a yield plateau and a strain hardening region. The unloading and reloading response includes the Bauschinger effect (i.e., reduction in yielding strength due to change in the direction of strains under cyclic loading conditions).

4.4.1 Reinforcement Buckling

The buckling of the longitudinal bars was considered using the Akkaya et al. (2013) model. This model is a refined form of the Dhakal and Maekawa model (2002a). The compression stress-strain curve is developed by defining an intermediate point (f_i, ε_i):

$$r_b = \sqrt{\frac{f_y}{100}}\frac{L}{D} \tag{4.1}$$

$$\varepsilon_i = \beta\varepsilon_y(55 - 2.3r_b) \geq 7\varepsilon_y \tag{4.2}$$

$$f_i = \alpha f_y \leq f_{it} \tag{4.3}$$

where r_b is the slenderness ratio, L and D are the buckling length and diameter of the bar, f_y and ε_y are the stress and strain at the yielding point, and f_{it} is the stress in the tension curve (i.e., original curve) corresponding to the intermediate strain (ε_i). α and β constants and f_{it} are computed as follows:

$$f_{it} = \begin{cases} f_y & \text{for} \quad (\varepsilon_i \leq \varepsilon_{sh}) \\ f_u + (f_y - f_u)\left(\dfrac{\varepsilon_u - \varepsilon_i}{\varepsilon_u - \varepsilon_{sh}}\right)^P & \text{for} \quad (\varepsilon_{sh} < \varepsilon_i \leq \varepsilon_u) \end{cases} \tag{4.4}$$

$$P = 1 \quad \text{for} \quad (\varepsilon_{imax} \geq \varepsilon_u \text{ and } \varepsilon_i = 7\varepsilon_y) \quad ; \quad \text{otherwise } P = 4 \tag{4.5}$$

$$\alpha = \begin{cases} 0.75(1.1 - 0.016r_b)\left(0.8 + 1.8\dfrac{f_u}{f_y}\dfrac{D}{L}\right) & \text{for} \quad (\varepsilon_i \leq \varepsilon_{sh}) \\ (1.1 - 0.016r_b)\left(0.8 + 1.8\dfrac{f_u}{f_y}\dfrac{D}{L}\right) & \text{for} \quad (\varepsilon_{sh} < \varepsilon_i \leq \varepsilon_u) \\ 0.75\dfrac{f_{it}}{f_y}(1.1 - 0.016r_b) & \text{for} \quad (\varepsilon_{imax} \geq \varepsilon_u \text{ and } \varepsilon_i = 7\varepsilon_y) \end{cases} \tag{4.6}$$

$$\beta = \frac{\varepsilon_u}{\varepsilon_{imax}} \quad \text{for} \quad (\varepsilon_i < \varepsilon_u \text{ and } \varepsilon_{imax} > \varepsilon_u) \quad ; \quad \text{otherwise} \quad \beta = 1.0 \tag{4.7}$$

where ε_{sh} is the strain hardening strain, f_u and ε_u are the stress and strain at the ultimate point, and ε_{imax} is the maximum intermediate strain defined as:

$$\varepsilon_{imax} = \varepsilon_y \left(55 - 2.3 \sqrt{\frac{f_y}{100}} \times 5 \right) \tag{4.8}$$

The stress in the tension curve corresponding to the current strain ε_{sc} can be computed as:

$$f_{st} = \begin{cases} f_y & \text{for} \quad (\varepsilon_{sc} \le \varepsilon_{sh}) \\ f_u + (f_y - f_u)\left(\frac{\varepsilon_u - \varepsilon_{sc}}{\varepsilon_u - \varepsilon_{sh}}\right)^P & \text{for} \quad (\varepsilon_{sh} < \varepsilon_{sc} \le \varepsilon_u) \end{cases} \tag{4.9}$$

Knowing the intermediate point and the f_{it} and f_{st} stresses, the compressive stress-strain relationship (f_{sc}, ε_{sc}) can be computed from the following relationships:

$$f_{sc} = \begin{cases} E_s \varepsilon_{sc} & \text{for} \quad (\varepsilon_{sc} \le \varepsilon_y) \\ f_{st}\left[1 - \left(1 - \frac{f_i}{f_{it}}\right)\left(\frac{\varepsilon_{sc} - \varepsilon_y}{\varepsilon_i - \varepsilon_y}\right)\right] & \text{for} \quad (\varepsilon_y < \varepsilon_{sc} \le \varepsilon_i) \\ \max\left[f_i - 0.02E_s(\varepsilon_{sc} - \varepsilon_i), 0.2\, f_y\right] & \text{for} \quad (\varepsilon_i < \varepsilon_{sc} \le \varepsilon_{ii}) \\ \max\left[0.75f_i - 0.01E_s(\varepsilon_{sc} - \varepsilon_{ii}), 0.2\, f_y\right] & \text{for} \quad (\varepsilon_{ii} < \varepsilon_{sc} \le \varepsilon_u) \end{cases} \tag{4.10}$$

The graphical demonstration of the model is provided in Figure 4.10.

The accuracy of the reinforcement buckling models mainly relies on determining the correct unsupported length ratio (L/D). In this study, the buckling length is defined according to the Dhakal and Makeawa model (2002b):

$$L = n.s \tag{4.11}$$

where s is the tie spacing and n is the number of spaces between the ties over the buckling length which can be selected from Table 4.2.

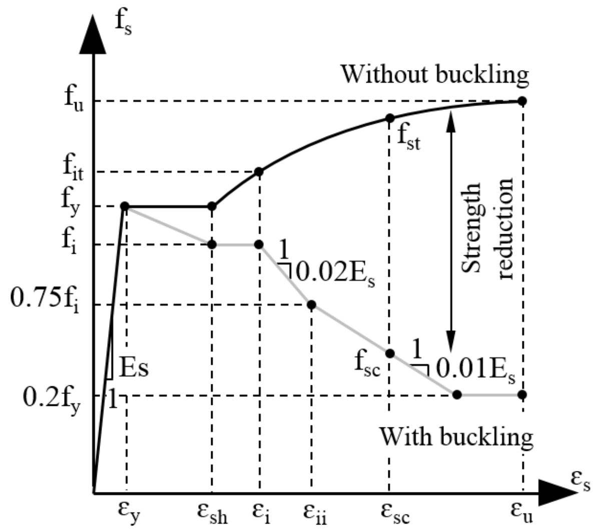

Figure 4.10 Graphical demonstration of reinforcement buckling model (Akkaya et al., 2013)

Table 4.2 Determining variable “n” in Dhakal and Maekawa model (2002b)

L = n.s										
	k_{eq}	> 0.75	0.750-0.500	0.500-0.165	0.165-0.098	0.098-0.045	0.045-0.008	0.008-0.006	0.006-0.004	0.004-0.003
	n	1	1 or 2	2	3	4	5	6	7	8

To use Table 4.2 and determine n, an equivalent stiffness (k_{eq}), which is a function of the normalized stiffness of the rebar (k) and the tie stiffness (k_t), must be calculated:

$$k = \frac{\pi^4 E_r I}{s^3} \quad ; \quad k_t = \frac{E_t A_t}{l_e} \frac{n_l}{n_b} \quad ; \quad k_{eq} = \frac{k_t}{k} \tag{4.12}$$

where E_t is the modulus of elasticity of the tie, l_e is the length of the tie leg, n_b is the number of longitudinal bars supported by the tie legs, n_l is the number of tie legs parallel to the lateral load, and E_tI is the reduced flexural rigidity of the rebar defined as follows:

$$I = \frac{\pi D^4}{64} \quad ; \quad E_r I = \frac{E_s I}{2\sqrt{\frac{f_y\,[\mathrm{MPa}]}{400}}} \tag{4.13}$$

where I, D, E_s, and f_y are the moment of inertia, diameter, modulus of elasticity, and yield strength of the reinforcing bar, respectively.

4.4.2 Concrete Cover Spalling

RC columns under cyclic loads can experience a softening behaviour before reaching the ultimate stress value defined in their constitutive relationships. This behaviour initiates due to spalling of the concrete cover and extends as buckling of the longitudinal reinforcement occurs. A cover spalling criterion was used in which if the inclination between crack and the longitudinal reinforcement (α) was less than 30 degrees, the principal net compressive strain (ε_{c2}) and crack width (w_{cr}) were limited to -3.5×10^{-3} mm/mm and 2.0 mm, respectively. α can be computed from angle between the reinforcing bar and the horizontal axis (Θ_R) and the angle between the crack direction and the horizontal axis (Θ_{cr}) using Eq. 4.14. w_{cr}, Θ_{cr}, and ε_{c2} are computed according to the DSFM procedure.

$$\alpha = \cos^{-1}\{|\cos\Theta_R \cos\Theta_{cr} + \sin\Theta_R \sin\Theta_{cr}|\} < 30 \text{ degrees} \tag{4.14}$$

According to this criterion, if an element located in the concrete cover zone reaches one of the aforementioned limits, the element will be deactivated, meaning that its strength and stiffness will be set to near-zero values. For a concrete element to be considered as the cover element the following four requirements must be satisfied: 1) the element does not include any in-plane smeared reinforcement component, 2) the element must be located between a truss element representing the longitudinal reinforcement and a free surface, 3) the distance between the truss element and the free surface should be less than 7.5 times the longitudinal bar diameter, and 4) the angle between the truss element and the free surface should be less than 45 degrees. Figure 4.11 is a schematic demonstration of spalling of a concrete cover element in an RC column. In addition to providing more realistic analysis results, considering the cover spalling mechanism significantly improves the stability of the unloading and reloading portions of the load-deflection response, particularly under high deformations.

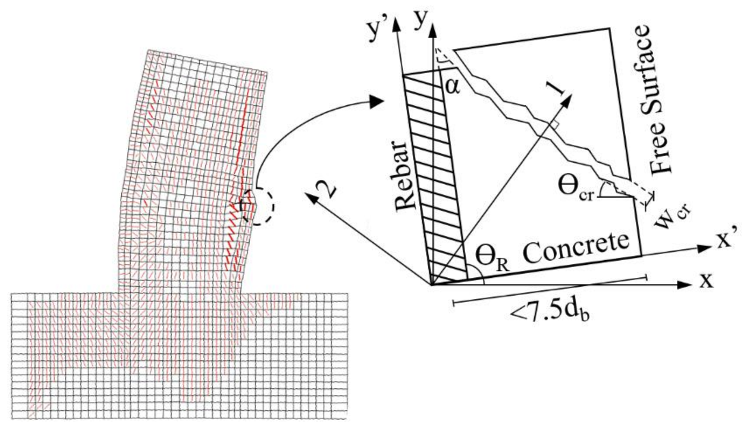

Figure 4.11 Schematic concrete cover spalling in an RC column

4.4.3 Damage Effects Prior to Repair

To simulate damage effects prior to the repair of an RC structure, an analysis was performed in two separate stages. In the first stage, which represented the structure prior to the repair, the elements and materials related to the FRP wraps were deactivated in the model. Similar to the experimental procedure, the analysis was performed until the concrete cover started to spall off. In the second stage, which represented the structure after repair, the FRP elements and materials were activated in the model. Using a binary file which stores the strain and stress history of the structure, the damage effects prior to repair were taken into account and the analysis was resumed and continued until failure.

In the VecTor programs analysis procedure, total concrete and reinforcement strains were formulated to take into account plastic offset strains caused by concrete damage and yielding of reinforcement under cyclic loads. To track the plastic offset strains and compute maximum and minimum strains obtained during previous cycles, a set of transformation equations based on the Mohr's circle approach were used. This enabled the analysis to define the strain values in any arbitrary direction (local x and y, or principal 1 and 2) and be consistent with rotating crack formulations, meaning the principal strain directions were free to rotate.

4.5 Modelling FRP-Related Mechanisms

In the detailed FE sub-model, two-noded truss elements were used to model FRP sheets. Each node of the truss element has two translational degrees of freedom (DOFs). A uniform cross-sectional area computed from the thickness and tributary width of the FRP sheets is assigned to the truss elements. The stress-strain response is assumed linear-elastic up to the rupture of FRP in tension, and with zero stress in compression. In the following subsequent sections, the FRP-related mechanisms which are considered in the detailed sub-model (VecTor2 sub-model) of the multi-platform analysis are presented.

4.5.1 Bond-Slip Effects

To accurately model bond-slip effects, link elements were used at the interface between RC rectangular elements and FRP truss elements. The link element is a two-noded non-dimensional element with a total of four translational DOFs. The element consists of two orthogonal springs connecting RC elements and FRP truss bars. One spring deforms tangentially to the FRP truss element, representing bond-slip behaviour. The other spring deforms radially to the truss element, representing radial displacements and stresses. Figure 4.12 demonstrates the configurations of the springs for a link element at the interface of FRP and concrete elements in the local t and r axes. The nodal displacements of the element in the global X and Y coordinate system, [D], are transformed to deformations in the local directions of the FRP truss, [d], using a transformation matrix, [T]. The force in the tangential spring (f_t) is found by multiplying the bond slip (d_t) by the corresponding stiffness (k_t), and the bonded tributary area (A). The radial force (f_r) can be computed using a similar procedure. The tangential stiffness is determined from the bond-slip curve. The radial stiffness is given a very large value to prevent any displacement in the radial direction (i.e., delamination mechanism is not being modelled). Using the transformation matrix, the forces in the X and Y directions, [F], can be determined from the forces in the local directions. Based on the above-mentioned procedure, the equilibrium relationship of the link element in the X and Y directions is presented as follows:

$$[\mathrm{F}] = \mathrm{A}[\mathrm{K}][\mathrm{D}] \tag{4.15}$$

$$[\mathrm{K}] = [\mathrm{T}]^{\mathrm{T}} \begin{bmatrix} \mathrm{k_t} & 0 \\ 0 & \mathrm{k_r} \end{bmatrix} [\mathrm{T}] \tag{4.16}$$

$$[\mathrm{T}] = \begin{bmatrix} -\cos\theta & -\sin\theta & \cos\theta & \sin\theta \\ \sin\theta & -\cos\theta & -\sin\theta & \cos\theta \end{bmatrix} \tag{4.17}$$

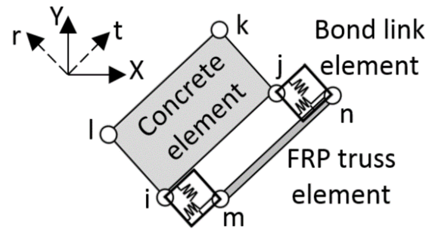

Figure 4.12 Link elements for modelling interface of FRP and concrete elements

In this study, the bond stress-strain relationship was computed using the Nakaba model (2001). This model was derived based on double-face shear-type bond tests. The test variables included various types of fibre and concrete. The test results concluded that fibre stiffness and concrete compressive strength influence the maximum bond strength and the shape of the stress distribution. However, the bond stress-strain behaviour was not influenced by the type of fibre. Sato and Vecchio (2003) conducted a series of bond tests and demonstrated that the Nakaba model can capture the bond-slip behaviour reasonably well for fibre sheets with different lengths. This bilinear bond model, based on concrete fracture energy, is expressed as follows:

$$\tau_{b,Fy} = (54f_c')^{0.19} \tag{4.18}$$

$$S_{Fy} = 0.057{G_F}^{0.5} \tag{4.19}$$

$$G_F = \left(\frac{\tau_{b,Fy}}{6.6}\right)^2 \tag{4.20}$$

$$S_{Fu} = \frac{2G_F}{\tau_{b,Fy}} \tag{4.21}$$

where $\tau_{b,Fy}$, f_c', S_{Fy}, G_F, and S_{Fu} are the maximum bond shear stress, compressive strength of concrete, bond slip at the maximum shear stress, fracture energy of concrete, and ultimate bond slip, respectively. Because of the separation of FRP from the concrete at failure, Wong and Vecchio (2003) recommended that the maximum FRP bond stress be limited to the modulus of rupture of concrete (f_r):

$$\tau_{b,Fy} \le f_r = 0.6 \times (f_c')^{0.5} \tag{4.22}$$

4.5.2 Tension Stiffening Effects

Crack formation is another factor which can influence the behaviour of repaired RC members. FRP sheets can control crack width and reduce crack spacing. Also, premature debonding of the sheets, before attainment of the tensile strength of the FRP, can initiate at crack locations, and thus can be influenced by crack spacing. In this study, the crack formation and tension stiffening effects were considered using the Sato and Vecchio model (2003). The model computes the crack spacing and the contribution of FRP to the tensile strength by formulating the equilibrium at the crack location based on the Tension Chord concept (Kaufmann and Marti, 1998). Figure 4.13 is a graphical demonstration of the contribution of FRP to the tensile strength of concrete.

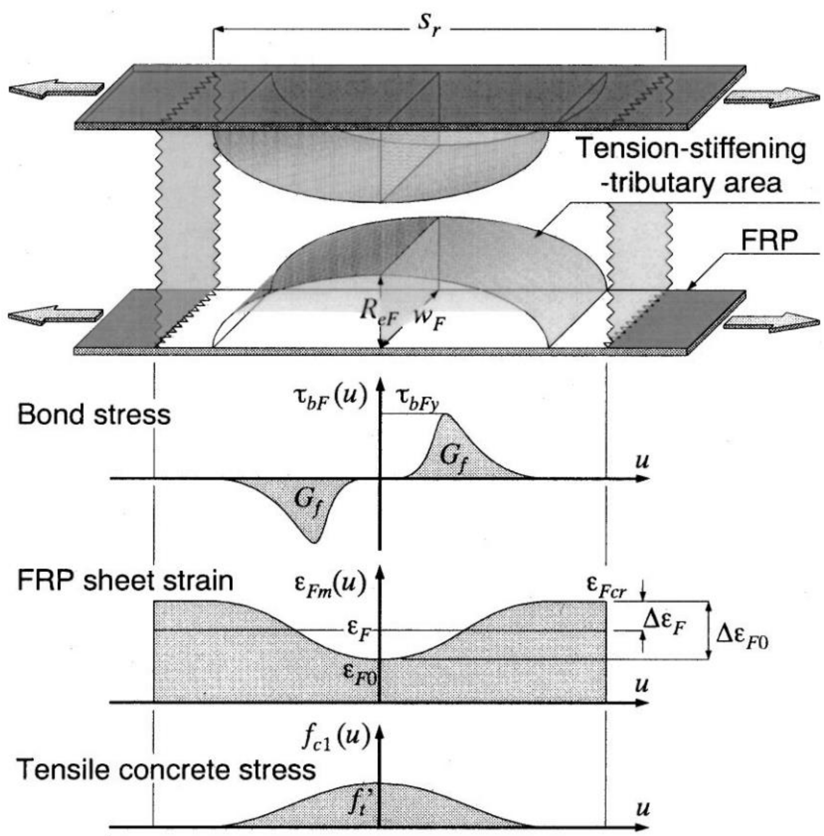

Figure 4.13 Tension stiffening effects of FRP sheets (taken from Sato and Vecchio, 2003)

The average concrete tensile stress contributed by the FRP sheets (f_{c1}) is computed as follow:

$$f_{c1} = \sum_{j=1}^{n} \rho_{F,j} E_{F,j} \Delta\varepsilon_F \cos^2 \Theta_{F,j} \tag{4.23}$$

where subscript "j" indicates a component of FRP sheets. E_F, $\Delta\varepsilon_F$, and Θ_F are stiffness, difference between average strain and local crack strain, and angle between the FRP strip direction and the principal tensile stress direction, respectively. ρ_F is the effective reinforcement ratio for the FRP sheet:

$$\rho_F = \frac{t_f}{R_{ef}} \tag{4.24}$$

where t_f is the thickness of the FRP sheet and R_{ef} is the distance from the FRP sheet over which the tension stiffening is effective:

$$R_{ef} = \frac{1}{f_t'} \sum_{j=1}^{n} \left(15.8 + 1.34\sqrt{t_{fj} E_{fj}}\right) \sqrt{G_{fj}} \tag{4.25}$$

The strain difference ($\Delta\varepsilon_F$) is modelled by the curve formulated as:

$$\frac{\Delta\varepsilon_F}{\Delta\varepsilon_{F\,max}} = \frac{\varepsilon_{Fm}}{\varepsilon_{F1}} \times \frac{\alpha}{(\alpha - 1) + (\frac{\varepsilon_{Fm}}{\varepsilon_{F1}})^{\alpha}} \tag{4.26}$$

where ε_{Fm} is the average tensile strain in the FRP. $\Delta\varepsilon_{Fmax}$, ε_{F1}, and α parameters are calculated based on Eq. 4.27 to Eq. 4.30 which were derived by Vecchio and Sato (2003).

$$\Delta\varepsilon_{F\,max} = \sqrt{G_F}\left\{\frac{1340}{\sqrt{t_F E_F}} - 1.27 - \left[c_2\left(\frac{S_r}{\cos\Theta_F} - 640\right)\right]^4\right\} \times 10^{-3} \tag{4.27}$$

$$\varepsilon_{F1} = \sqrt{G_F}\left[\left(\frac{185000}{t_F E_F} + 25\right)\sqrt{\frac{\cos\Theta_F}{S_r}} - 0.32\right] \times 10^{-3} \tag{4.28}$$

$$\alpha = 2.7 - \left(\frac{S_r}{640\cos\Theta_F}\right)^2 \tag{4.29}$$

$$c_2 = \left[\frac{9.3}{(t_F E_F)^{0.05}} - 3.1\right] \times 10^{-3} \tag{4.30}$$

where t_F and G_F are the thickness and fracture energy of the FRP. G_F is computed based on Eq. 4.20. S_r is the crack spacing parameter which is expressed as:

$$S_r = \frac{\lambda}{\frac{|\sin\Theta|}{S_{rx}} + \frac{|\cos\Theta|}{S_{ry}}} \tag{4.31}$$

where λ is the crack formation parameter equal to 0.75. Θ is the angle between the longitudinal axis (X) and the principal tensile stress direction. S_{rx} and S_{ry} are the crack spacings perpendicular to the X and Y directions, respectively. A detailed description of the crack spacing calculations are described in Sato and Vecchio (2003).

4.5.3 Confinement Effects

The confinement effects of FRP wraps were simulated with a smeared out-of-plane FRP component in the concrete element. The out-of-plane stresses and strains were utilized to compute the strength and ductility enhancements due to confinement. The out-of-plane concrete strain was approximated as:

$$\varepsilon_{cz} = \frac{-E_c}{E_c + \rho_{Fz} E_F}\left(\nu_{12}\frac{f_{c2}}{\bar{\bar{E}}_{c2}} + \nu_{21}\frac{f_{c1}}{\bar{\bar{E}}_{c1}}\right) \tag{4.32}$$

where E_c, $\bar{E}_c$, f_c, ν are the initial stiffness, secant stiffness, stress, and Poisson's ratio of concrete, E_F is the stiffness of the FRP, and ρ_{Fz} is the FRP ratio in the Z direction (i.e., the out-of-plane direction of the FE model) which is equal to the volume of the FRP sheets divided by the volume of concrete. Subscripts 1 and 2 indicate in-plane principal stress directions.

Using equilibrium, the out-of-plane concrete compressive stress (f_{cz}) can be determined as:

$$f_{cz} = -\rho_{Fz} \times f_{Fz} \tag{4.33}$$

where f_{Fz} is the stress in the out-of-plane FRP sheet which is calculated based on Eq. 4.34 and must be less than the ultimate strength of FRP (f_{FU}).

$$f_{Fz} = E_F \varepsilon_{cz} \leq f_{FU} \tag{4.34}$$

4.6 Verification Examples

This section presents two verification studies carried out to assess the performance of the proposed multi-platform modelling approach for RC structures strengthened with CFRP and GFRP wraps. The aforementioned material models and mechanisms were considered in the component-level analysis. For other second-order material effects, the default material models and analysis parameters defined in all VecTor software programs were used. Table 4.3 summarizes the models and analysis options which have been utilized in the analyses reported herein.

Table 4.3 Material models and analysis options utilized in verification studies

Concrete Models		Reinforcement Models	
Compression Pre-Peak	Hognestad	Hysteretic Response	Seckin
Compression Post-Peak	Modified Park-Kent	Dowel Action	Tassios (Crack Slip)
Compression Softening	Vecchio 1992-A	Buckling	Akkaya 2013
Tension Stiffening[*]	Tension Chord 1998		
Tension Softening	Bilinear	**Analysis Options**	
Confined Strength	Kupfer/Richart	Strain History	Considered
Dilation	Variable - Orthotropic	Geometric Nonlinearity	Considered
Cracking Criterion	Mohr-Coulomb (Stress)	Section Analysis[**]	Nonlinear
Crack Stress Calculation	Basic (DSFM/MCFT)	Shear Analysis[**]	Parabolic Shear Strain
Crack Width Check	Max Crack (Agg/2.5)		
Crack Slip Calculation	Walraven		
Hysteretic Response	Nonlinear-Plastic Offsets		
Bond	Nakaba 2001		

[*] Default model is “Modified Bentz 2003” which is only applicable to conventional reinforcing bars.

[**] Analysis options in VecTor5.

4.6.1 Shear-Critical RC Frame

Duong et al. (2007) tested a one-span two-storey RC frame with shear-critical beams under constant axial force and lateral displacement applied in a reversed cyclic manner, as shown in Figure 4.14. This frame will be referred to as the Duong frame hereafter. The experimental study consisted of two test phases. In Phase A, the imposed lateral displacement was increased until significant diagonal shear cracks were observed in the beams. At this load stage, the shear crack width in the first-storey beam was 9 mm and the second-storey beam experienced a shear crack of 2 mm width. Also, both the longitudinal and transverse reinforcement yielded in the beams, resulting in a flexural-shear damage mode. Then the frame was unloaded to zero displacement and reloaded in the reversed direction to the same displacement amplitude reached in the first half-cycle (44 mm). In Phase B, the damaged beams were repaired by replacing unsound concrete, injecting epoxy into the cracks, and shear-strengthening the beams with CFRP strips. After the repair process was completed, the frame was loaded in a reversed cyclic manner with the increasing displacement amplitude equal to the yield displacement (25 mm) measured in Phase A of the experiment.

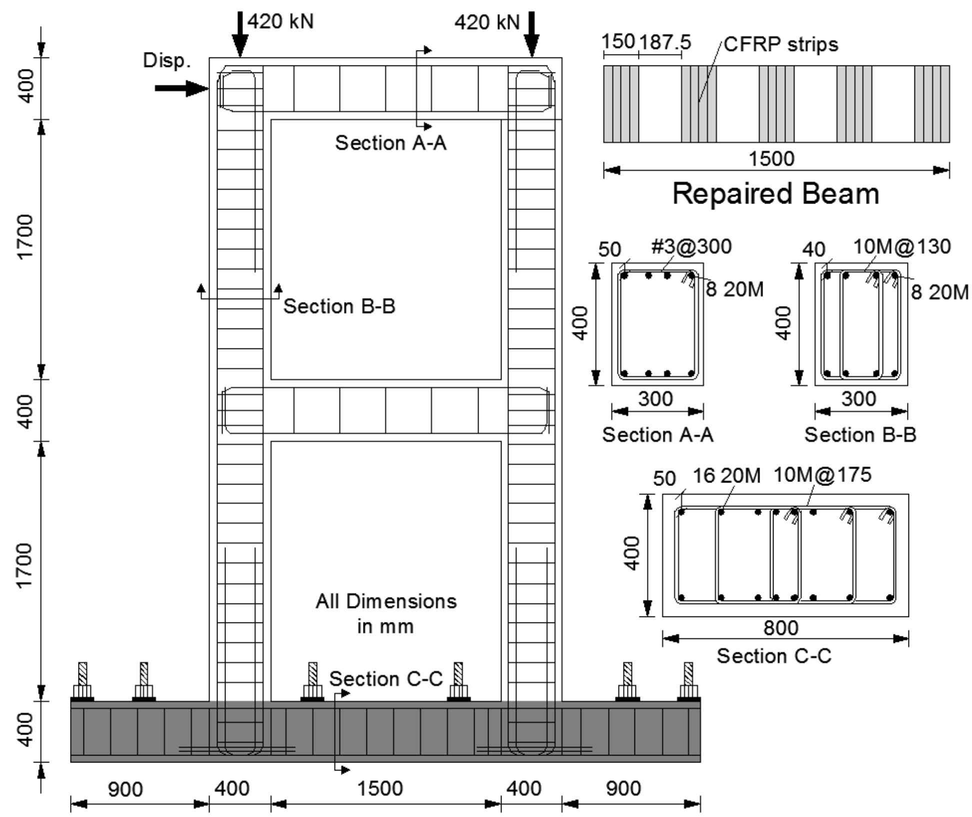

Figure 4.14 Details of Duong frame and repaired FRP beam (dimensions in millimeters)

The material properties of the concrete obtained from compressive cylinder tests and the properties of the reinforcement and the CFRP determined from tensile coupon tests are presented in Table 4.4.

Table 4.4 Material properties of Duong frame

Concrete		
f'c (MPa)	ε_o ($\times 10^{-3}$)	Max Agg. Size (mm)
43	2.31	10

Reinforcement							
Bar Size	Diameter (mm)	Area (mm^2)	f_y (MPa)	f_u (MPa)	E (MPa)	E_{sh} (MPa)	ε_{sh} ($\times 10^{-3}$)
10M	10	100	455	583	192,400	1195	22.8
20M	20	300	447	603	198,400	1372	17.1
US #3	9.5	71	506	615	210,000	1025	28.3

CFRP				
Product Name	f't (MPa)	E (MPa)	ε_u ($\times 10^{-3}$)	Thickness (mm)
Tyfo® SCH41S	876	72,400	12.1	1.0

Kim and Vecchio (2008) performed a stand-alone FE analysis of the frame using VecTor2 software. Due to the detailed meshing requirements, the cyclic analysis after the repair was extremely time consuming and not applicable to larger structures. In addition, although the computed response of the first nine cycles agreed well with the experimentally observed behavior, the analysis significantly underestimated the peak load of the last cycle. In this section, several analyses were conducted to verify the application of multi-platform simulation to repaired RC structures and demonstrate the advantages of this approach compared to stand-alone frame-type programs and stand-alone detailed FE-type programs. Furthermore to improve the analysis at the component-level, the contribution of the FRP to the tensile response of the concrete was considered using the Tension Chord model. Two types of analysis were conducted:

1) Stand-alone analyses of Phase A using a frame-type program, VecTor5, and a detailed FE-type program, VecTor2.
2) Mixed-type analyses of Phase A and Phase B by integrating the VecTor2 and VecTor5 programs.

The following is a description of the model and computed results for each case.

Stand-Alone Analysis of Phase A

In the stand-alone frame analysis, the entire structure was modelled using a total of 76 two-noded nonlinear layered beam elements with VecTor5. The joint panels were modelled with stiffened elements to avoid premature failure and to account for overlapping portions at the end zones. For stiffened elements, the amounts of the longitudinal and transverse reinforcement were increased by a factor of two to avoid artificial damage as suggested by Guner and Vecchio (2010b). The nodes approximately corresponding to the locations of the bolts, used to fix the base beam to the strong floor, were fully restrained in the translational and rotational directions. To model the axial loads, a constant vertical load of 420 kN was applied at the top node of each column. The lateral load was imposed by controlling the lateral displacement of the top node of the left column, in 0.5 mm increments, in a reversed cyclic manner. Also, because the frame specimen was tested nine months after casting of the concrete, it was influenced by drying shrinkage. Therefore, a constant uniform shrinkage strain of -0.0004 was assigned to all layered beam elements. In Section 5.7 of Chapter 5, a similar analysis was performed without considering the shrinkage strain. From a comparison of the results it can be seen that although the shrinkage strain influenced the initial stiffness and peak load to some extent, the load-deflection responses obtained from both analysis cases (with and without shrinkage strain) were sufficiently close to the experimental results.

In the stand-alone detailed FE analysis, the concrete was modelled using four-noded rectangular elements. The heavily reinforced base beam was modelled with a mesh size of 80 mm × 80 mm while the beams and columns were modelled using a finer mesh size of 40 mm × 40 mm. The transverse reinforcement was added as a smeared component to the concrete elements. The longitudinal reinforcement was modelled as discrete using truss elements. A total of 4,131 elements were used to model the entire structure. To model the fixed end condition of the frame (no base slip was reported in the experiment), all the nodes located along the bottom row of the base beam were fully restrained in both the X and Y translational directions. To model the uniform distribution of the applied vertical loads under the loading plates in the experiment and avoid artificial local failure in the analysis, the vertical load of each column was distributed over eight nodes (i.e., 52.5 kN was applied on each node). The lateral load and shrinkage strains were modelled similar to how they were done in the stand-alone frame analysis.

Figure 4.15 demonstrates the stand-alone layered frame model and the stand-alone detailed FE model of the structure.

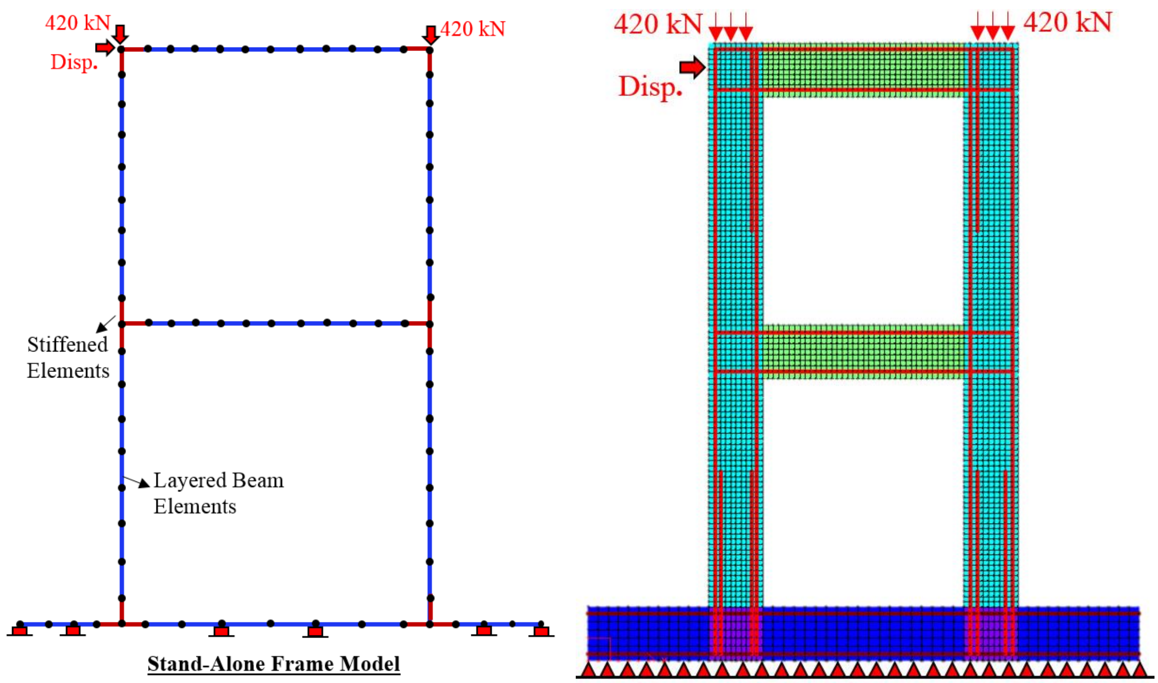

(a) (b)

Figure 4.15 Stand-alone models of frame: (a) frame-type model; (b) detailed FE model

The computed load-deflection responses of the frame analysis and detailed FE analysis are compared against the experimental results of Phase A in Figure 4.16. In the forward half-cycle, the frame analysis overestimated the peak load and failed to accurately capture the behaviour of the shear-critical beams due to highly nonlinear strain and stress distributions within the cracked regions. This resulted in a premature failure of the first storey beam which can be seen as a sudden strength drop in the load-deflection response and a large deformation in the deflected shape of the structure (see Figure 4.18). Unlike the frame analysis, the detailed FE analysis was able to accurately capture the shear behaviour of the beams without resulting in any premature failures. Also, the peak load and effective stiffness were computed with better accuracy. In the reversed half-cycle, due to the failure of the first storey beam, the frame analysis significantly underestimated the stiffness and energy dissipation of the structure. In the detailed FE analysis, however, the computed peak load and effective stiffness of both the loading and unloading portions of the response correlated well with the experimental results. Both analyses underestimated the peak load of the reversed half-cycle and overestimated the pinching effect.

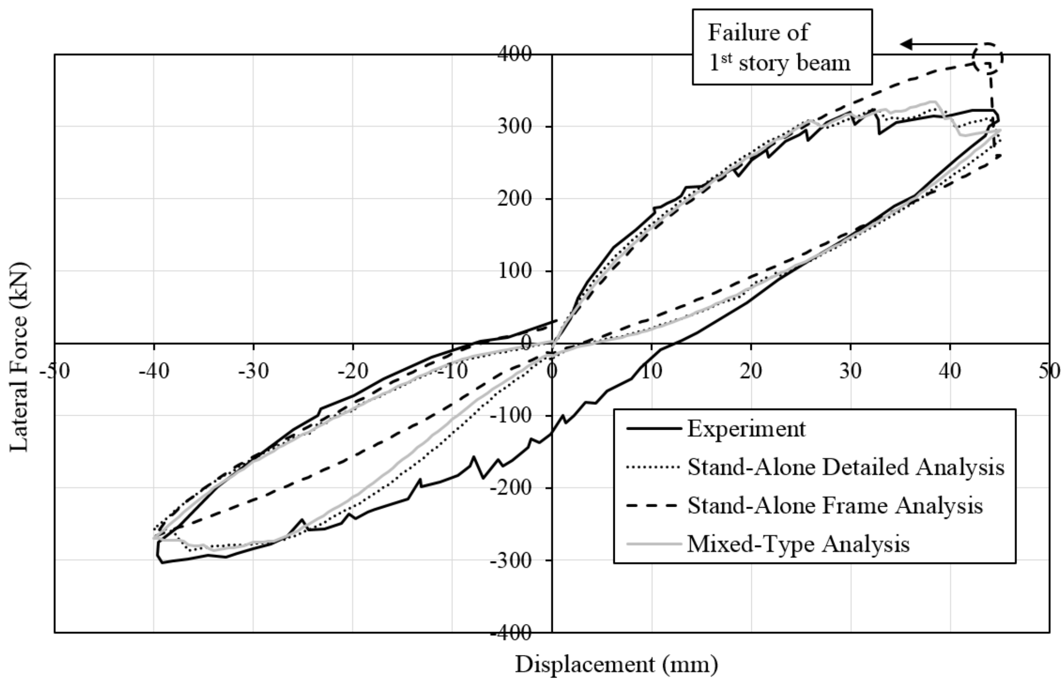

Figure 4.16 Load-deflection response of Duong frame for Phase A

Mixed-Type Analysis of Phase A and Phase B

The stand-alone frame analysis was limited to Phase A of the test, since VecTor5 is unable to consider externally bonded FRP in detail nor is it able to analyze repaired structures. On the other hand, a stand-alone detailed FE analysis of a repaired structure under a high number of loading cycles is extremely time consuming. Therefore, to accurately capture the response of the shear-critical beams in Phase A and provide a detailed analysis of the frame repaired with CFRP wraps in Phase B in a practical manner, a mixed-type analysis was conducted.

As demonstrated in Figure 4.17, the two shear-critical beams were modelled with a detailed FE program, VecTor2, while the rest of the structure was modelled with a frame analysis software, VecTor5. The beams were modelled using rectangular concrete elements with an approximately 40 mm × 40 mm mesh size. The transverse reinforcement was added as a smeared component to the concrete elements. The longitudinal reinforcement was modelled as discrete using truss elements. A total of 984 elements were used to model the two shear-critical beams for analysis of Phase A. Compared to the detailed FE model of the entire frame structure, about 4.2 times less membrane and truss elements were required. The two sub-models were connected using the newly developed F2M interface elements. The multi-platform framework, Cyrus, was used to combine the sub-models and coordinate the mixed-type analysis.

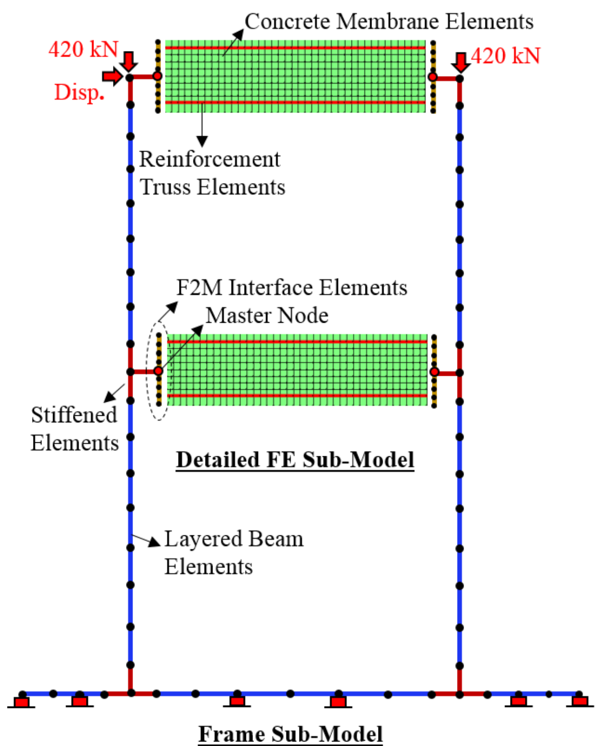

Figure 4.17 Multi-platform model of Duong frame prior to the repair (Phase A)

The mixed-type analysis load-deflection response is compared against the stand-alone analyses and experimental results in Figure 4.16. The mixed-type analysis computed the stiffness, peak load, and energy dissipation with the same level of accuracy as the stand-alone detailed FE analysis and eliminated deficiencies associated with the frame-type analysis in capturing the highly nonlinear response of the shear-critical beams. Both the stand-alone detailed FE analysis and the mixed-type analysis underestimated the peak load of the reversed half-cycle and overestimated the pinching effect.

The maximum stresses in the longitudinal and transverse reinforcement of the mixed-type analysis, the stand-alone analysis, and the experiment are presented in Table 4.5. The maximum stresses and their corresponding applied lateral displacements of the mixed-type analysis were in excellent agreement with the stand-alone analysis results. Also, the results of both analyses correlated well with the stress and deformation values reported from the experiment.

Table 4.5 Maximum stresses in steel and corresponding applied displacements for Phase A

		Transverse Reinforcement			Longitudinal Reinforcement		
	Beam	Max. Stress (MPa)	Disp.* (mm)	Condition	Max. Stress (MPa)	Disp. (mm)	Condition
Mixed-Type Analysis	Top	506	25.5	Yielded	395	37.5	0.88fy
	Bottom	506	17.5	Yielded	392	25.0	0.88fy
Stand-Alone Analysis	Top	506	25.5	Yielded	383	38.5	0.86fy
	Bottom	506	17.5	Yielded	408	25.5	0.91fy
Experiment	Top	506	30.0	Yielded	447	30.0	Yielded
	Bottom	506	30.0	Yielded	447	25.5	Yielded

* Applied lateral displacement corresponding to the beginning of yielding or maximum stress in steel

In regard to the damage mode, similar to the stand-alone detailed FE analysis, the mixed-type analysis predicted large diagonal shear cracks at the ends of the beams that continued to the mid-span at the top and bottom sections. A similar crack pattern was observed in the experiment. Figure 4.18 and 4.19 demonstrate the deformed shape and crack pattern from the different types of analyses and the experiment in the forward half-cycle and reversed half-cycle, respectively.

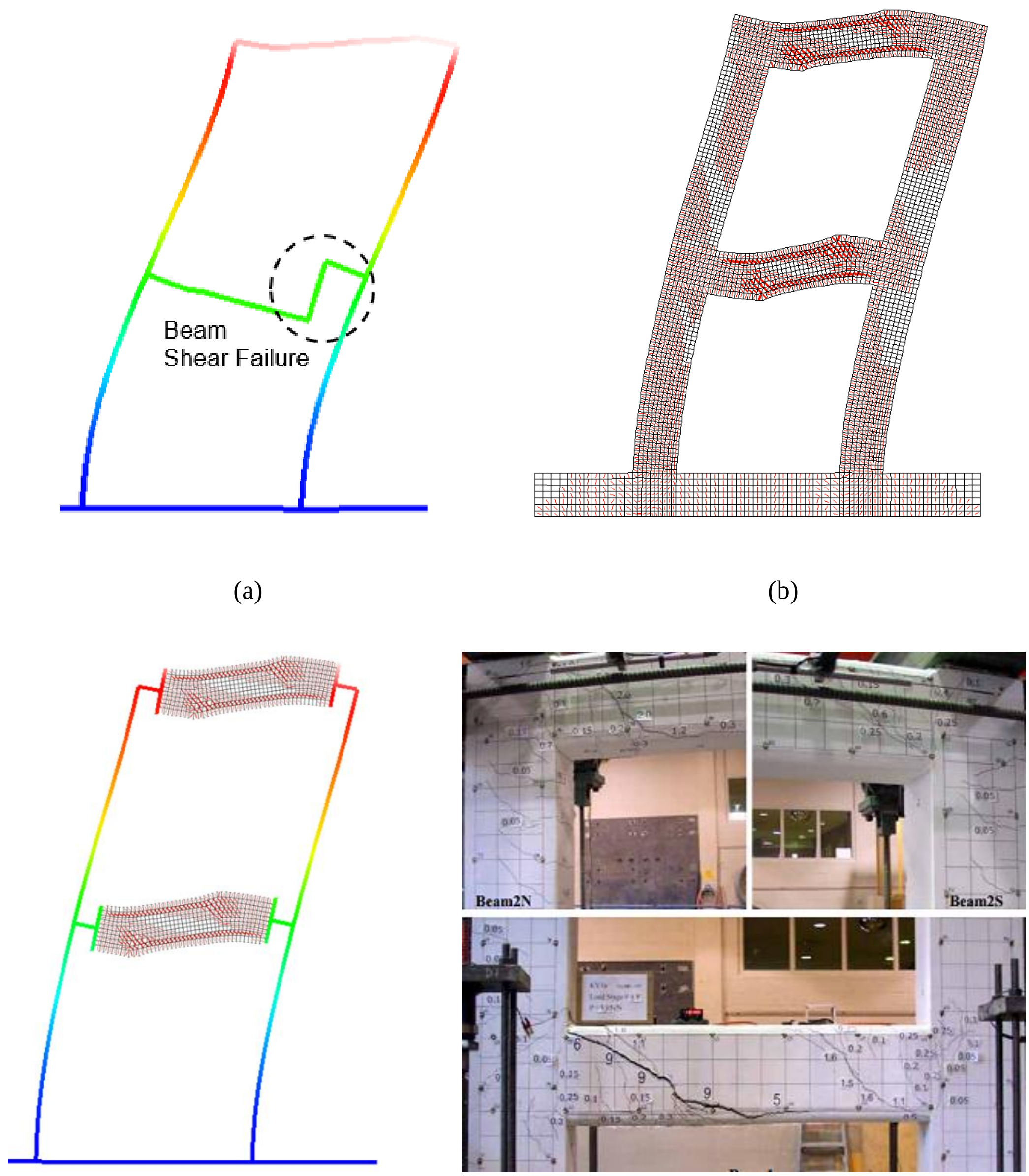

(a) (b)

(c) (d)

Figure 4.18 Duong frame crack pattern at peak forward half-cycle in Phase A: (a) stand-alone frame analysis; (b) stand-alone detailed analysis; (c) mixed-type analysis; (d) experiment

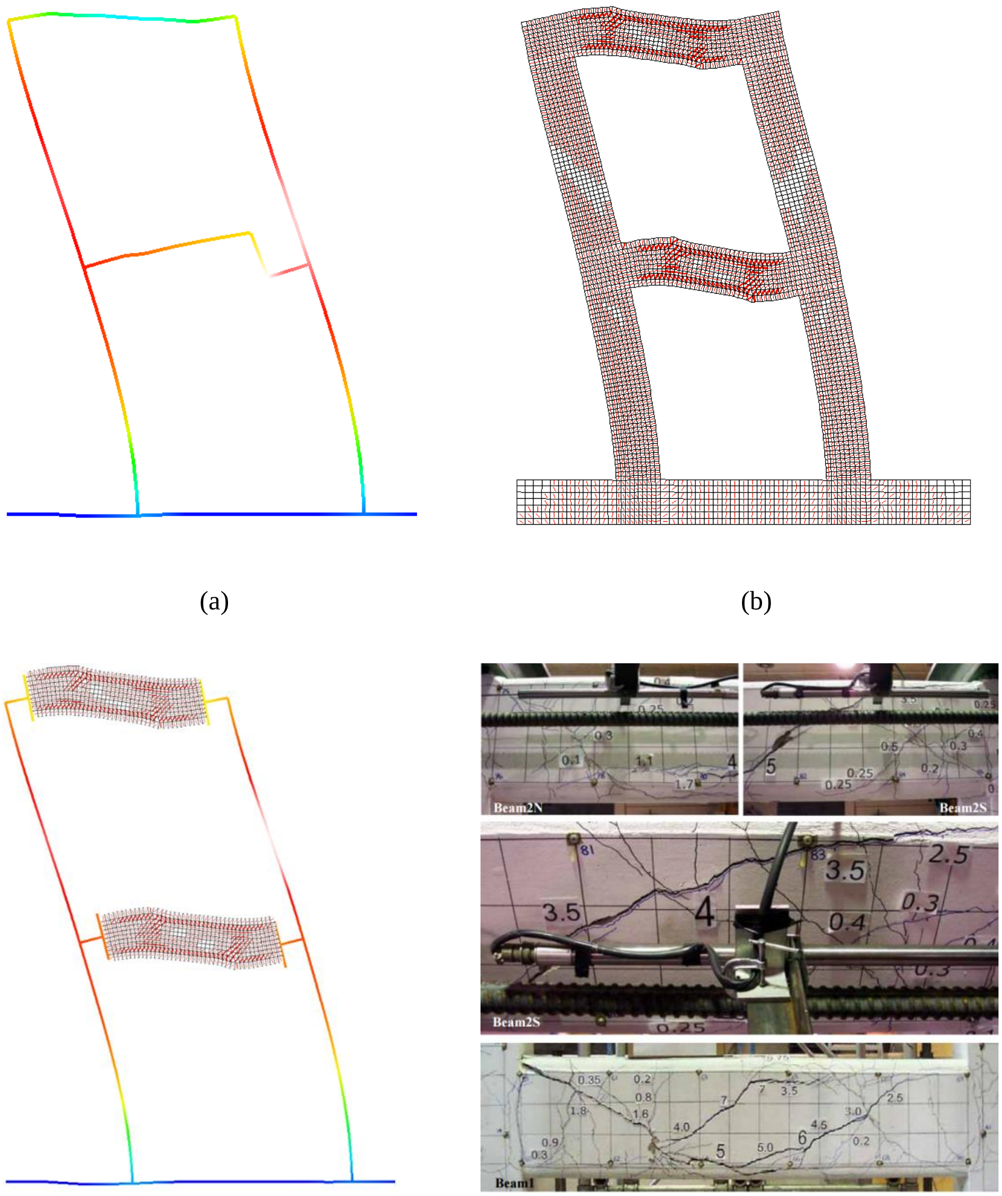

(a) (b)

(c) (d)

Figure 4.19 Duong frame crack pattern at peak reversed half-cycle in Phase A: (a) stand-alone frame analysis; (b) stand-alone detailed analysis; (c) mixed-type analysis; (d) experiment

To assess the practical application of the mixed-type analysis to larger structures, the time required for each type of analysis to complete a single load stage (which typically required 100 iterations) are presented in Table 4.6. Compared to the stand-alone detailed FE analysis, the mixed-type approach was about 3.8 times faster without any noticeable difference in terms of accuracy. It should be noted that Phase A and Phase B of the analysis required 340 and 2150 load stages, respectively. For a real-world structural system such as a high-rise building which includes frames with several bays and storeys, or a bridge structure which consists of a deck and multiple piers, the number of members that can be considered to be non-critical and modelled using layered beam elements will be significantly larger compared to the critical members of the structure; this will result in a much more pronounced performance improvement when the multi-platform approach is used.

Table 4.6 Number of elements and analysis time for different types of models

Analysis Type	Nonlinear Solution	Element Type	No. of Elements	Total No. of Elements	Analysis Time Per Load Stage (s) *
Stand-Alone VT2	Secant	Rectangular	3151	4131	20.5
		Truss	980		
Stand-Alone VT5	Tangent-Secant	Layered Beam	76	76	1.5
Mixed-Type VT2 - VT5	Tangent-Secant	Rectangular	820	1080	5.4
		Truss	164		
		Layered beam	56		
		F2M	40		

* The load stage considered was at the applied displacement = 30 mm and consisted of 100 iterations.

To investigate the behaviour of the F2M interface elements, nonlinear stress distributions through the cross section at the first storey beam (Beam 1) and the second storey beam (Beam 2) of the mixed-type analysis were compared against the corresponding stresses of the stand-alone detailed FE analysis. The stress distributions were assessed at the applied lateral displacement of 20 mm in the forward half-cycle of Phase A in two different locations: 1) at the interface section, 2) at about 0.25% of the beam's height, 109 mm, from the interface section.

As shown in Figure 4.20, at the interface section of the first storey beam, the stress distributions computed by the F2M elements matched only marginally well with the stand-alone analysis results. In the stand-alone model, disturbed regions at the connection of the beams and columns caused high stress concentrations at the corner elements (see Figure 4.21). To satisfy equilibrium and account for the stress concentration at the corner elements, stresses of other elements at the interface section were lower compared to a similar section at a non-disturbed region. In the mixed-type analysis, the F2M elements computed interface stress distributions based on the assumptions that plane sections remain plane and that the shear strain distribution is parabolic. Therefore, the stress concentrations at the corner elements were not fully captured. Conversely, at the interface section between the second storey beam and the left column, there was no stress concentration and all three stress components (horizontal and vertical normal stresses and shear stresses) of the mixed-type analysis correlated reasonably well with the stand-alone analysis results.

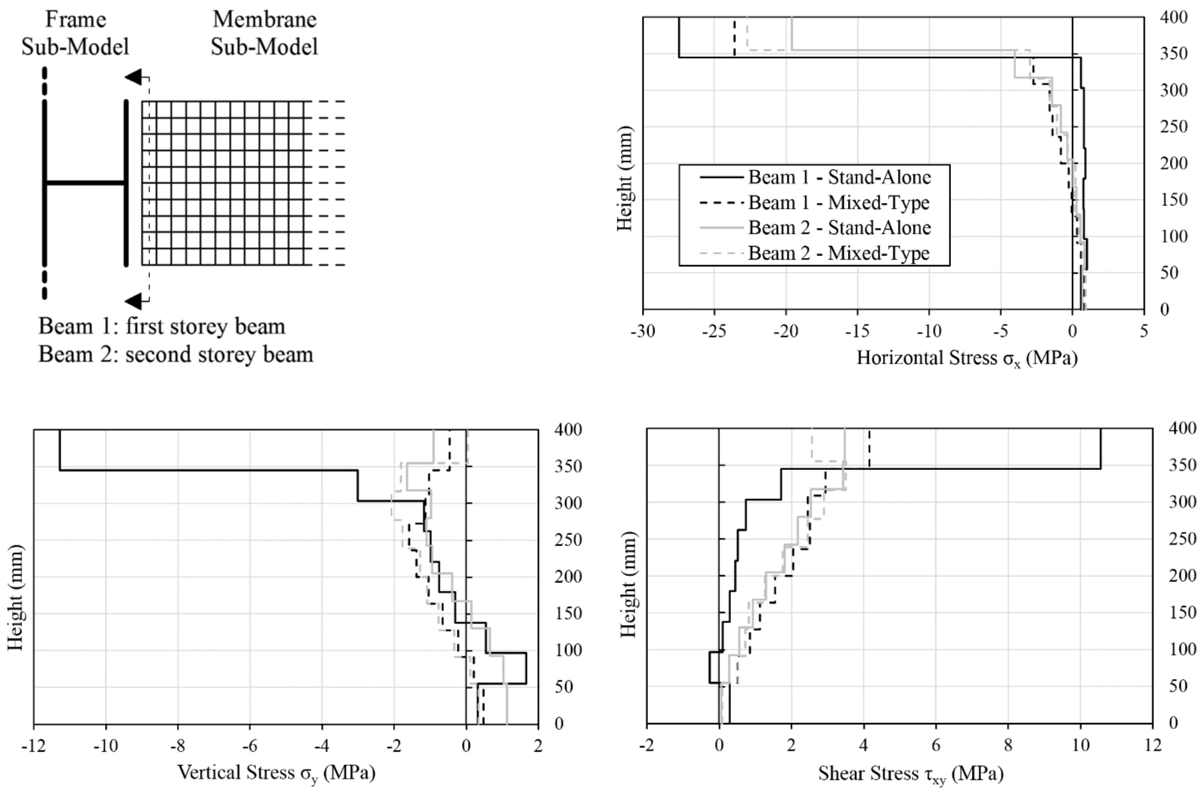

Figure 4.20 Stress distributions at interface of beam and column for mixed-type and stand-alone VecTor2 analyses in forward half-cycle of Phase A (Displacement = 20 mm)

To further investigate the effect of stress concentration at the corner nodes on the response of the beams, the stress distributions at another section located 109 mm (approximately 25% of the beam's height) from the interface section were examined. As shown in Figure 4.22, the vertical and shear stress concentrations computed at the interface section of the first storey beam were dissipated at this section and all the three stress components of the mixed-type analysis for both the first storey beam and the second storey beam matched reasonably well with the stand-alone analysis results. Therefore, because stress concentrations dissipated quickly and no local type of failure was reported at the disturbed regions in the stand-alone analysis or in the experiment, it can be concluded that stress concentrations did not have any noticeable effect on the response of the beams.

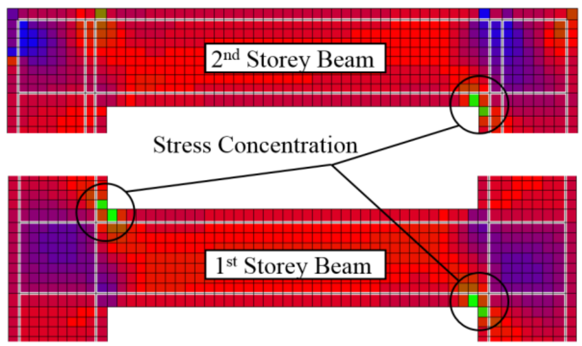

Figure 4.21 Shear stress concentration at corner nodes

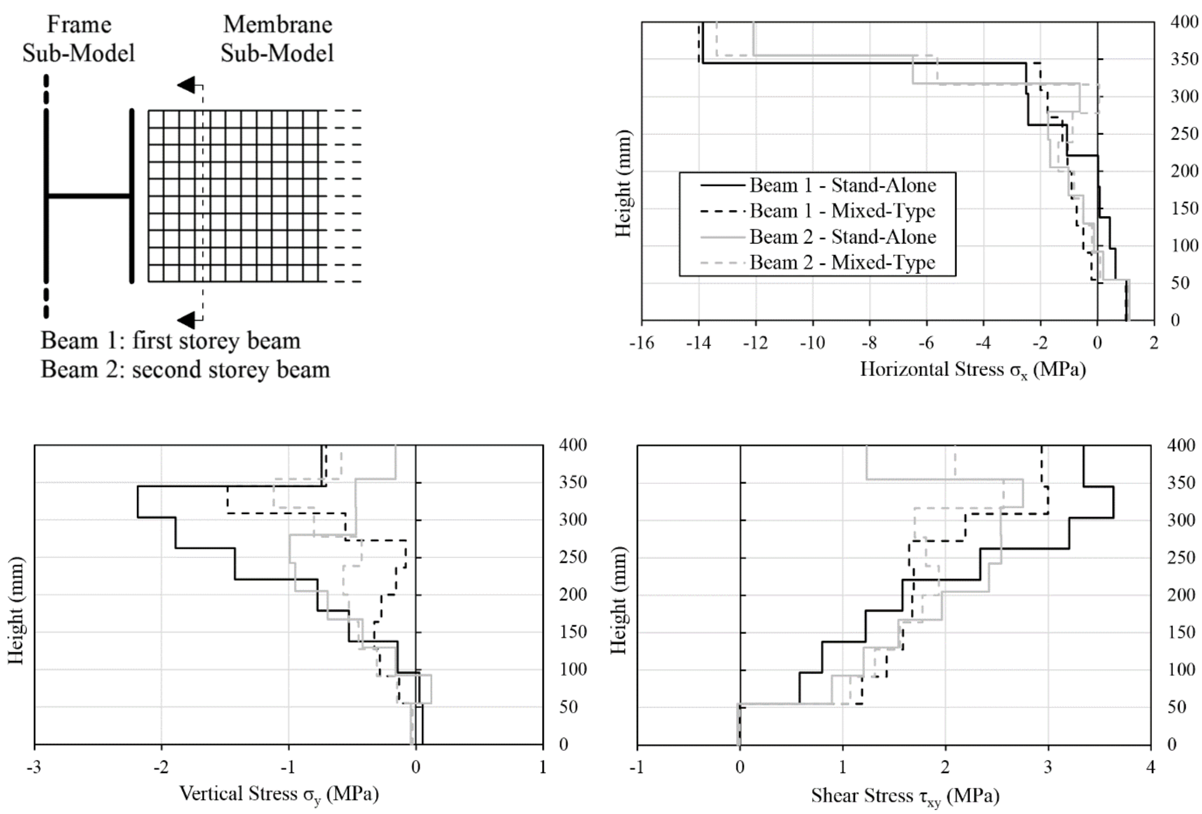

Figure 4.22 Stress distributions at 109 mm from interface section for mixed-type and stand-alone VecTor2 analyses in forward half-cycle of Phase A (Displacement = 20 mm)

For the analysis of the repaired frame in Phase B, the FRP sheets were modelled using "Tension-Only" truss elements which were connected with rectangular RC elements through link elements. For the concrete compressive strength of 43 MPa, the maximum bond shear stress ($\tau_{b,Fy}$) was computed as 4.36 MPa from Eq. 4.18. To account for debonding of FRP from the concrete at failure, as recommended by Wong and Vecchio (2003), $\tau_{b,Fy}$ was limited to the modulus of rupture of concrete which was 3.93 MPa from Eq. 4.22. Using Eq. 4.19 to Eq. 4.21 S_{Fy}, G_F, and S_{Fu} were calculated as 0.034 mm, 0.354 N/mm, and 0.180 mm, respectively. The confinement effects of FRP wraps were considered by the addition of an out-of-plane component to the rectangular elements located in the cover regions. To consider damage effects, Phase B of the analysis was started by reading and taking into account the stress and strain history of the elements from Phase A. Details of the mixed-type model after the repair are shown in Figure 4.23.

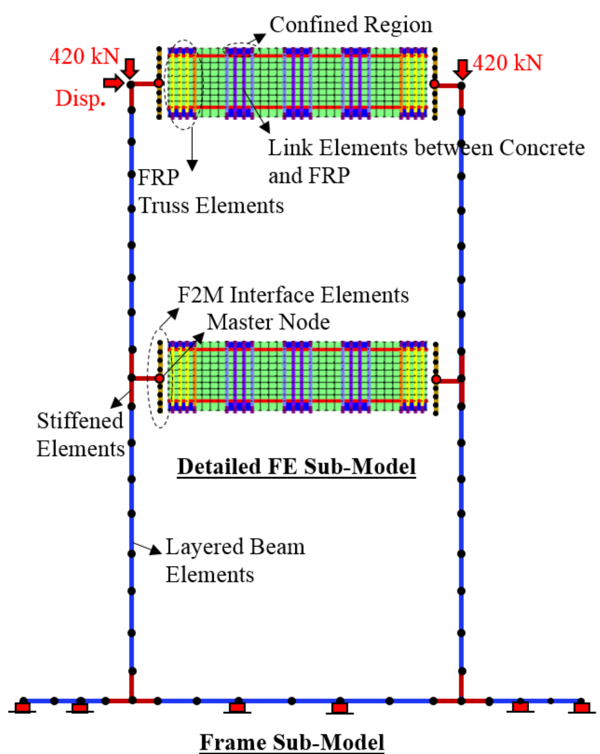

Figure 4.23 Multi-platform model of Duong frame after the repair (Phase B)

Figure 4.24 compares the load-deflection responses of the mixed-type analysis and the experiment for the repaired structure. The computed peak loads in the negative cycles, the initial stiffness, and the pinching effects correlated exceptionally well with the experiment. The analysis had a tendency to overestimate the peak loads associated with the positive cycles.

The mixed-type analysis computed maximum CFRP stresses of 323 MPa at the first storey beam and 306 MPa at the second storey beam. In the experiment, average maximum CFRP stresses of 270 MPa and 209 MPa were reported, respectively. The average stresses were taken from five CFRP wraps located along the length of the beam. In the analysis, link elements representing the interface between the CFRP and the concrete started to reach their bond strength during the third and fourth load cycles (±25 mm) with a maximum computed slip of 0.4 mm. During the last two cycles, (±100 mm) some of the link elements experienced slip values as large as 14.4 mm. In the experiment, partial debonding of the CFRP wraps was first observed at the fifth load stage (±50 mm), and during the ninth load stage (±100 mm) more than half of the bonded area was reported as broken.

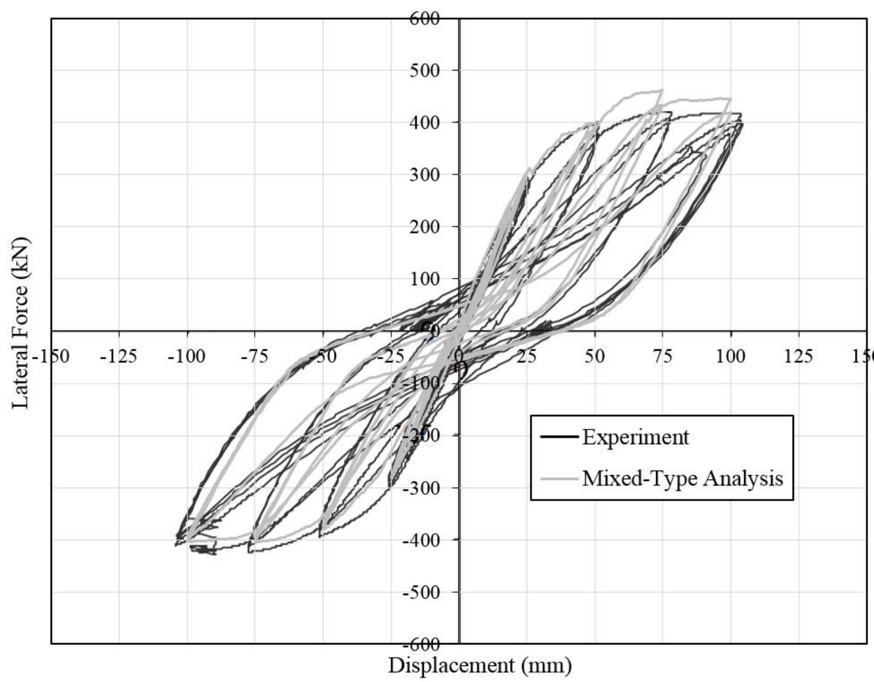

Figure 4.24 Load-deflection response of experiment and mixed-type analysis for Phase B

Figure 4.25 shows the influence of considering the contribution of CFRP to the tension stiffening response of cracked concrete using the Tension Chord model. Although taking into account the CFRP tension stiffening effect did not influence the peak strength and had a marginal effect on the effective stiffness, it provided a more ductile behaviour and eliminated the sudden drop in the last cycle of the analysis. A similar behaviour was observed in the experiment.

Compared to the Kim and Vecchio (2008) analysis, the mixed-type analysis predicted the response of the frame structure with the same level of accuracy as the stand-alone detailed FE model in significantly less computation time. In addition, although the usage of the Tension Chord model resulted in a slightly higher peak strength in the positive cycles, the pinching effects and effective stiffness of the last cycles were predicted with better accuracy compared to the Kim and Vecchio (2008) analysis.

In all of the study cases (the experiment, the stand-alone analysis, and the mixed-type analysis) a comparison between the response of Phase A and Phase B indicates that strengthening the shear-critical frame with CFRP sheets greatly improved the ductility of the structure and changed the failure mode from shear to flexure with the formation of hinges at the ends of the beams.

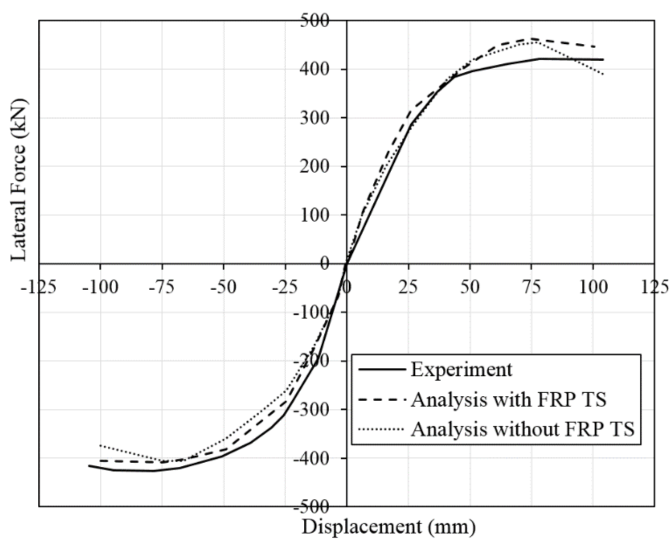

Figure 4.25 Envelopes of the hysteresis response for the experiment and the mixed-type analysis with and without CFRP tension stiffening effects

4.6.2 Seismically Deficient RC Columns

Memon and Sheikh (2005) examined the seismic resistance of large-scale square RC columns with insufficient confinement constructed according to pre-1971 design codes. The test program consisted of five columns retrofitted with GFRP wraps without initial damage, two columns damaged and then repaired with GFRP wraps, and a control column to assess the benefits of retrofitting and repairing. The specimens were tested under constant axial load and reversed cyclic lateral load simulating seismic loading conditions. The test setup and dimensions of the specimen are provided in Figure 4.26 and Figure 4.27, respectively. The test parameters included the number of GFRP layers, the axial load, and the presence of column damage (see Table 4.7). The specimen represented a portion of a column in a bridge or building between the section of maximum moment and the point of contraflexure. Figure 4.28 presents the relationships between forces and deflections in the horizontal test setup and a column standing in the vertical direction in a real-world structure.

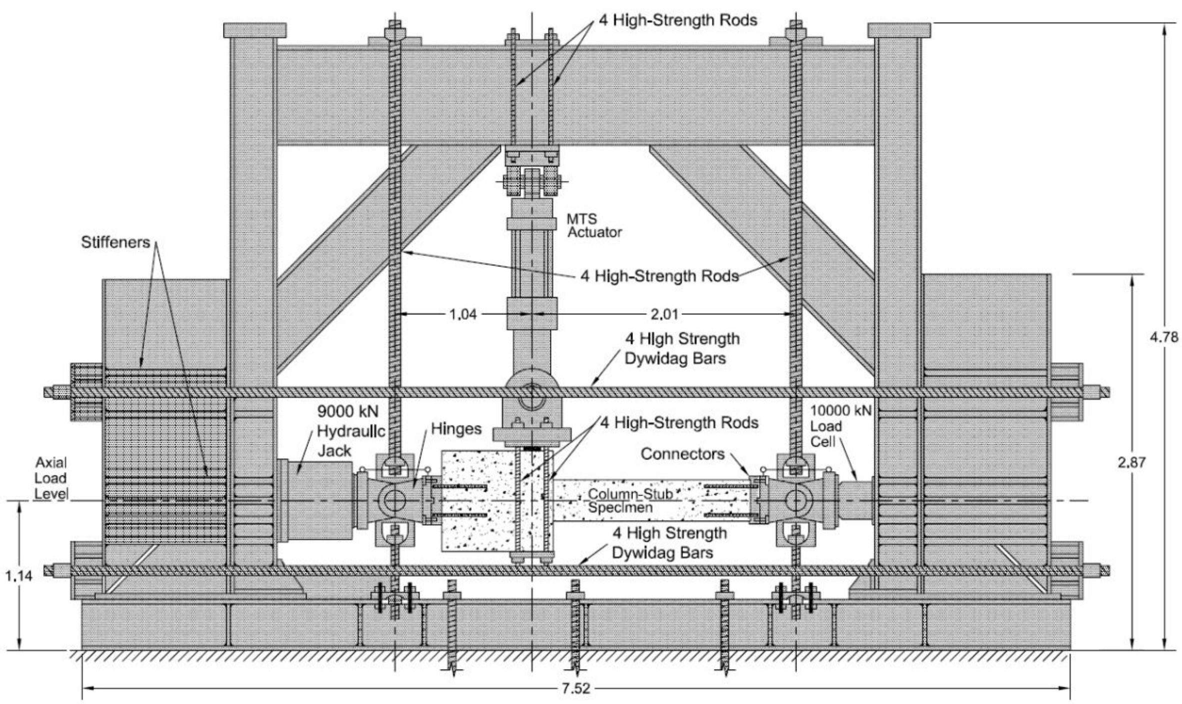

Figure 4.26 Test setup of RC columns (taken from Memon and Sheikh, 2005)

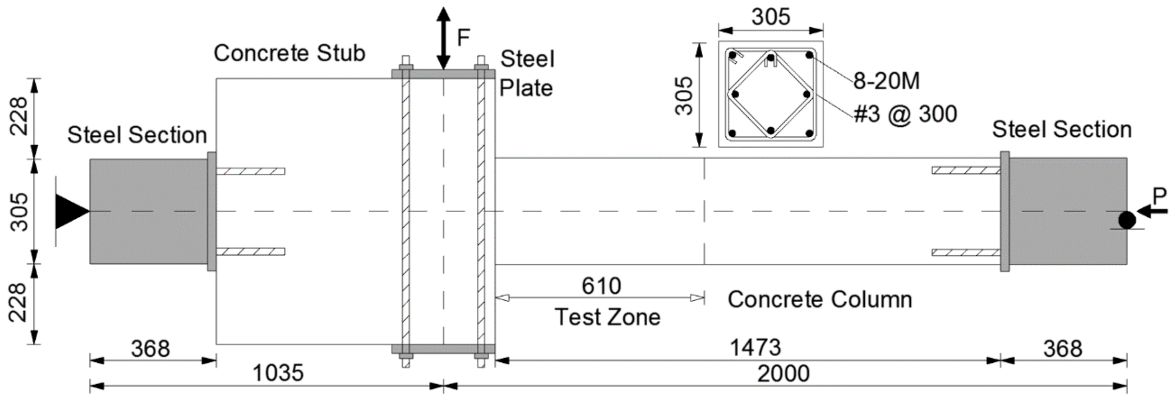

Figure 4.27 Cross section details and dimensions of columns (dimensions in millimeters)

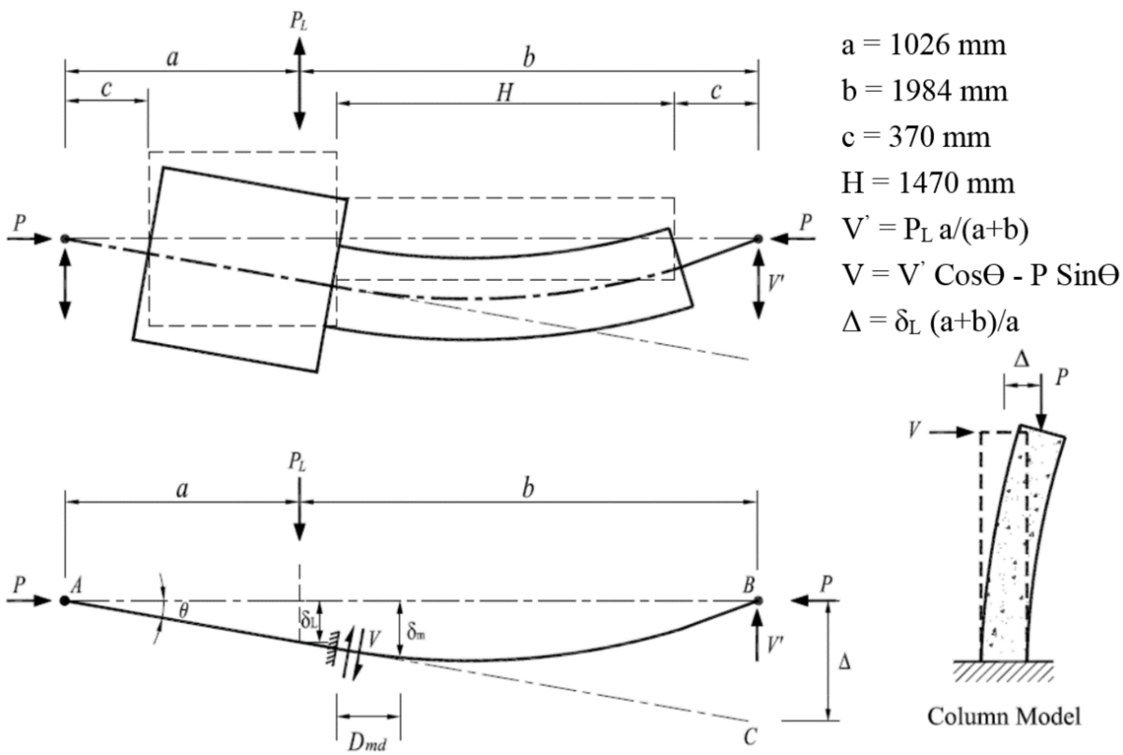

Figure 4.28 Forces and deformations of RC column specimen (taken from Memon and Sheikh, 2005)

The columns were cast using ready-mixed concrete with a 30 MPa nominal compressive strength, a specified slump of 100 mm, and a maximum aggregate size of 10 mm. At the time of testing, the compressive strength of the concrete varied from 42.4 MPa to 44.3 MPa for different specimens (see Table 4.7) as determined from standard six inch diameter cylinder tests. The material properties of the reinforcement and GFRP are presented in Table 4.8.

Table 4.7 Details of the RC column test specimens

Specimen	f_c' (MPa)	GFRP Wrap	Axial Load (P/P_o)	Description
AS-1NSS	42.4	None	0.56	Control
ASG-2NSS	42.5	2 Layers	0.33	Retrofitted*
ASG-3NSS	42.7	4 Layers	0.56	Retrofitted
ASG-4NSS	43.3	2 Layers	0.56	Retrofitted
ASG-5NSS	43.7	1 Layers	0.33	Retrofitted
ASG-6NSS	44.2	6 Layers	0.56	Retrofitted
ASGR-7NSS	44.2	2 Layers	0.33	Repaired**
ASGR-8NSS	44.2	6 Layers	0.56	Repaired

* Specimen was initially undamaged

** Specimen was initially damaged

Table 4.8 Material properties of reinforcement and GFRP

Reinforcement						
Bar Size	Diameter (mm)	Area (mm^2)	E_s (MPa)	f_y (MPa)	f_u (MPa)	ε_u ($\times 10^{-3}$)
US #3	9.5	71	207,730	457	739	141
10M	11.3	100	180,360	505	680	215
20M	19.5	300	202,170	465	640	202

GFRP			
f't (MPa)	E (MPa)	ε_u ($\times 10^{-3}$)	Thickness (mm)
563	24,700	22.8	1.25

In this section, two types of analyses were conducted to assess the performance of the multi-platform modelling approach: 1) component-level analysis: to verify the multi-platform analysis against the experimental results, 2) system-level analysis: to demonstrate the application of multi-platform analysis to RC structural systems.

Component-Level Analysis

As shown in Figure 4.29, the multi-platform model consisted of two components: a detailed FE sub-model which had the capability to analyze repaired structures within the VecTor2 program, and a computationally fast frame sub-model in the VecTor5 program. The two-dimensional detailed FE sub-model was created using 8-DOF RC rectangular elements with a 20 mm × 20 mm mesh size. All the reinforcement was modelled as discrete using 4-DOF steel truss elements, except the transverse reinforcement of the stub which was modelled as smeared. The GFRP sheets were modelled with discrete truss bars which were indirectly attached to the underlying RC rectangular elements via link elements. Due to the high axial force in the columns, instead of applying the confinement enhancements to the boundary elements, it was distributed through the height of the section to avoid premature failure of core elements. Since the GFRP was applied as a wrap, it was assumed that there would be no slip at the corner nodes. This was modelled by using perfect bond between the GFRP and the concrete for boundary nodes at the top and bottom sections.

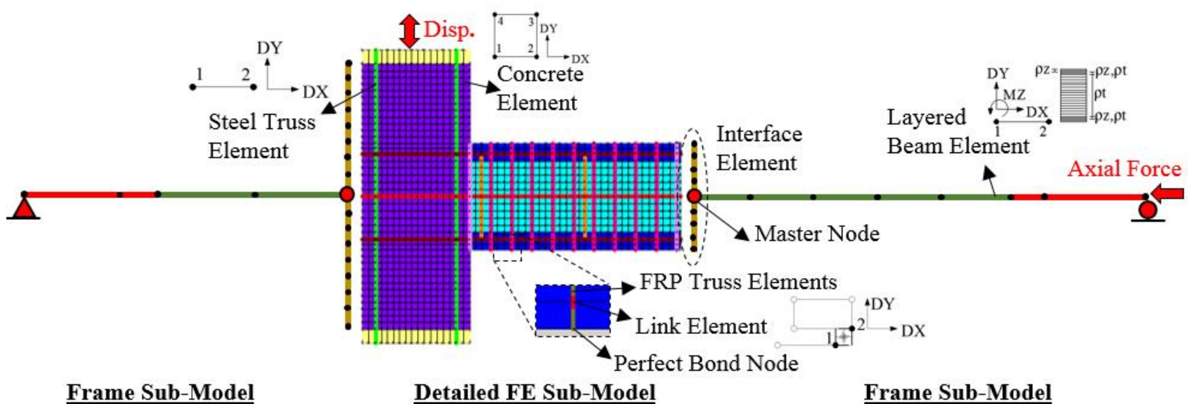

Figure 4.29 Mixed-type FE model of RC column

The loading plate was modelled using structural steel rectangular elements. The vertical load was applied as a nodal displacement load at the midpoint of the loading plate with a reversed cyclic pattern similar to the experiment. In the first cycle, 0.75% of the yielding displacement (Δ_1), determined from a sectional analysis of the column, was applied. In subsequent cycles, displacements were increased by the addition of Δ_1 to the previous cycle's peak displacement until the analysis could not converge and failure occurred. In each cycle, displacements were changed in increments of 0.5 mm. The axial force was modelled using a constant nodal load imposed on the frame sub-model. In addition, to take into account the self-weight of the structure, a constant gravity load was applied in the vertical direction on both the FE detailed sub-model and the frame sub-model. The support conditions were represented by defining a pinned support (restraining the X and Y translational DOFs) and a roller support (restraining the Y translational DOF) for the nodes located at the left end and the right end of the frame sub-model, respectively.

The analytical and experimental peak loads and load-deflection responses of the columns are compared in Table 4.9 and Figure 4.30. In general, the computed responses agreed reasonably well with the experimentally observed behaviour. The multi-platform analysis was able to accurately capture the strength degradation under repeated cycles at the same applied displacement. Also, the computed pinching effects correlated well with the experimental results. For specimens with more than two layers of GFRP, the analysis had a tendency to overestimate the peak load. This might be because of the possible slip between GFRP layers or lower confinement enhancement due to an arching effect in square columns. Neither of these mechanisms was considered in the analysis.

Table 4.9 Experimental and numerical peak loads for RC column specimens

Specimen	Experimental Peak Load (kN)			Numerical Peak Load (kN)			$\frac{\text{Num}}{\text{Exp}}$	Damaged Zone* (mm)	
	Positive	Negative	Ave.	Positive	Negative	Ave.		Test	Analysis
AS-1	327	-293	310	324	-305	314	1.015	458	400
ASG-2	371	-317	344	392	-359	375	1.091	188	180
ASG-3	364	-318	341	397	-371	384	1.127	207	200
ASG-4	342	-269	306	378	-319	349	1.140	189	180
ASG-5	375	-334	354	392	-372	382	1.078	202	180
ASG-6	419	-370	395	447	-424	435	1.103	204	180
ASGR-7	363	-310	337	382	-369	376	1.115	179	160
ASGR-8	355	-362	358	391	-355	373	1.042	199	200
			Mean				1.089		
			COV (%)				3.9		

* Distance measured from column-stub interface to center of most damaged area

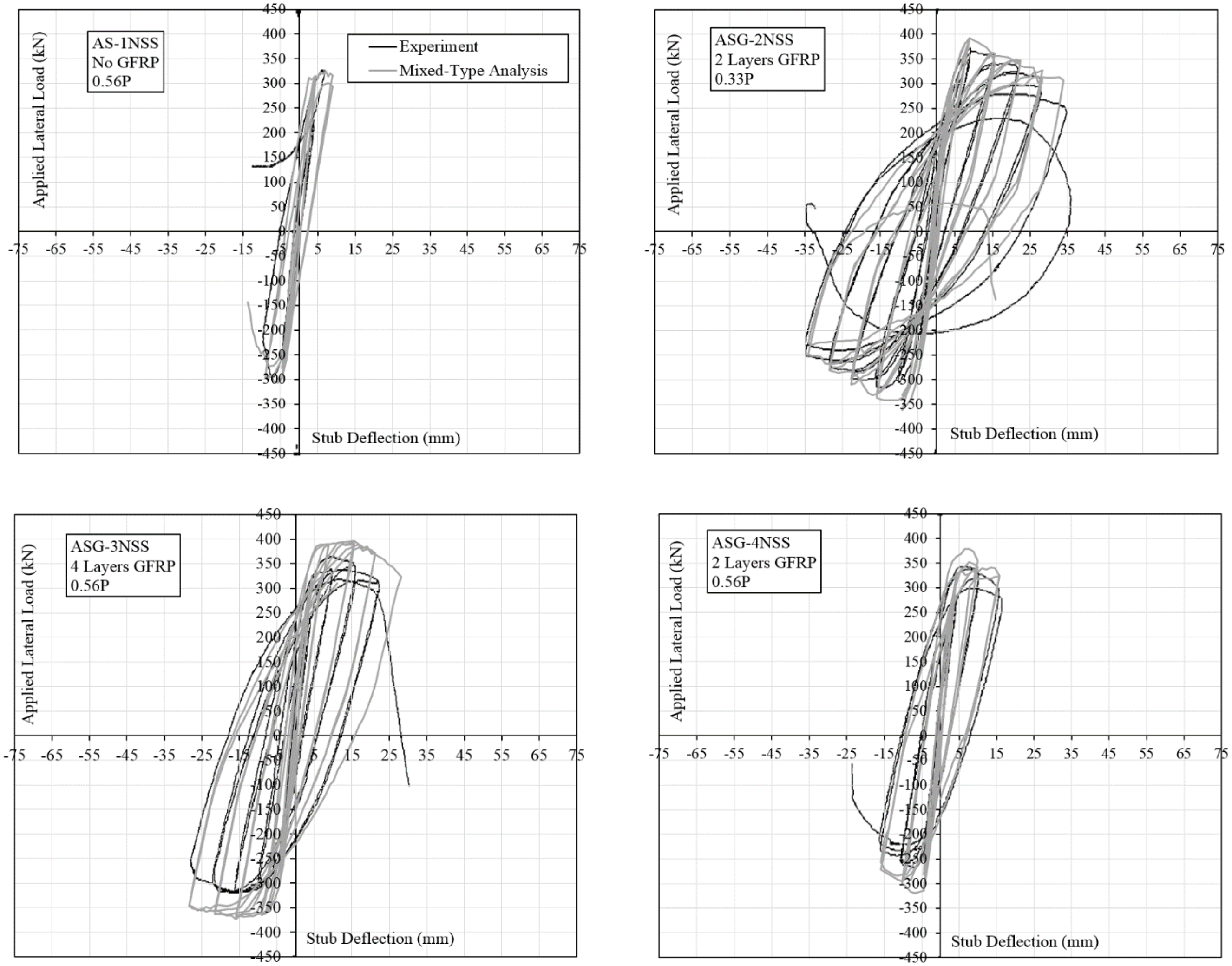

Figure 4.30 Analytical and experimental load-deflection responses of columns

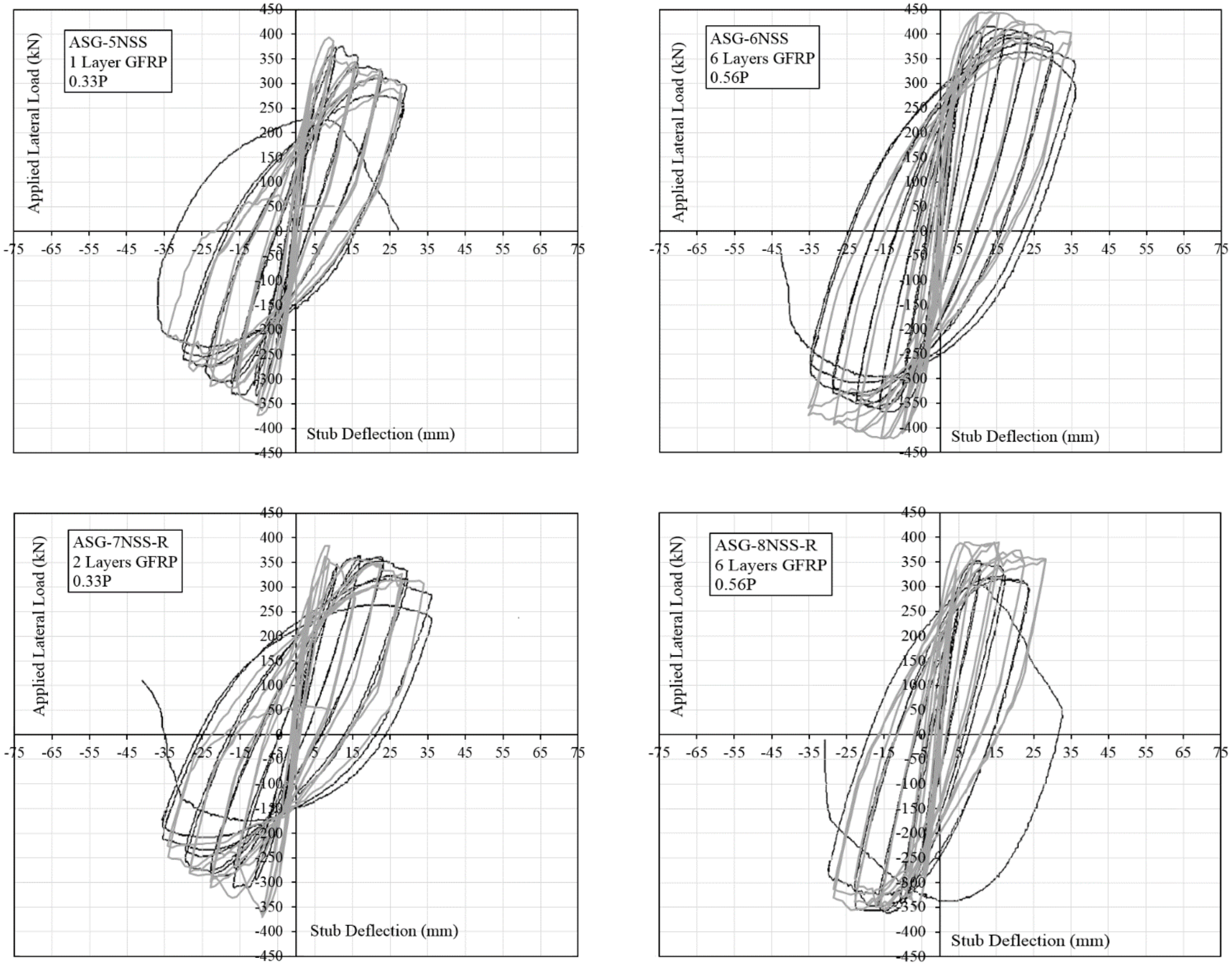

Figure 4.30 Analytical and experimental load-deflection responses of columns (continued)

In terms of the failure mode, the control column showed a different behaviour compared to the other columns strengthened with GFRP (see Figure 4.31). In the control specimen, the failure was initiated by spalling of the concrete followed by yielding of the transverse reinforcement and buckling of the longitudinal bars. On the other hand, in the retrofitted specimens, no concrete spalling was observed due the high confinement provided by GFRP wraps. In these specimens, failure occurred due to rupture of the GFRP sheets. Similar damage sequences and failure modes were computed by the mixed-type analysis. Furthermore, all the specimens experienced buckling of the longitudinal reinforcement prior to failure. As shown in Figure 4.32, not considering the buckling behaviour resulted in the analysis giving a significantly overestimated peak load and post-peak strength.

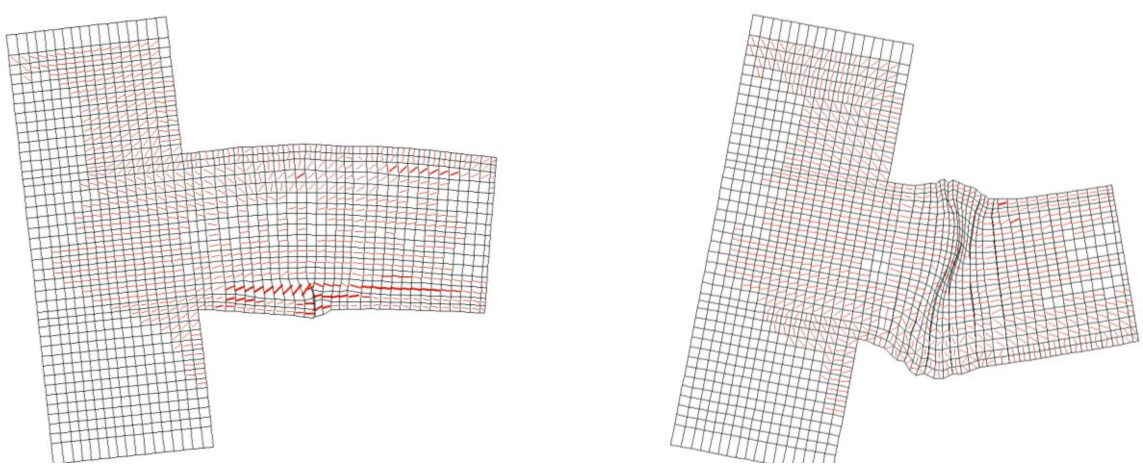

(a) (b)

Figure 4.31 Computed failure mode: (a) column without GFRP (AS-1NSS); (b) column with two layers of GFRP (ASG-4NSS)

For the two repaired specimens (ASG-7NSS-R and ASG-8NSS-R) which were initially damaged and then strengthened with GFRP, the analysis response was greatly affected by the level of axial load. Under low level axial force ($0.33P_o$), a comparison of the computed response of the initially damaged specimen (ASG-7NSS-R) with the similar undamaged specimen (ASG-2NSS), indicated that the damage only affected the initial cycles; the overall behaviours of the specimens were similar. However, under higher level axial force ($0.56P_o$), the damage effects were much more pronounced. In this case, the initially damaged specimen

(ASG-8NSS-R) showed significantly lower strength and ductility compared to the similar undamaged specimen (ASG-6NSS). A similar behaviour was observed in the experiment. Figure 4.33 shows the influence of damage effects on the response of the column under high axial force for both the experiment and the analysis.

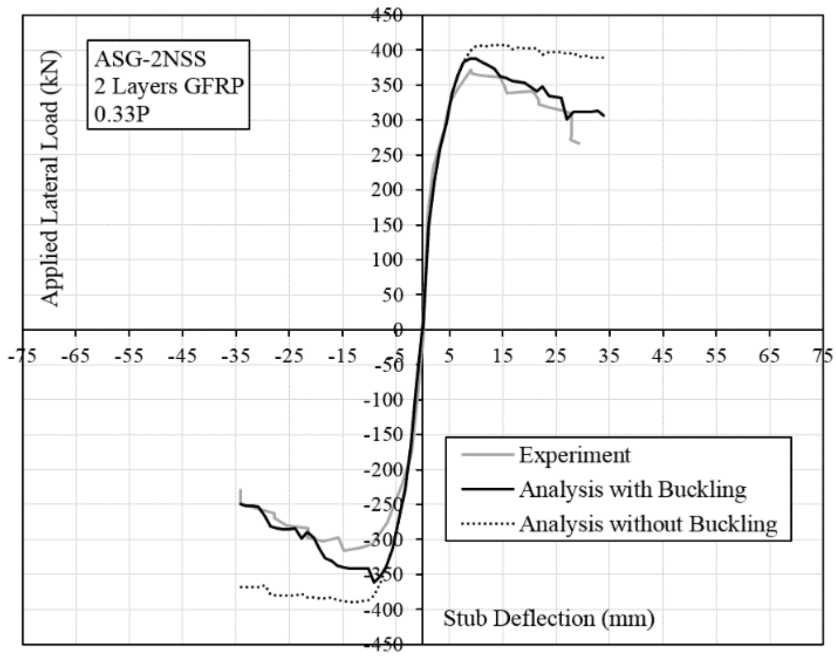

Figure 4.32 Influence of bar buckling on the behaviour of RC columns

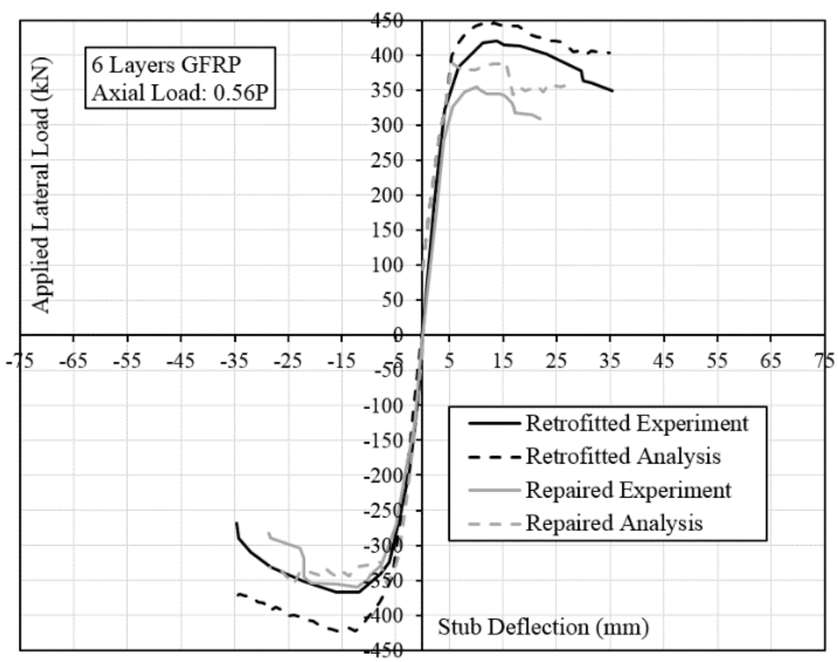

Figure 4.33 Influence of damage effects on the behaviour of RC columns

System-Level Analysis

As a demonstration example, the behaviour of an RC bridge structure strengthened with GFRP wraps was investigated at both the system-level and the component-level. The bridge had four 10 m long spans supported by three piers with a height of 3 m. The connections between the deck and piers were assumed to be pinned. The cross sections of the piers were identical to the cross section of the RC columns tested by Memon and Sheikh (2005). The level of gravity load on each span was selected so that the axial forces in Pier 1, Pier 2, and Pier 3 were approximately equal to the values used in the component-level example ($0.56P_o$, $0.33P_o$, and $0.10P_o$, respectively). The gravity loads were applied as nodal forces distributed over all nodes of the bridge deck. Assigning different levels of axial forces enabled better demonstration of the force redistribution between piers. The lateral load was imposed by controlling the lateral displacement of the node located at the left end of the deck, in 1 mm increments, in a reversed cyclic manner.

It must be noted that this is an illustration example and the structural details and loading configuration do not represent a real structure. For instance, $0.56P_o$ axial force was selected to be consistent with the component-level analysis, however, it is quite a high axial load for a bridge structure.

First, a stand-alone frame analysis was conducted which indicated formation of plastic hinges at the base of the piers. For a more comprehensive analysis of the structure, the lower portions of the piers were modelled in VecTor2, while the rest of the structure was modelled in VecTor5 (see Figure 4.34). The multi-platform analysis revealed more details about the response of the system and of the critical components. The final failure was initiated by spalling of the concrete cover at about 300 mm from the base of Pier 1 which was followed by buckling of the longitudinal bars and crushing of the concrete core. The force redistribution between the three piers under monotonically increasing lateral displacement is demonstrated in Figure 4.35(a). Zone 1 corresponds to extensive cracking of Pier 3 on the tension side which resulted in a reduction in its force capacity and consequently a large increase in the percentages of force carried by Pier 1 and Pier 2. Zone 2 indicates a significant force redistribution from Pier 1 to Pier 2 and Pier 3 due to spalling of the concrete cover, buckling of the longitudinal bars, and crushing of some of the concrete core elements. Zone 3 and Zone 4 correspond to tensile yielding of the longitudinal bars in Pier 3 and extensive crushing of the concrete core elements in Pier 1, respectively. A comparison of the graphs in all four zones clearly shows that as the force capacity percentage in Pier 1 reduces due to failure mechanisms, Pier 2 and Pier 3 must carry higher percentages of the total lateral force.

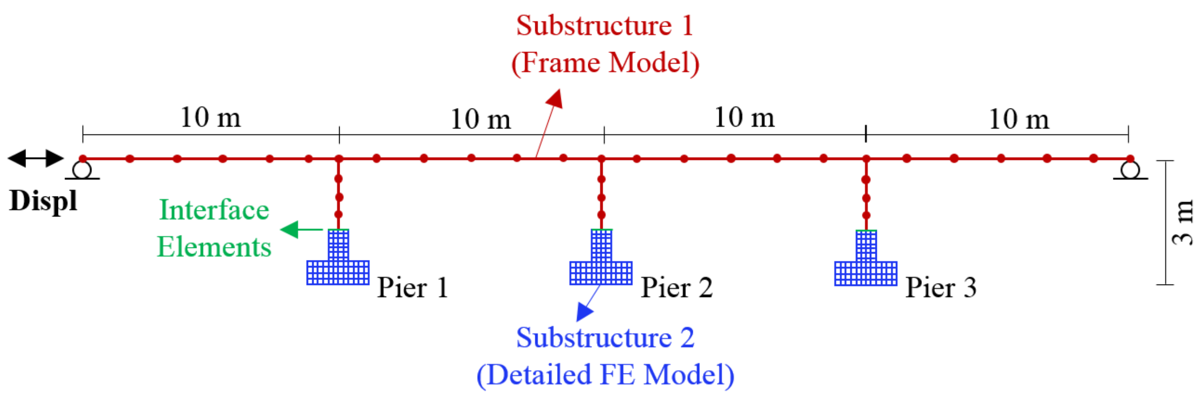

Figure 4.34 Multi-platform model of an RC bridge with critical piers (dimensions in meters)

In the next phase of the analysis, the base of the most critical pier, Pier 1, was confined with six layers of GFRP using a similar modelling procedure as described in the previous component-level analysis subsection. The analysis results showed a significant increase in the strength and ductility of the structure (see Figure 4.36). In addition, as shown in Figure 4.35(b), there was a much more stable force distribution between the three piers compared to the prior-to-repair analysis case. As a result of the GFRP confinement, buckling of the longitudinal bars in Pier 1 was prevented. Failure occurred by crushing of the concrete core elements in Pier 1 and Pier 2 (Zone 2) and shortly after in Pier 3 (Zone 3).

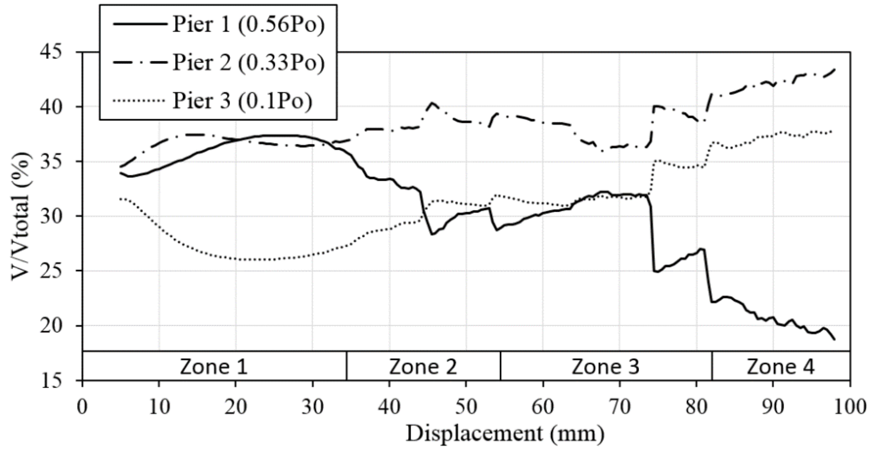

(a)

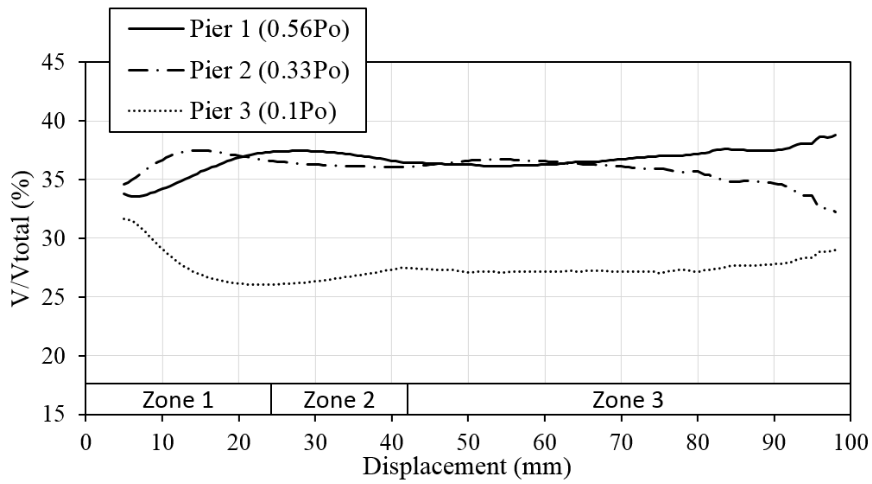

(b)

Figure 4.35 Force redistribution in RC bridge piers: (a) without GFRP; (b) Pier 1 confined with GFRP

In the last phase of the analysis, the base of the remaining piers (Pier 2 and Pier 3) were confined. However, the analysis results indicated an almost identical load-deflection response as obtained in the previous analysis case. The reason was that when Pier 1 lost its strength due to crushing of its concrete core elements, it imposed additional force on Piers 2 and 3. The GFRP confinement enhancement in Pier 2 and Pier 3 was not sufficiently adequate to avoid crushing of the concrete elements under additional force. This force redistribution can be seen in the improvement of strength in the last three cycles of the analysis in the load-deflection response. Therefore, it is crucial to consider the influence of the component-level response on the system-level behaviour in order to provide the most effective repair strategy.

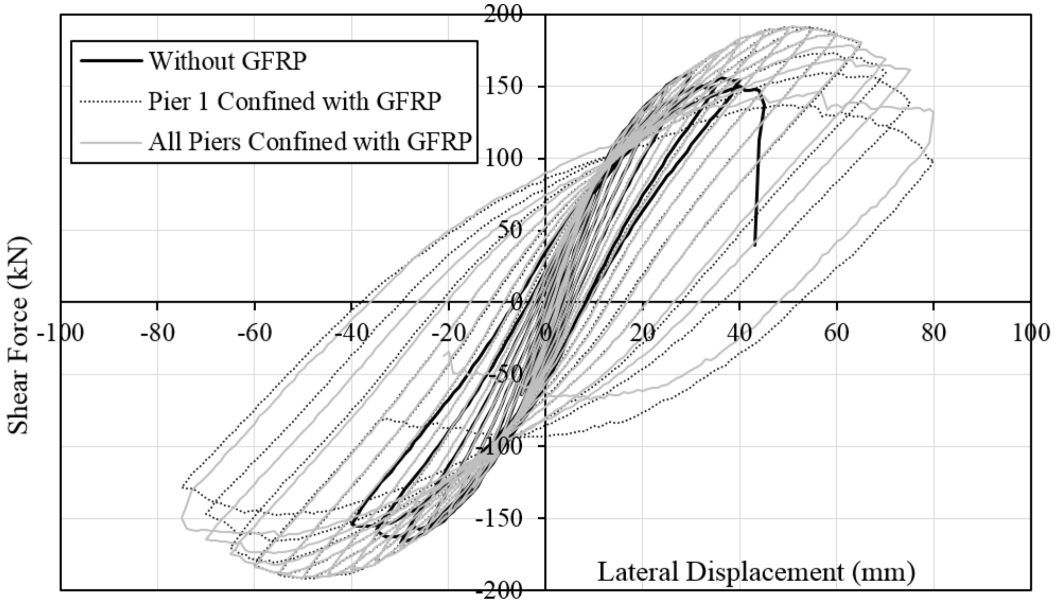

Figure 4.36 Load-deflection response of RC bridge prior and after repair with GFRP

4.7 Summary and Conclusions

The proposed multi-platform analysis framework was employed for modelling and analysis of structures strengthened with FRP wraps. In this procedure, the repaired components were modelled in finer detail using a 2D FE program, while the rest of the structure was modelled with a computationally-fast frame analysis program. The sub-models were connected using a newly developed interface element, the F2M element, which satisfies equilibrium and compatibility conditions and produces a reasonably accurate shear stress distribution for cracked concrete at the interface section.

A practical and reliable method was presented to model FRP-related mechanisms for repaired components. Link elements with appropriate bond-slip models were used to consider stresses at the interface of the concrete and FRP. The confinement enhancement of FRP was modelled by the addition of an out-of-plane smeared component to the corresponding rectangular RC elements. Second-order material effects such as tension stiffening and reinforcement buckling were taken into account using proper models. Other RC-related mechanisms such as cover spalling and damage effects prior to repair were also considered.

The proposed modelling procedure was verified using data from two experimental programs: an RC frame with shear-critical beams and a series of RC columns. The following conclusions can be drawn from the studies conducted:

- In general, the mixed-type analyses were able to accurately predict the behaviour of the specimens particularly in terms of stiffness, peak load, ductility, and failure mode. The proposed method was capable of considering the effects of previous damage with the use of stress and strain histories of the elements. In addition, the change in the damage mode prior to and after the repair of the frame structure was captured accurately.

- The frame-type analysis of the shear-critical RC frame demonstrated that insufficient consideration of shear-related effects can lead to significant overestimations of strength and deformation capacity, and inaccurate predictions of structure behaviour. Most frame analysis procedures, including plastic hinge and layered analysis approaches, require difficult assumptions and inputs to account for shear mechanisms which can significantly affect structural response.

- For axially loaded members such as bridge piers and columns, the buckling of longitudinal reinforcement and damage effects prior to repair can significantly affect the response of the repaired structure. The influence of these mechanisms were investigated in detail.

- Although the analyses gave satisfactory results for RC columns, they had a tendency to overestimate the peak loads for specimens with more than two layers of GFRP sheets. This may be a consequence of slip between layers of FRP sheets or lower effective confinement due to the square shape of the columns, known as arching action.

- The RC bridge example demonstrated the importance of considering the influence of component-level analysis on the system-level behaviour and recognizing the force redistributions within the structure in order to have an effective and efficient repair strategy.

- The bond-slip material model utilized in the analysis was derived for externally bonded FRP sheets under monotonic loading conditions. To take into account plastic deformations and stress degradations of link elements under cyclic loading conditions, a more comprehensive bond-slip model is required.

- For link elements representing the interface between FRP and concrete, displacements in the radial direction were prevented by assigning a very large value to the radial stiffness. This compromised the ability to consider delamination of the FRP sheets. Further development is required to define the radial stiffness of link elements according to available models in the literature, particularly for the analysis of repaired structures experiencing a delamination type of failure.

CHAPTER 5

EXPERIMENTAL INVESTIGATION OF RC STRUCTURES USING SMALL-SCALE MULTI-AXIAL HYBRID SIMULATION

5.1 Introduction

Small-scale testing is frequently used to assess the behaviour of reinforced concrete (RC) members since, in most instances, there are unmanageable impediments to large-scale testing such as budgetary limitations and availability of large-scale laboratory facilities. To ensure small-scale tests accurately represent the response of a large-scale prototype specimen, in addition to imposing proper similitude laws, special considerations should be taken into account for scale-related effects. Each material component (concrete and reinforcement) should be carefully prepared to adequately represent the large-scale behaviour. Furthermore, since reinforced concrete is a composite material, the interaction between the concrete and the reinforcement should be realistically replicated. If these issues are addressed properly, for most types of structures, small-scale testing can be considered as a reliable alternative to large-scale testing. Comprehensive discussions on similitude considerations and small-scale behaviour of different types of structures are presented in this chapter.

In the field of seismic assessment of reinforced concrete structures, regardless of the scale of the test specimen, various types of testing techniques have been developed. The most realistic simulations of response are obtained from shake table tests. However, shake table tests are prohibitively expensive with numerous restrictions on the size, weight and range of applied loads that can be tested. As a result, most shake table tests are performed on specimens of a reduced scale, and typically involve only components or sub-systems of the structure rather than the entire structure. Thus, it is difficult to capture the crucial interactions that occur between the overall behaviour of the structure and the localized behaviour of a critically damaged element or component.

Another experimental testing technique commonly used is to apply loads quasi-statically. Although this method utilizes conventional laboratory loading equipment and is more economical, it is always a concern that the prescribed loading history on the specimen may not fully represent the actual seismic loading condition. Again, there is concern that the interactions between the overall structural behaviour and the localized behaviour are not adequately represented.

Hybrid simulation is an experimental-numerical simulation technique which attempts to consider both the realism of shake table tests and the economic and convenience features of quasi-static testing. The basis of hybrid simulation is to predict overall structural displacements by computer simulation and impose them on the critical element represented in the form of a laboratory test specimen. The displacements are calculated based on the external load, inertia and damping characteristics of the test specimen, and the restoring forces are measured directly from the deformed test specimen. Using a computer simulation allows one to consider the dynamic characteristics and the influence of other structural members on the response of the test specimen.

The concept of hybrid simulation can equally be applied to the analysis of deficient or deteriorated structures as it is to seismically loaded structures. Most reinforced concrete structures involve varying degrees of redundancy; as one part of the structure exhibits a weakened or failed state of response, load may be redistributed to other parts of the structure. As it is impractical to test a model of an entire structure that is deficient, hybrid simulation can be of great value here as well. It will enable the testing of critical components of a deficient or repaired structure, while accounting for the overall structural interactions and load redistributions that may occur.

In this study, the newly developed multi-platform analysis framework, Cyrus, was further extended to combine numerical models with experimental components to accommodate hybrid testing. A small-scale experimental program was conducted using a six degree-of-freedom (DOF) hydraulic testing facility to verify the proposed hybrid simulation framework and assess the reliability of small-scale testing under a multi-axial loading condition. The test program consisted of three parts:

- *Hybrid simulations of two steel frame structures within the linear elastic range*. The first frame was a one-span one-storey structure in which one of the columns was considered the experimental component. The second frame was a one-span two-storey structure in which the lower storey beam was selected as the test specimen. In both structures, the remainder of the frame was modelled via computer software. The test results were compared against the linear elastic analysis results of the full-frame models.
- *Hybrid simulations of two one-span one-storey reinforced concrete frames with critical columns under a reversed-cyclic loading condition.* The test variable was the amount of shear reinforcement in the columns. One of the frame was designed to be shear-critical while the other frame was designed to exhibit a ductile behaviour containing adequate transverse reinforcement. One of the columns was represented by the test specimen and the rest of the structure was modelled in a detailed finite element (FE) analysis software, VecTor2, and a frame analysis program, VecTor5. The load-deflection responses and failure modes of the hybrid simulations were compared against the analysis results of the full-frame models.
- *Hybrid simulation of a one-span two-storey reinforced concrete frame with shear-critical beams.* A 1/3.23-scale specimen of the lower-storey beam was built and considered as the experimental substructure while the remainder of the structure was modelled using the VecTor nonlinear analysis programs. A similar structure was tested as a large-scale full-frame specimen at the University of Toronto in 2007. The results of the hybrid simulation were compared against those obtained from the large-scale full-frame test and a detailed FE analysis software.

It should be noted that all the test specimens were 1/3.23-scale representations of the prototype members. The scale factor was selected based on the force capacity of the actuators. Details of the actuators and test setup are presented in Section 5.3.3.

All the hybrid simulations were conducted in a quasi-static manner allowing the determination of important parameters such as damage type, ductility, and energy dissipation which can be used to evaluate the performance of a structure during an earthquake. By implementing a time integration method into the simulation framework, a similar hybrid simulation configuration can be used to assess the performance of a structure under seismic loads and consider dynamic effects such as inertia, mass, and damping.

In this chapter, a summary of previous studies on the small-scale testing of reinforced concrete structures is first described. Emphasis is given to the small-scale tests which were conducted using the hybrid simulation technique, and also to the influence of scaling effects on shear behaviour. Then, details of the experimental program including material preparation and tests, construction of the specimens, test setup, hybrid simulation components, and testing procedure are fully presented. Lastly, extensive comparisons and discussions regarding the results of the small-scale hybrid tests including load-deflection response, crack pattern, and failure mode are provided.

5.2 Literature Review

The concept of small-scale testing is based on dimensional analysis which is a means of simplifying a complex physical problem by reducing the relevant variables. The basis of the dimensional analysis was established in Buckingham's Pi Theorem in 1914. According to this theory, if an equation consists of "n" dimensionally homogeneous variables, it can be expressed using a relationship between "n-k" independent dimensionless parameters (π terms), where "k" is the minimum required number of reference dimensions. The reference dimensions are defined as: force, length, and time. Depending on the type of the problem, some studies use mass instead of force as the reference dimension. Since the two variables are related through Newton's law, both options result in identical answers.

Therefore, a prototype problem which is originally stated in terms of n variables:

$$y_p = f(x_{1p}, x_{2p}, \ldots, x_{np}) \tag{5.1}$$

can be restated in terms of a set of dimensionless parameters as:

$$\pi_p = f(\pi_{1p}, \pi_{2p}, .. \pi_{(n-k)p}) \tag{5.2}$$

Using a similar procedure for the model problem, the original function and dimensionless relationship can be written as:

$$y_m = f(x_{1m}, x_{2m}, \dots, x_{nm}) \tag{5.3}$$

$$\pi_m = f\left(\pi_{1m}, \pi_{2m}, \ldots \pi_{(n-k)m}\right) \tag{5.4}$$

If the model structure is constructed such that its dimensionless parameters are equal to that of the prototype structure:

$$\pi_{im} = \pi_{ip} \qquad \text{for } i = 1 \text{ to } (n-k) \tag{5.5}$$

then the two systems are considered to be similar:

$$\pi_m = \pi_p \tag{5.6}$$

From Eq. 5.5 the relationships between the original variables of the model structure and prototype structure can be found and therefore the scale factors between the two systems can be established. Holub (2005) demonstrated the application of Buckingham's Pi Theorem on a simple cantilever beam example and derived the corresponding scale factors. Similarly, several sources including Noor and Boswell (1992) and Harris and Sabnis (1999) presented scale factors for commonly used variables in static and dynamic similitudes. Table 5.1 provides a summary of static scale factors (S) based on reference dimensions of length (l), mass (m), and time (t). These scale factors are applicable to pseudo-dynamic testing and used throughout this experimental program.

For dynamic testing, the similitude laws are more complicated because of the challenges associated with scaling the time variable. It is worth noting that variables which are originally dimensionless such as Poisson's ratio and strain are not scalable. For similitude models in which material types are different than the one used in the prototype system, this can be a source of distortion in the experimental results. While some studies such as Kim et al. (2004) developed procedures to remedy this type of distortion, it is always recommended to replicate material behaviour to the fullest extent possible. Other types of scaling effects can also cause distortion in the similitude results. For instance, simulating gravitational acceleration in dynamic models or scaling the mass of structures for which self-weight consideration is critical in both static and dynamic models is often challenging. Murphy (1950) provided further discussions regarding the distortion phenomenon in small-scale models.

Table 5.1 Scale factors for static similitude testing

Quantity	Reference Dimension	Scale Factor
Rotation, θ	---	1
Length, l	l	S
Area, A	l^2	S^2
Volume, V	l^3	S^3
Moment of Inertia, I	l^4	S^4
Concentrated Force, P	ml/t^2	S^2
Moment, M	ml^2/t^2	S^3
Mass, m	m	S^2
Modulus of Elasticity, E	m/lt^2	1
Poisson's Ratio, ν	---	1
Mass Density, γ	m/l^3	1/S
Stress, σ	m/lt^2	1
Strain, ε	---	1

To investigate the reliability of similitude models for assessing the behaviour of reinforced concrete structures, several researchers employed the aforementioned scaling factors and conducted small-scale experimental tests. The influence of a wide range of parameters, such as scaling factor, member type, failure mode, material properties, loading condition, and reinforcement ratio, on the response of the structure was investigated. Comparison of small-scale test data with the behaviour obtained from similar medium-scale or large-scale tests resulted in several valuable conclusions discussed below; these helped to improve the performance of similitude models by reducing the scaling effects and also identified the limitations of small-scale testing when applied to reinforced concrete members. In the following, a summary of the related previous studies and their findings are provided in three subsections:

1) Influence of model material properties on small-scale testing;

2) Influence of scaling-effects on shear behaviour;

3) Hybrid simulation of small-scale specimens.

5.2.1 Influence of Model Material Properties on Small-Scale Testing

One of the earliest small-scale studies was conducted by Gilbertsen and Moehle in 1980. The test program consisted of eight reinforced concrete column specimens which were constructed to be similar to the first-storey columns of a nine-storey three-bay frame structure tested at the University of Illinois. The test variables were the reinforcement ratio and the level of axial load. The column specimens had a shear span of 250 mm and cross section dimensions of 51 mm by 38 mm. The microconcrete was cast using small sand aggregates, Type III cement (i.e., high early strength cement) and water. Longitudinal and transverse reinforcement were constructed from wires with 2.33 mm and 1.65 mm diameters, respectively. The specimens were subjected to a shear force applied in a reversed cyclic manner. The level of axial force varied depending on the applied shear force. The damage mode consisted of flexural cracks and concrete spalling near the base of the column. The small-scale test results agreed well with the calculated response of the full-scale column based on the moment-curvature relationships.

Wallace and Krawinkler (1985) investigated the influence of the failure mode and member type on the accuracy of small-scale test results. The specimens included 1/12.5-scale models of two interior and two exterior beam-column joints, a seven-storey isolated shear wall, and a seven-storey frame-shear wall system. The specimens represented scale models of prototype buildings or full-scale components previously tested as part of a US-Japan cooperative research project. The microconcrete mix comprised of Type III cement, three sizes of sand with a maximum aggregate size of 2.4 mm, and water. Uniaxial compressive strength tests were conducted on 51 mm by 102 mm (2” by 4”) concrete cylinders to obtain the stress-strain relationship. While the stiffness and peak strength of microconcrete was greatly higher than the prototype concrete, no further effort was made to modify the microconcrete mix. Three sizes of wires with 0.726 mm, 1.57 mm, and 1.83 mm diameters were used to represent the reinforcement. To simulate the bond behaviour and produce a flat yield plateau in the stress-strain response, a series of surface treatments and heat treatment processes were carried out. The stress-strain response of wires obtained from uniaxial tensile tests correlated reasonably well with the behaviour of prototype reinforcements.

The study concluded that, in general, the behaviour of all model specimens was similar to that observed in the prototype structures. In the beam-column joint specimens, the small-scale tests accurately captured the shape of the hysteresis loops. There was a tendency to overestimate the stiffness and strength which was attributed to the difference in the concrete material behaviour. The strain measurements at the interface of the column and beam showed that the similitude models were able to adequately capture the bond deterioration. In the frame-wall specimen, the damage mode was also similar to that observed in the prototype structure. Both small-scale and prototype structures exhibited considerable concrete spalling at the bottom of longitudinal beams and at the base of boundary columns. In the prototype wall, severe cracking and spalling was observed over the height of the first storey, but in the model the wall damage was concentrated at the base leading to some sliding. Although the crack patterns of all the model specimens were similar to the prototype structures, in general, fewer cracks with wider spacing were observed in the model tests. From the comparison of the shear wall results with other similar studies, the authors concluded that the rate of reduction in the number of observed cracks reduced as the scaling factor increased. Figure 5.1 shows the relationship between the number of cracks in the boundary elements of the first storey shear wall and the scaling factor. Therefore, care should be taken in small-scale testing of structures in which crack spacing is critical in determining the behaviour.

Kim et al. (1988) performed a series of tests at both the material-level and structural-level to improve the modelling techniques of small-scale reinforced concrete structures. At the material-level, four types of microconcrete mixes with different aggregate gradations and mix ratios were cast in 51 mm by 102 mm (2” by 4”) cylinders. Type III cement was used for its rapid curing rate and its finer grinding compared to Type I cement as desired for similitude considerations. Two different sizes of sand were used for aggregate gradations: “model gravel” with maximum size of 4.75 mm and “model sand” with maximum size of 2.8 mm. To determine the microconcrete properties, uniaxial compressive strength tests and tensile splitting tests were conducted and the results were compared against the behaviour of a reference prototype concrete. It was concluded that by using proper aggregate gradation and aggregate-to-cement ratio, an adequately low tensile strength can be achieved without major reduction in the compressive stiffness and strength. The study also assessed the behaviour of four types of model reinforcement with different bond characteristics: smooth wires, commercially deformed wires, standard deformed wires, and threaded rods. Based on the results of tensile tests, several recommendations were made to perform a proper heat treatment process to achieve the desired yielding strength and ductility.

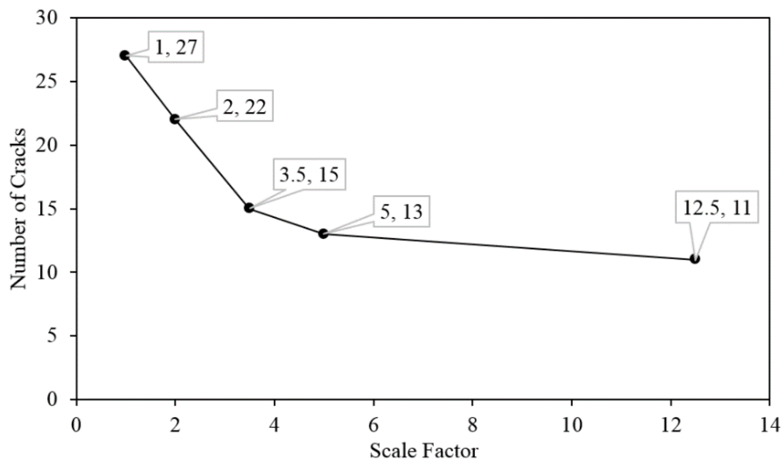

Figure 5.1 Influence of scaling effects on number of cracks in the boundary elements of a first-storey shear wall (Wallace and Krawinkler, 1985)

In the structural-level study, using the above-mentioned material models, the bond behaviour between the model concrete and the model reinforcement was evaluated through testing a series of 1/6-scale cantilever beam specimens with cross section dimensions of 38 mm by 51 mm subjected to a reversed-cyclic loading condition. The specimens were designed to be flexure-critical and represented a half-span of a beam in a frame structure carrying lateral loads. It was concluded that the crack pattern and load-deflection response of the small-scale specimen constructed with threaded rods correlated well with the prototype test results. The small-scale model slightly underestimated the pinching effect compared to the prototype structure. Figure 5.2 illustrates the crack pattern of the specimens with different types of model reinforcement.

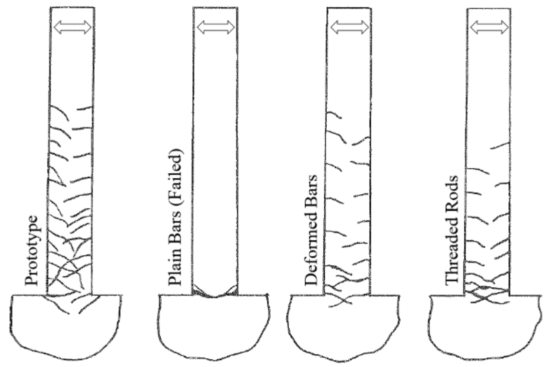

(a) Ductility Factor = 2.0

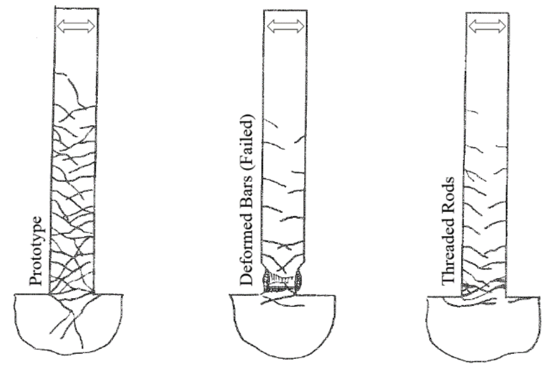

(b) Ductility Factor = 4.0

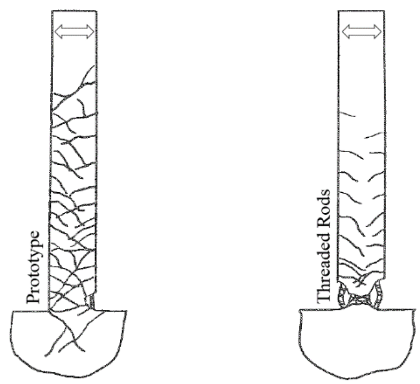

(c) Ductility Factor = 6.0

Figure 5.2 Influence of type of model reinforcement on the crack pattern (taken from Kim et al., 1988)

Lu et al. (1999) tested a series of reinforced concrete columns, constructed on three different scales (1/2, 1/3, and 1/5.5), under a reversed-cycle loading condition. The primary objective of the study was to evaluate a recommendation made by Abrams (1987) that the scaling factor for testing reinforced concrete structures should not be less than 1/4. Also, the influences of axial load level and confinement due to transverse reinforcement in small-scale testing were investigated. The maximum aggregate size used for normal concrete (1/2- and 1/3-scale specimens) was 25 mm, and for microconcrete (1/5.5-scale specimens) it was 5 mm. According to the tensile splitting and uniaxial compressive strength test results, the microconcrete exhibited a similar tensile strength as the normal concrete but the compressive peak strength was underestimated. The longitudinal reinforcement was represented using three sizes of deformed bars. A heat treatment process was used to attain a similar stress-strain relationship for all the reinforcing bars. The specimens were subjected to a constant axial load applied at the bottom of the column and a reversed-cyclic transverse displacement was imposed at the mid-height of the column. Overall, all the specimens, regardless of their scale, exhibited comparable load-deflection responses and crack patterns. The small-scale tests resulted in a lower number of cracks which were more concentrated near the mid-height of the specimen compared to the large-scale columns. This was mainly attributed to the insufficient bond strength between the small reinforcing bars and the microconcrete because of its lower compressive strength compared to the normal concrete. Table 5.2 and Figure 5.3 present the specimen details and observed crack patterns.

Table 5.2 Details of the RC column specimens

Test Specimen	Scale Factor	ρ_v (%)	P/P_o
C2H1	1:2	0.28	0.07
C2L1	1:2	0.12	0.07
C3H2	1:3	0.28	0.20
C3L2	1:3	0.12	0.20
C5H1	1:5	0.28	0.07
C5L1	1:5	0.12	0.07
C5H2	1:5	0.28	0.20
C5L2	1:5	0.12	0.20

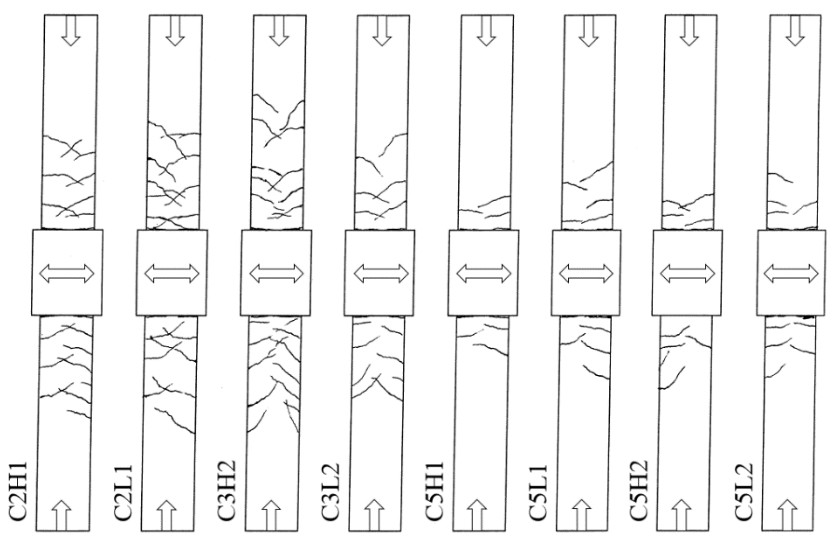

Figure 5.3 Crack pattern of RC column specimens (taken from Lu et al., 1999)

5.2.2 Influence of Scaling-Effects on Shear Behaviour

Generally, with reinforced concrete structures, scaling has more pronounced effects on the shear behaviour than on the flexural behaviour. The primary parameters that influence the flexural behaviour are the yield strength of the reinforcing bars and the compressive strength of the concrete, both of which can be accurately simulated in reduced-scale models if proper procedures are used in the material preparation and specimen construction. However, the mechanisms involved in shear behaviour are more complex and relate to variables which are more sensitive to size effects such as concrete fracture, crack spacing, and aggregate interlock. Therefore, caution should be used when small-scale testing procedures are applied to shear-critical concrete structures.

Several studies demonstrated that the shear stress at failure for concrete members without stirrups decreased as the member size increased (Kani, 1967; Shioya, 1989; Bazant and Kazemi, 1991; Collins and Kuchma, 1999; among others). Shioya (1989) conducted an extensive experimental study on a series of beam specimens with effective depths ranging from 100 mm to 3000 mm and three different maximum aggregate sizes (2.5 mm, 10 mm, and 25 mm); the beams contained no shear reinforcement. The study concluded that the shear stress at failure reduced as the beam depth or maximum aggregate size increased. The main results of the study are summarized in Figure 5.4. Collins and Kuchma (1999) also performed a comprehensive test program on a series of simple span and continuous beams with light amounts of flexural reinforcement to investigate the factors influencing shear strength. The main test variables were member depth (varying from 125 mm to 1000 mm for simple span beams and from 500 mm to 1000 mm for continuous beams), longitudinal reinforcement ratio, and concrete compressive strength. The test results confirmed the findings of previous studies that, for beams without stirrups, as the member became deeper the shear stress at failure reduced. For beams with high strength concrete, this reduction was more noticeable due to their smooth crack surfaces. However, beams which had minimum shear reinforcement or distributed longitudinal reinforcement (i.e., crack control reinforcement) did not show any reduction in shear stress at failure and were not sensitive to size effects. The minimum required shear reinforcement was computed according to the MCFT theory (Vecchio and Collins, 1986) which has been the basis of the shear design provisions of the AASHTO LRFD Bridge Design

Specifications (2012) and the Canadian Standard Association for the "Design of Concrete Structures" (CSA-A23.3) (2014). Also, the study found that the beam width did not have any influence on the shear stress at failure of the beams. Figure 5.5 and Figure 5.6 present the main findings from the test results of simple span and continuous beams, respectively.

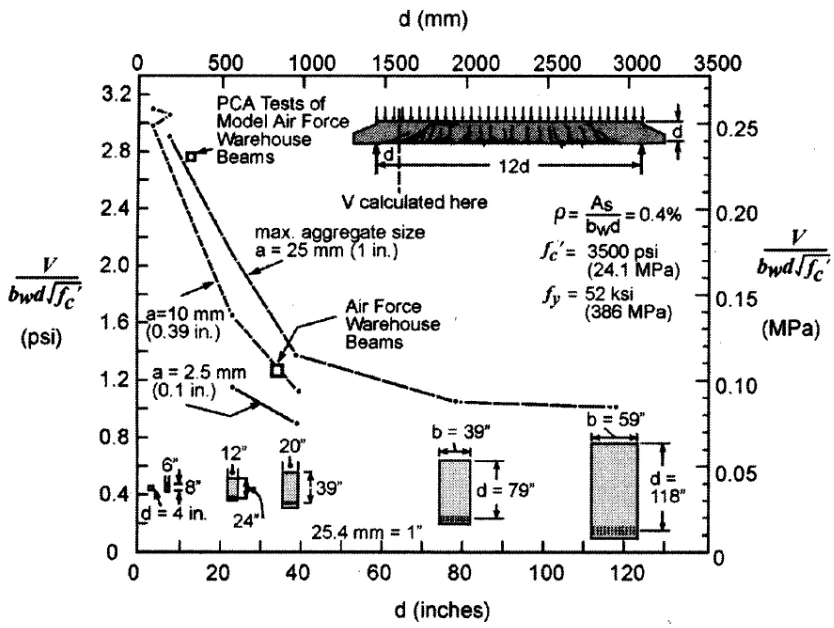

Figure 5.4 Influence of member depth and maximum aggregate size on shear stress at failure of RC beams without stirrups (taken from Collins and Kuchma, 1999)

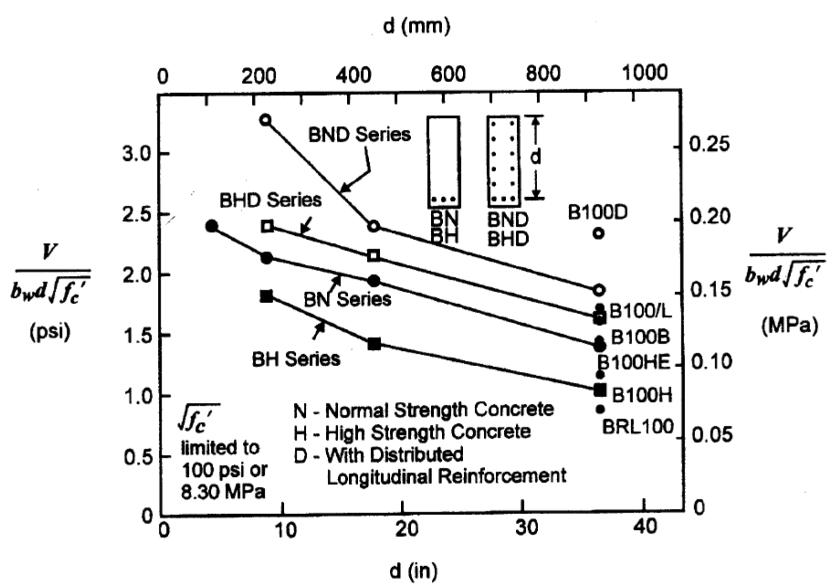

Figure 5.5 Influence of beam depth on shear stress at failure (taken from Collins and Kuchma, 1999)

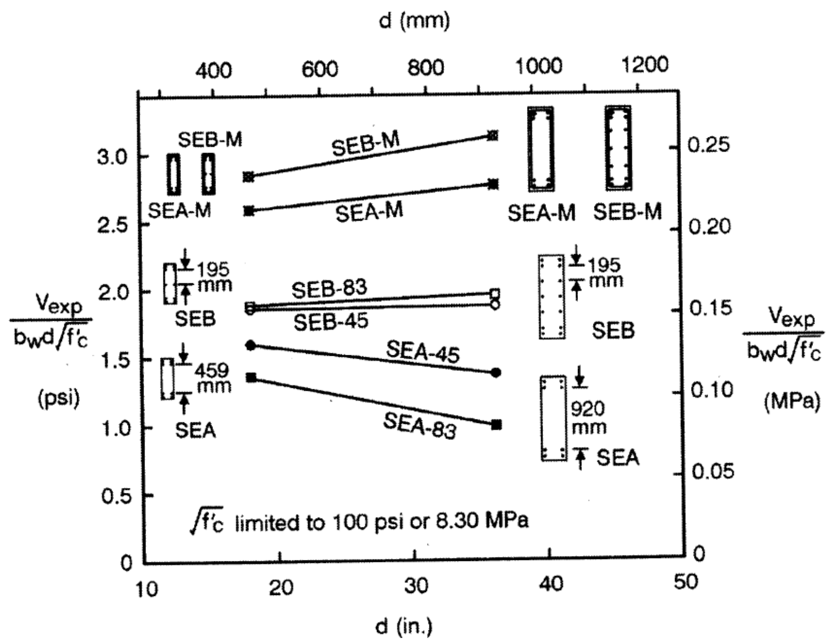

Figure 5.6 Influence of spacing of longitudinal reinforcement and presence of stirrups on size effect and shear stress at failure (taken from Collins and Kuchma, 1999)

The above-mentioned studies mainly focused on the influence of size effects on the shear behaviour of beams which were deeper than 100 mm and did not have stirrups. Other researchers performed similar studies on other types of shear-critical members. McDaniel (1997) compared the shear strength of 1/3-scale reinforced concrete column models with the capacity of a similar full-scale bridge pier. The columns were designed to be shear-critical with a transverse reinforcement ratio of 0.1%. The concrete and reinforcement were properly scaled to produce similar stress-strain behaviour as the prototype materials. The load-deflection responses obtained from the full and reduced-scale tests were sufficiently close.

Ohtaki (2000) tested a series of shear-critical reinforced concrete columns with a rectangular cross section under a reversed-cyclic loading condition in three different scales: one full-scale specimen, two 1/2-scale specimens, and three 1/4-scale specimens. The test variable was the maximum size of the aggregate (5 mm, 10 mm, and 20 mm). While for the large-scale and medium-scale specimens the concrete compressive strength was close to the target compressive strength (30 MPa), for the small-scale specimens the concrete compressive strength was higher ranging from 35 MPa to 48 MPa. The longitudinal and transverse reinforcement ratios were 1.82% and 0.07%, respectively. The transverse reinforcement ratio was slightly lower than the minimum shear reinforcement specified by the CSA-A23.3 ($\rho_{v,min} = 0.09\%$). The longitudinal reinforcement was represented with deformed bars which were scaled accordingly and had similar yielding strength for all the specimens. In general, the load-deflection response and crack pattern of the scaled specimens agreed well with the full-scale test results. Except for one small-scale specimen, which had a very high concrete compressive strength, all other specimens exhibited a shear failure before yielding of the longitudinal reinforcement. The shear strength of the small-scale specimen with 5 mm maximum aggregate size (scaled according to the similitude laws) had the best correlation with the prototype shear strength. However, because of the variation in the concrete compressive strength, it was difficult to draw any conclusions. According to the crack inclination and width measurements, the shear strength degradation of the full-scale column started at earlier load stages than the scaled columns. Also similar to most previous small-scale studies, as the scale of the specimen reduced, fewer cracks with wider spacings were observed. Details of the test specimens and main findings of the study are summarized in table 5.3 and Figure 5.7 to Figure 5.9, respectively.

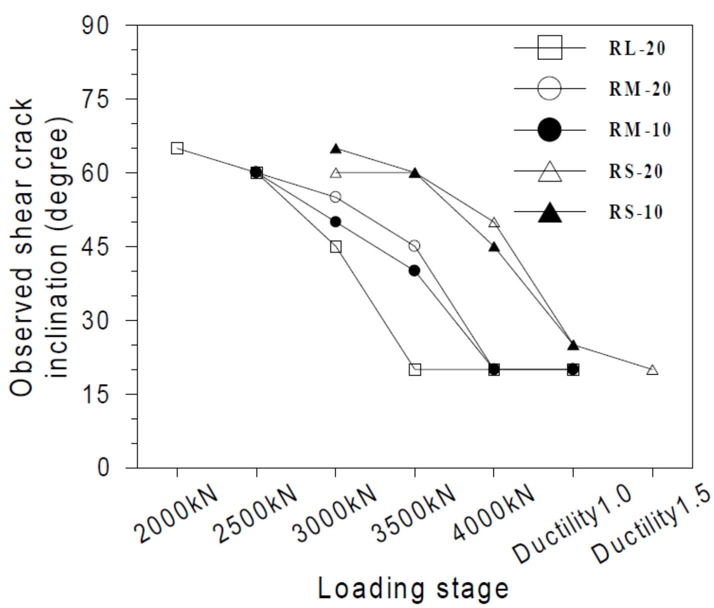

Figure 5.7 Influence of size effects on shear crack inclination (taken from Ohtaki, 2000)

Table 5.3 Details of the RC column specimens

Test Specimen	Cross Section (mm × mm)	f_c' (MPa)	Max. Agg. Size (mm)
RL-20	2000 × 2000	29.7	20
RM-20	1000 × 1000	30.9	20
RM-10	1000 × 1000	32.1	10
RS-20	500 × 500	43.1	20
RS-10	500 × 500	48.4	10
RS-05	500 × 500	35.3	5

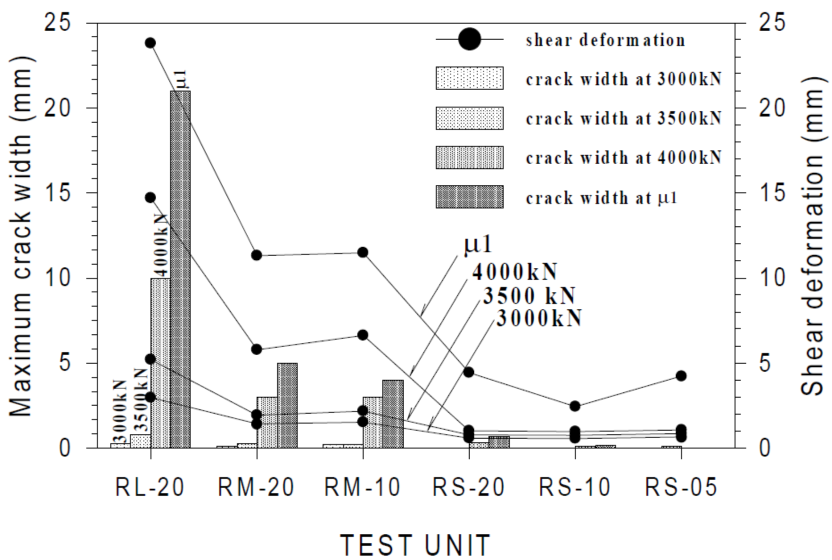

Figure 5.8 Maximum crack width for different RC columns (taken from Ohtaki, 2000)

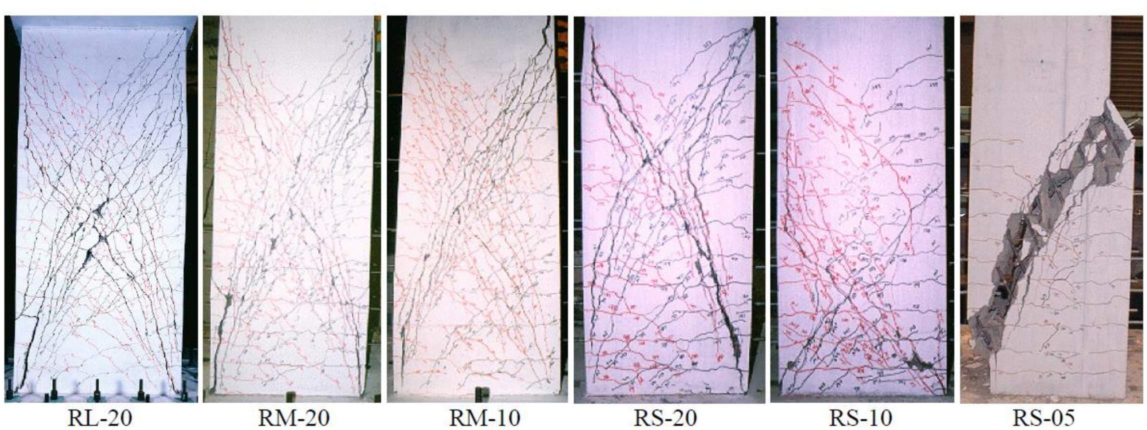

Figure 5.9 Influence of size effects on crack pattern of columns (taken from Ohtaki, 2000)

Ghorbani et al. (2009) investigated the influence of size effects on the behaviour of shear walls by testing two large-scale and two 1/2.37 reduced-scale specimens subjected to monotonic and reversed-cyclic loadings. The maximum aggregate size was selected as 14 mm and 5 mm for the large-scale and reduced-scale specimens, respectively. To properly simulate the bond characteristics, deformed bars were used for all reinforcement in the horizontal and vertical directions. Based on the material test results, the properties of the reinforcement were similar in the both prototype and scaled specimens, whereas the model concrete exhibited significantly higher compressive strength than the prototype concrete (47 MPa versus 28 MPa). An actuator was attached to the top of the wall specimen to control the horizontal displacement. No external axial load was considered on the specimen. Both the large-scale and reduced-scale walls exhibited a ductile flexural response which was followed by large inelastic shear deformations and strength degradation due to shear sliding occurred along the base of the wall. The load-deflection response of the model specimen correlated well with the prototype results. The model specimen slightly overestimated the elastic stiffness which was attributed to the higher compressive strength of the microconcrete. The strength reduction started earlier and was more gradual in the model specimen compared to the prototype specimen.

5.2.3 Hybrid Simulation of Small-Scale Specimens

The concept of hybrid simulation was originally developed by Japanese researchers in 1960s, but the present form of the method was established in the mid 1970s led by Takanashi et al. (1975) mainly for dynamic simulations. The primary tactic in the hybrid simulation method is to divide the structure into two components: a numerical model and a physical model. The numerical model accounts for the dynamic effects and computes the displacements of the entire structure. The displacements are then imposed on the physical model which is a test specimen with the strength and stiffness characteristics of a critical part of the structure. Considering dynamic effects in the computer model enables the use of a conventional quasi-static loading system in the experimental portion. Over the last few decades, the method has come to be considered an economical and practical alternative means to shake table testing in providing a realistic response of the structure under seismic loads, attracting extensive research interests (Dermitzakis and Mahin, 1985; Takahashi and Fenves, 2005; among others).

The hybrid simulation method can also improve the assessment of the behaviour of deficient or deteriorated reinforced concrete structures. Since testing the entire structure with several deficient parts is impractical and prohibitively expensive, most conventional tests are limited to the component-level behaviour, neglecting the influence of other parts of the structure. Conversely, in the hybrid simulation technique, the integration of computer models with physical test specimens provides a realistic simulation of load redistribution between different structural elements, resulting from inelastic material behaviour (e.g., cracking of concrete or yielding of reinforcement), strength degradation, or failure of one part of the structure.

In recent years, application of hybrid simulation to small-scale testing was the focus of several research studies. The main benefit of performing a small-scale test in a hybrid simulation manner is that the scaling effects are only applied to the physical component while the rest of the structure is numerically modelled in full-scale. With a proper integration of the small-scale physical component and prototype numerical component, a more accurate response of the structure can be obtained compared to conventional small-scale testing. The following is an overview of the previous small-scale hybrid simulations on reinforced concrete structures with deficient members.

Kim et al. (2004) developed a modified similitude law for small-scale testing of reinforced concrete structures which attempted to consider inelastic material behaviour and also account for dissimilarities between the material properties of the microconcrete and prototype concrete. Based on a series of compressive strength tests, equivalent stiffness modulus ratios (S_e) between microconcrete and normal concrete were evaluated and defined in multi-phase damage levels. The equivalent modulus ratios were implemented in a hybrid simulation algorithm. At each load stage of hybrid testing, the scale factor was adjusted according to the current state of S_e. The accuracy of the method was evaluated through testing three prototype and six 1/5-scale column specimens. Two types of S_e were examined (constant and variable). However, the composite nature of reinforced concrete introduced several challenges in defining S_e. Also, the preliminary quasi-static tests showed that the small-scale tests based on the variable S_e could not accurately capture the prototype behaviour, particularly under high damage levels.

Holub (2009) performed a comprehensive experimental study to investigate the effects of variable and tensile axial loads on the response of circular bridge piers subjected seismic loading. The study consisted of two large-scale columns with constant and variable axial loads tested in the hybrid simulation manner, two large-scale columns with constant compressive and tensile axial loads tested under quasi-static loads, and a large number of 1/10-scale specimens. The intent was to examine the scaling effects and provide more insight into the structure behaviour. The cross section of the small-scale columns had a diameter of 70 mm. In the hybrid simulations, the physical model represented a pier of a reinforced concrete bridge structure comprised of three spans (30.5 m, 36.6 m, and 30.5 m) and a box girder deck with two interior webs. The rest of the structure was modelled in a nonlinear frame analysis program, Zeus-NL (Elnashai et al., 2008). The physical and numerical models were integrated using a hybrid simulation framework named UI-SIMCOR (Kwon et al., 2008). Figure 5.10 shows the reference bridge structure including numerical and physical components.

As a preliminary study, similitude considerations for scaled hybrid testing were reviewed and a large number of material tests were carried out to provide the desired stress-strain responses (Holub, 2005). To properly model the concrete, compressive strength and tensile splitting tests were conducted on eight types of microconcrete mixes and the results were compared against the response of a reference prototype concrete. To simulate the reinforcement, several types of wires and threaded rods were heat treated and tested under uniaxial tension to obtain an acceptable yielding strength and ductility. The bond characteristics and strain hardening region of the reinforcement response were not investigated. Based on the test results, threaded rods and smooth wires were chosen to represent the longitudinal and transverse reinforcement, respectively.

One of the objectives of the study was to examine the shear behaviour of the piers. To minimize the size effects on the shear response, all the specimens contained continuous spirals with volumetric ratios ranging from 0.3% to 0.9%, higher than the minimum shear reinforcement stipulated by CSA-A23.3. As shown in Figure 5.10, a load and boundary condition box (LBCB) was used to control the translational displacements and rotation at the top of the column specimen resulting from the applied ground motion. The response obtained from the small-scale tests had excellent agreement with the large-scale experiment results in terms of the stiffness, strength, energy absorption, and failure mode. More cracking and damage was observed in the large-scale tests. However, the overall crack pattern including crack inclination was captured in the small-scale tests with sufficient accuracy. In general, the columns subjected to high compressive axial loads experienced a brittle shear failure, while specimens under tensile axial loads showed a relatively ductile flexural failure. Figure 5.11 presents a comparison between the observed crack patterns of the large-scale and small-scale specimens under different loading scenarios.

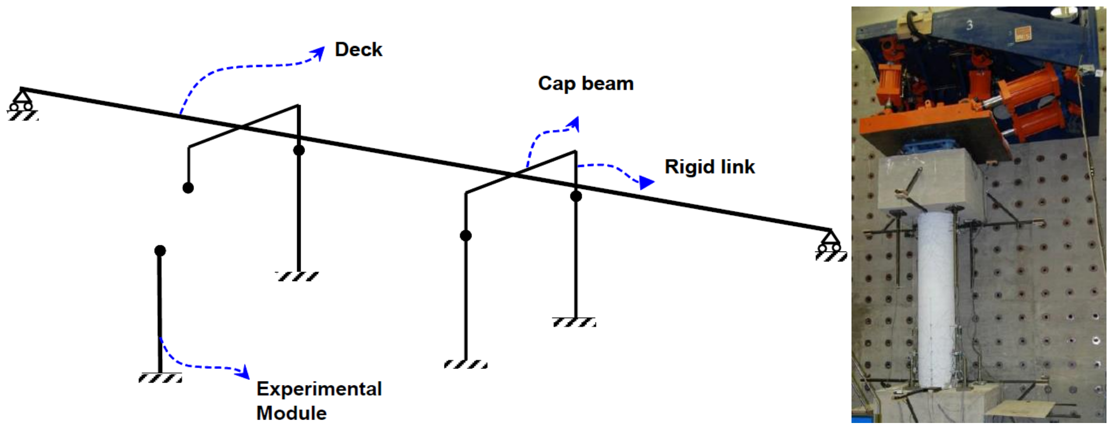

Figure 5.10 Numerical and physical components of the RC bridge (taken from Holub, 2009)

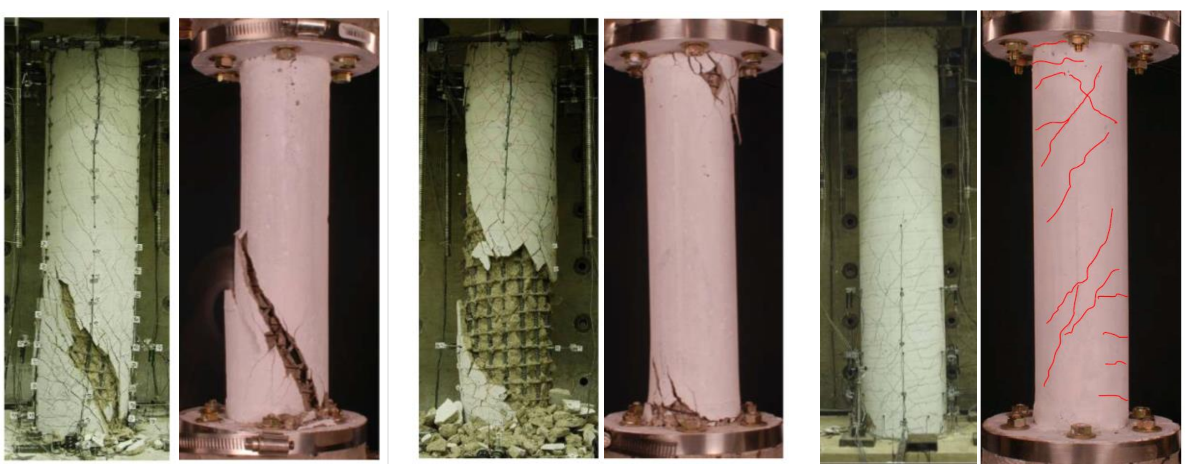

(a) (b) (c)

Figure 5.11 Crack pattern of large-scale (left) and small-scale (right) RC columns under: (a) constant axial compressive force; (b) constant axial tensile force; (c) combined horizontal and vertical excitations (taken from Holub, 2009)

Gencturk and Hosseini (2015) utilized a similar hybrid simulation configuration as that used by Holub (2009) to study the behaviour of 1/8-scale columns constructed from reinforced concrete and reinforced engineered cementitious composite (ECC) materials. Based on the suggestions proposed by Holub (2005), proper considerations were given to preparing the materials in small-scale. The cost-efficient nature of small-scale testing allowed investigating the influence of several parameters including longitudinal and transverse reinforcement ratios, mix designs, and loading scenarios.

Saouma et al. (2014) conducted a real-time hybrid simulation of a non-ductile three-storey three-bay reinforced concrete frame and compared the results with those obtained from a shake table test at the University of California, Berkeley. The frame represented a 1/3-scale representation of a typical 1960s office building in California with a light amount of transverse reinforcement in the columns. Two columns were designed according to old practice to exhibit flexure-shear failure (ρ_v = 0.15% and ρ_l = 2.45%) while the other two columns were designed to be ductile containing adequate shear reinforcement (ρ_v = 1.10% and ρ_l = 1.09%). In the hybrid simulation, one of the flexure-shear-critical columns with cross section dimensions of 152 mm by 152 mm was represented as the physical specimen. The longitudinal and transverse reinforcement were modelled using #3 deformed bars and smooth wires with 3.2 mm diameter, respectively. No information was provided regarding the concrete mix. As shown in Figure 5.12, the top of the column specimen was attached to a strong beam which was connected to a horizontal actuator imposing transverse displacement and two vertical actuators controlling the axial displacement and rotation. The rest of the structure was modelled in a frame analysis program using fibre elements. Rigid elements were used to represent the beam-column joints. Also, the bond-slip effects were simulated using zero length springs located at the ends of the fibre elements. An in-house hybrid simulation framework was used to combine the physical numerical models. Figure 5.12 shows different components of the hybrid simulation.

The drift-time response of the hybrid simulation was within 10% of the response obtained from the shake table test. Also, the two types of tests resulted in reasonably similar failure modes and crack patterns. Discrepancies between the results were mainly attributed to two factors: 1) the difference between the concrete material properties (the concrete compressive strengths of the shake table and hybrid simulations were 24.5 MPa and 29 MPa, respectively) and 2) inability of the analysis procedure to accurately capture the highly nonlinear response of the rest of the frame structure, particularly the damage in the joint panels and shear behaviour of the other flexure-shear-critical column which was modelled numerically. Figure 5.13 shows the crack pattern observed in the shake table and hybrid simulations at failure.

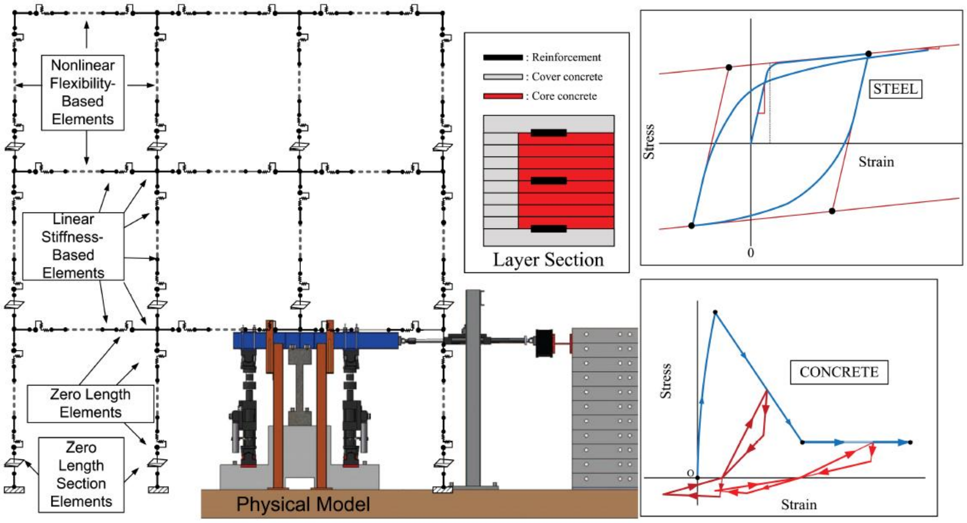

Figure 5.12 Numerical and physical models of RC frame (taken from Saouma et al., 2014)

(a)

(b)

Figure 5.13 Crack pattern at ultimate load stage: (a) shake table test; (b) hybrid simulation (taken from Saouma et al., 2014)

5.2.4 Conclusions

Several other researchers including Caccese and Harris (1990), Panahshahi et al. (1991), and Aycardi et al. (1994) also examined the reliability of small-scale testing of reinforced concrete structures and found similar results to those described in the aforementioned studies. Based on the reviewed literature, the following conclusions can be drawn regarding the small-scale testing of reinforced concrete structures:

- For RC members containing at least the minimum shear reinforcement as specified by CSA-A23.3, if standard similitude laws are imposed and proper procedures are used in material preparation and specimen construction, acceptable results can be obtained from small-scale tests regardless of the scaling factor, member type, failure mode, loading scenario, or testing method. Based on the literature review, the minimum reported scale factor was 1/10 (diameter of model columns was 70 mm) used in the experimental program carried out by Holub (2009). It should be noted that the scale factor is a relative parameter representing the ratio between the dimensions of the prototype and model specimens. A better measurement of the scaling effects can be obtained by comparing the absolute dimensions of the specimens rather than the scaling factors.

- In some of the earlier studies (e.g., Abrams, 1976), the discrepancies observed between the small-scale and prototype test results, particularly at high damage levels of the response, were mainly attributed to the use of mortar and smooth wires to represent concrete and longitudinal reinforcement, respectively, which had dissimilar material properties compared to the prototype structure.

- In general, microconcrete exhibits a higher tensile strength and lower compressive stiffness and strength compared to a normal concrete with a similar mix design. Special considerations should be given to the aggregate gradation and aggregate-to-cement ratio of the microconcrete to produce a similar stress-strain response as normal concrete. A more detail explanation of these considerations are provided in the Microconcrete Preparation section (Section 5.6.2) of this chapter.

- To simulate the reinforcement in small-scale, in most instances, heat treatment procedures are necessary to achieve the desired yield strength and ductility. To properly model the bond behaviour between the concrete and reinforcement, deformed bars or threaded rods should be utilized to represent the longitudinal reinforcement. A few studies found that for some particular types of failures, the strain hardening state of the small-scale reinforcement response was critical, recommending specific remedies to accurately model the behaviour of this region.

- While most small-scale tests resulted in a similar crack pattern and final crack inclination as that observed in the large scale tests, in general, the small-scale specimens exhibited a lower number of cracks with more concentrated damage zones compared to the large-scale specimens. However, it was found that the rate of the reduction in number of observed cracks reduced as the scaling factor increased. Thus, the distortion in crack spacing has less influence when small-scale tests are compared with medium-scale tests than when medium-scale tests are compared against large-scale tests.

- Compared to the flexural behaviour, the variables influencing the shear behaviour such as concrete fracture, crack spacing, and aggregate interlock are more sensitive to size effects. Therefore, caution should be used when small-scale testing procedures are applied to shear-critical concrete structures.

- Existing studies found that, for beams without stirrups, as the member became deeper the shear stress at failure reduced. For beams with high strength concrete, this reduction was more noticeable due to their smooth crack surfaces. However, beams which had minimum shear reinforcement as stated by CSA.A23.3 or distributed longitudinal reinforcement (i.e., crack control reinforcement) did not show any reduction in shear strength and were not sensitive to size effects. Small-scale tests on other types of shear-critical members including columns and shear walls which contained the minimum shear reinforcement resulted in similar findings.

- Compared to conventional test methods, performing a small-scale test in a hybrid simulation manner can improve the accuracy of the results since the scaling effects are only applied to the physical model and the interaction of the specimen with the remainder of the structure is taken into account using a numerical model in full-scale. This requires the use of a detailed finite element analysis software which is capable of accurately considering local behaviour in reinforced concrete such as bond-slip effects and stresses at the crack, second-order material effects, a proper simulation framework to integrate the physical and numerical models, and a realistic representation of the interface between the substructures in both the computer models and boundary conditions of the test setup.

5.3 Hybrid Simulation Components

5.3.1 Simulation Framework

The proposed multi-platform simulation framework Cyrus, which was primarily developed to integrate various types of numerical models, was further extended to accommodate hybrid testing. A comprehensive discussion of the framework is provided in Chapter 2. Hybrid tests were conducted based on the Modified Newton Raphson procedure implemented in the simulation framework (similar to the Module Type 2 described in Section 2.3.2 of Chapter 2). Because dynamic effects were not considered in this study, a numerical time integration scheme was not required. Several iterations were performed at each load stage to fulfill the compatibility and equilibrium requirements between the test specimen and numerical models. To reduce the communication data between the simulation framework and numerical models, only the equivalent restoring forces and displacements at the interface DOFs were transferred. The equivalent values were computed by performing a static condensation procedure which eliminated the displacements and forces of the internal DOFs. Unbalanced forces resulting from the nonlinear behaviour of the test specimen were calculated based on the initial stiffness and measured force reactions. The initial stiffness of each test specimen was estimated using the measured elastic modulus of the related microconcrete. The initial stiffness was increased by 10% to avoid underestimating the actual stiffness of the specimen and divergence of the nonlinear solution. The initial stiffness estimation was deemed reasonable since no fluctuation was observed in the measured reactions and load-deflection response of the system. The accuracy of the imposed displacements at the specimen control point and the potential relative deformations of the concrete end blocks with respect to the end steel plates were monitored using a 3D scanner and external LED targets. Figure 5.14 shows an overview of the proposed hybrid simulation configuration and its components.

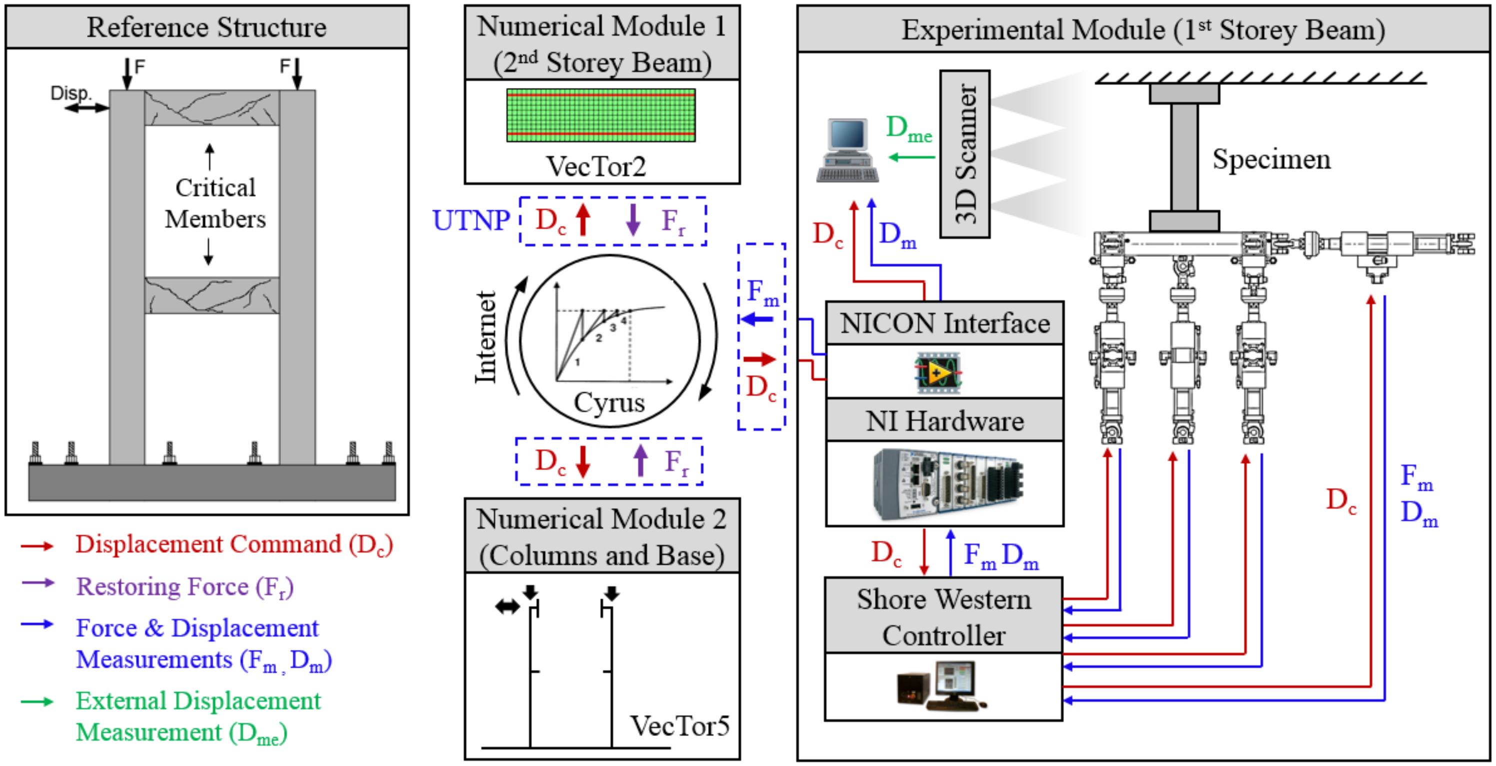

Figure 5.14 Overview of the proposed hybrid simulation configuration and its components

5.3.2 Interface Program

One of the essential components of a hybrid simulation is an interface program between the actuator controller and the simulation framework. In most previous hybrid tests, the interface program was developed for a specific test configuration which makes it difficult to adopt the program to other experiments with different specimen orientations, control point positions, or number of control DOFs and actuators. In 2005, Takahashi and Fenves used the object-oriented approach to develop a more flexible hybrid simulation framework in which, depending on the test configuration, only a specific class containing all the test setup information required modifications. In this study, Cyrus was connected to a generalized controller interface program named the Network Interface for Controllers (NICON) (Zhan and Kwon, 2015) applicable to a wide range of test configurations. NICON was developed based on the LabView programming software and the National Instrument (NI) hardware. The main capabilities of NICON which are utilized in this experimental study are presented briefly in the following. A more detailed description of each part is provided in Zhan (2015).

- *Network Command:* This feature allows NICON to communicate with the simulation framework through the Internet network. NICON can receive commands (e.g., initiate or terminate a test) and target displacements from the simulation framework and can send back the measured forces and displacements.

- *User Input Command:* This feature enables the user to directly impose displacement commands to each individual actuator. It can be used for actuator calibration or mounting the specimen on the loading platform.

- *Coordinate System Conversion:* In multi-axial hybrid simulation, multiple actuators are used to control coupled DOFs of a specimen (e.g., a member under axial and lateral forces and moment). The displacement commands received from the simulation framework are in the Cartesian coordinate system of the numerical model and should be transformed to the loading platform coordinate system and then the actuator strokes (forward conversion). Also, the measured displacements and forces from the actuators should be converted back to the loading platform coordinate system and then the Cartesian coordinate system of the numerical model (backward conversion). In NICON, the coordinate transformations are performed according to an iterative approach developed by Nakata et al. (2010). The procedure is based on the Newton-Raphson method and takes into account the geometric nonlinearity of the test setup. It is implemented in a generalized form to support various test setup configurations such as single DOF, three coupled DOFs, six coupled DOFs, and ten uncoupled DOFs.

- *Conversion of Relative Motion:* In hybrid simulations, where the physical specimen is a beam, brace, or an upper-level column, DOFs at both ends of the member should be controlled. However, because of loading equipment limitations, it is more practical to fix one end of the specimen and impose the relative motion at the other end. NICON can compute the relative deformation of the specimen based on the rigid body motion.

- *Command Loop:* At the beginning of the simulation, the current measured displacements are assigned to the input commands to prevent any sudden movement in the actuators, protecting the specimen and actuators. To impose command displacements, a timed loop is continuously executed in which the command displacements and the increments of displacements from the previous load step are checked against the limits specified for the actuator strokes and displacement increments, respectively. If the command fails to pass either of the checks, it is corrected to fall within the limit range, the simulation mode is set to manual, and an error message is shown to the user. The verified commands are then sent to a ramp and hold generation function which gradually changes the actuator strokes to reach the target displacements. Two types of ramp functions are available in the program: a linear function and a sine wave function. To avoid force relaxation in the actuators, the hold phase can be eliminated. However, in situations where the new commands cannot be obtained before the end of the ramp phase, the hold phase is essential (e.g., geographically distributed tests or tests which contain computationally expensive numerical models). At each ramp stage, the program generates analog voltage commands, equivalent to the displacement ramp values, and sends them to the actuator controller. The command displacement limits, ramp and hold durations, and update rate of the command loop are defined by the user.

- *Measurement Loop:* A timed loop is repetitively executed to collect the measured voltage signals. In this loop, first a low pass filter is used to filter out the background noise from the measured voltage. Then, based on the calibration factors, the voltage values are converted to displacements in millimeters and forces in Newtons. The measured forces and displacements are checked against predefined limits before being sent to the simulation framework.

- *Data Logging:* This feature records displacement commands and measured forces and displacements in both the global and actuator coordinate systems at a predefined logging rate.

In this study, several modifications were made to NICON to improve its performance and facilitate hybrid testing. The changes and new features are described in the following:

- *Coordinate System Conversion Verification:* Different parts of the coordinate system transformation, including the forward conversion of displacement commands and the backward conversion of displacement and force measurements, were examined using a MATLAB code. In the force conversion, the sign convention of the equations at the control point of the loading platform required modification. Details of the equations are presented in Section 3.3.1.2 of Zhan (2015).

- *Force Equilibrium in Relative Motion:* As explained before, NICON is capable of considering the relative motion between the two ends of a specimen. Based on the equilibrium conditions in the specimen, the equations for calculating the forces and moments at the fixed end of the specimen were added to the program.

- *Global User Input Command:* The existing User Input Command was limited to control each actuator separately. The Global User Input Command enables the user to manually control the movement of an arbitrary reference point with respect to a predefined coordinate system. This feature is particularly useful in mounting the specimen on loading platforms with multiple actuators. Figure 5.15 shows the Global Displacement Input Command option which is located under the User Input tab in the main front panel of NICON.

- *Set Offset and Lock User Input:* After adjusting and fixing the specimen on the loading platform, the actuator strokes are different than the initial zero position. Also because of the self-weight and small forces generated due to restraining the specimen, the actuator load cells record nonzero force values. By clicking on the Set Offset button, the program stores the current position of the actuators and the measured forces as the displacement and force offsets, respectively. During the test, the actual displacement commands are computed by subtracting the displacement offsets from the input displacement commands obtained from the numerical model. Similarly, the offset values are considered in determining the actual displacement and force measurements. The Lock User Input option changes the type of input command from the manual command to the network command to initiate the hybrid simulation. Figure 5.16 shows the offset force and displacement arrays and the Set Offset and the Lock User Input buttons located under the Network tab of the main front panel of NICON.

- *Ramp and Hold Limit Check:* During the calibration phase of the loading platform some random jumps were observed in the actuator strokes which were attributed to a problem with the time step definition in the Ramp and Hold function. To avoid any fluctuation in the command and to ensure that the increment of displacements from the previous ramp values are within a specific limit, a new set of limit checks were added at the last step of the command loop located after the Ramp and Hold function and before converting displacements to equivalent voltages. If the ramp value fails to pass the increment check, it is corrected to fall within the limit range, and then converted to the equivalent voltage. Figure 5.17 shows the block diagram of the displacement limit checks.

Figure 5.15 Global Displacement Input Command on the main front panel of NICON

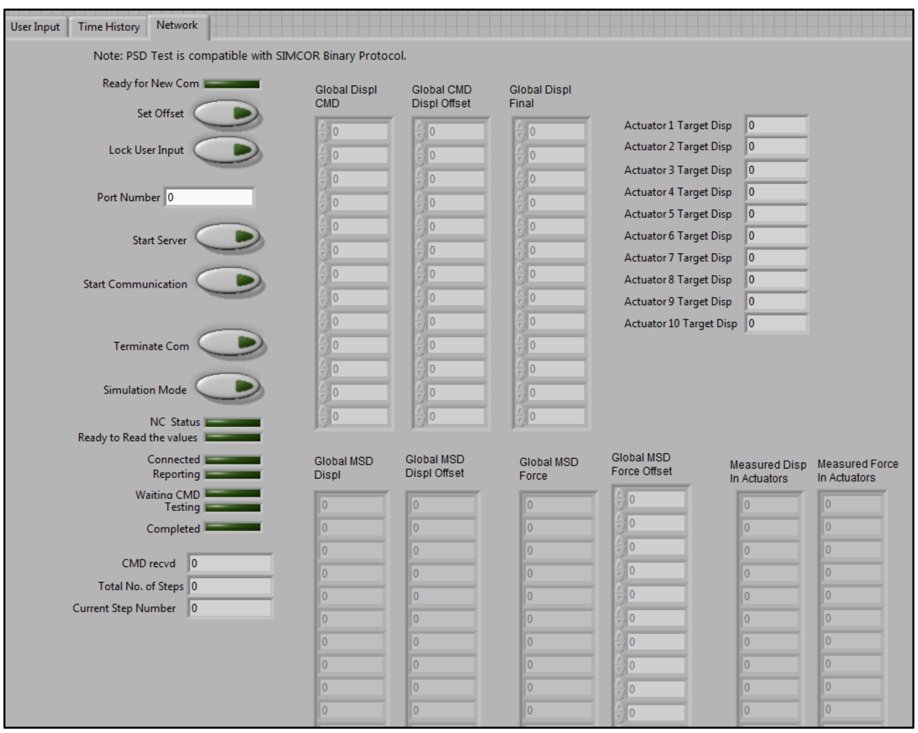

Figure 5.16 Offset arrays and the Set Offset and the Lock User Input buttons under the Network tab of the main front panel

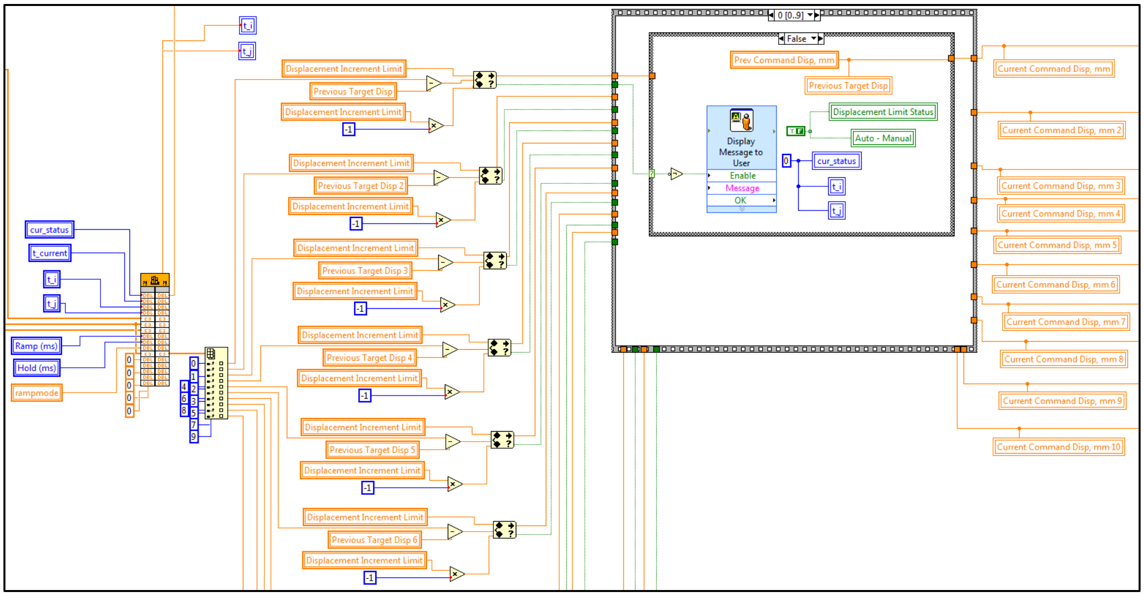

Figure 5.17 Ramp and Hold function displacement limit checks

The communication between the NICON interface program and the actuators controller was established through analog I/O (i.e., input/output) signals using hardware from National Instruments named CompactRIO. The analog I/O communication approach was used for two main reasons: 1) most actuator controllers can exchange data (receive commands and send measurements) with an external source using analog signals and 2) the hardware required to generate and read analog signals is more economical compared to other communication methods. This approach requires D/A (i.e., digital to analog) and A/D (i.e., analog to digital) conversion processes, but for real-time hybrid simulation the time lag of these processes are negligible. Another means of communication is to use controllers with SCRAMNet cards which allow the integration module to directly access the same memory address as the controller. This approach, however, requires proprietary SCRAMNet cards and controllers, which are more costly compared to the analog I/O communication method.

To provide the analog I/O communication between the NICON and actuators controller, a NI hardware box was assembled which contained the following parts:

- *NI cRIO-9022*: a high performance real-time controller with 2 GB memory storage and a high speed USB port connection.
- *Chassis*: a base frame which can hold up to eight NI I/O modules.

- *NI 9264 Module:* an analog output module with 16 differential channels and ± 10 volts range.
- *NI 9205 Module:* an analog input module with 16 differential channels and ± 10 volts range.
- *BNC connectors*
- *Power supply*

As shown in Figure 5.18, the NI hardware box was wired to the actuators controller (the Shore Western controller). Because the setup was intended to control a 6-DOF system, it required six channels of command outputs to the controller (displacements) and twelve channels of measured inputs from the controller (displacements and reaction forces). Also, four additional input channels were placed to record external measurements.

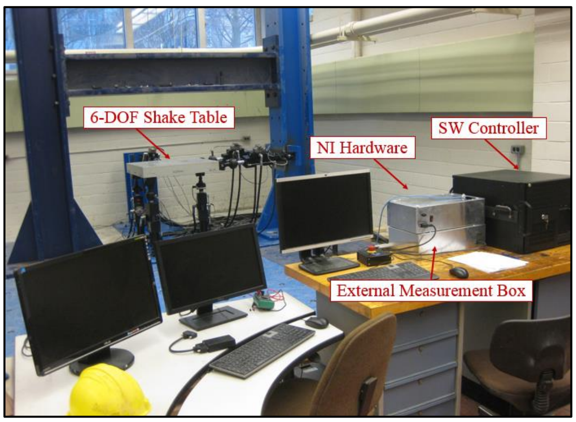

(a)

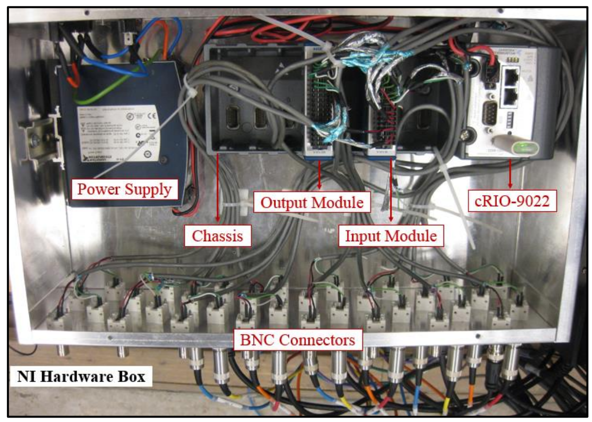

(b)

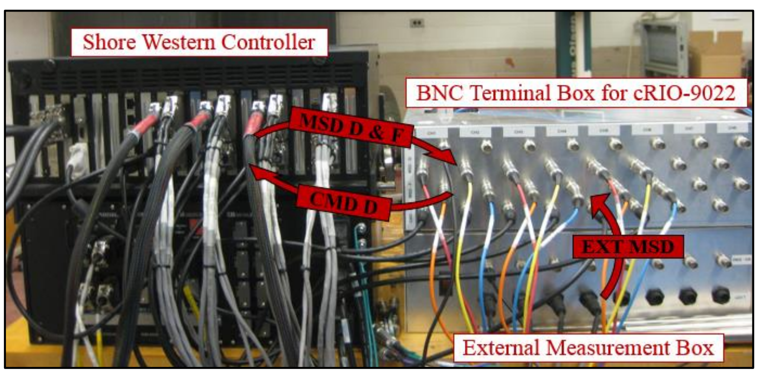

(c)

Figure 5.18 Different parts of 6-DOF system: (a) overview of system; (b) NI hardware; (c) connections among controller, NI hardware, and external measurement box

5.3.3 Test Setup

The test setup preparation comprised three activities: 1) testing floor construction, 2) loading platform preparation, and 3) calibration process. The following is a brief description of each part.

Testing Floor Construction

To provide a nearly perfectly flat and level surface base for the loading platform, a reinforced concrete slab with dimensions of 8200 mm × 4700 mm × 200 mm was constructed. The slab was orthogonally reinforced at the mid-depth of the cross section using 20M bars spaced at approximately 200 mm. The concrete was cast in several layers and a power float machine was used to produce a flat surface. After the concrete set, eight large steel plates with thicknesses of 38 mm (1.5”) were anchored to the slab using threaded rods and epoxy. To attach the loading platforms (6-DOF hydraulic testing table and uniaxial shake table) and the supporting frame to the testing floor, several threaded holes with a uniform pattern on the steel plates were provided. Figure 5.19 shows different stages of the testing floor construction.

Loading Platform Preparation

As shown in Figure 5.20 and Figure 5.21, a 6-DOF hydraulic testing facility equipped with three actuators in the horizontal direction (two actuators in the X direction and one actuator in the Y direction) and three actuators in the vertical direction (the Z direction) was used as the loading platform. The strokes of the horizontal and vertical actuators are 76.2 mm (3”) and 50.8 mm (2”), respectively. Each actuator has a force capacity of 14.7 kN (3.3 kips). The actuators are attached to a testing table with dimensions of 762 mm × 762 mm × 99 mm (30” × 30” × 3.9”). To mount the specimen, the testing table contains a grid of threaded holes, each spaced at 127 mm (5”). To support the other end of the specimen and actuators in the X direction, a steel frame with two 2600 mm tall columns and a 2146 mm wide beam was assembled. Each column contains seven rows of holes with 250 mm spacing, allowing adjustment of the clearance between the beam and the testing table according to the length of the specimen. The actuator in the Y direction is supported against a single 900 mm tall column. Both the frame and the single column are constructed from W310×342 standard steel section and attached to the base plates using 25.4 mm (1") diameter bolts. The actuators in the Z direction are directly bolted to the base plates.

(a)

(b)

(c)

(d)

Figure 5.19 Different stages of testing floor construction: (a) reinforcement cage and wooden formwork; (b) concrete slab cast; (c) drilling holes in slab; (d) anchoring steel plates

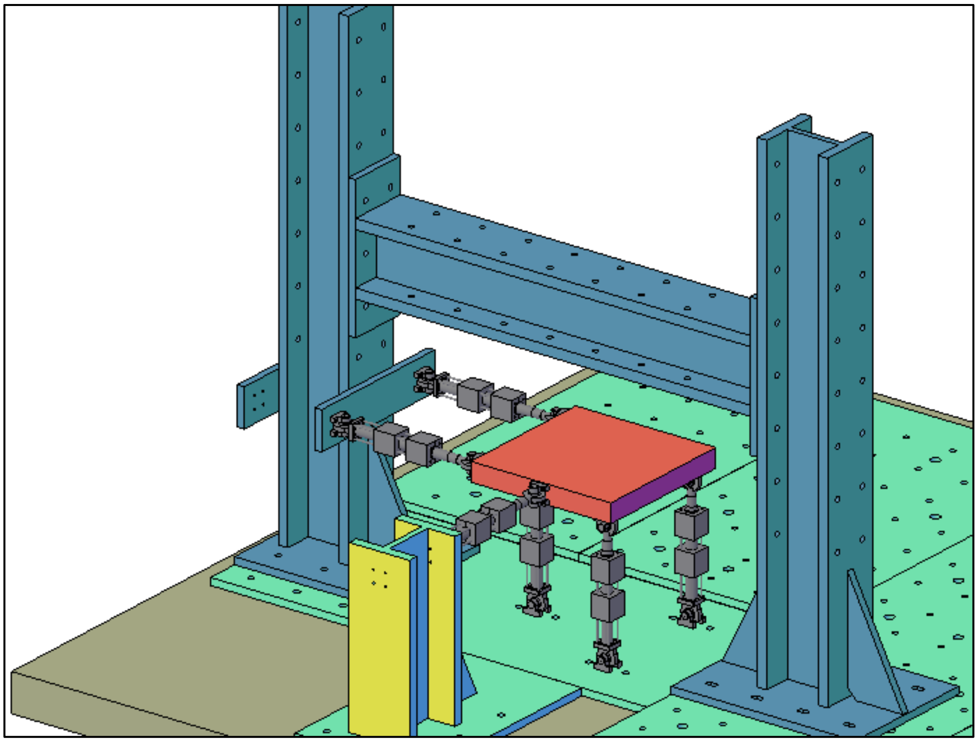

(a)

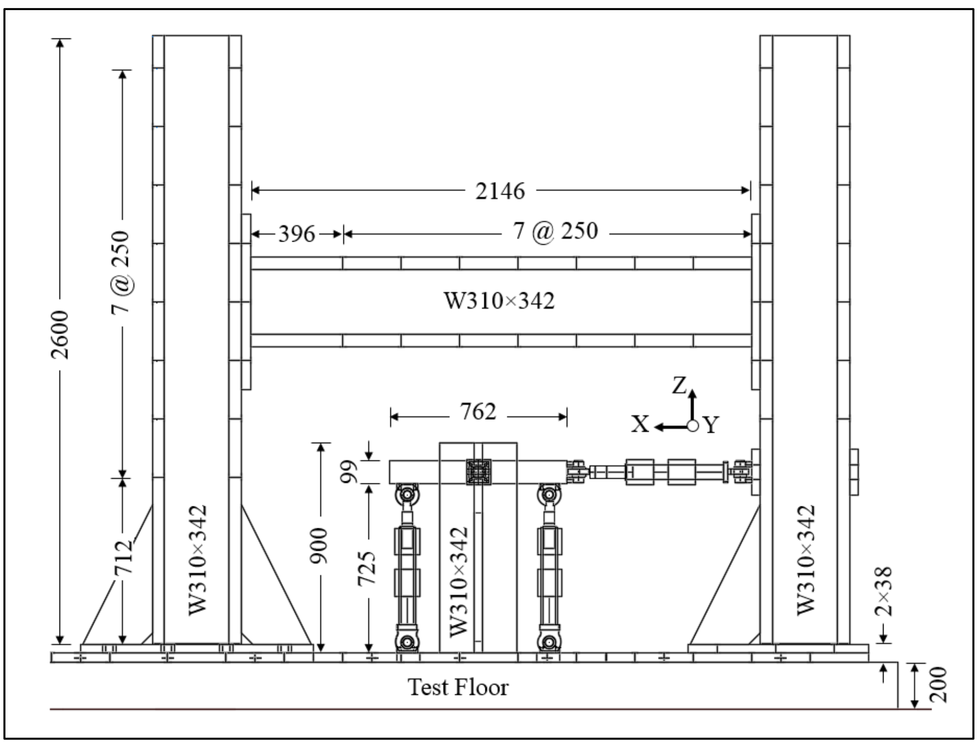

(b)

Figure 5.20 Details of 6-DOF loading platform (dimensions in millimeters)

Figure 5.21 An RC specimen mounted on the 6-DOF hydraulic testing equipment

Calibration Process

Each actuator required two types of calibrations: a feedback calibration and a command calibration. In the feedback calibration, the LVDT and load cell of the actuators were calibrated using an external ± 25 mm LVDT and a 30K ohm resistance shunt box, respectively. The command signal from the controller to the actuators also required calibration. Since during the hybrid simulation the actuators were externally controlled from NICON, the feedback and command calibration procedures were repeated considering the NI hardware as an external input and output voltage source for the controller. Detailed descriptions of the calibration procedure and different parts of the Shore Western controller including controlling the actuators using internal and external commands, logging data, internal and external signal tuning, and wiring the NI hardware to the controller are provided in the 6-DOF Hydraulic Testing Equipment Controller User's Manual (Sadeghian et al., 2016).

5.3.4 Numerical Components

VecTor analysis programs were used to model the numerical components of the hybrid simulation. The programs are capable of detailed nonlinear analysis of reinforced concrete structures accounting for second-order material effects such as tension-stiffening, compression softening, shear slip along crack surface, and other mechanisms important to the accurate representation of cracked reinforced concrete behaviour. The critical component of the numerical substructure was modelled in the VecTor2 finite element program using membrane elements while the rest of the substructure was modelled in the VecTor5 frame analysis program using layered beam elements. F2M interface elements were used to connect the membrane elements and beam elements at the interface of the two sub-models. A complete description of the numerical sub-models are provided in the following sections for each hybrid simulation. For more information regarding the analysis programs refer to the VecTor2 User's Manual (Wong et al., 2013) and the VecTor5 User's Manual (Guner and Vecchio, 2008).

In hybrid simulation, typically the numerical substructures are modelled in full-scale while the physical substructures may be constructed in reduced-scale with scaling factors determined according to the available laboratory equipment. To integrate the numerical substructures with physical substructures in different scales, the input and output of each component should be properly scaled according to its scaling factor and similitude laws. For a pseudo-dynamic hybrid test, the displacements computed by the simulation framework should be scaled with a length scale factor (S) prior to applying them to the physical specimens. Similarly, the reactions forces and displacements measured from the physical components should be scaled using force and moment scale factors (S^2 and S^3) and a length scale factor (S), respectively, prior to sending them to the simulation framework and numerical models. The computed and measured rotational displacements do not require scaling.

5.4 Verification Tests without Specimen

To evaluate the accuracy of the displacements obtained from the hydraulic testing equipment and verify the coordinate transformation algorithm of NICON, a series of verification tests were performed prior to mounting the specimen. A three-dimensional coordinate scanning system (Nikon K-Series Optical CMM) was used to measure the actual movement of the table.

The scanner continuously recorded the coordinates of ten LED targets attached to the steel frame and the testing table. Figure 5.22 shows the three-dimensional scanner and the configurations of the LED targets. To define a fixed coordinate system, three LED targets were attached to the steel frame beam in the form of two perpendicular lines. To measure translational displacements and rotations, an LED target was located at the predefined control point of the testing table. Also, six LED targets were glued to the two sides of an L-shaped wooden piece with a nearly perfect 90 degree angle and bolted to the table. The coordinates of the external measurement points were transformed to the testing table coordinate system.

According to the predictions of the stand-alone analytical models, the required ranges for translational and rotational displacements at the control point of the table for hybrid simulations were determined. A MATLAB code was used to send the command displacements to NICON through the Internet network based on UTNP protocol. NICON transformed the commands from the global coordinate system to the actuator strokes, generated corresponding ramp signals, and sent them as an external voltage to the actuator controller. The measured displacements from actuator LVDTs were sent back to NICON and were converted to the global coordinate system. The command and measured displacements of loading platform were compared against the external measurements obtained from the 3D scanner. Verification tests were performed for several different control points defined on the table. The test results indicated that the maximum error for translational displacements in the range of ± 25 mm was ± 0.05 mm. Also, for rotational displacements in the range of ± 4 degrees, the maximum error was ± 0.01 degrees. When the rotational displacements were examined, the maximum error observed in the translational displacements was ± 0.05 mm. In these tests, the error was defined as the difference between the measurements of the hybrid system and the 3D scanner. Considering the resolution of the 3D scanner, the observed levels of translational and rotational errors were considered acceptable and therefore it was concluded that the displacements at the reference point of the 6-DOF hydraulic testing equipment can be accurately controlled in the Cartesian coordinate system of the numerical model using NICON.

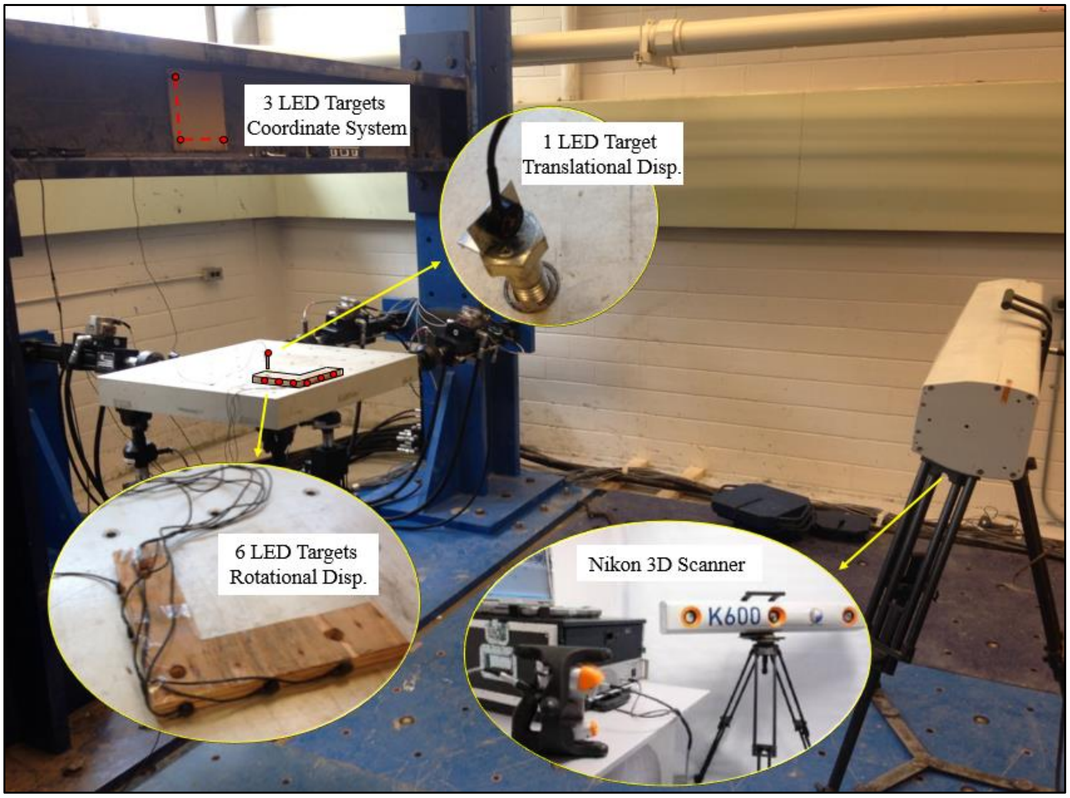

Figure 5.22 Verifying the testing table displacements using 3D scanner

5.5 Hybrid Simulations of Two Steel Frame Structures

5.5.1 Reference Structures

To verify the performance of the hybrid simulation framework and the multi-axial loading platform, two steel frame structures (Frame 1 and Frame 2) were tested within the linear elastic range in a pseudo-dynamic manner. Details of Frame 1 and Frame 2 are shown in Figure 5.23. Frame 1 was a one-span one-storey structure in which the left column was considered the experimental component. Translational and rotational displacements at the top end of the column specimen were controlled as the interface DOFs between the numerical and physical substructures while the bottom end was assumed to be fixed. Frame 2 was a one-span two-storey structure in which the lower storey beam was selected as the test specimen. The beam specimen consisted of two interface nodes each with two translational and one rotational DOFs. To control the displacements at the two ends of the beam specimen, NICON computed relative deformations by subtracting the rigid body motion and applied them on one end of the specimen while the other end was considered to be fixed. In both structures, the remainder of the frames were modelled using two-dimensional beam elements in the VecTor5 analysis software. The external load was modelled by controlling the lateral displacement of the left joint node in a quasi-static reversed cyclic manner. Cyrus was used as the hybrid simulation framework to integrate the numerical and physical substructures.

In both frame structures, all the beams and columns had a length of 1900 mm and a similar hollow circular cross section with an outside diameter of 156 mm and wall thickness of 13 mm. The test specimen was a 1/3.25-scale representation of the prototype beam and column members with a length of 584.5 mm, outside diameter of 48 mm, and wall thickness of 4 mm. The top and bottom of the specimen were welded to two 25.4 mm (1”) thick steel plates. To attach the specimen to the top support beam and testing table, four 25.4 mm (1”) diameter and four 12.7 mm (0.5”) diameter bolts were used, respectively. Figure 5.24 shows the steel specimen and the top and bottom steel plates placed in the test setup. To externally monitor the displacements of the specimen at the control point and possible relative movements of the steel plates with respect to the top support beam and testing table, four LED targets were placed on different parts of the loading platform and the specimen as shown in Figure 5.25.

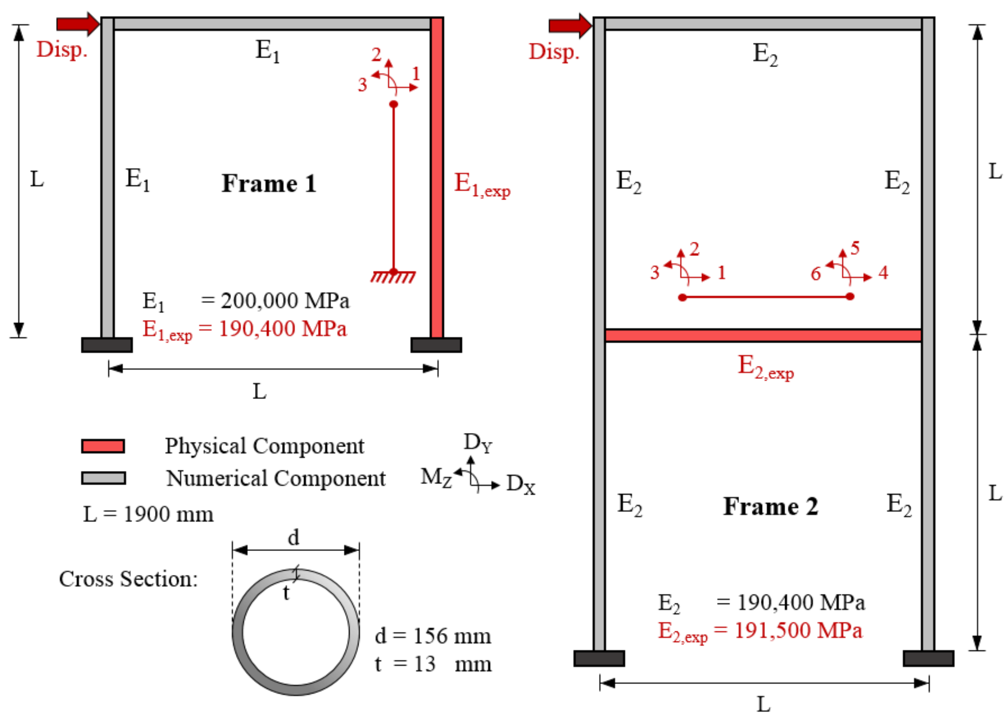

Figure 5.23 Details of steel frame structures

Figure 5.24 Steel specimen and top and bottom steel plates placed in the test setup

Figure 5.25 LED targets attached to the steel specimen and loading platform

5.5.2 Stiffness Evaluation

The test specimen was made from steel material. However, due to a previously carried out heat treatment process, its exact stiffness was not known. Therefore prior to conducting the hybrid simulation, a series of tests were performed to determine the stiffness of the physical specimen. For these tests, a MATLAB code was used to define and send displacements to the interface program, NICON. To evaluate the transverse and rotational stiffness, the transverse displacement of the specimen at the control point was varied in the range of ± 1.5 mm in a reversed cyclic manner while the displacements of the other DOFs were kept zero. Similarly, the rotational stiffness was evaluated by imposing rotation in the range of $\pm 2 \times 10^{-3}$ radians at the control point while the movement of the other interface DOFs were fixed. Due to the high stiffness of the specimen in the axial direction, evaluating the axial stiffness required imposing extremely small axial displacements. Imposing such small deformations are prone to error because of the limited resolution of the control system and the stiffness of the test setup. Therefore, the axial stiffness was computed based on the stiffness moduli obtained from the transverse and rotational stiffness tests.

For a test specimen representing a column with three interface DOFs, the measured horizontal and vertical forces and moment under different levels of applied horizontal displacement and rotation are shown in Figure 5.26 and Figure 5.27, respectively. It can be seen that, for the measured horizontal force and moment diagrams, the data obtained fitted well to linear equations (coefficient of determination, $R^2 > 0.95$). However, there was a discrepancy in the measured vertical force data (i.e., axial direction of the specimen) due to the small applied vertical displacement ($D_{Y,max} = 0.03$) which was close to the limit of displacements that can be controlled with the test setup. Using the fitted linear regression equations from the measured horizontal force and moment diagrams and the Timoshenko elastic stiffness terms including shear deformation effects (K_1, K_2, and K_3), the average elastic modulus of the test specimen ($E_{1,ave}$) was estimated as 190,400 MPa.

$$K_1 = \frac{12EI}{(1+\Phi)L^3} \tag{5.7}$$

$$K_2 = \frac{6EI}{(1+\Phi)L^2} \tag{5.8}$$

$$K_3 = \frac{(4+\Phi)EI}{(1+\Phi)L} \tag{5.9}$$

where E is the elastic Young’s modulus, I is the moment of inertia of the section, L is the member length, and Φ is the shear deformation factor defined as:

$$\Phi = 24\alpha(1 + \upsilon)\left(\frac{r}{L}\right)^2 \tag{5.10}$$

$$r = \sqrt{\frac{I}{A}} \tag{5.11}$$

where α is the shear area coefficient determined based on the shape of the section, υ is Poisson's ratio of steel, r is the "radius of gyration" of the cross section, and A is the area of the cross section.

Prior to conducting hybrid simulations on Frame 2, another set of stiffness evaluation tests were performed to ensure that the specimen was not damaged during the hybrid simulation of Frame 1 and also to examine the reproducibility of the results. In the new set of stiffness tests, the specimen represented a beam with six interface DOFs. The range of applied transverse displacements and rotations was similar to that used in the previous stiffness tests. The horizontal and vertical forces and moment were measured at the control end of the beam specimen and calculated at the other end by NICON based on the equilibrium equations. The measured and calculated reactions under applied transverse displacement and rotation are shown in Figure 5.28 to Figure 5.31. It can be seen that the measured results were similar to those obtained from the previous stiffness tests. It is worth noting that because the calculated moment at the fixed end was influenced by both the shear and moment measured at the other end, its coefficient of determination was much less than that of the measured moment. Using the aforementioned procedure and based on the measured reactions, the average elastic modulus of the test specimen ($E_{2,ave}$) was estimated as 191,500 MPa which was sufficiently close to the stiffness value found from the previous tests.

Some of the load-deflection responses did not pass through the zero point and resulted in offset values. The reason for that can be the friction in the swivel of the actuators. By measuring the restoring forces directly from the specimen, instead of measuring them from the load cells attached to the actuators, the offsets can be suppressed.

Also, in Figure 5.29 and Figure 5.31, the calculated moments resulted in larger hysteresis responses compared to the other related load-deflection responses. The moment at the N1 end is calculated by the summation of the measured moment and the measured shear force multiplied by the specimen length at the N2 end. Therefore, the calculated moment error contains the uncertainties associated with both the measured moment and shear force variables which is higher than the individual error of the variables.

It should be noted that according to the LED target measurements, no relative movement was observed between the bottom steel plate and the testing table or between the top steel plate and the support beam. Also the external measurements at the control point of the specimen were adequately close to the actuators LVDTs measurements.

5.5.3 Results and Discussions of Hybrid Simulations

As mentioned in the previous section, the average experimentally evaluated stiffness of the physical specimen for Frame 1 and Frame 2 were 190,400 MPa and 191,500 MPa, respectively. The difference in the evaluated stiffness is 0.6%, which is within the range of linearity errors of typical LVDTs or load cells. For the hybrid simulations, a typical steel stiffness of 200,000 MPa was assigned to the numerical members of Frame 1, and a stiffness of 190,400 MPa obtained from the first set of stiffness tests was used for the numerical members of Frame 2. The lateral displacement of the top left corner node in the numerical substructure of the frames was controlled in a reversed cyclic manner representing the external applied load. Displacement increments of 0.1 mm and 0.2 mm were used for Frame 1 and Frame 2, respectively. Cyrus integrated the two substructures and computed the displacements at the interface DOFs. To avoid underestimating the actual stiffness of the specimen and divergence of the solution algorithm, stiffness factors of 1.1 and 2.1 were used for Frame 1 and Frame 2. Because of the higher number of physical control DOFs, the test specimen of Frame 2 required a larger stiffness factor than Frame 1. Using a stiffness factor lower than 2.1 resulted in significant noise in the Frame 2 response. In each load stage, several iterations were performed to ensure the convergence of the physical substructure and account for the addition of the stiffness factor. During the hybrid simulations, the LED targets recorded no movement at the support locations and the displacements at the control point of the specimen matched with the actuator LVDT readings.

The hybrid simulation results were compared against the stand-alone linear elastic analysis results. Figure 5.32 and Figure 5.33 show the load-deflection responses of the two frame structures. Also, the scaled forces and displacements at the interface node between the numerical and physical substructures were compared with those computed by stand-alone analysis model. These results are presented in Figure 5.34 and Figure 5.35 for Frame 1 and Figure 5.36 to Figure 5.39 for Frame 2. The hybrid simulation results of Frame 1 and Frame 2 agreed well with the linear elastic analysis responses. The discrepancies in the axial force graphs were attributed to low levels of applied axial displacements ($D_{Y,\,max}$ = 0.02 mm).

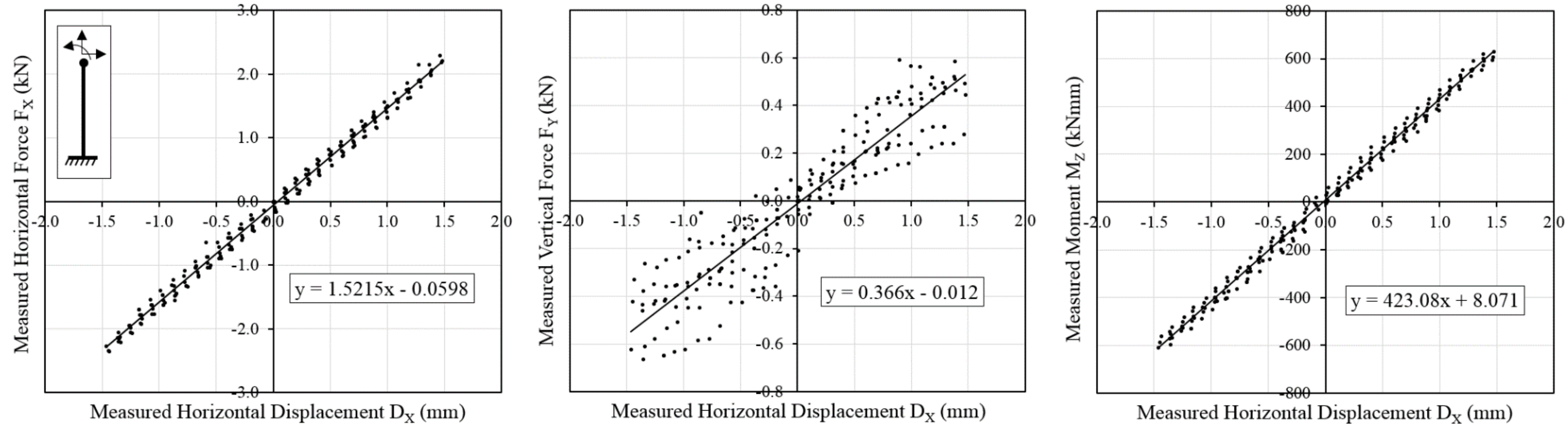

Figure 5.26 Stiffness evaluation of steel column specimen: measured forces and moments under applied horizontal displacements

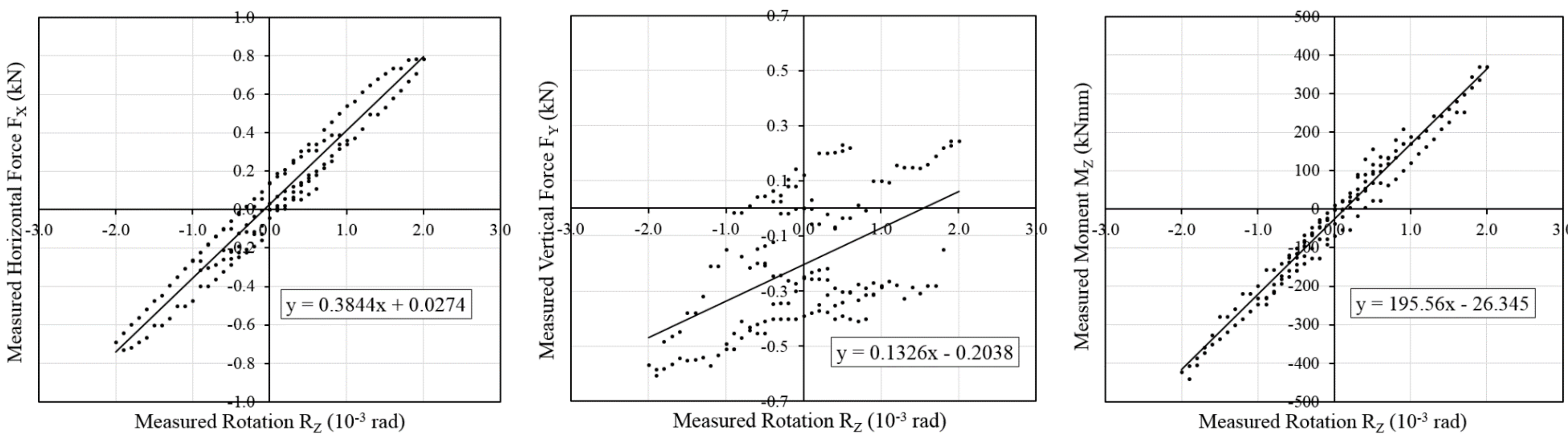

Figure 5.27 Stiffness evaluation of steel column specimen: measured forces and moments under applied rotations

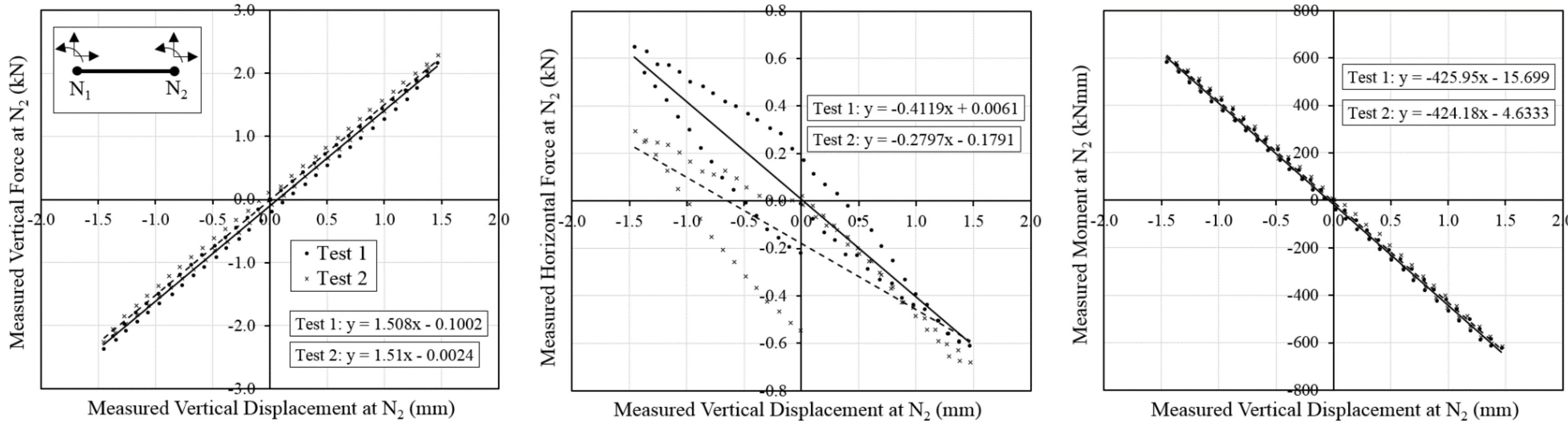

Figure 5.28 Stiffness evaluation of steel beam: measured forces and moments at N_2 under applied vertical displacements at N_2

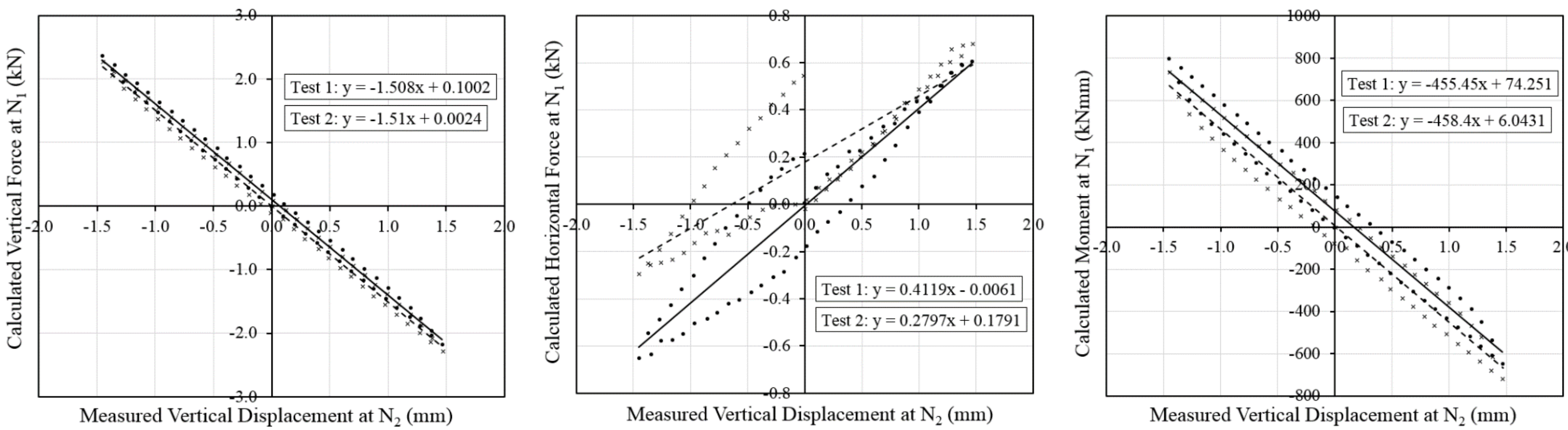

Figure 5.29 Stiffness evaluation of steel beam: calculated forces and moments at N_1 under applied vertical displacements at N_2

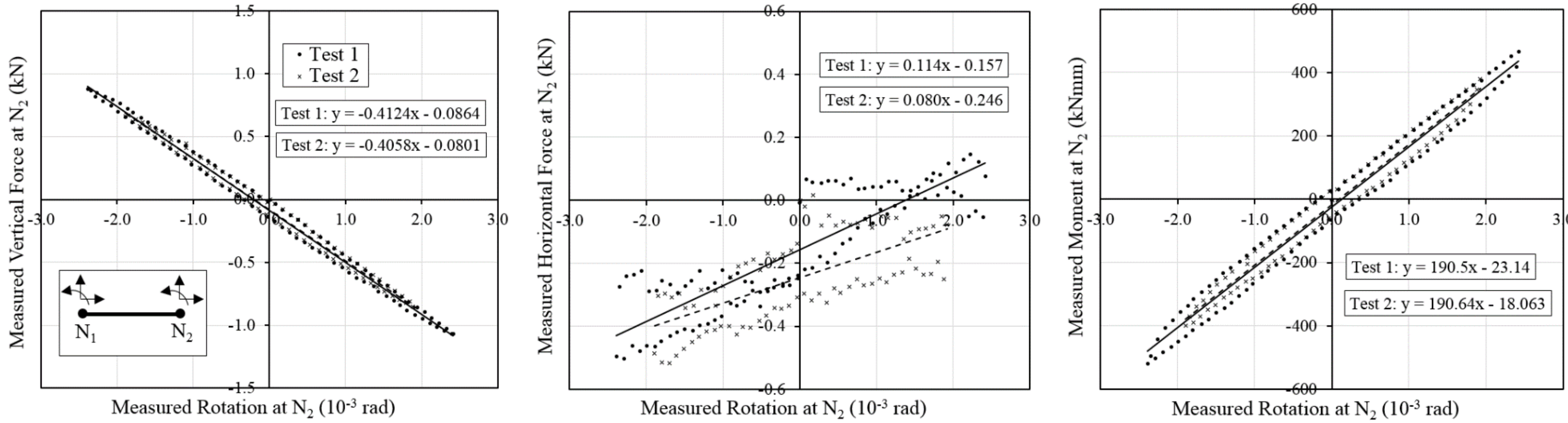

Figure 5.30 Stiffness evaluation of steel beam: measured forces and moments at N_2 under applied rotations at N_2

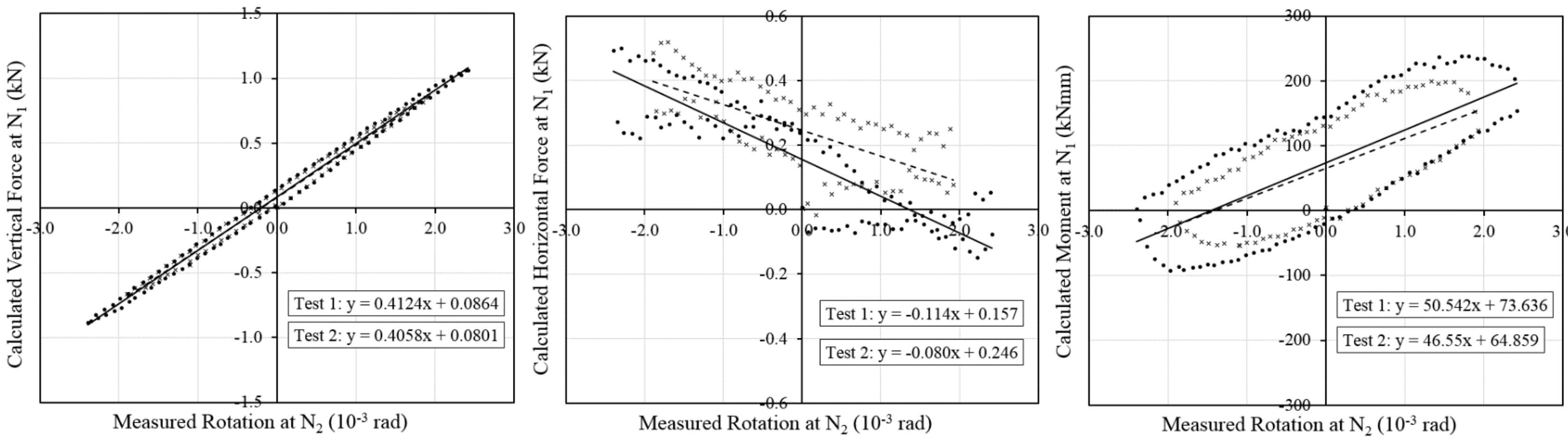

Figure 5.31 Stiffness evaluation of steel beam: calculated forces and moments at N_1 under applied rotations at N_2

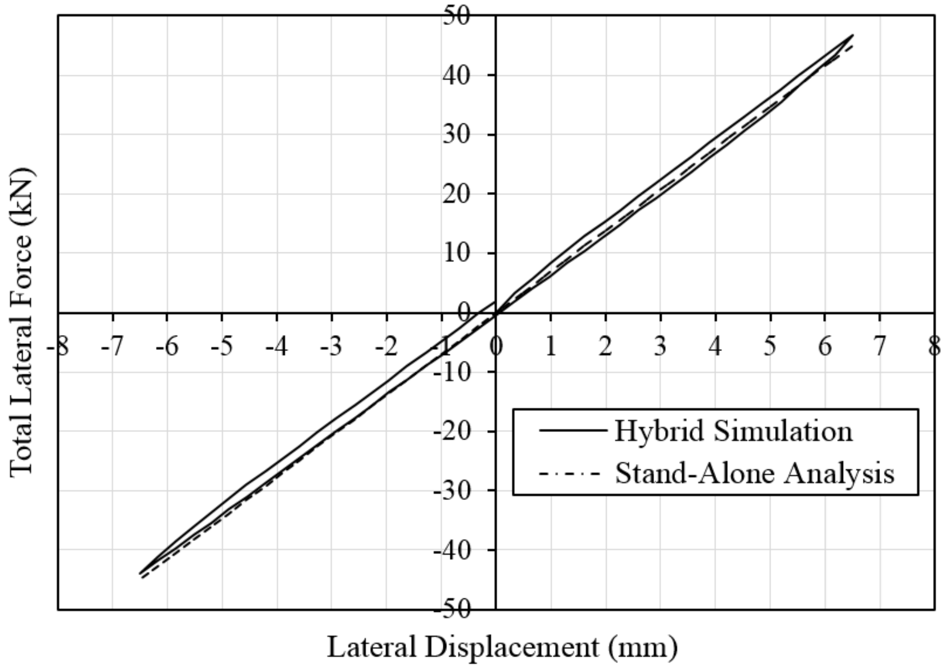

Figure 5.32 Comparison of load-deflection responses for Frame 1

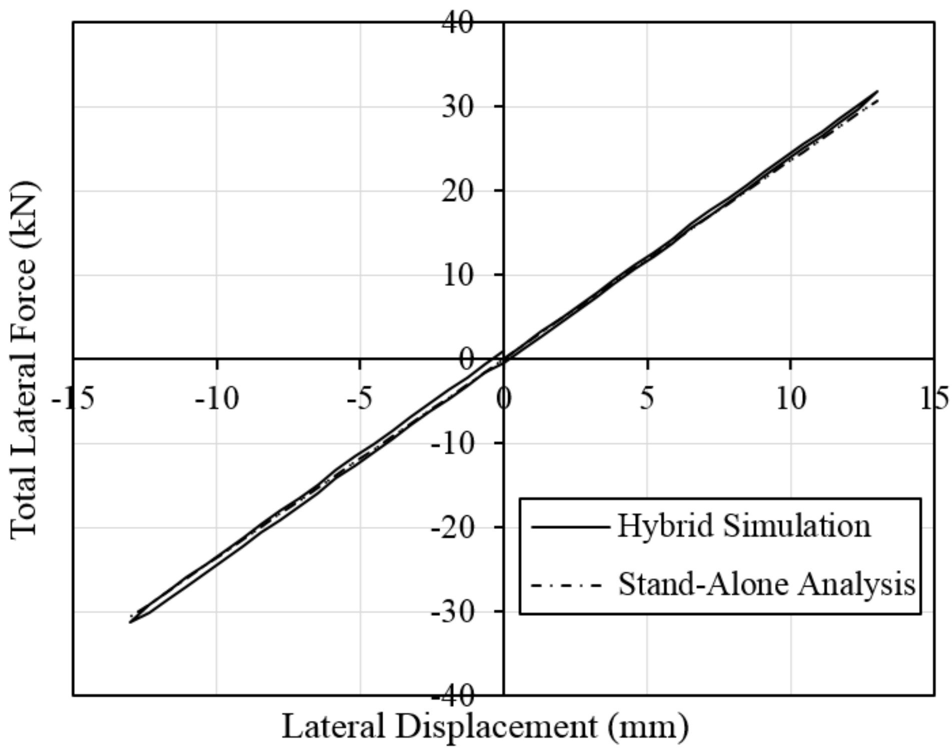

Figure 5.33 Comparison of load-deflection responses for Frame 2

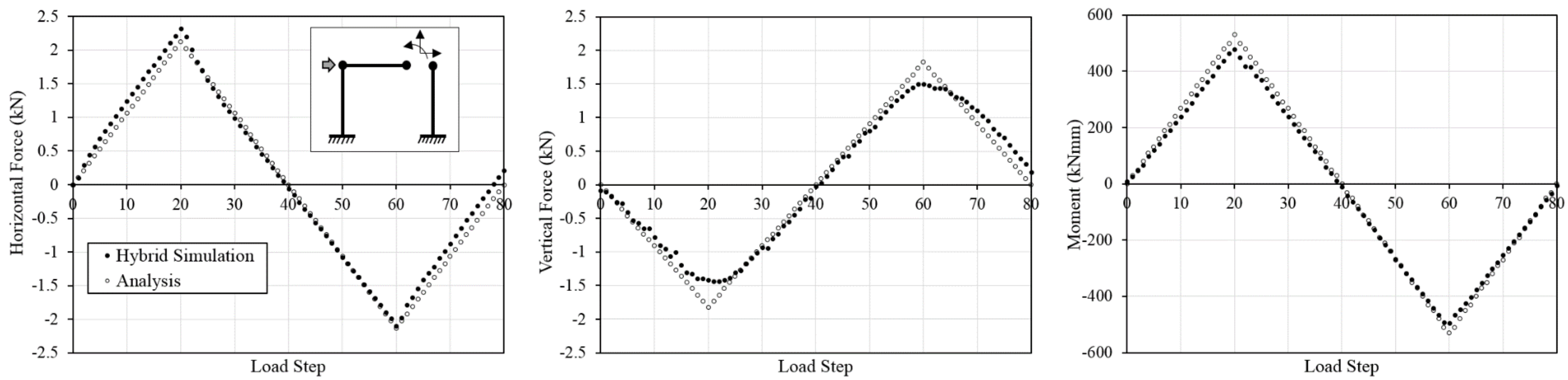

Figure 5.34 Comparison of scaled forces and moments at the interface node of column for Frame 1

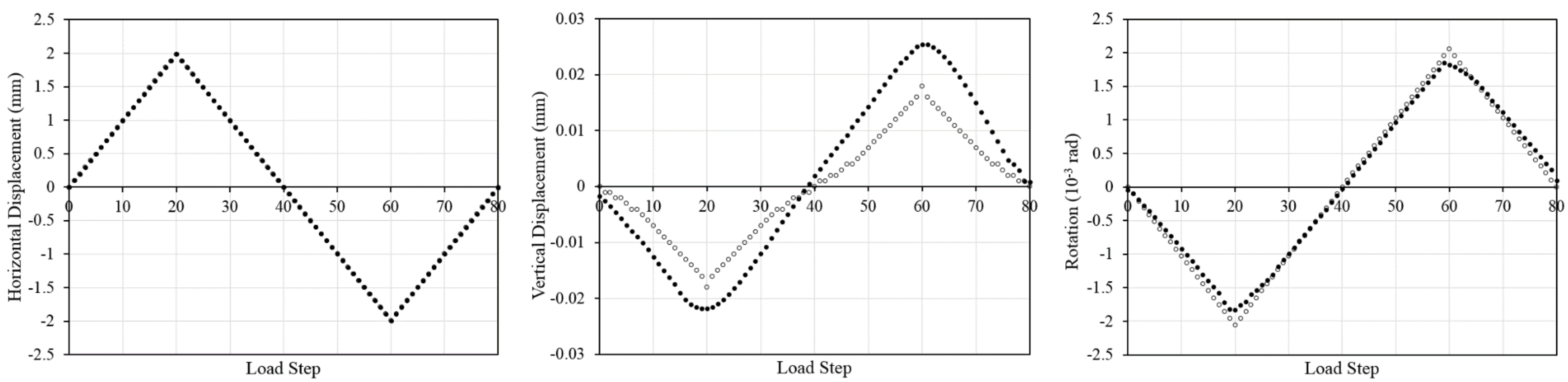

Figure 5.35 Comparison of scaled displacements and rotations at the interface node of column for Frame 1

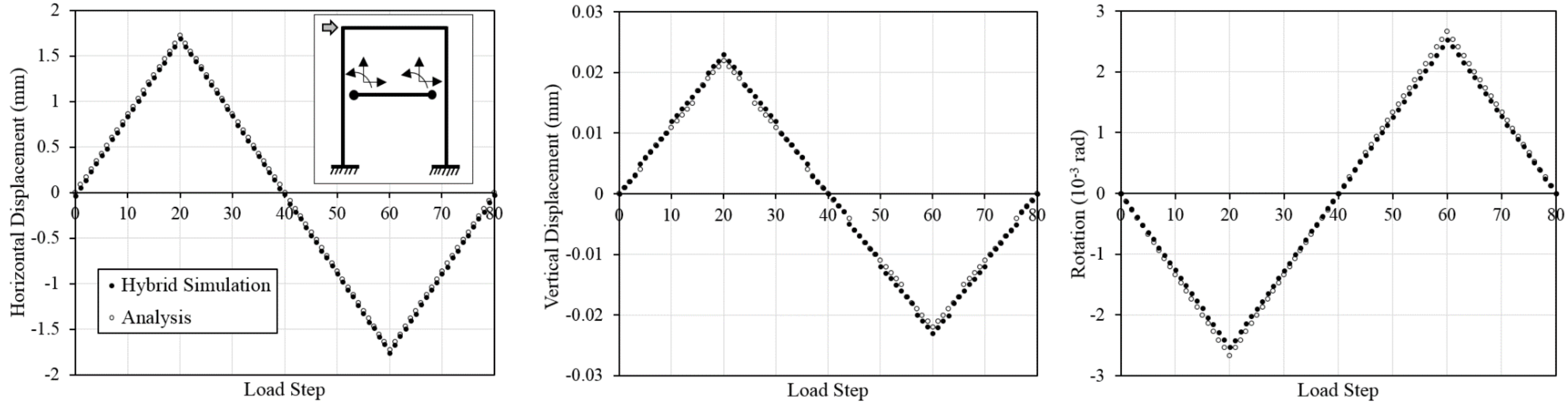

Figure 5.36 Comparison of scaled displacements and rotations at the left interface node of beam for Frame 2

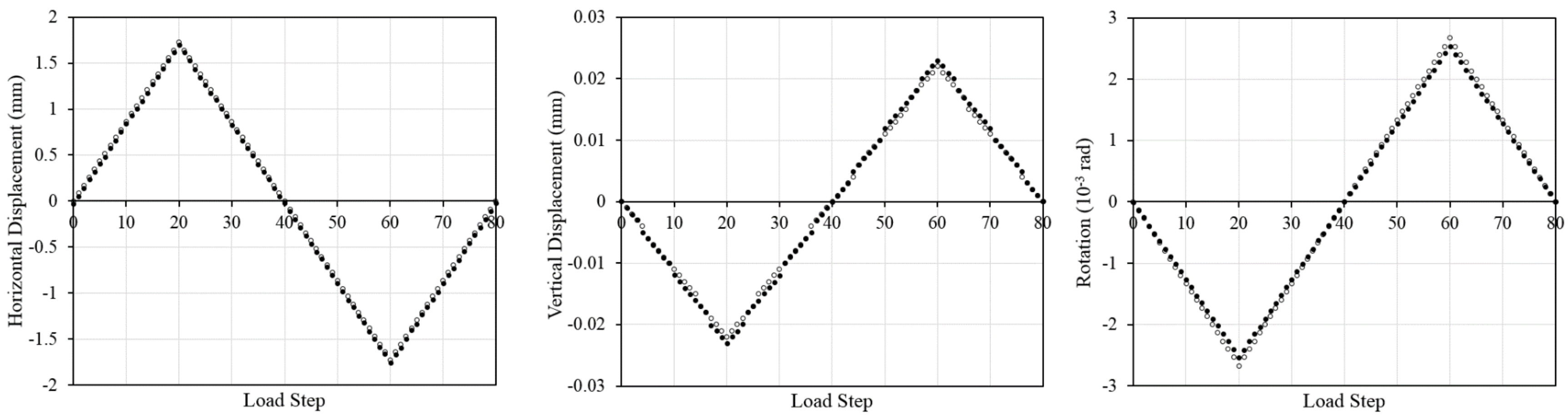

Figure 5.37 Comparison of scaled displacements and rotations at the right interface node of beam for Frame 2

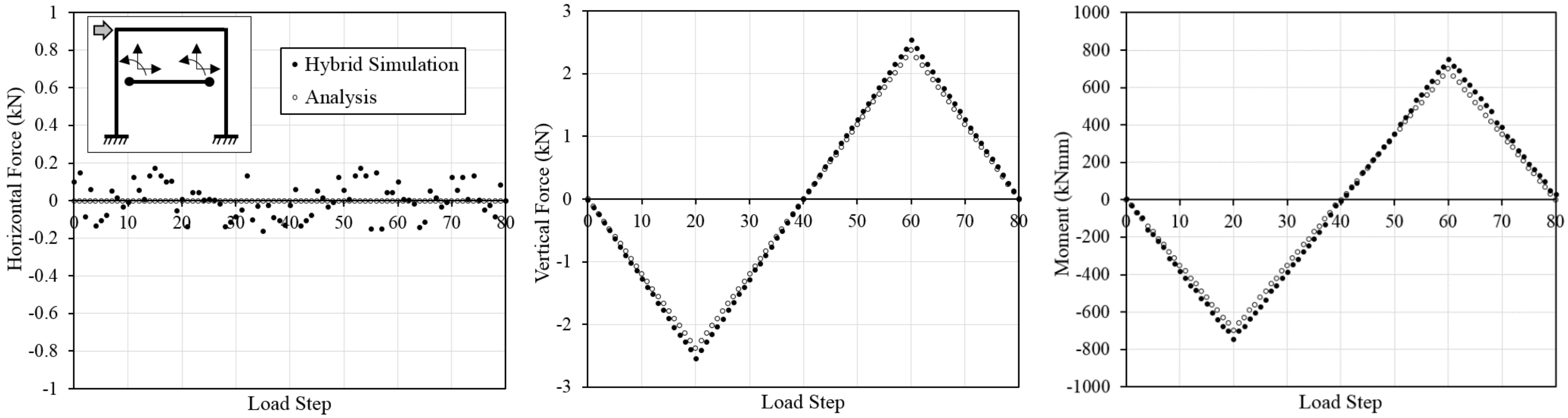

Figure 5.38 Comparison of scaled forces and moments at the left interface node of beam for Frame 2

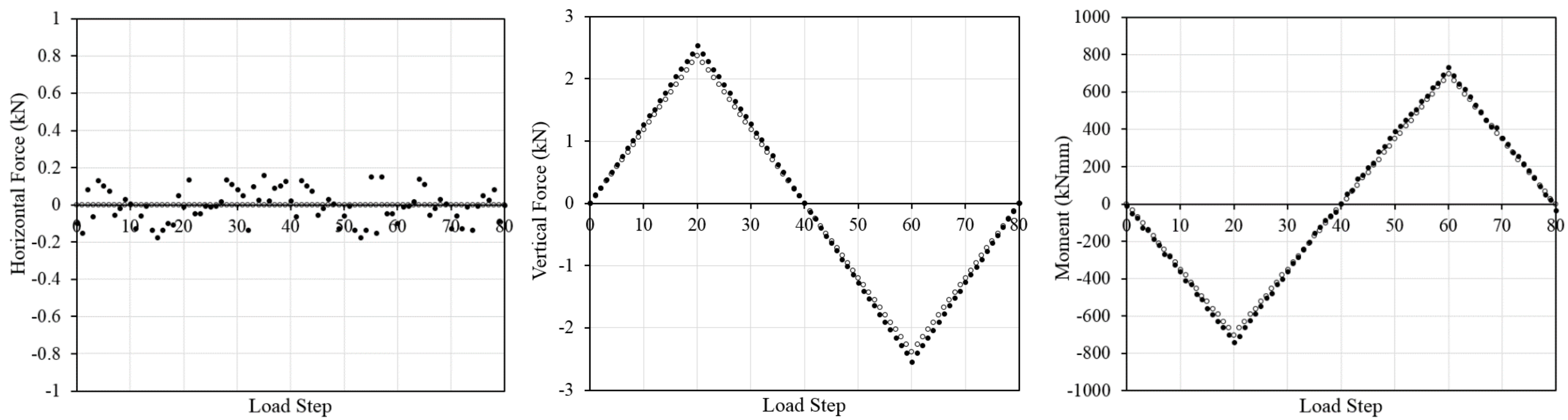

Figure 5.39 Comparison of scaled forces and moments at the right interface node of beam for Frame 2

5.6 Hybrid Simulations of Two RC Frame Structures with Critical Columns

5.6.1 Reference Structures

The main objective of the tests was to sample the accuracy of small-scale pseudo-dynamic hybrid simulation in capturing the response of reinforced concrete structures with different failure modes. Two one-storey one-bay reinforced concrete frame structures with critical columns were tested under a quasi-static reversed cyclic loading condition. The test variable was the amount of shear reinforcement in the columns. The first frame was designed to exhibit a ductile behaviour containing an adequate transverse reinforcement (ρ_v = 0.4%); the other frame was designed to be shear-critical with a low amount of transverse reinforcement (ρ_v = 0.1%) which was slightly higher than the minimum requirement specified by CSA-A23.3. To conduct a hybrid simulation on each frame, one of the columns was considered as the test specimen and the rest of the structure was modelled using the nonlinear VecTor analysis programs. The test specimens were a 1/3.23-scale model of the prototype columns. Cyrus was used to integrate the numerical and physical substructures. The test results were compared against those obtained from the detailed finite element analysis of the full-frame models.

Details of the two frame structures are presented in Figure 5.40. The column clear height was 1370 mm and the beam clear span was 1700 mm. Both the column and the beam had dimensions of 300 mm by 300 mm. Each column was attached to a foundation block with dimensions of 900 mm long, 800 mm wide, and 300 mm thick, providing a fixed support condition at the base. The properties of the reinforcing bars and concrete for each member are summarized in Table 5.4. The material properties of the column were selected based on the material tests presented in Section 5.6.2.1.

The external load was applied as a lateral displacement at the mid-depth of the beam in the numerical substructure. The load had a reversed cyclic pattern with a load stage increment of 0.5 mm. For the flexure-critical frame, a constant cycle increment of 10 mm was utilized; in the shear-critical frame, due to its brittle behaviour, the cycle increments were smaller and varied through the simulation (2 mm for the first four cycles and 4 mm, 6 mm, and 18 mm for the next cycles). The lateral load patterns are demonstrated in Figure 5.41. Due to the limitations of the actuator's capacity, no external axial load was applied to the frame.

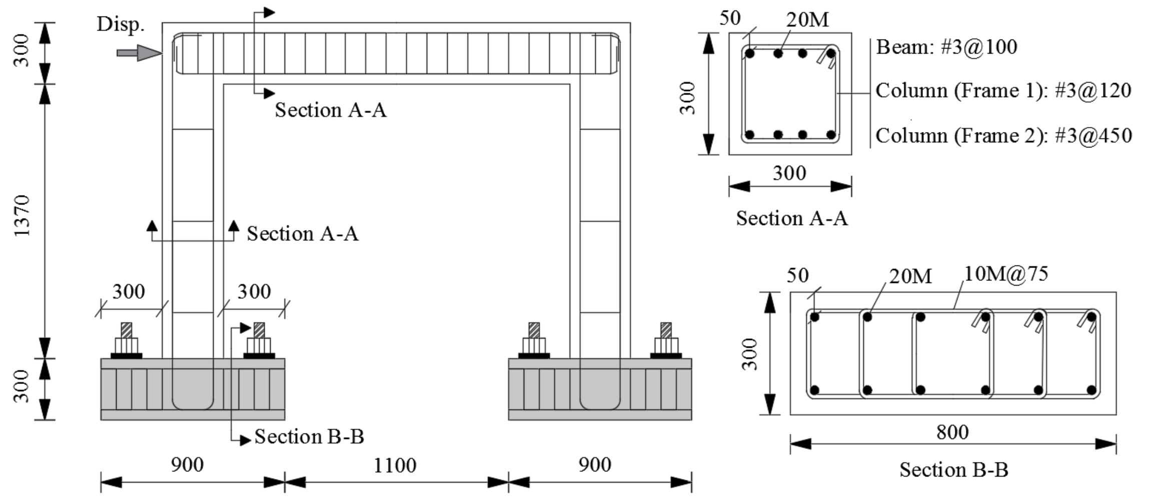

Figure 5.40 Details of shear-critical and flexure-critical frames (dimensions in millimetres)

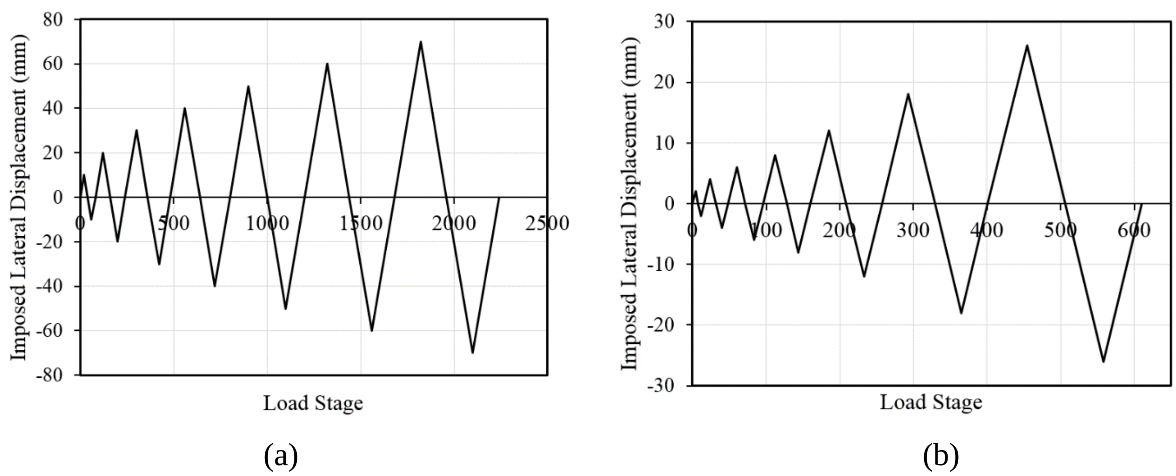

Figure 5.41 Loading protocol: (a) flexure-critical frame; (b) shear-critical column

5.6.2 Physical Specimens

5.6.2.1 Material Properties

To properly replicate the actual response of a reinforced concrete member in small-scale, the material properties of the scale model should be similar to that exhibited by the prototype structure. In particular, the stress-strain responses of the concrete and steel in tension and compression, and bond-slip effects resulting from the interaction between the material components, should be accurately represented in the reduced-scale tests. This task becomes more challenging if the laboratory constraints dictate a scaling factor which demands the use of an alternative material for the concrete (e.g., gypsum mortar) or reinforcing bars (e.g., smooth wires).

Table 5.4 Material properties of frame structures

Concrete

Member Type	f'c (MPa)	ε_o ($\times 10^{-3}$)	Max Agg. Size (mm)
Beam	42.9	2.31	14
Column & Foundation	46.9	2.78	14

Reinforcement

Member Type	Bar Size	Diameter (mm)	Area (mm^2)	f_y (MPa)	E_s (MPa)	f_u (MPa)	ε_u ($\times 10^{-3}$)
Beam	20M	20.0	300	447	198,400	603	130
	US #3	9.5	71	506	210,000	615	120
Column & Foundation	10M	10.0	100	400	200,000	600	100
	20M	20.0	300	503	194,000	543	57
	US #3	9.5	71	498	181,000	620	52

In this study, the size of the scale model allowed utilizing similar material types for the concrete and longitudinal reinforcement. The transverse reinforcement was represented with smooth wires which is deemed appropriate since the bond strength development in stirrups is negligible for the reference structure. The prototype structure was a two-storey frame previously tested in large-scale as a full-frame specimen at the University of Toronto (Duong et al., 2007). This frame will be referred to as the Duong frame hereafter. To re-examine the behaviour of the frame in small-scale using the hybrid simulation technique, two types of material tests were performed on several scale specimens to properly simulate the properties of the prototype concrete and reinforcing bars. The data obtained from the material tests were also used to determine the material properties for the hybrid simulations of one-storey frame structures with critical columns. In the following subsections, the material tests and several recommendations for preparing small-scale concrete mix and reinforcing materials are discussed in detail.

Concrete for Small-Scale Specimen

Model concrete, also known as microconcrete, is defined as a concrete mix comprised of fine aggregates, cement, water, and possibly admixtures. The maximum size of the fine aggregates is scaled to fulfill similitude requirements. The other components of the mix are identical to the prototype concrete. Based on the results of previous studies, some considerations were made in scaling the aggregate size which are discussed in subsequent sections.

The compressive stress-strain relationship of a model concrete is considered to be the most important property of the material that needs replication because of the following three reasons: 1) the main task of concrete as a structural material is to carry the compressive stresses, 2) in many large-scale tests only the compressive behaviour of concrete material is reported, and 3) the tensile response of model concrete has shown to be a challenging parameter to control and a wide scatter in test results has been reported in the literature (Harris and Sabnis, 1999). In general, the compressive strength of a concrete mix is largely a function of the water-to-cement ratio (W/C). Typically, microconcrete requires a higher W/C ratio than ordinary concrete to exhibit a similar compressive strength. According to the literature, for a specific compressive strength, microconcrete tends to overestimate the ultimate strain and underestimate the modulus of elasticity when compared to a similar prototype concrete (Noor and Wijayasri, 1982; Garas and Armer, 1980). Figure 5.42 compares a schematic compressive stress-strain response of microconcrete with that of prototype concrete. In addition, the tensile strength of microconcrete was found to be higher than that obtained from a prototype concrete with similar mix design (ACI, 1970; Harris and Sabnis, 1999).

To compensate for the softer compressive behaviour and higher tensile strength of microconcrete, several methods have been proposed which are mainly based on adjusting the aggregate gradations. To avoid high tensile strength and an unworkable mix, some studies imposed limitations on the minimum size of aggregate. Harris and Sabnis (1999) recommended limiting the amount of aggregate passing the US No. 100 sieve (0.149 mm) to less than 10%. Also, reducing the aggregate surface area and bond between the aggregate and cement paste lowers the tensile strength and compressive strains of microconcrete. Noor and Boswell (1992) suggested using a steeper gradation curve to increase the amount of large particles which have a lower surface area-to-weight ratio. Several researchers applied different types of aggregate coatings (e.g., silicon resins) or substituted other materials (e.g., glass beads) for a portion of the aggregate to reduce the bond effects (Kim et al., 1988; Noor and Boswell, 1991). Furthermore, to better represent the interaction between coarse and fine particles of prototype concrete in small-scale, some of the intermediate sieve sizes of the gradation curve can be eliminated (Harris and Sabnis, 1999).

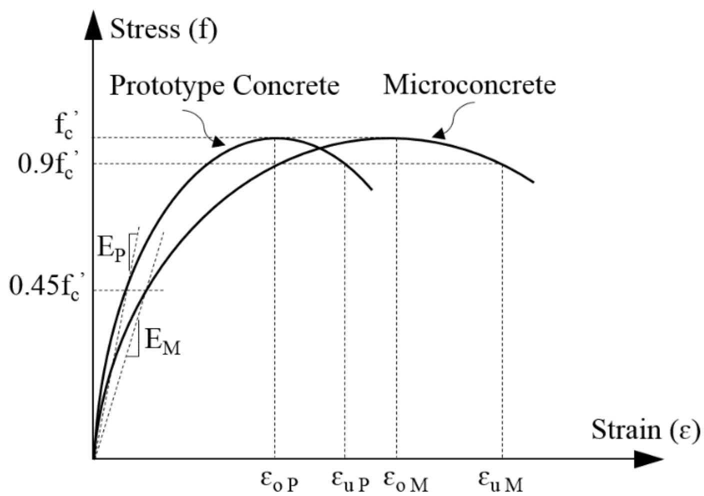

Figure 5.42 Schematic compressive stress-strain response of microconcrete and prototype concrete (Noor and Boswell, 1992)

In this study, as shown in Table 5.5, three types of aggregate gradations were examined (G1, G2, and G3). The maximum aggregate size for the G1 and G3 gradations was 3.36 mm (US No. 6 sieve), and for the G2 gradation 4.00 mm (US No. 5 sieve). These sizes approximately represented 1/3.23-scale of the maximum aggregate size utilized in the prototype structures (10 mm for the Duong frame and 14 mm for the one-storey frames). The particle size proportions for the G1 gradation were determined based on a commonly used aggregate gradation curve proposed by Fuller and Thompson (1907). To reduce the aggregate surface area and avoid high tensile strength in the microconcrete, much higher coarse-to-fine particle ratios were utilized in the G2 and G3 gradations than in the G1 gradation. Also for all three types of gradations, the minimum size of aggregate was restricted to 0.297 mm (US No. 50 sieve). To assess the influence of intermediate size particles, they were eliminated in the G3 gradation.

To find a microconcrete mix design which properly represented the behaviour of the prototype concrete, six batches were cast in standard size cylinders, 100 mm × 200 mm (4” × 8”), and tested under uniaxial compression. According to the literature, different sizes of cylinders with diameters ranging from 12.5 mm to 150 mm were used by researchers to determine model concrete compressive behaviour. Tokyay and Ozdemir (1997) examined the specimen shape and size effects on the compressive strength of concrete. The study concluded that for normal strength concrete, the influence of the cylinder diameter, ranging from 75 mm to 150 mm, and length-to-diameter (L/D) ratio, for L/D equal to or greater than 1.5, on the compressive strength was negligible. In addition, scaling the cylinder size based on similitude laws can result in significantly small cylinders which are not practical to test. For the trial batches, the influence of three parameters were investigated: W/C ratio, A/C ratio, and aggregate gradation type. Type III cement was employed to accelerate the testing process. Since the aggregate has higher stiffness than the cement paste, most of the mix designs utilized a high aggregate content to compensate for the low modulus of elasticity of microconcrete. Details of the concrete mix designs are presented in Table 5.6.

Prior to testing the concrete cylinders, the cylinder ends were ground smooth to remove surface paste and to reduce the occurrence of stress concentrations resulting from surface defects. The cylinders were loaded to failure in an MTS testing machine with a load capacity of 4,500 kN. Testing was performed in a displacement controlled manner at a rate of 0.00667 mm/s. Cylinders were instrumented using two ± 2.5 mm LVDTs, mounted over a gauge-length of 150 mm, for the purpose of measuring the axial strains of the cylinders (see Figure 5.43).

Table 5.5 Details of aggregate gradations

Gradation Type	US Sieve Size				
	Model Coarse Aggregate			Model Fine Aggregate	
	No. 5 4.00 mm	No. 6 3.36 mm	No. 8 2.38 mm	No. 16 1.19 mm	No. 50 0.30 mm
G1	---	100%*	82%	54%	0%
G2	100%	70%	40%	20%	0%
G3	---	100%	20%	20%	0%

*Percentage passing through sieve

Table 5.6 Details of concrete mixes

Mix Name	Mix Properties					Average Test Results	
	W/C	A/C	SP* (ml)	Aggregate Gradation	Description	f'_c (MPa)	ε_{cu} ($\times10^{-3}$)
Mix 1	0.45	2.75	---	G1	Harsh	57.1	2.93
Mix 2	0.55	3.25	---	G1	Workable	49.7	2.97
Mix 3	0.60	4.25	700	G1	Highly Workable	39.1	2.83
Mix 4	0.60	4.00	700	G3	Highly Workable	39.0	2.43
Mix 5	0.57	3.50	700	G2	Workable	46.9	2.78
Mix 6	0.57	3.50	700	G3	Workable	45.3	2.57

*Superplasticizer per 100 kg of cement

(a) (b)

Figure 5.43 Concrete cylinder compression test: (a) initial stage; (b) at failure

Figure 5.44 compares the average stress-strain responses of the microconcrete, obtained from testing three cylinders for each mix design, with the prototype concrete behaviour used in the Duong frame test. The cylinders were tested at 7 and 14 days (Mix 1 and Mix 2 at 7 days, Mix 3 at both 7 and 14 days, and Mix 4 to Mix 6 at 14 days). It was found that, as expected, the W/C ratio was the primary factor that influenced the strength and stiffness. In addition, the results of Mix 3 showed that the level of concrete maturity had great effect in reducing the compressive strains of the microconcrete. The average initial stiffness of cylinders tested at 14 days was higher than that measured at 7 days; however, the ultimate strength was almost the same. Furthermore, comparing the response of Mix 2 with Mix 5 and Mix 6 demonstrated the influence of aggregate gradation. Although Mix 2 had a higher ultimate strength, the use of a modified aggregate gradation in Mix 5 and Mix 6 resulted in a significantly higher stiffness. It should be noted that part of the stiffness gain was due to the higher maturity level of Mix 5 and Mix 6 compared to Mix 2. It was concluded that Mix 5 and Mix 6 exhibited the closest responses to the prototype concrete behaviour. Therefore, Mix 5 was used for the hybrid simulations of the one-storey frame structures with critical columns and Mix 6 was employed for the hybrid simulation of the Duong frame structure. All hybrid tests were conducted 14 days after casting the specimens.

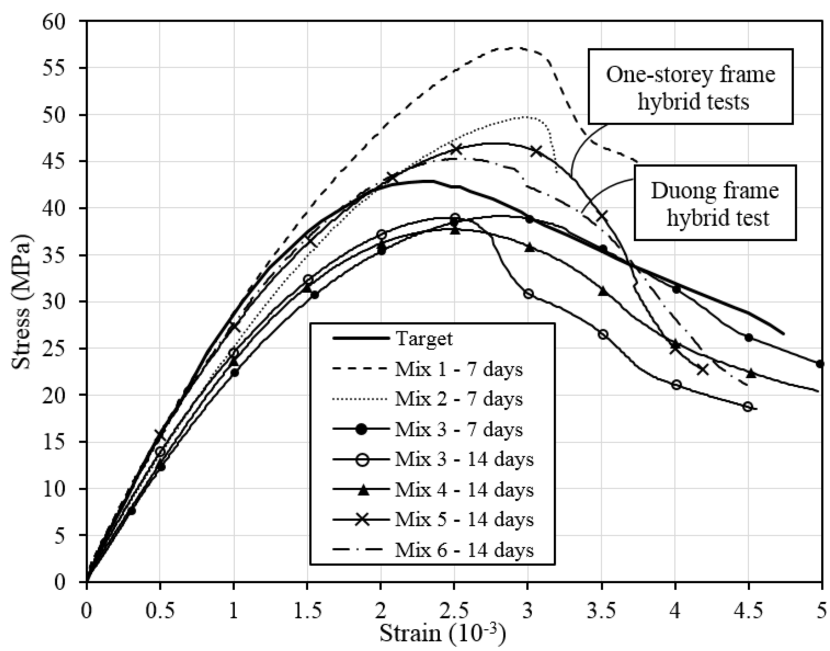

Figure 5.44 Concrete average compressive stress-strain response for different mix types

Since the concrete tensile strength of the Duong frame at the time of testing was not reported, no tensile test was conducted on the model concrete. However, as previously mentioned in detail, some of the recommendations provided in previous studies, namely limiting the minimum size of aggregate, using higher course-to-fine particle ratios, and eliminating intermediate size particles in the aggregate gradation, were incorporated in the final mix design to control the tensile strength of microconcrete.

Reinforcement for Small-Scale Specimen

The lower storey beam of the Duong frame, which was considered the critical member of the prototype structure, contained two types of reinforcements; #3 US bars (9.5 mm diameter) were used for the transverse reinforcement, and 20M bars (19.5 mm diameter) were utilized as the longitudinal reinforcement. To construct a 1/3.23-scale model of the beam member representing the physical component of the hybrid simulation, the reinforcement dimensions had to be scaled according to similitude requirements. For the transverse reinforcement, using smooth wires was deemed suitable since the bond-slip effects are typically insignificant in stirrups. Three types of wires made from different grades of stainless steel material were tested under uniaxial tension. The properties of the wires are summarized in Table 5.7. The specimens were 25 mm (10”) long and loaded to failure in an INSTRON testing machine with a load capacity of 45 kN. An MTS extensometer was attached to the middle of the specimen to measure the axial displacements (see Figure 5.45). The stress versus strain response of the wires are compared against the prototype #3 US bar in Figure 5.46. Based on the results, wire Type 2 (316L stainless steel material) with 3.175 mm (0.125”) nominal diameter was selected for the heat treatment process.

Table 5.7 Nominal properties of wires

Wire Type	Material	Diameter (mm)	Tensile Strength (MPa)	Description
Type 1	302/304 Stainless Steel	3.175	517	Bend & Stay
Type 2	316L Stainless Steel	3.175	517	Bend & Stay; Corrosion Resistance
Type 3	410 Stainless Steel	2.667	483	Bend & Stay

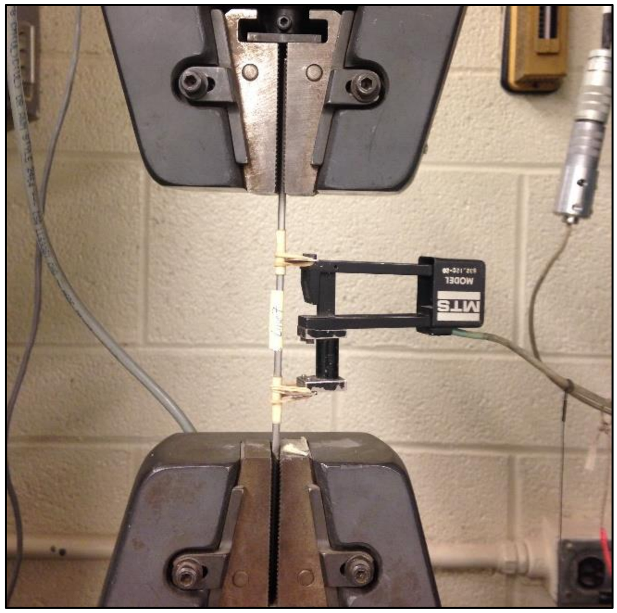

Figure 5.45 Model reinforcement uniaxial tensile test

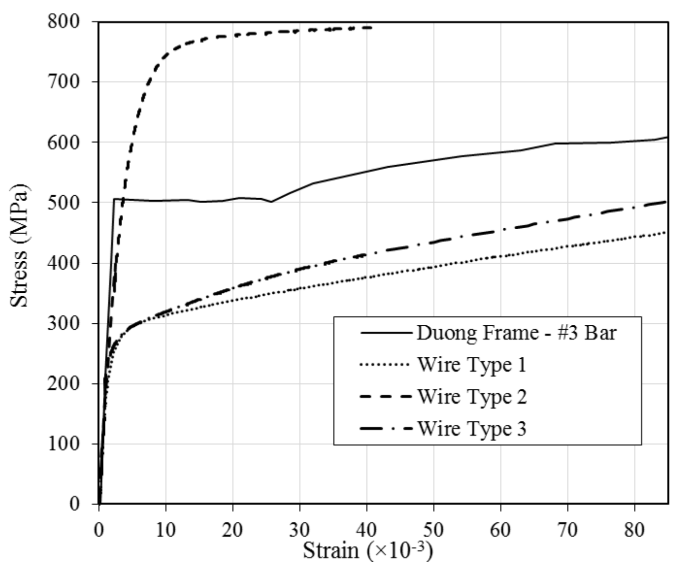

Figure 5.46 Measured stress versus strain response of different types of wires

Heat treatment manipulates the behaviour of the model reinforcement to better match the prototype response by lowering the yielding strength and increasing the ductility. Six batches of wires were sent for heat treatment to a local metal working facility equipped with high quality furnaces. Temperatures ranging from 843 °C (1550 °F) to 1015 °C (1860 °F) were investigated using a heating time of 20 minutes. To ensure the wires were exposed to a uniform temperature and had similar material properties, three tensile tests were performed on each batch. The average stress versus strain responses are compared against the prototype #3 US bar behaviour in Figure 5.47. According to the numerical analysis of the Duong frame, the maximum strain in the beam transverse reinforcement was computed as 35 × 10^{-3} mm/mm. It was concluded that the two batches with temperatures of 871 °C (1600 °F) and 899 °C (1650 °F) had the best correlation with the prototype behaviour. Therefore, wires heat treated under the lower temperature were employed for the hybrid simulations of the one-storey frame structures and wires exposed to the higher temperature were utilized in the hybrid testing of the Duong frame structure. The wires used for the one-storey frame tests had an average measured diameter of 3.175 mm (equal to the nominal diameter), while the wires utilized for the Duong frame test had an average measured diameter of 3.100 mm.

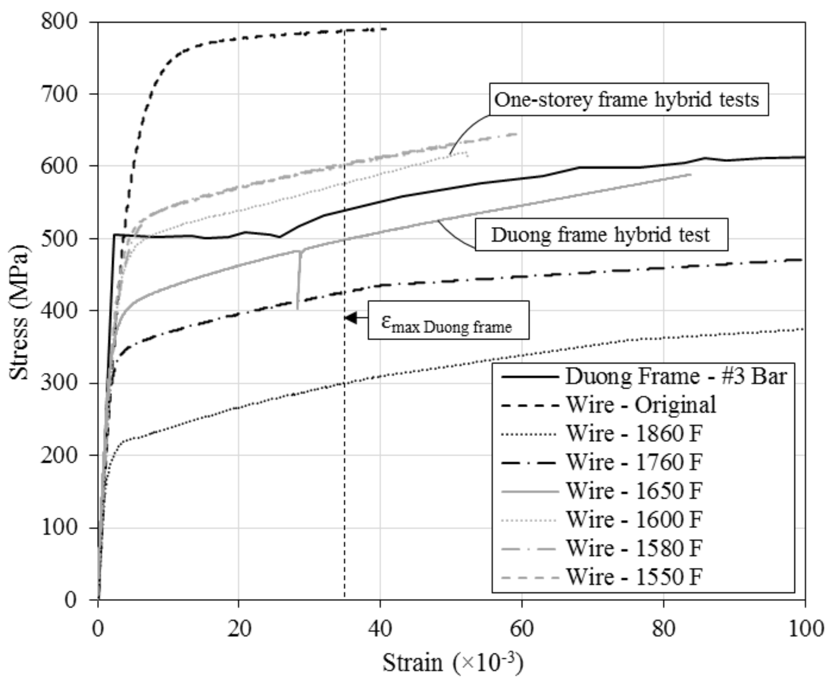

Figure 5.47 Comparison of the average responses of Type 2 wires heat treated under different temperatures with prototype #3 US bar behaviour

Unlike with transverse reinforcement, for the longitudinal reinforcement the bond between the reinforcing bar and concrete can significantly influence the behaviour of the structure. To properly simulate the bond characteristics in small-scale, deformed bars with 5.72 mm nominal diameter (D4 bars) were used as the model longitudinal reinforcement. Similar to the model transverse reinforcement, a heat treatment process was carried out on the D4 bars to achieve the same stress-strain relationship as that exhibited by 20M bars in the prototype structure. Five batches of reinforcing bars were heat treated with temperatures ranging from 538 ^{o}C (1000 ^{o}F) to 671 ^{o}C (1240 ^{o}F) and heating times of 1.5 hours to 3.0 hours. To ensure all the reinforcing bars were exposed to a uniform temperature and had similar material properties, three tensile tests were performed on each batch. The average stress versus strain responses are compared against the prototype 20M bar behaviour in Figure 5.48.

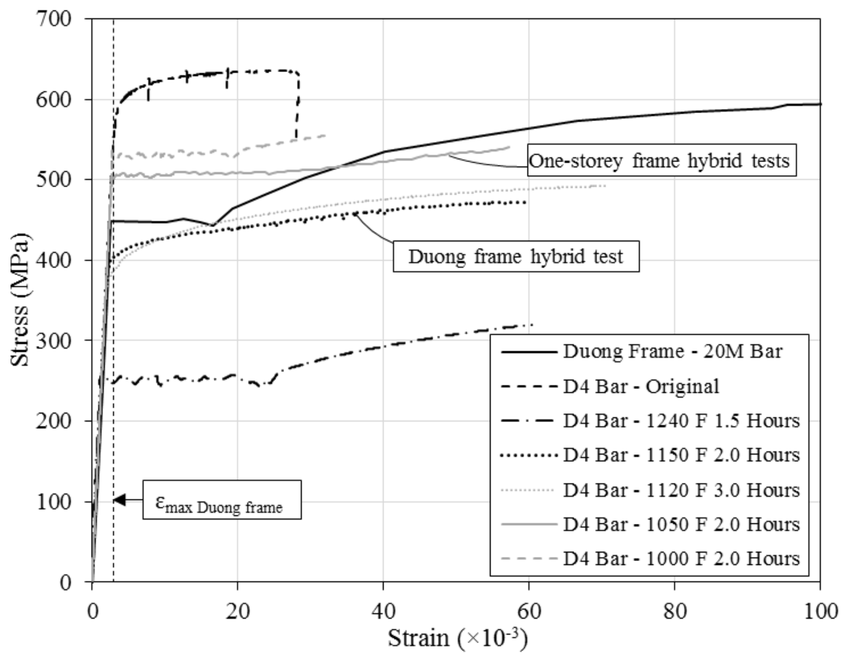

Figure 5.48 Comparison of the average responses of D4 bars heat treated under different temperatures and times with prototype 20M bar behaviour

It is worth noting that according to the full-frame test results, the beam longitudinal reinforcement experienced a maximum strain of 3.3×10^{-3} mm/mm which was slightly higher than the yielding strain value (2.25×10^{-3} mm/mm). The maximum strain computed by the nonlinear analysis was 2.5×10^{-3} mm/mm. Based on the results presented in Figure 5.48, D4 bars heat treated under temperatures of 565 ^{o}C (1050 ^{o}F) and 621 ^{o}C (1150 ^{o}F) for two hours were selected as the longitudinal reinforcement for the test specimens of the one-storey frames and the Duong frame, respectively.

5.6.2.2 Specimen Preparation

Two I-shaped reusable wooden formworks were constructed, each comprised of two end blocks with dimensions of 250 mm × 250 mm × 90 mm and a test region with dimensions of 424 mm × 93 mm × 93 mm. The test region represented a 1/3.23-scale of the prototype column which was 1370 mm long with cross section dimensions of 300 mm × 300 mm. The remainder of the frame structure was numerically modelled. The specimen contained four D4 bars as the top and bottom longitudinal reinforcement and 3 (shear-critical frame) and 10 (flexure-critical frame) 316L stainless steel wire stirrups with 3.175 mm nominal diameter as the transverse reinforcement. Figure 5.49 and Figure 5.50 show details of the specimen and formwork. To model the anchorage of the longitudinal reinforcement, both ends of the D4 bars were threaded and screwed to two 12.7 mm (0.5”) thick end steel plates. To prevent the wires from premature opening, each end was bent 180 degrees and fixed with small tie wires (see Figure 5.51).

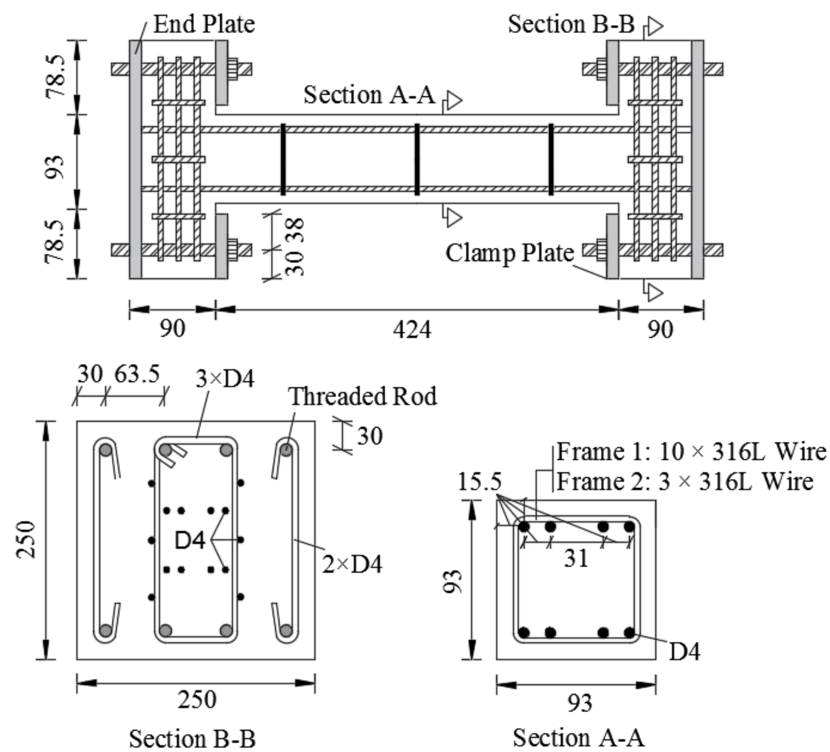

Figure 5.49 Details of the model specimen (dimension in millimeters)

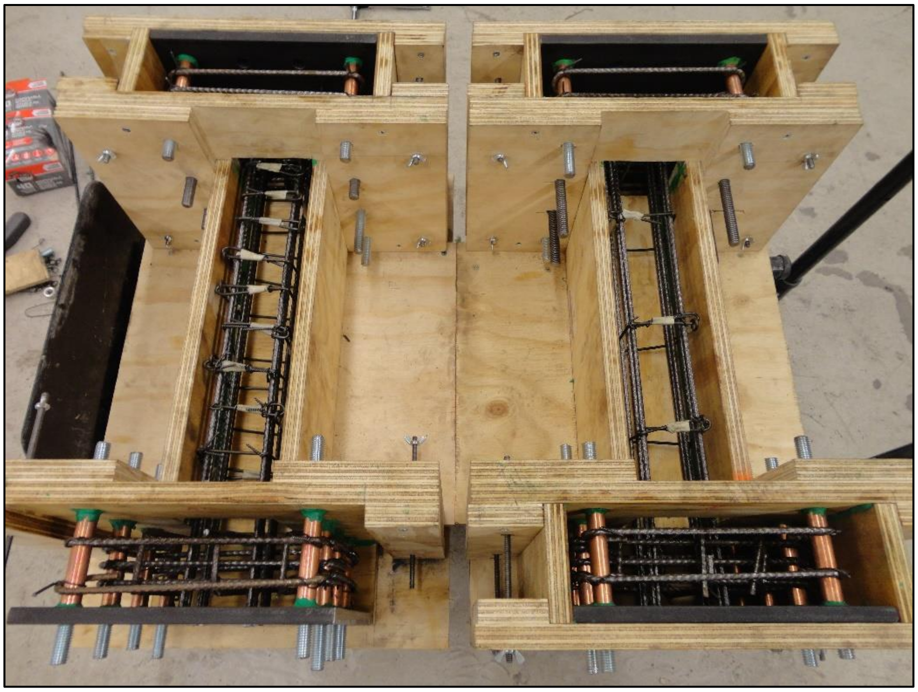

Figure 5.50 Formwork and reinforcement cage for flexure-critical specimen (left) and shear-critical specimen (right)

Figure 5.51 Details of wire end bending

Including the end blocks was deemed necessary for realistic simulation of the stress distributions at the top and bottom parts of the test region. To avoid cracking and failure of the end blocks, they were heavily reinforced in the longitudinal and transverse directions using D4 bars. Also, the top and bottom steel plates and 12.7 mm (0.5”) diameter threaded rods provided additional confinement and strength for the end blocks. Details of the end blocks and steel plates are given in Figure 5.49 and Figure 5.52. Twelve threaded rods (eight at the bottom and four at the top) were used to bolt the specimen to the steel plates of the test setup. Inside the end blocks, the threaded rods were covered by thin copper pipes that were to be cast-in-place.

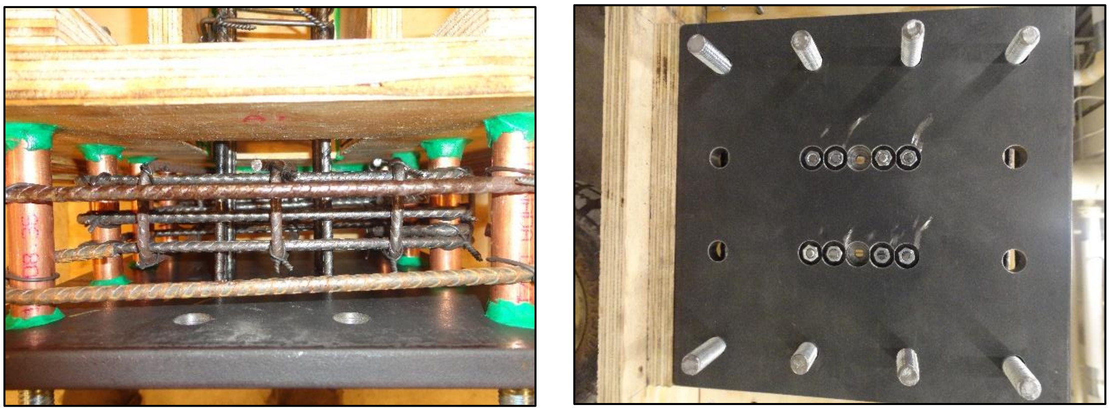

(a) (b)

Figure 5.52 Details of end block: (a) reinforcement cage; (b) end steel plate

Once the formwork, reinforcement cage, and end steel plates were assembled, the specimens were cast. The concrete was prepared using a 50 liter mechanical concrete mixer and according to the mix design Type 5 described in Section 5.6.2.1. To eliminate voids in the concrete, specimens were placed on a vibrating table for approximately 30 seconds (see Figure 5.53).

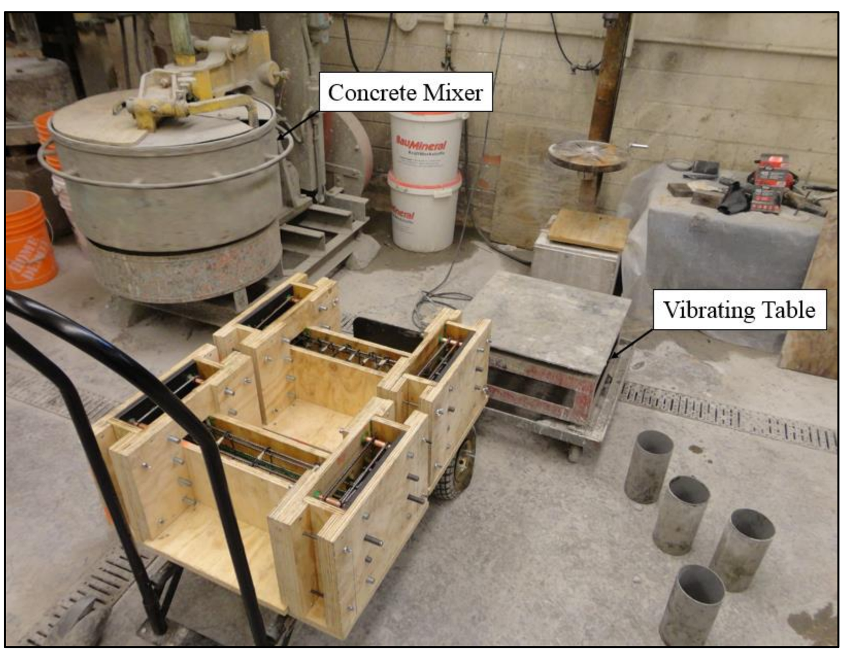

Figure 5.53 Concrete mixer and vibrating table

The concrete surface was finished with a small trowel to produce a smooth and void-free surface. Once the cast was finished, the specimens were tented under plastic and allowed to cure for a period of three days under moistened burlap. In addition to the test specimen, four cylinders (100 mm × 200 mm) were cast and cured to later obtain the microconcrete material properties. Figure 5.54 shows different stages of the concrete cast.

Figure 5.54 Different stages of concrete column specimens cast

5.6.3 Numerical Models

Two finite element models were created for each structure: 1) a substructure model including the beam, joint panels, and right column for hybrid simulation and 2) a full-frame model for mixed-type analysis. The beam and joint panels (not-critical members) were modelled in a frame analysis program, VecTor5, while the column (critical member) was simulated in a detailed membrane finite element program, VecTor2. The two sub-models were connected using F2M frame-membrane interface elements. Cyrus combined the two programs and performed the simulation in an integrated manner. Figure 5.55 shows both the hybrid simulation and mixed-type models. A brief description of each numerical sub-model is provided in the following.

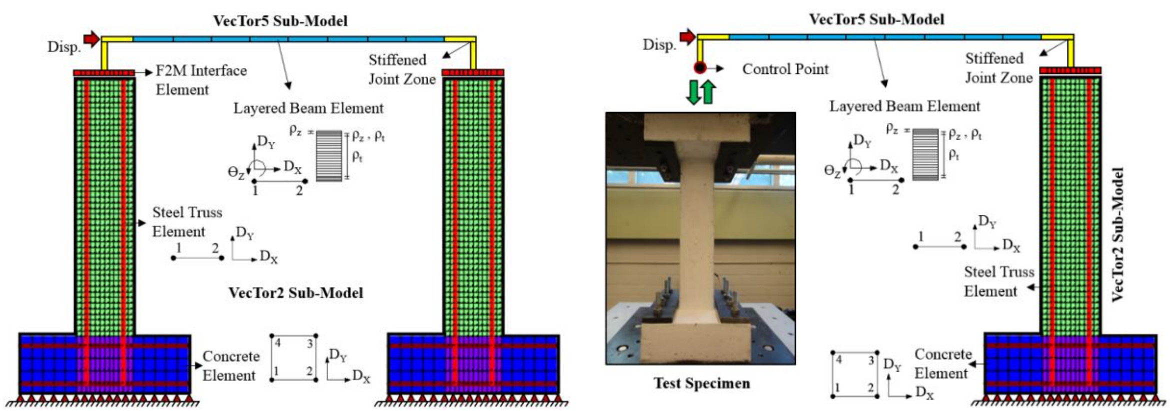

Figure 5.55 Numerical models for mixed-type analysis (left) and hybrid simulation (right)

The VecTor5 sub-model was comprised of 12 layered beam elements of approximately 200 mm length. Each frame element was divided into 30 concrete layers, enabling accurate analysis through the section. Based on the stirrup details presented in Figure 5.40, the out-of-plane and transverse reinforcement ratios were determined and assigned to the outer and core layers of the cross section, respectively. The joint panels were modelled with stiffened elements to avoid artificial damage. The amounts of the longitudinal and transverse reinforcement of the stiffened elements were increased by a factor of two, as suggested by Guner and Vecchio (2010b). To model the external load, the lateral displacement of the left joint node was controlled in a reversed cyclic manner with 0.5 mm increments according to the loading protocol presented in Figure 5.41.

For the VecTor2 sub-model, each column, including the base foundation, was modelled with 662 concrete rectangular elements and 144 steel truss elements. A mesh size of 60 mm × 60 mm was used for the heavily reinforced base foundation while the columns were modelled using a finer mesh size of 25 mm in the horizontal direction by 30 mm in the vertical direction. The longitudinal reinforcement was represented with truss elements. The transverse reinforcement was added as a smeared component to the rectangular concrete elements. To provide a fixed end condition for the frame, all the nodes located at the bottom row of the foundation were fully restrained in both the X and Y translational directions.

The default material models and analysis parameters, as defined in all VecTor software programs, were used. These material models and analysis options are summarized in Table 2.1 of Chapter 2.

5.6.4 Results and Discussions

Hybrid simulation (the integration of the test specimen and numerical model) was conducted according to the Modified Newton Raphson method. Several iterations were performed at each load stage to fulfill the compatibility and equilibrium requirements between the test specimen and numerical model. Unbalanced forces resulting from the nonlinear behaviour of the test specimen were computed based on the initial stiffness and measured force reactions. The initial stiffness of the specimen was estimated as 29,300 MPa using the stress and strain values obtained at 45% of the microconcrete ultimate compressive strength (Noor and Boswell, 1992). It was increased by 10% to avoid underestimating the actual stiffness of the specimen resulting in possible divergence of the nonlinear solution. The initial stiffness estimation was deemed reasonable since no fluctuation was observed in the measured reactions and load-deflection response of the system.

The load-deflection responses obtained from the small-scale hybrid tests are compared against the finite element analysis results of the prototype structures in Figure 5.56 and Figure 5.57. For both the flexure-critical and shear-critical frames, the overall response obtained from the hybrid simulation agreed well with that computed by the analysis. The hybrid tests had a tendency to underestimate the stiffness and peak loads of the initial loading cycles. This was primarily attributed to the lower stiffness of the microconcrete (E_c = 29,300 MPa obtained from material tests) compared to the prototype concrete (E_c = 31,800 MPa computed based on the Hognestad parabola). For the flexure-critical frame, the energy dissipation (i.e., area under the load-deflection curve) of the analysis and hybrid test correlated reasonably well. However, for the shear-critical frame, the analysis resulted in a lower energy dissipation than the test, mainly due to the lower computed plastic offsets (i.e., permanent deformations under cyclic loading), particularly in the last two loading cycles.

As expected, the flexure-critical frame exhibited a ductile behaviour with failure occurring at lateral displacements of 60 mm for the hybrid test and 63 mm for the analysis. Conversely, the shear-critical frame response was brittle with strength decay initiating at displacements of 17.5 mm for the hybrid test and 12 mm for the analysis. For the shear-critical frame, the strength degradation of the hybrid test initiated at later load stages and was more gradual compared to the analysis. Figure 5.58 compares the hybrid simulation response of the two frames. It can be seen that addition of more stirrups increased the ultimate strength and ductility of the frame by 32% and 243%, respectively.

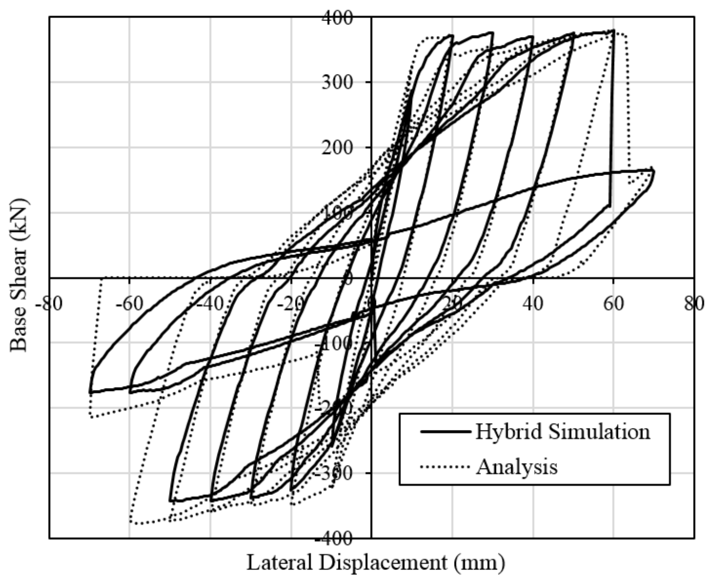

Figure 5.56 Load-deflection response for flexure-critical frame

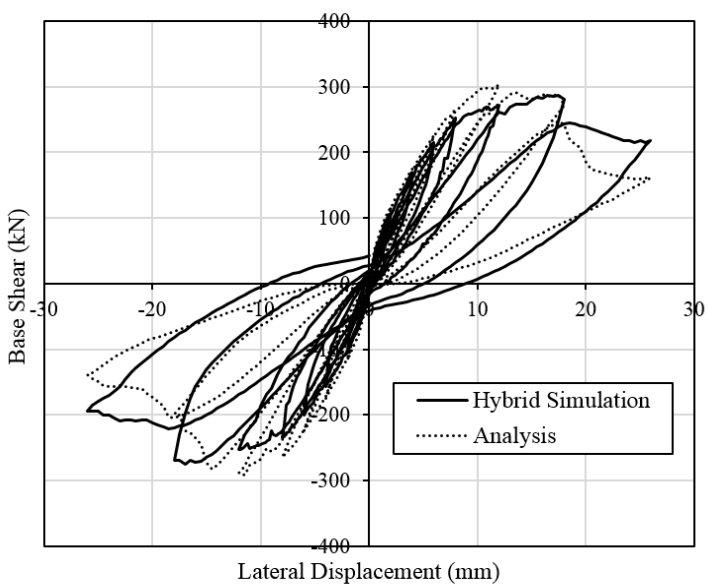

Figure 5.57 Load-deflection response for shear-critical frame

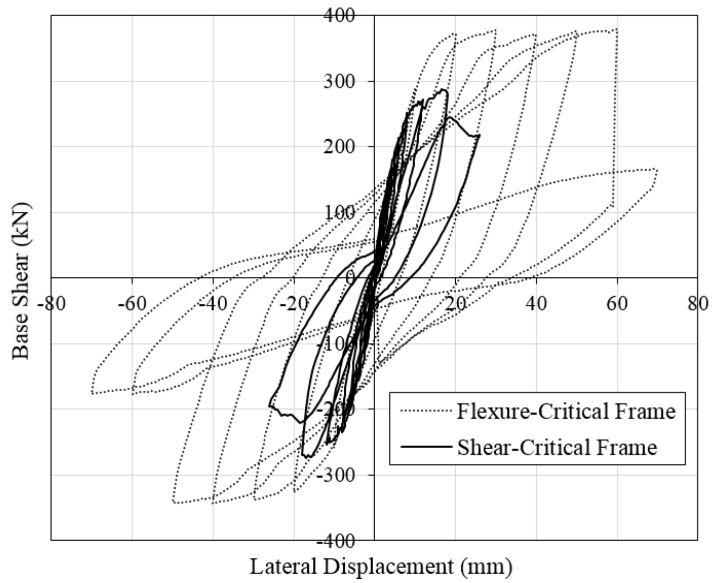

Figure 5.58 Comparison between behaviours of flexure-critical and shear-critical frames

Based on the analysis results of the flexure-critical frame, the yielding of the longitudinal reinforcement and transverse reinforcement initiated at the base of the column in the second and third loading cycles (20 mm and 30 mm), respectively. From the fifth loading cycle (50 mm), the concrete elements located at the toe of the column started to reach the crushing strength. For the shear-critical frame, however, the maximum computed stress in the longitudinal reinforcement was below yielding ($0.89f_y$). Also, yielding of the stirrups and crushing of concrete elements initiated at much lower ductility levels (6 mm and 12 mm, respectively) compared to the flexure-critical frame. For the hybrid tests, the stress and strain of the material components were not measured. To ensure the accuracy of the imposed displacements at the specimen control point, the relative deformations of the concrete end blocks with respect to the end steel plates were monitored using a 3D scanner and external LED targets. Details of the 3D scanner external measurements are provided in Section 5.4.

The crack patterns obtained from the test and analysis at the peak load stage of the final cycle are presented in Figure 5.59 and Figure 5.60 for the flexure-critical and shear-critical frames, respectively. The crack patterns at the peak load stage of all the cycles are provided in Appendix A. It can be seen that, for both structures, the crack pattern of the hybrid test correlated reasonably well with that computed by the analysis. The following is a brief description of the crack development for each frame structure.

For the flexure-critical frame, the primary crack which ultimately caused the failure of the test specimen developed in the horizontal direction along the base of the column. Two minor flexural cracks with approximately 80 mm spacing from the base were also observed. In addition to flexural cracks, the specimen experienced two small diagonal shear cracks extending from the base to about the mid-height of the specimen in the opposite direction. A similar crack pattern was computed by the analysis. As seen in Appendix A, by the fourth loading cycle, the first four rows of the elements at the base exhibited major flexural cracks. After this loading cycle, these cracks were accompanied by two diagonal shear cracks which continued as vertical cracks along the longitudinal reinforcement layers. By the final loading cycle, the first eight rows of the elements at the base demonstrated large flexural cracks. The lower number of flexural cracks and the highly concentrated damage zone observed in the small-scale specimen were aligned with the findings of most previous small-scale tests reported in the literature (see Section 5.2).

For the shear-critical frame, both the test and analysis exhibited two large diagonal shear cracks, in an X-shaped at each end of the column, which then continued as sliding cracks along the longitudinal reinforcement layers. The specimen experienced a brittle type of failure due to sudden opening of the shear and sliding cracks at the positive loading cycles, matching the behaviour obtained from the analysis. Compared to the positive loading cycles, a fewer number of cracks with smaller crack widths was observed during the negative loading cycles, possibly the result of material property variation in the specimen or scaling effects. As seen in Appendix A, the shear crack development in the analysis initiated at an earlier load stage compared to the small-scale specimen. A similar behaviour was observed in the shear-critical reinforced concrete columns tested by Ohtaki (2000). He reported that the full-scale column experienced cracking and shear strength degradation at earlier load stages than the scaled columns.

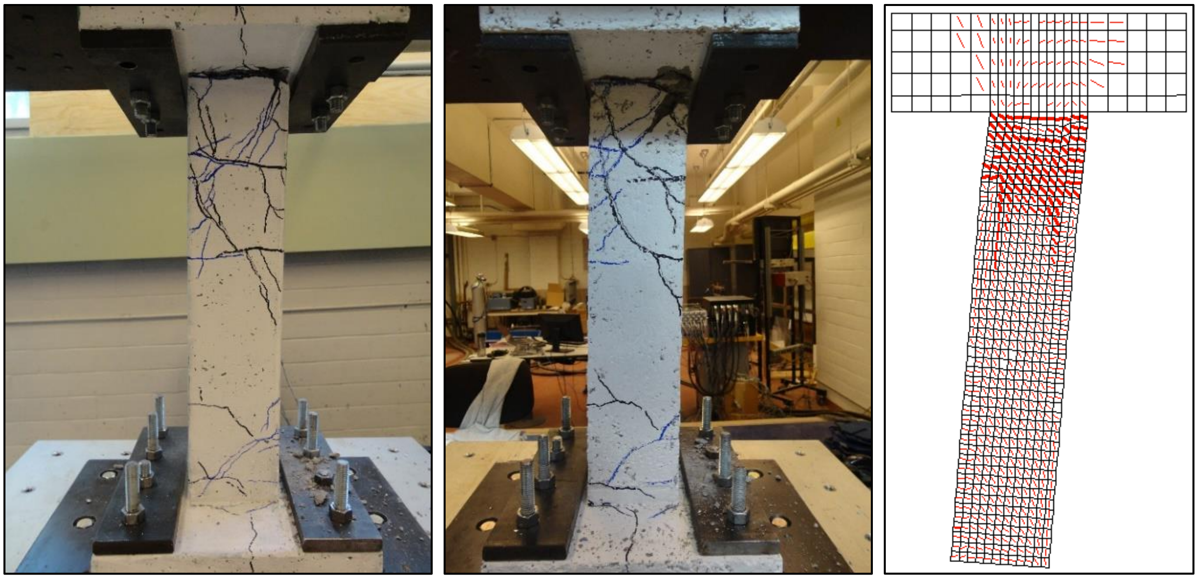

(a) (b) (c)

Figure 5.59 Flexure-critical column crack pattern at the final loading cycle: (a) specimen front view; (b) specimen back view (reversed); (c) FE analysis (magnification factor = 2)

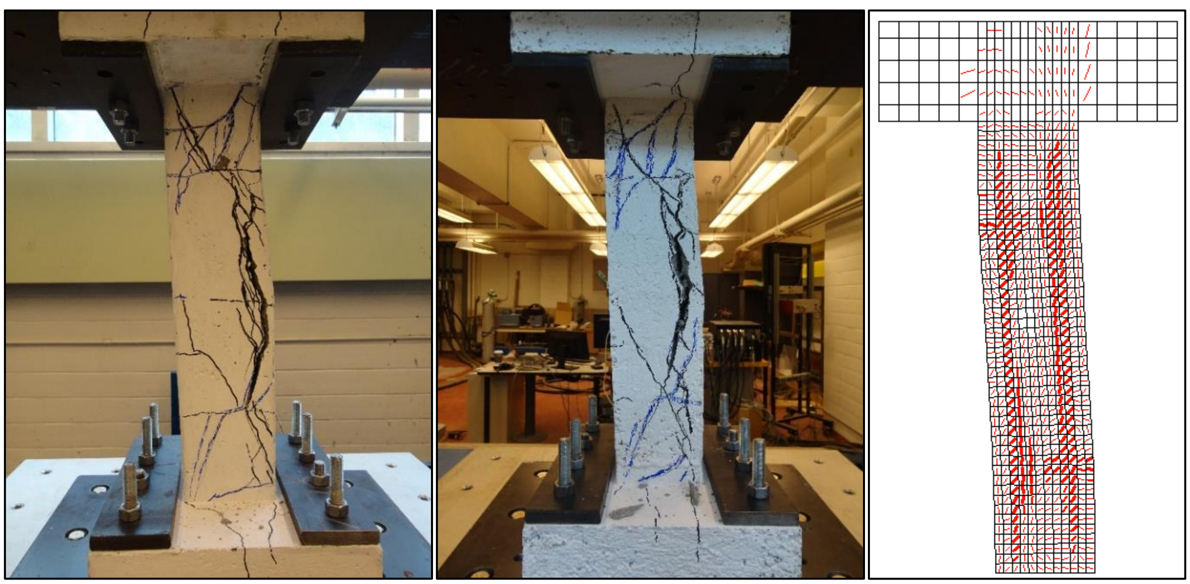

(a) (b) (c)

Figure 5.60 Shear-critical column crack pattern at the final loading cycle: (a) specimen front view; (b) specimen back view (reversed); (c) FE analysis (magnification factor = 2)

5.7 Hybrid Simulation of a RC Frame Structure with Shear-Critical Beams

5.7.1 Reference Structure

In 2007, an experimental study was conducted at the University of Toronto to assess the behaviour of a shear-critical reinforced concrete frame under simulated seismic loads (Duong et al., 2007). A one-bay two-storey frame with inadequate shear reinforcement in the beams was tested under a constant axial load and a reversed cyclic lateral displacement. The test frame suffered large shear cracks in both the first-storey and second-storey beams. In this study, the behaviour of the frame was re-examined in small-scale using a multi-axial hybrid simulation technique. To evaluate the scaling effects on the shear behaviour and assess the performance of the multi-axial hybrid simulation, the test results were compared against those obtained from the full-frame test and from the finite element analysis.

Details of the frame are shown in Figure 5.61. An axial load of 420 kN was imposed on each column and maintained constant during the test in a force-controlled manner. The lateral load was applied in a displacement-controlled manner at the mid-depth of the second-storey beam. The beams had a clear span of 1500 mm and the columns' clear storey height was 1700 mm. Both the beams and columns had a rectangular cross section with dimensions of 300 mm × 400 mm. The columns were attached to a reinforced concrete base having dimensions of 4100 mm × 800 mm × 400 mm, post-tensioned to the strong floor. The longitudinal reinforcement of the beams and columns consisted of eight 20M bars located at top and bottom of the section (ρ_l = 2.00%). US #3 bars with a spacing of 300 mm and 10M bars with a spacing of 130 mm were used as the shear reinforcement in the beams and columns, respectively. The transverse reinforcement ratio of the columns (ρ_v = 1.02%) was markedly higher than the respective value of the beams (ρ_v = 0.16%). It is worth noting that the minimum shear reinforcement ratio of the section required by CSA-A23.3 was 0.08%. Table 5.8 presents the concrete and reinforcement material properties reported in the original test.

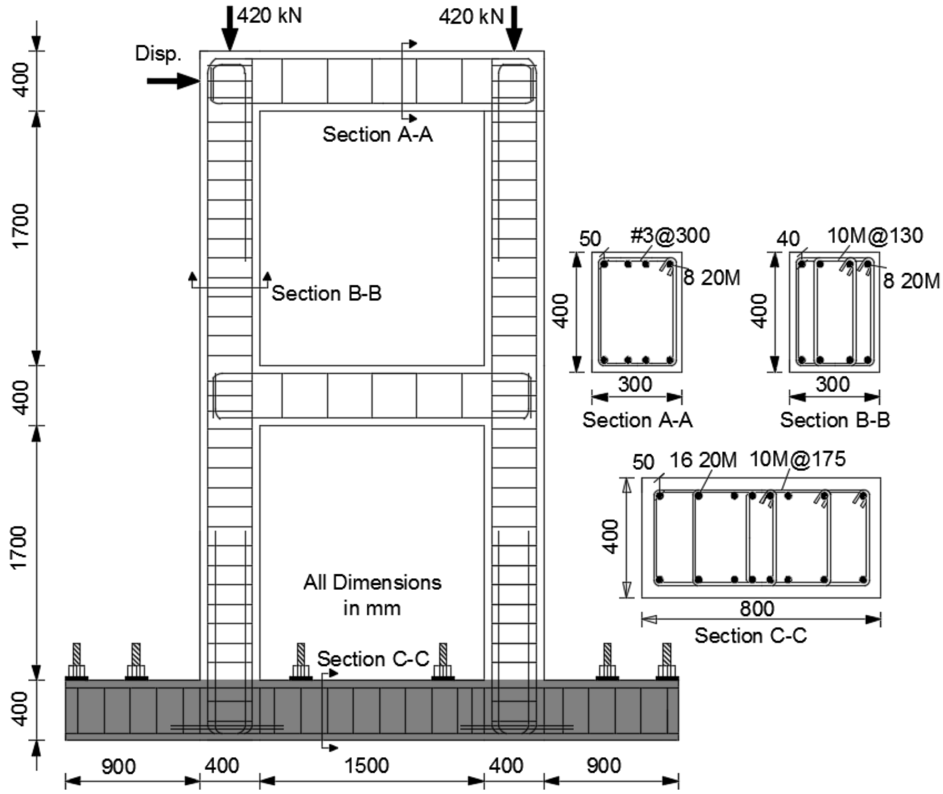

Figure 5.61 Details of Duong frame (dimensions in millimeters)

Table 5.8 Material properties of Duong frame

Concrete		
f'c (MPa)	ε_o ($\times 10^{-3}$)	Max Agg. Size (mm)
43	2.31	10

Reinforcement							
Bar Size	Diameter (mm)	Area (mm^2)	f_y (MPa)	f_u (MPa)	E (MPa)	E_{sh} (MPa)	ε_{sh} ($\times 10^{-3}$)
10M	10	100	455	583	192,400	1195	22.8
20M	20	300	447	603	198,400	1372	17.1
US #3	9.5	71	506	615	210,000	1025	28.3

5.7.2 Physical Specimen

For the hybrid simulation, a 1/3.23-scale representation of the lower storey beam, the most critical member of the frame, was constructed. Details of the model material preparation including microconcrete mix design, reinforcing bar heat treatment process, and the related stress-strain responses are presented in Section 5.6.2.1. It can be seen that the behaviour of the small-scale materials was comparable to that reported from the prototype test.

A similar formwork to that prepared for the column specimen described in Section 5.6.2.2 was constructed. The formwork included two reinforced concrete end blocks with dimensions of 250 mm × 93 mm × 70 mm and a test region representing the scaled beam with dimensions of 464 mm × 124 mm × 93 mm. The end block was heavily reinforced with three D4 closed stirrups, four 12.7 mm (0.5”) diameter threaded rods, two 25.4 mm (1”) thick steel clamp plates, and a 12.7 mm (0.5”) thick steel end plate. High strength threaded rods and bolts were used to post-tension the end blocks to the loading table and the top support beam. Figure 5.62 shows dimensions of the model specimen.

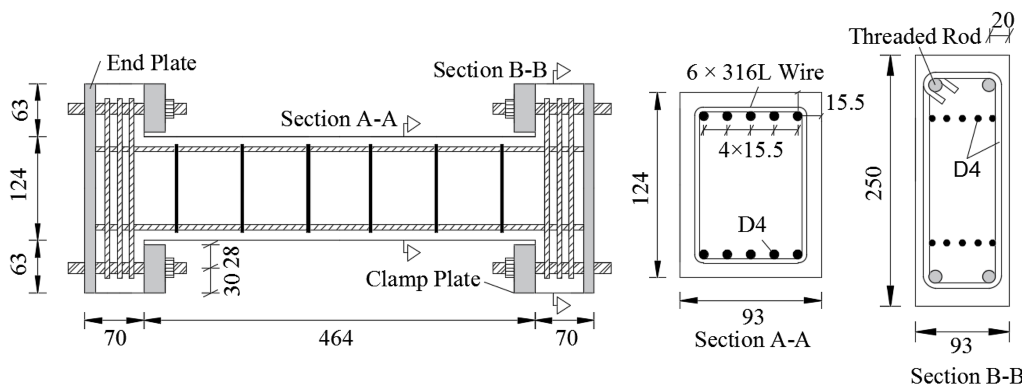

Figure 5.62 Details of small-scale beam specimen (dimensions in millimeters)

The reinforcement configuration of the scaled beam was adjusted so that the yielding forces of the model specimen and the prototype beam were in correct proportion. For the longitudinal reinforcement, 10 heat treated D4 bars with an average measured diameter of 5.73 mm and an average yielding strength of 413 MPa were used. For the transverse reinforcement, six 316L stainless steel wires with an average measured diameter of 3.10 mm and an average yielding strength of 411 MPa were employed. The computed yielding forces of the model beam were 4% and 8% higher in the longitudinal and transverse directions, respectively, to those obtained from the prototype beam, and thus were deemed acceptable. According to the scaling factor, a concrete cover thickness of 15.5 mm was used for the model beam specimen. A similar procedure to that described in Section 5.6.2.2 was used to assemble the formwork and cast the specimen and four standard size cylinders (100 mm × 200 mm). Figure 5.63 depicts different stages of the specimen preparation.

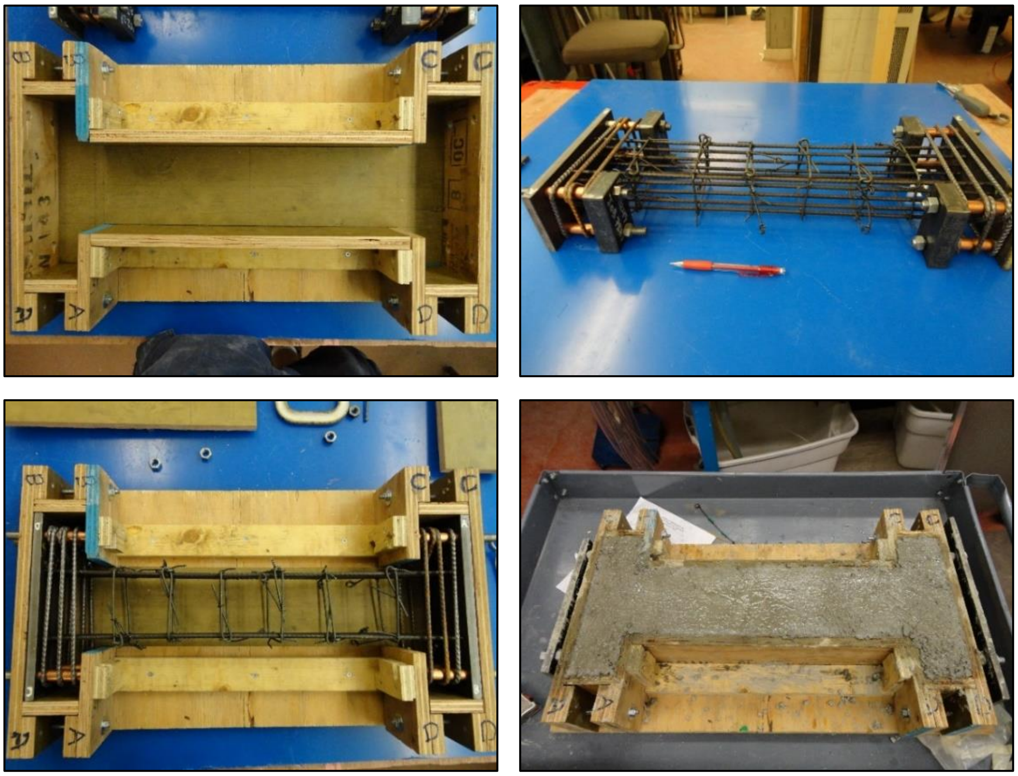

Figure 5.63 Model beam specimen preparation steps

5.7.3 Numerical Models

For the mixed-type analysis, the shear-critical beams were modelled in VecTor2 using membrane elements, while the remainder of the frame was modelled in VecTor5 with layered beam elements. The VecTor2 sub-model comprised of 820 concrete rectangular elements and 164 steel truss elements. The longitudinal reinforcement was represented discretely using truss elements, and the transverse reinforcement was uniformly smeared over the height of the section. The VecTor5 sub-model, which represented non-critical members of the frame, contained 56 layered beam elements each divided into 30 concrete layers. A stiffer section was used for the joint panels to avoid artificial failure. A constant nodal force of 420 kN was imposed in the downward direction at the top node of each column. Also, the horizontal displacement of the top left corner node was controlled in a reversed cyclic manner with increments of 0.1 mm. The post-tensioned bolts that provided a fix support for the frame base were modelled by restraining the corresponding nodes in the translational and rotational directions. For the hybrid simulation, the numerical substructure was identical to that used for the mixed-type analysis except that the first-storey beam was replaced with the test specimen. The default material models and analysis parameters defined in all VecTor software programs were used. Figure 5.64 shows details of the mixed-type analysis and hybrid simulation models.

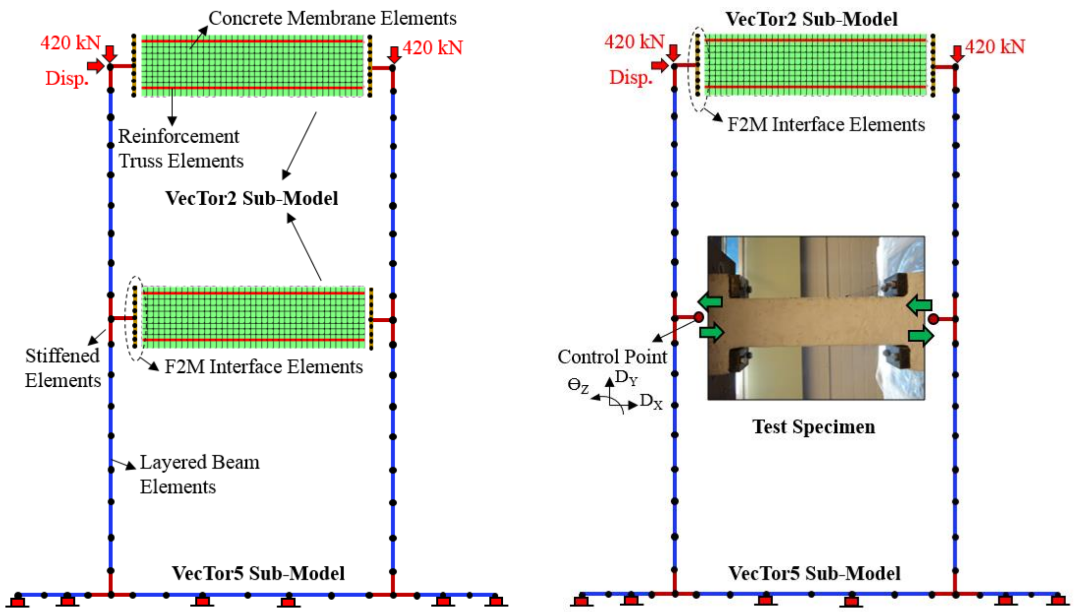

Figure 5.64 FE models for mixed-type analysis (left) and hybrid simulation (right)

5.7.4 Results and Discussions

The hybrid simulation testing procedure for the Duong frame was similar to that used for the one-storey frame structures presented in Section 5.6.4. Likewise, the initial stiffness of the specimen was estimated as 29,600 MPa and increased by 10% to prevent any potential noise in the simulation.

The load-deflection response of hybrid simulation was compared against those obtained from the full-frame test and mixed-type analysis in Figure 5.65. In general, the hybrid simulation response correlated well with the mixed-type analysis results and was comparable to the full-frame test data. Both the hybrid simulation and analysis overestimated the stiffness and strength of the frame in the forward loading cycle. This was mainly attributed to the effects of the drying shrinkage that occurred in the full-frame specimen during the nine months between casting the concrete and testing the specimen. Conversely, the model specimen was not influenced by shrinkage effects because the time between the casting and testing was short (14 days) and also the beam specimen was not restrained by the columns as they were numerically modelled. To be consistent with the physical component, the shrinkage effects were not considered in the hybrid simulation numerical component nor the mixed-type analysis. In Section 4.6.1 of Chapter 4, the same structure was analyzed with inclusion of shrinkage strains which resulted in a better estimation of stiffness and ultimate strength. Furthermore, the stiffness and strength of the initial loading cycles were lower for the hybrid simulation compared to the mixed-type analysis which was reasonable given that the microconcrete exhibited a softer response than the prototype concrete at the material-level.

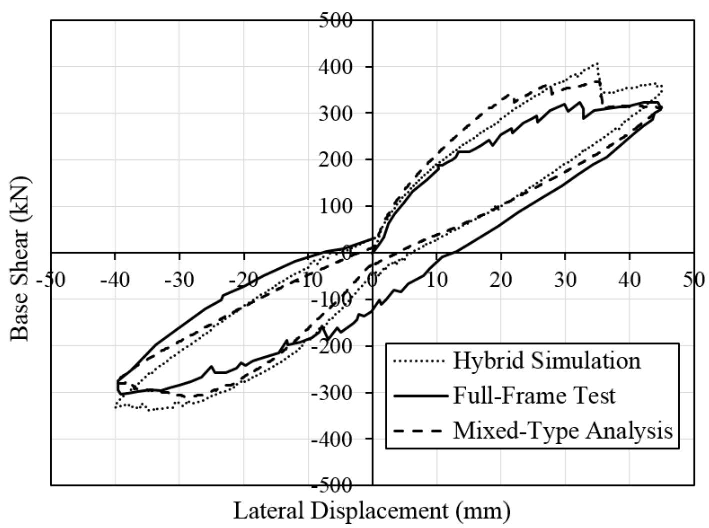

Figure 5.65 Comparison of the load-deflection responses for the Duong frame

As seen in Figure 5.65, both the hybrid simulation and the analysis overestimated the pinching effect compared to the full-frame test. For the full-frame test, the longitudinal reinforcement in the beam reached the yielding stress (447 MPa) at the lateral displacement of 25.5 mm; however, the maximum stress computed by the analysis was marginally below the yielding stress (434 MPa). Thus due to the yielding of the longitudinal reinforcement in the beams, the full-frame test experienced higher plastic strains and permanent damage than the analysis, resulting in a fatter hysteretic response. A similar argument can be made for the hybrid simulation since the second-storey beam was numerically modelled. It is worth noting that the hybrid test resulted in slightly better simulation of pinching behaviour than the analysis. In addition, the analysis computed yielding of the transverse reinforcement in the first- and second-storey beams in the forward loading cycle which agreed with the results reported from the full-frame test. The numerical model of the hybrid simulation also led to similar stress values in the second-storey beam. For the physical component of the hybrid simulation, due to the scaled dimensions of the specimen, the strain values in the reinforcing bars and wires were not measured.

The crack pattern of the lower-storey beam obtained from the hybrid simulation, full-frame test, and finite element analysis, at the peak displacement in the forward and backward loading cycles, are presented in Figure 5.66 and Figure 5.67, respectively. Also, the experimental and numerical crack development for the intermediate loading cycles are provided in Appendix A. It can be seen that the crack pattern of the hybrid simulation correlated reasonably well with those reported from the full-frame test and computed by the analysis. In addition, the final crack inclinations in the model specimen and full-frame test were similar. However, like most previously reported small-scale tests, for a particular loading cycle the model beam exhibited a fewer number of cracks and smaller crack widths than did the prototype structure. A brief description of the experimental and numerical crack development is provided in the following.

In the forward loading cycle, the model specimen experienced two diagonal shear cracks located at each end of the specimen. Also, two flexural cracks developed at the interface of the beam and the end blocks. Although the crack pattern was similar to those exhibited by the prototype beam and analysis, the following differences were observed: 1) the shear crack width was significantly smaller in the model specimen, 2) for the prototype beam, a horizontal crack developed along the longitudinal reinforcement at the bottom of the section which was not fully captured in the model specimen, and 3) the prototype specimen experienced several flexural cracks near the interface of the beam and the column, while the flexural cracks in the model specimen were more concentrated. These discrepancies were primary the consequence of the scaling effects as it has been shown that small-scale tests experience shear strength degradation in later load stages with a lower number of cracks compared to large-scale tests (see Section 5.2).

The crack pattern of the backward loading cycle was similar to that observed in the forward cycle. The shear crack width and the horizontal crack along the longitudinal reinforcement was captured with better accuracy. However, the shear crack that developed at the mid-span of the prototype beam was not simulated in the model specimen.

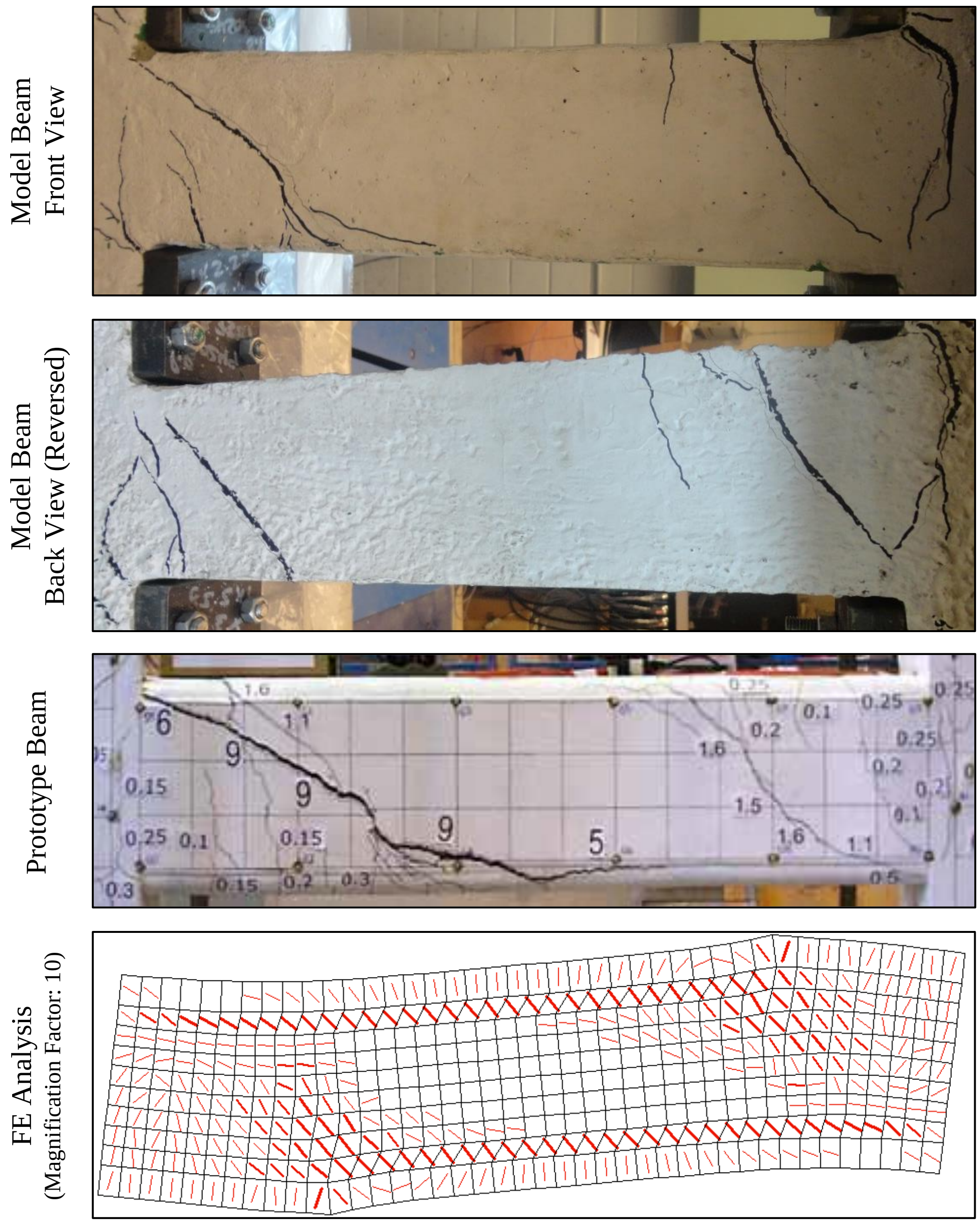

Figure 5.66 Crack pattern of Duong frame first-storey beam at peak displacement of forward cycle (Displacement = +45 mm)

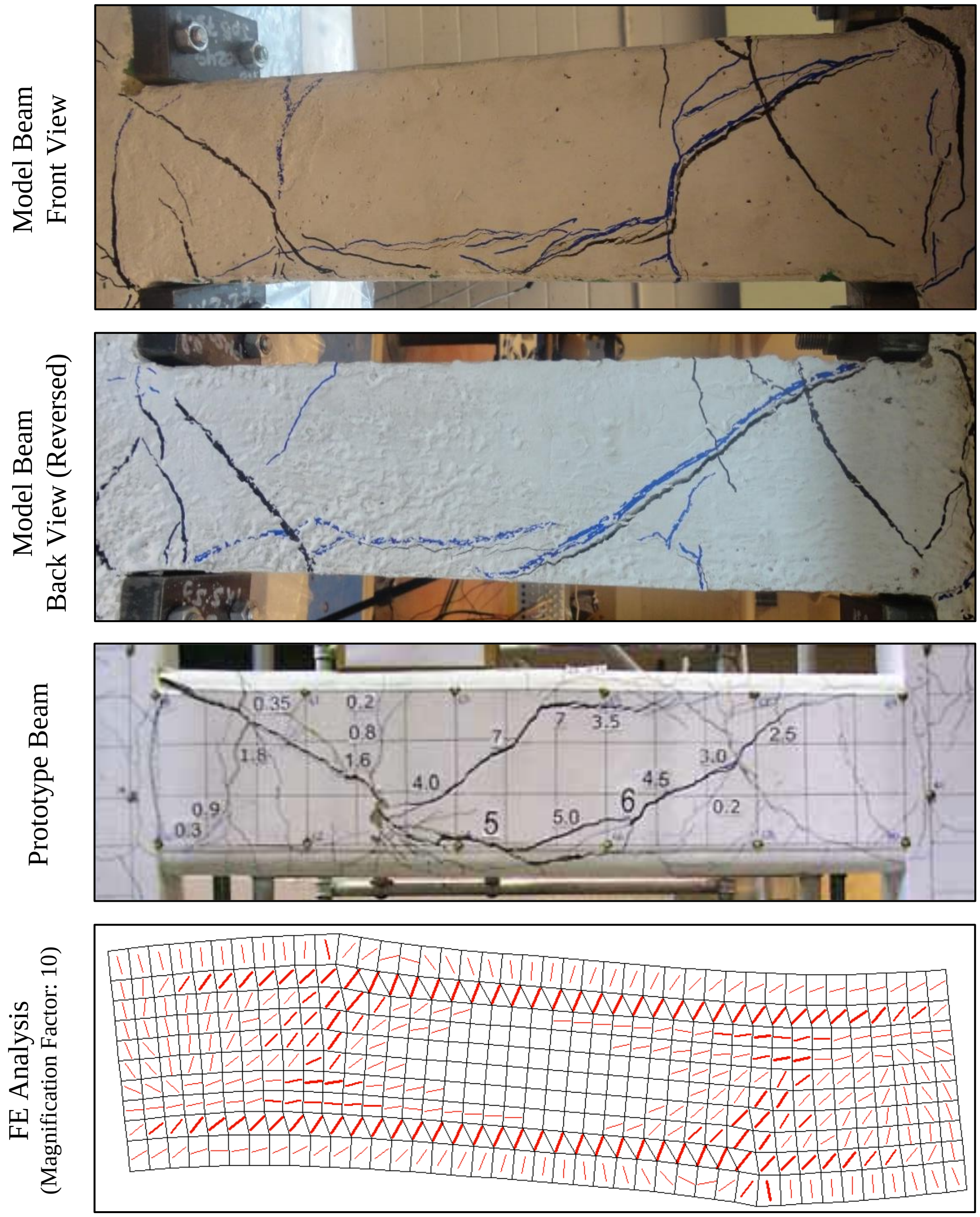

Figure 5.67 Crack pattern of Duong frame first-storey beam at peak displacement of backward cycle (Displacement = -40 mm)

In conclusion, based on the load-deflection response, crack pattern of the physical substructure, and stress values of the numerical substructure, the small-scale hybrid simulation found significant shear degradation in the beams due to inadequate shear reinforcement which was consistent with the results reported from the full-frame test.

5.8 Summary and Conclusions

The multi-platform framework, Cyrus, was enhanced with hybrid simulation capability enabling the integration of physical test specimens with numerical models. To evaluate the performance of the hybrid simulation framework and investigate the behaviour of model reinforced concrete members, a small-scale testing program was carried out using multi-axial hydraulic testing equipment. The experimental program was comprised of three parts: 1) hybrid simulations of two steel frame structures within the linear elastic range, 2) hybrid simulations of two reinforced concrete frame structures with different failure modes, and 3) hybrid simulation of a shear-critical reinforced concrete frame that had been previously tested as a full-frame specimen. All the hybrid simulations were conducted using 1/3.23 scale test specimens and in a quasi-static manner. In addition, material tests were performed to properly simulate the behaviour of concrete and reinforcement in small-scale. The material and structural test results support the following conclusions:

- The results obtained from the external LED displacement measurements and steel frame tests verified the accuracy of the proposed hybrid simulation system. The displacements and reactions at the control point of the specimen were accurately measured.

- The material test results showed that with the use of a proper mix design for the microconcrete and a heat treatment process for the reinforcing bars, the stress-strain response of the prototype material can be sufficiently well simulated in small-scale. To control the excessive compressive strains of microconcrete, adjusting the W/C ratio, limiting the minimum size of aggregate, modifying the aggregate gradation, and considering the maturity level of the mix was necessary.

- The hybrid test results of the reinforced concrete frames demonstrated that, if proper precautions are taken in preparing the model materials and constructing the scale specimen, small-scale hybrid simulation can represent the behaviour of the prototype structure reasonably well. In particular, the failure mode, load-deflection response, and crack pattern were accurately captured. However, for all three specimens, the small-scale test led to a fewer number of cracks with a more concentrated damage zone compared to the prototype specimen and finite element analysis. Also, due to scaling effects, the strength degradation occurred in later load stages, resulting in smaller final crack widths in the model specimens. These discrepancies between the small-scale and prototype behaviours were considered acceptable as most previous small-scale studies have reported similar findings.

- The main motivation behind the Duong frame large-scale test was to investigate the behaviour of an existing cement preheater tower located in El Salvador which had several deficiencies including inadequate shear reinforcement amount in the beams. In this study, the same structure was successfully tested in a hybrid simulation manner with a small-scale model of the lower-storey beam representing the physical component. Compared to the full-frame test, the hybrid test required significantly less preparation time, labor, and laboratory space. Although the promising results of this study demonstrated the effectiveness of the small-scale hybrid simulation technique as an affordable testing method in assessing the general behaviour of a real-world structure, more test data are required to further investigate the application of hybrid simulation to model test specimens. Specifically, measuring the strain values in the model specimen to determine potential yielding of the reinforcing bars and crushing of the microconcrete can greatly benefit the assessment process. Due to the above-mentioned limitations in small-scale testing, care should be taken in interpreting the results and drawing conclusions regarding the behaviour of similar real-size structures.

CHAPTER 6

SUMMARY, CONCLUSIONS AND RECOMMENDATIONS

6.1 Summary

The primary focus of this research study was to develop a new multi-platform simulation framework that addressed some of the deficiencies of previous formulations, allowing for a more realistic analysis of complex reinforced concrete structures or multi-disciplinary systems. The integrated simulation procedure developed accordingly is applicable to both academic and commercial analysis programs. The mathematical basis for integration of analysis tools with different solution schemes was provided. The object-oriented architecture of the framework and the implementation of a standardized data exchange format facilitates the addition of new analysis tools to the framework. The effectiveness of the framework was demonstrated by several verification and application examples.

In addition, the application of the multi-platform analysis to reinforced concrete structures repaired with FRP sheets was investigated by modelling and analyzing specimens of two experimental studies reported in the literature. The influence of damage effects, FRP-related mechanisms, and buckling of longitudinal bars were discussed in detail.

As a secondary analytical objective, a new beam-membrane interface element, the F2M element, was developed. It was specifically formulated for mixed-dimensional analysis of reinforced concrete structures. The procedure satisfies equilibrium and compatibility requirements at the connection section. Also, it is capable of computing linear and nonlinear stress distributions including shear stresses at the interface section reasonably well. The accuracy of the proposed interface element was compared against the full membrane models and two other commonly used coupling methods.

The proposed simulation framework was further extended to combine numerical models with experimental components to accommodate hybrid testing. The experimental modules were integrated using a generalized interface program compatible with a wide range of laboratory equipment and testing configurations. A small-scale experimental program was conducted using a six degree-of-freedom hydraulic testing facility to verify the framework and provide additional data for small-scale testing of shear-critical reinforced concrete structures. The hybrid simulation results were compared against those obtained from a similar large-scale test and from finite element analyses.

6.2 Conclusions

This section describes the main conclusions from the research program. For clarity, findings from the experimental and the analytical parts are presented separately.

With respect to the analytical phase, the main conclusions of the research study are the followings:

- Multi-platform analyses enable the computation of the behaviour of large complex structures with a level of accuracy that was previously difficult to achieve with most single-platform analysis software (verification examples are presented in Section 2.4.1 and Section 2.4.2 of Chapter 2).
- The multi-platform simulation method provides global frame-type analysis with an effective solution technique for the detailed modelling of disturbed regions, such as beam-column joints, and bond effects between the reinforcement and concrete.
- Taking into account soil-structure interaction can influence the behaviour of a structure and result in new damage zones, especially if the structure is located on soft soil. Multi-platform simulation can be a reliable analysis procedure to consider the soil effects, providing a more realistic behaviour of the structure (a demonstration example is presented in Section 2.4.3 of Chapter 2).
- Multi-platform analysis enables the use of parallel computing which can substantially reduce the overall simulation time. However, for systems with a large number of substructures, the communication time between the substructure modules and the framework can be significant and can adversely affect the total simulation time (a demonstration example is presented in Section 2.4.4 of Chapter 2).

- In general, multi-platform analyses were able to accurately predict the behaviour of the specimens repaired with FRP sheets particularly in terms of stiffness, peak load, ductility, and failure mode. Changes in the damage mode prior to and after the repair of the frame structure were captured sufficiently well (verification examples are presented in Section 4.6.1 and Section 4.6.2 of Chapter 4).

- For RC frame structures, insufficient consideration of shear-related effects can lead to significant overestimations of strength and deformation capacity, and inaccurate predictions of structure behaviour. Most frame analysis procedures, including plastic hinge and layered analysis approaches, require difficult assumptions and inputs to account for shear mechanisms which can significantly affect structural response.

- For axially loaded members such as bridge piers and columns, buckling of the longitudinal reinforcement and damage effects prior to repair can significantly affect the response of the repaired structure.

- For RC specimens repaired with more than two layers of GFRP sheets, the analysis had a tendency to overestimate the peak loads. This may be a consequence of slip between layers of FRP sheets or lower effective confinement due to the square shape of the columns, known as arching action.

- In order to have an effective and efficient repair strategy, taking into account the influence of component-level analysis on the system-level behaviour and recognizing the force redistributions within the structure is important (a demonstration example is presented in Section 4.6.2 of Chapter 4).

- Overall, mixed-type analyses based on the F2M element provided reliable and consistently accurate calculations of the initial stiffnesses, peak loads, and ductilities for the beam specimens studied. Using a proper substructuring configuration, the mixed-type analysis results were sufficiently close to the stand-alone analysis results and to the experimentally reported values (a verification example is presented in Section 3.4 of Chapter 3).

- The F2M element was able to capture the shear failure at the interface section and accurately compute the reduction in stress levels of the cracked concrete elements and consequently the increase in the stress values of uncracked elements, resulting in axial and shear stress distributions which correlated reasonably well with the stand-alone detailed FE analysis results. Conversely to the F2M element, the Rigid Links method and the McCune et al. (2000) method had major limitations in capturing both the global and local behaviour of cracked reinforced concrete members.

- Caution must be taken in using a mixed-type simulation method. Creating a proper mixed-type model requires having a good understanding of the expected behaviour of the structure and an anticipation of the location of critical regions prior to the analysis.

With respect to the experimental phase, the following conclusions can be drawn:

- The results obtained from the hybrid simulations of the steel frame structures agreed well with the external measurements and linear elastic analysis responses, verifying the performance of the proposed hybrid simulation framework.

- The material test results showed that with the use of a proper mix design for the microconcrete and a heat treatment process for the reinforcing bars, the stress-strain response of the prototype material can be sufficiently well simulated in small-scale. To control the excessive compressive strains of microconcrete, adjusting the W/C ratio, limiting the minimum size of aggregate, modifying the aggregate gradation, and considering the maturity level of the mix was necessary.

- The hybrid test results of the reinforced concrete frames demonstrated that, if proper precautions are taken in preparing the model materials and constructing the scale specimen, small-scale hybrid simulation can represent the behaviour of the prototype structure reasonably well. In particular, the failure modes, load-deflection responses, and crack patterns were accurately captured.

- The small-scale tests led to a fewer number of cracks with a more concentrated damage zone compared to the prototype specimen and to the finite element analysis. Also, due to scaling effects, the strength degradation occurred in later load stages, resulting in smaller final crack widths in the model specimens. These discrepancies between the small-scale and prototype behaviours were considered acceptable as most previous small-scale studies reported similar findings.

6.3 Recommendations

Throughout the numerical and experimental parts of this research study, there were several issues identified that could benefit from some level of further development or investigation:

- The interface program used in the simulation framework is compatible with Zeus-NL, OpenSees, ABAQUS, and the VecTor suite of software. The integration of the different types of VecTor programs with each other and with OpenSees was verified in this study. The application of the framework to the remainder of the analysis tools should also be verified.

- Although the soil-structure interaction example and the computational performance evaluation study demonstrated the capabilities of the simulation framework to some extent, they were limited to simplified systems. To fully illustrate the value of the multi-platform simulation in the areas of multi-disciplinary modelling and parallel computing, more realistic systems should be investigated. Particularly, the performance evaluation tests should be performed on larger structural systems. Also, for structural-geotechnical systems, the behaviour of the soil at the material-level and the mechanisms at the soil interface with the structure (e.g., friction effects) should be studied in detail.

- The current version of the simulation framework can integrate different VecTor programs for dynamic analysis (details are provided in Section 2.5 of Chapter 2). A comprehensive verification study is required to assess the performance of the analysis procedure and identify its capabilities and limitations.

- To integrate other analysis tools or test specimens for dynamic simulation, a time integration scheme should be implemented in the framework. The time integration scheme enables the framework to account for the dynamic characteristics of the structure including the mass and damping. The measured and computed restoring forces are collected by the framework from the substructure modules and incorporated into the equation of motion.

- The simulation framework provides a unique analysis technique for RC frame structures with critical joint panels. The comparison of the method with other approaches available in the literature can help to identify its strengths and weaknesses.

- With respect to the multi-platform modelling of repaired RC structures, the bond-slip material model utilized in the analysis was derived for externally bonded FRP sheets under monotonic loading conditions. To take into account plastic deformations and stress degradations of link elements under cyclic loading conditions, a more comprehensive bond-slip model is required to be implemented in the VecTor2 finite element program.

- For link elements representing the interface between FRP and concrete, displacements in the radial direction were prevented by assigning a very large value to the radial stiffness. This compromised the ability to consider delamination of the FRP sheets. Further development is required to define the radial stiffness of link elements according to available models in the literature, particularly for the analysis of repaired structures experiencing a delamination type of failure.

- The idea of F2M interface element can be extended to other types of mixed-dimensional problems such as connection between three-dimensional layered frame elements and solid elements. In addition, the formulations can be used to develop a new type of nonlinear shear spring, based on the MCFT and DSFM models, to take into account shear behaviour in frame-type analysis procedures.

- Although the promising results of this study demonstrated the effectiveness of the small-scale hybrid simulation technique as an affordable testing method in assessing the general behaviour of structures, more test data are required to further investigate the application of hybrid simulation to model test specimens. Specifically, measuring the strain values in the model specimen to determine potential yielding of the reinforcing bars and crushing of the microconcrete can greatly benefit the assessment process. Due to the above-mentioned limitations in small-scale testing, care should be taken in interpreting the results and drawing conclusions regarding the behaviour of similar real-size structures.

REFERENCES

AASHTO LRFD Bridge Design Specifications (2012). 6th edition, American Association of State Highway and Transportation Officials, Washington, D.C., U.S.A., 1661 pp.

ABAQUS (2012). "ABAQUS/CAE Users' Manual", Dassault Systèmes Simulia Corp., Providence, R.I., U.S.A., 1137 pp.

Abrams, D.P. (1976). "Measured Hysteresis Relationships for Small-Scale Beams", Issue of 432 of Civil Engineering Studies, University of Illinois at Urbana-Champaign, I.L., U.S.A., 160 pp.

Abrams, D.P. (1987). "Scale Relations for Reinforced Concrete Beam-Column Joints", *ACI Structural Journal*, Vol. 84, No. 6, pp. 502-512.

ACI Committee 444 (1970). "Models of Concrete Structures", *ACI Special Publication*, No. 24, 448 pp.

ACI/ASCE Committee 447 "Finite Element Analysis of RC Structures".

Adams, V. and Askenazi, A. (1999). "Building Better Products with Finite Element Analysis", On Word Press, Santa Fe, N.M., U.S.A., 624 pp.

Akkaya, Y., Guner, S., and Vecchio, F.J. (2013). "Modeling Inelastic Buckling Behavior of Reinforcing Bars", *Proceedings of ACI Conference*, Phoenix, A.Z., U.S.A.

Al-Mahaidi, R., Lee, K., and Taplin, G. (2001). "Behavior and Analysis of RC T-Beams Partially Damaged in Shear and Repaired with CFRP Laminates", *Proceedings of Structural Congress and Exposition, ASCE*, Reston, V.A., U.S.A.

Aycardi, L., Mander, J., and Reinhorn, A. (1994). "Seismic Resistance of Reinforced Concrete Frame Structures Designed for Gravity Loads: Experimental Performance of Subassemblages", *ACI Structural Journal*, Vol. 91, No. 5, pp. 552-563.

Balay, S., et al. (2014). "Portable, Extensible Toolkit for Scientific Computation (PETSc) User's Manual" Argonne National Laboratory, University of Chicago, I.L., U.S.A.

Bathe, K.J. (1982). "Finite Element Procedures in Engineering Analysis", Prentice-Hall, Englewood Cliffs, N.J., U.S.A., 736 pp.

Bathe, K.J., Wilson, E.L., and Iding, R. (1974). "NONSAP - A Structural Analysis Program for Static and Dynamic Response of Nonlinear Systems", Report UCSESM 74-3, University of California, Berkeley, C.A., U.S.A., 72 pp.

Bazant, Z.P. and Kazemi, M.T. (1991). "Size Effect on Diagonal Shear Failure of Beams without Stirrups", *ACI Structural Journal*, Vol. 88, No. 3, pp. 268-276.

Bentz, E.C. (2000). "Presentation at ACI Convention", Toronto, Canada.

Bresler, B. and Scordelis, A.C. (1963). "Shear Strength of Reinforced Concrete Beams", *ACI Journal*, Vol. 60, No. 1, pp. 51-74.

Buckingham, E. (1914). "On Physically Similar Systems; Illustrations of the Use of Dimensional Analysis", *Physical Review Letters*, Vol. 4, No. 4, pp. 345-376.

Caccese, V. and Harris, H.G. (1990). "Earthquake Simulation Testing of Small-Scale Reinforced Concrete Structures", *ACI Structural Journal*, Vol. 87, No. 1, pp. 72-80.

Calvi, G.M., Magenes, G., and Pampanin, S. (2002). "Experimental Test on a Three Storey RC Frame Designed for Gravity Only", *12th European Conference on Earthquake Engineering*, London, U.K.

Carr, A.J. (2005). "User's Manual for the 2-Dimensional Version Ruaumoko2D", Department of Civil Engineering, University of Canterbury, Christchurch, New Zealand, 87 pp.

Castaneda, N., Gao, X., and Dyke, S.J. (2015). "Computational Tool for Real-Time Hybrid Simulation of Seismically Excited Steel Frame Structures", *ASCE Journal of Computing in Civil Engineering*, Vol. 29, No. 3, 1943-5487.0000341.

CEB-FIP (1990). "Model Code for Concrete Structures", Design Code, Comité EURO International du Béton, 437 pp.

Chang, S.C. and Lin, T.W. (1988). "Constraint Relation Implementation for Finite Element Analysis from an Element Basis", *Advances in Engineering Software*, Vol. 10, No. 4, pp. 191-194.

Chen, H.M. and Archer, G.C. (2001). "A Distributed Object-Oriented Finite-Element Analysis Program Architecture", *Computer-Aided Civil and Infrastructure Engineering*, Vol. 16, No. 5, pp. 326-336.

Chen, H.M. and Lin, Y.C. (2011). "An Internet-Based Computing Framework for the Simulation of Multi-Scale Response of Structural Systems", *Structural Engineering and Mechanics*, Vol. 37, No. 1, pp. 17-37.

Cho, I.H. and Hall, J.F. (2012). "A Parallelized Implicit Nonlinear FEA Program for Real Scale RC Structures under Cyclic Loading", *Journal of Computing in Civil Engineering*, Vol. 26, No. 3, pp. 356-365.

Collins, M.P. and Kuchma, D. (1999). "How Safe Are Our Large, Lightly Reinforced Concrete Beams, Slabs, and Footings?", *ACI Structural Journal*, Vol. 96, No. 4, pp. 482-490.

Collins, M.P., Vecchio, F.J., and Mehlhorn, G. (1985). "An International Competition to Predict the Response of Reinforced Concrete Panels", *Canadian Journal of Civil Engineering*, Vol. 12, No. 3, pp. 624-644.

Collins, M.P., Vecchio, F.J., and Selby, R.G. (1997). "The Failure of an Offshore Platform", *Canadian Journal of Civil Engineering*, Vol. 24, No. 3, pp. 460-470.

Combescure, D. and Pegon, P. (1997). "α-Operator Splitting Time Integration Technique for Pseudodynamic Testing Error Propagation Analysis", *Soil Dynamics and Earthquake Engineering*, Vol. 16, No. 7-8, pp. 427-443.

Cook, R.D., Malkus, D.S., and Plesha, M.E. (1989). "Concepts and Applications of Finite Element Analysis", Third Edition, John Wiley & Sons Inc., N.J., U.S.A., 630 pp.

Cross, H. (1930). "Analysis of Continuous Frames by Distributing Fixed-End Moments", *ASCE Annual Convention*, Vol. 56, No. 5, pp. 919-928.

CSA Committee A23.3 (2014). “Design of Concrete Structures”, Canadian Standard Association, Rexdale, Ontario, Canada, 297 pp.

CSI (2005). “Analysis Reference Manual for SAP2000, ETABS, SAFE, and CSI-Bridge”, Computers and Structures Inc., Berkeley, C.A., U.S.A., 415 pp.

CSI (2015). “Analysis Reference Manual for SAP2000, ETABS, SAFE, and CSI-Bridge”, Computers and Structures Inc., Berkeley, C.A., U.S.A., 552 pp.

Curiskis, J.L. and Valliappan, S. (1978). “A Solution Algorithm for Linear Constraint Equations in Finite Element Analysis”, *Computers and Structures,* Vol. 8, No. 1, pp. 117-124.

Davis, T.A. (2004). “Algorithm 832: UMFPack-an Unsymmetric-Pattern Multifrontal Method with a Column Pre-Ordering Strategy”, *ACM Transactions on Mathematical Software*, Vol. 30, No. 2, pp. 196-199.

De Lorezis, L., Miller, B., and Nanni, A. (2001). “Bond of Fiber-Reinforced Polymer Laminates to Concrete”, *ACI Material Journal,* Vol. 98, No. 3, pp. 256-264.

Dermitzakis, S.N. and Mahin, S.A. (1985). “Development of Substructuring Techniques for On-Line Computer Controlled Seismic Performance Testing”, Earthquake Engineering Research Center, Report No. 85/04, Department of Commerce, U.S.A., 153 pp.

Dhakal, R.P. and Maekawa, K. (2002a). “Modeling for Post-Yield Buckling of Reinforcement”, *ASCE Journal of Structural Engineering,* Vol. 128, No. 9, pp. 1139-1147.

Dhakal, R.P. and Maekawa, K. (2002b). “Path-Dependent Cyclic Stress-Strain Relationship of Reinforcing Bar Including Buckling”, *Engineering Structures*, Vol. 24, No. 11, pp. 1383-1396.

Duong, K.V., Sheikh, S.A., and Vecchio, F.J. (2007). “Seismic Behavior of Shear-Critical Reinforced Concrete Frame: Experimental Investigation”, *ACI Structural Journal*, Vol. 104, No. 3, pp. 303-310.

ElMohandes, F. and Vecchio, F.J. (2013). “VecTor3 User’s Manual”, Department of Civil Engineering, University of Toronto, Toronto, Canada, 153 pp.

Elnashai, A.S., Papanikolaou, V., and Lee, D. (2008). “Zeus NL - A System for Inelastic Analysis of Structures User’s Manual”, Mid-America Earthquake Center, University of Illinois at Urbana-Champaign, I.L., U.S.A., 149 pp.

El-Sayed, M.E.M. and Hsiung, C.K. (1990). “Parallel Finite Element Computation with Separate Substructures”, *Computers and Structures,* Vol. 36, No. 2, pp. 261-265.

Eslami, A. and Ronagh, H.R. (2013). “Effect of FRP Wrapping in Seismic Performance of RC Buildings with and without Special Detailing - A Case Study”, *Composites Part B: Engineering Journal,* Vol. 45, No. 1, pp. 1265-1274.

Farhat, C. (1987). ‘‘Multiprocessors in Computational Mechanics”, Ph.D. Dissertation, University of California, Berkeley, C.A., U.S.A., 121 pp.

Federal Highway Administration (FHWA) (2014). “Deficient Bridges by Highway System”, Department of Transportation, U.S.A.

Felippa, C.A. (1978). “Iterative Procedures for Improving Penalty Function Solutions of Algebraic Systems”, *International Journal for Numerical Methods in Engineering*, Vol. 12, No. 5, pp. 821-836.

Fuller, W.B. and Thompson, S.E. (1907). “The Laws of Proportioning Concrete”, *Proceedings of ASCE*, Vol. 33, No. 3, pp. 222-298.

Fulton, R.E. and Su, P.S. (1992). “Parallel Substructure Approach for Massively Parallel Computers”, *ASME International Computers in Engineering Conference,* San Francisco, Vol. 2, pp. 75-82.

Galal, K. and El-Sokkary, H. (2008). “Analytical Evaluation of Seismic Performance of RC Frames Rehabilitated using FRP for Increased Ductility of Members”, *ASCE Journal of Performance of Constructed Facilities,* Vol. 22, No. 5, pp. 276-288.

Gambarova, P.G. (1981). “On Aggregate Interlock Mechanism in Reinforced Concrete Plates with Extensive Cracking”, IABSE Reports of the Working Commissions 34, ETH Zurich, pp. 99-120.

Garas, F.K. and Amer, G.S.T. (1980). “Reinforced and Prestressed Microconcrete Models”, Construction Press, London, U.K., 387 pp.

Garcia, R., Hajirasouliha, I., and Pilakoutas, K. (2010). “Seismic Behaviour of Deficient RC Frames Strengthened with CFRP Composites”, *ASCE Journal of Structural Engineering,* Vol. 32, No. 10, pp. 3075-3085.

Garusi, E. and Tralli, A. (2002). “A Hybrid Stress-Assumed Transition Element for Solid-to-Beam and Plate-to-Beam Connections”, *Computers and Structures,* Vol. 80, No. 2, pp. 105-115.

Gencturk, B. and Hosseini, F. (2015). “Evaluation of Reinforced Concrete and Reinforced Engineered Cementitious Composite (ECC) Members and Structures using Small-Scale Testing”, *Canadian Journal of Civil Engineering,* Vol. 42, No. 3, pp. 164-177.

Gere, J.M. and Timoshenko, S.P. (1991). “Mechanics of Materials”, Nelson Thornes Ltd., Cheltenham, U.K., 832 pp.

Ghorbani-Renani, I., Velev, N., Tremblay, R., Palermo, D., Massicotte, B., and Léger, P. (2009). “Modeling and Testing Influence of Scaling Effects on Inelastic Response of Shear Walls”, *ACI Structural Journal*, Vol. 106, No. 3, pp. 358-367.

Gilbertsen, N.D. and Moehle, J.P. (1980). “Experimental Study of Small-Scale R/C Columns Subjected to Axial and Shear Force Reversals”, Technical Report, Civil Engineering Studies SRS-481, University of Illinois at Urbana-Champaign, I.L., U.S.A., 95 pp.

Gmur, T.C. and Kauten, R.H. (1993). “Three-Dimensional Solid-to-Beam Transition Elements for Structural Dynamics Analysis”, *International Journal for Numerical Methods in Engineering*, Vol. 36, No. 9, pp. 1429-1444.

Godat, A., Neale, K., and Labossière, P. (2007). “Numerical Modeling of FRP Shear-Strengthened Reinforced Concrete Beams”, *ASCE Journal of Composites for Construction,* Vol. 11, No. 6, pp. 640-649.

Goodier, J.N. (1938). “On the Problems of the Beam and the Plate in the Theory of Elasticity”, *Royal Society of Canada's Transactions*, Vol. 32, pp. 65-68.

Guner, S. and Vecchio, F.J. (2008). “User’s Manual of VecTor5”, Department of Civil Engineering, University of Toronto, Canada, 88 pp.

Guner, S. and Vecchio, F.J. (2010a). “Pushover Analysis of Shear-Critical Frames: Formulations”, *ACI Structural Journal*, Vol. 107, No. 1, pp. 63-71.

Guner, S. and Vecchio, F.J. (2010b). "Pushover Analysis of Shear-Critical Frames: Verification and Application", *ACI Structural Journal*, Vol. 107, No. 1, pp. 72-81.

Guzelbey, I.H. and Kanber, B. (2000). "A Practical Rule for the Derivation of Transition Finite Elements", *International Journal for Numerical Methods in Engineering,* Vol. 47, No. 5, pp. 1029-1056.

Harris, H.G. and Sabnis, G.M. (1999). "Structural Modeling and Experimental Techniques", CRC Press, Boca Raton, F.L., U.S.A., 808 pp.

Hirai, I. (1985). "An Exact Zooming Method", *Finite Element Analysis and Design,* Vol. 1, No. 1, pp. 61-69.

Ho, R.J., Meguid, S.A., Zhu, Z.H., and Sauve, R.G. (2010). "Consistent Element Coupling in Nonlinear Static and Dynamic Analyses Using Explicit Solvers", *International Journal of Mechanics and Materials in Design,* Vol. 6, No. 4, pp. 319-330.

Holand, I. and Bell, K. (1969). "Finite Element Method in Stress Analysis", Tapir Academic Press, Norway, 500 pp.

Holub, C.J. (2005). "Similitude Considerations for Small Scale Distributed Hybrid Testing of Reinforced Concrete Bridges", M.A.Sc. Thesis, University of Illinois at Urbana Champaign, I.L., U.S.A., 82 pp.

Holub, C.J. (2009). "Interaction of Variable Axial Load and Shear Effects in RC Bridges", Ph.D. Dissertation, University of Illinois at Urbana Champaign, I.L., U.S.A., 480 pp.

Houlsby, G.T., Liu, G., and Augarde, C.E. (2000). "A Tying Scheme for Imposing Displacement Constraints in Finite Element Analysis", *Communications in Numerical Methods in Engineering,* Vol. 16, No. 10, pp. 721-732.

Hrynyk, T.D. (2013). "Behaviour and Modelling of Reinforced Concrete Slabs and Shells under Static and Dynamic Loads", Ph.D. Dissertation, Department of Civil Engineering, University of Toronto, Canada, 455 pp.

Hrynyk, T.D. and Vecchio, F.J. (2015). "Capturing Out-of-Plane Shear Failures in the Analysis of Reinforced Concrete Shells", *ASCE Journal of Structural Engineering*, Vol. 141, No. 12, 04015058.

Huang, X., Sadeghian, V., and Kwon, O-S. (2015). "Development of Integrated Framework for Distributed Multi-Platform Simulation", *6th International Conference on Advances in Experimental Structural Engineering,* University of Illinois at Urbana-Champaign, I.L., U.S.A.

Jialin, W., Zhiwen, L., Xing, M., and Jianzheng, Z. (1996). "A DOF Expanding Method for Connecting Solid and Shell Element", *Numerical Methods in Biomedical Engineering,* Vol. 12, No. 6, pp. 321-330.

Jourawski, D. (1856). "Remarques sur la résistance d'un corps prismatiques et d'une pièce composée en bois ou en tôle de fer à une force perpendiculaire à leur longeur", *Annales des Ponts and Chaussées*, Vol. 12, pp. 328-351.

Kani, G.N.J. (1967). "How Safe Are Our Large Scale Concrete Beams?", *ACI Journal Proceedings*, Vol. 64, No. 3, pp. 128-141.

Karabinis, A.I., Rousakis, T.C., and Manolitsi, G.E. (2008). "3D Finite-Element Analysis of Substandard RC Columns Strengthened by Fiber-Reinforced Polymer Sheets", *ASCE Journal of Composites for Construction,* Vol. 12, No. 5, pp. 531-540.

Karavasilis, T.L., Seo, C.Y., and Ricles, J. (2008). "HybridFEM User's Manual: A Program for Dynamic Time History Analysis of 2D Inelastic Framed Structures and Real-Time Hybrid Simulation", Bethlehem, P.A., U.S.A., 76 pp.

Karbhari, V.M. and Gao, Y. (1997). "Composite Jacketed Concrete under Uniaxial Compression-Verification of Simple Design Equations", *ASCE Journal of Materials in Civil Engineering,* Vol. 9, No. 4, pp. 185-193.

Kaufmann, W. and Marti, P. (1998). "Structural Concrete: Cracked Membrane Model", *ASCE Journal of Structural Engineering,* Vol. 124, No. 12, pp. 1467-1475.

Kim, W., El-Attar, A., and White, R.N. (1988). "Small-Scale Modelling Techniques for Reinforced Concrete Structures Subjected to Seismic Loads", Technical Report, No. NCEER-88-0041, University of Cornell, N.Y., U.S.A., 92 pp.

Kim, H-S. and Hong, S-M. (1994). "Formulation of Transition Elements for the Analysis of Coupled Wall Structures", *Computers and Structures,* Vol. 57, No. 2, pp. 333-344.

Kim, N.S., Kwak, Y.H., and Chang, S.P. (2004). "Pseudodynamic Tests of Small-Scale Steel Models using the Modified Similitude Law", *13th World Conference of Earthquake Engineering,* Vancouver, Canada.

Kim, S. and Vecchio, F.J. (2008). "Modeling of Shear-Critical Reinforced Concrete Structures Repaired with Fiber-Reinforced Polymer Composites", *ASCE Journal of Structural Engineering,* Vol. 134, No. 8, pp. 1288-1299.

Ko, H., Matthys, S., Palmieri, A., and Sato, Y. (2014). "Development of a Simplified Bond Stress-Slip Model for Bonded FRP-Concrete Interfaces", *Construction and Building Materials,* Vol. 68, pp. 142-157.

Kohnke, P. (1994). "ANSYS Theory Reference", ANSYS Inc., Canonsburg, P.A., U.S.A., 1286 pp.

Kwon, O-S., Elnashai, A.S., and Spencer, B.F. (2008). "A Framework for Distributed Analytical and Hybrid Simulations", *Structural Engineering and Mechanics,* Vol. 30, No. 3, pp. 331-350.

Lam, L. and Teng, J.G. (2002). "Strength Models for Fiber-Reinforced Plastic-Confined Concrete", *ASCE Journal of Structural Engineering,* Vol. 128, No. 5, pp. 612-623.

Lam, L. and Teng, J.G. (2009). "Stress-Strain Model for FRP Confined Concrete under Cyclic Axial Compression", *Engineering Structures,* Vol. 31, No. 2, pp. 308-321.

Li, Z.J., Balendra, T., Tan, K.H., and Kong, K.H. (2005). "Finite Element Modeling of Cyclic Behavior of Shear Wall Structure Retrofitted Using GFRP", *FRP7RCS Special Publication, ACI,* Vol. 230, pp. 1305-1324.

Li, Z.X., Chan, T.H.T., Yu, Y., and Sun, Z.H. (2009). "Concurrent Multi-Scale Modeling of Civil Infrastructures for Analyses on Structural Deterioration-Part I: Modeling Methodology and Strategy", *Finite Elements in Analysis and Design,* Vol. 45, No. 11, pp. 782-794.

Lombard, J., Lau, D.T., Humar, J.L., Foo, S., and Cheung, M.S. (2000). "Seismic Strengthening and Repair of Reinforced Concrete Shear Walls", *Proceedings of 12th World Conference on Earthquake Engineering*, Auckland, New Zealand.

Lu, X.Z., Teng, J.G., Ye, L.P., and Jiang, J.J. (2005). "Bond-Slip Models for FRP Sheets/Plates Bonded to Concrete", *ASCE Journal of Structural Engineering*, Vol. 27, No. 6, pp. 920-937.

Lu, Y., Vintzileou, E., Zhang, G-F., and Tassios, T.P. (1999). "Reinforced Concrete Scaled Columns under Cyclic Actions", *Soil Dynamics and Earthquake Engineering*, Vol. 18, No. 2, pp. 151-167.

Lulec, A. (2017). "Simplified Analytical Tools for Impact and Impulsive Loading Analysis of Reinforced Concrete Structures", Ph.D. Dissertation, Department of Civil Engineering, University of Toronto, Toronto, Canada, 196 pp.

Mao, K.M. and Sun, C.T. (1991). "A Refined Global-Local Finite Element Analysis Method", *International Journal for Numerical Methods in Engineering*, Vol. 32, No. 1, pp. 29-43.

Mata, P., Barbat, A.H., and Oller, S. (2008). "Two-Scale Approach for the Nonlinear Dynamic Analysis of RC Structures with Local Non-Prismatic Parts", *Engineering Structures*, Vol. 30, No. 12, pp. 3667-3680.

Mazzoni, S., McKenna, F., Scott, M.H., and Fenves, G.L. (2007). "The OpenSees Command Language Manual, Version 2.0", Pacific Earthquake Engineering Research Center, University of California, Berkeley, C.A., U.S.A., 465 pp.

McCune, R.W., Armstrong, C.G., and Robinson, D.J. (2000). "Mixed-Dimensional Coupling in Finite Element Models", *International Journal for Numerical Methods in Engineering*, Vol. 49, No. 6, pp. 725-750.

McDaniel, C., Benzoni, G., and Priestley, N. (1997). "Scale Effects on the Shear Strength of Circular Reinforced Concrete Columns", Technical Report, No. SSRP- 97/02, University of California, San Diego, C.A., U.S.A., 186 pp.

McKenna, F. and Fenves, G.L. (1999). "G3 Class Interface Specification Version 0.1 - Preliminary Draft", Pacific Earthquake Engineering Research Center, University of California, Berkeley, C.A., U.S.A.

Memon, M.S. and Sheikh, S.A. (2005). "Seismic Resistance of Square Concrete Columns Retrofitted with Glass Fiber-Reinforced Polymer", *ACI Structural Journal*, Vol. 102, No. 5, pp. 774-783.

MKL (2012). "Intel Math kernel Library for Windows OS User's Guide", Intel Cop., C.A., U.S.A., 114 pp.

Montoya, E., Vecchio, F.J., and Sheikh, S.A. (2004). "Numerical Evaluation of the Behaviour of Steel- and FRP-Confined Concrete Columns using Compression Field Modelling", *Engineering Structures*, Vol. 26, No. 11, pp. 1535-1545.

Mote, C.D. (1971). "Global-Local Finite Element", *International Journal for Numerical Methods in Engineering*, Vol. 3, No. 4, pp. 565-574.

Mozos, C.M. and Luco, J.E. (2011). "Approximate Boundaries for Finite-Element Models of Static Soil-Foundation Interaction Problems", *ASCE Journal of Engineering Mechanics*, Vol. 137, No. 10, pp. 648-659.

Murphy, G. (1950). “Similitude in Engineering”, Ronald Press, N.Y., U.S.A., 302 pp.

Nakaba, K., Kanakubo, T., Furuta, T., and Yoshizawa, H. (2001). “Bond Behavior between Fiber-Reinforced Polymer Laminates and Concrete”, *ACI Structural Journal*, Vol. 98, No. 3, pp. 359-367.

Nakata, N., Spencer, B.F., and Elnashai, A.S. (2010). “Sensitivity-Based External Calibration of Multiaxial Loading System”, *ASCE Journal of Engineering Mechanics*, Vol. 136, No. 2, pp. 189-198.

Narayanaswamy, O.S. (1985). “Processing Nonlinear Multipoint Constraints in the Finite Element Method”, *International Journal for Numerical Methods in Engineering*, Vol. 21, No. 7, pp. 1283-1288.

Neubauer, U. and Rostasy, F.S. (1999). “Bond Failure of Concrete Fiber Reinforced Polymer Plates at Inclined Cracks-Experiments and Fracture Mechanics Model”, *ACI Special Publication*, Vol. 188, pp. 369-382.

Noor, A.K. (1986). “Global-Local Methodologies and Their Application to Nonlinear Analysis”, *Finite Elements in Analysis and Design*, Vol. 2, No. 4, pp. 333-346.

Noor, F.A. and Boswell, L.F. (1992). “Small Scale Modelling of Concrete Structures”, Elsevier, N.Y., U.S.A., 349 pp.

Noor, F.A. and Wijayasri, S. (1982). “Modeling the Stress-Strain Relationship of Structural Concrete”, *Magazine of Concrete Research*, Vol. 34, No. 118, pp. 25-34.

Nuclear Power Engineering Corporation (NUPEC) (1996), “Seismic Shear Wall ISP”, NUPEC’s Seismic Ultimate Dynamic Response Test, Report No. NU-SSWISP-D014.

Ohtaki, T. (2000). “An Experimental Study on Scale Effects in Shear Failure of Reinforced Concrete Columns”, *12th World Conference on Earthquake Engineering*, Auckland, New Zealand.

Okamura, H. and Maekawa, K. (1991). “Nonlinear Analysis and Constitutive Methods of Reinforced Concrete”, ISBN 7655-1506-0, University of Tokyo, Tokyo, Japan.

Onate, E. (1995). “On the Derivation and Possibilities of the Secant Stiffness Matrix for Non-Linear Finite Element Analysis”, *Computational Mechanics*, Vol. 15, No. 6, pp. 572-593.

OpenSeesWiki (2012). “Online User’s Manual for OpenSees”, Pacific Earthquake Engineering Research Center, University of California, Berkeley, C.A., U.S.A.

Palermo, D. and Vecchio, F.J. (2002). “Behavior of 3-D Reinforced Concrete Shear Walls”, *ACI Structural Journal*, Vol. 99, No. 1, pp. 81-89.

Pan, P., Tada, M., and Nakashima, M. (2005). “Online Hybrid Test by Internet Linkage of Distributed Test-Analysis Domains”, *Earthquake Engineering and Structural Dynamics*, Vol. 34, No. 11, pp. 1407-1425.

Panahshahi, N., Reinhorn, A.M., Kunnath, S.K., Lu, L.W., Huang, T., and Yu, K. (1991). “Seismic Response of a 1:6 Reinforced Concrete Scale-Model Structure with Flexible Floor Diaphragms”, *ACI Structural Journal*, Vol. 88, No. 3, pp. 315-324.

Park, K.C., Felippa, C.A., and Gumaste, U.A. (2000). “A Localised Version of the Method of Lagrange Multipliers and Its Applications”, *Computational Mechanics*, Vol. 24, No. 6, pp. 476-490.

Przemieniecki, I.S. (1963). “Matrix Structural Analysis of Substructures”, *AIAA Journal,* Vol. 1, No. 1, pp. 138-147.

Rougier, V.C. and Luccioni, B.M. (2007). “Numerical Assessment of FRP Retrofitting Systems for Reinforced Concrete Elements”, *Engineering Structures,* Vol. 29, No. 8, pp. 1664-1675.

Saadatmanesh, H. and Ehsani, M.R. (1991). “RC Beams Strengthened with GFRP Plates - Experimental Study”, *ASCE Journal of Structural Engineering*, Vol. 117, No. 11, pp. 3417-3433.

Saafi, M., Toutanji, H.A., and Li, Z. (1999). “Behavior of Concrete Columns Confined with Fiber Reinforced Polymer Tubes”, *ACI Material Journal,* Vol. 96, No. 4, pp. 500-509.

Sadeghian, V. and Vecchio, F.J. (2015). “A Graphical User Interface for Stand-Alone and Mixed-Type Modelling of Reinforced Concrete Structures”, *Computers and Concrete*, Vol. 16, No. 2, pp. 287-309.

Sadeghian, V., Vecchio, F.J., and Kwon, O-S. (2016). “Six Degree-of-Freedom Hydraulic Testing Equipment User’s Manual”, Department of Civil Engineering, University of Toronto, Canada, 39 pp.

Samaan, M., Mirmiran, A., and Shahawy, M. (1998). “Model of Concrete Confined by Fiber Composite”, *ASCE Journal of Structural Engineering,* Vol. 124, No. 9, pp. 1025-1031.

Saouma, V., Haussmann, G., Kang, D-H., and Ghannoum, W. (2014). “Real-Time Hybrid Simulation of a Nonductile Reinforced Concrete Frame”, *ASCE Journal of Structural Engineering,* Vol. 140, No. 2, 4013059.

Saouma, V., Kang, D.H., and Haussmann, G. (2012). “A Computational Finite-Element Program for Hybrid Simulation”, *Earthquake Engineering and Structural Dynamics*, Vol. 41, No. 3, pp. 375-389.

Sato, Y. and Vecchio, F.J. (2003). “Tension Stiffening and Crack Formation in Reinforced Concrete Members with Fiber-Reinforced Polymer Sheets”, *ASCE Journal of Structural Engineering,* Vol. 129, No. 6, pp. 717-724.

Sayed, A., Wang, X., and Wu, Z. (2013). “Modeling of Shear Capacity of RC Beams Strengthened with FRP Sheets Based on FE Simulation”, *ASCE Journal of Composites for Construction,* Vol. 17, No. 5, pp. 687-701.

Schenk, O. and Gartner, K. (2004). “Solving Unsymmetric Sparse Systems of Linear Equations with PARDISO”, *Journal of Future Generation Computer Systems,* Vol. 20, No. 3, pp. 475-487.

Schorderet, A. and Gmur, T.C. (1991). “Solid to Shell Transition Finite Elements for Structural Dynamics Analysis”, *Proceedings of the 9th International Modal Analysis Conference*, Vol. 2, pp. 1091-1097.

Scott, B.D., Park, R., and Priestley, M.J.N. (1982). “Stress-Strain Behavior of Concrete Confined by Overlapping Hoops at Low and High Strain Rates”, *ACI Structural Journal,* Vol. 79, No. 1, pp. 13-27.

Seckin, M. (1981). “Hysteretic Behaviour of Cast-in-Place Exterior Beam-Column-Slab Subassemblies”, Ph.D. Dissertation, Department of Civil Engineering, University of Toronto, Canada, 266 pp.

Sheikh, S.A. and Homam, S.M. (2004). “A Decay of Performance of FRP-Repaired Concrete Structures”, *Proceedings of ISIS-SHM Workshop,* Winnipeg, Canada.

Shepard, M.S. (1984). "Linear Multipoint Constraints via Transformation as Part of a Direct Stiffness Assembly Process", *International Journal for Numerical Methods in Engineering*, Vol. 20, No. 11, pp. 2107-2112.

Shioya, T. (1989). "Shear Properties of Large Reinforced Concrete Members", Special Report, No. 25, Institute of Technology, Shimizu Corp., 198 pp.

Surana, K.S. (1980). "Transition Finite Element for Three-Dimensional Stress Analysis", *International Journal for Numerical Methods in Engineering,* Vol. 15, No. 7, pp. 991-1020.

Takahashi, Y. and Fenves, G.L. (2005). "Software Framework for Distributed Experimental-Computational Simulation of Structural Systems", *OpenSees Developer Symposium*, University of California, Berkeley, C.A., U.S.A.

Takanashi, K., Udagawa, K., Seki, M., Okada, T., and Tanaka, H. (1975). "Non-Linear Earthquake Response Analysis of Structures by a Computer Actuator On-Line System", *Transaction of the Architectural Institute of Japan,* pp. 77-83.

Taucer, F.F., Spacone, E., and Filippou, F.C. (1991). "A Fiber Beam-Column Element for Seismic Response Analysis of RC Structures", Technical Report, Earthquake Engineering Research Center, University of California, Berkeley, C.A., U.S.A., 138 pp.

Teng, J., Lam, L., Lin, G., Lu, J., and Xiao, Q. (2016). "Numerical Simulation of FRP-Jacketed RC Columns Subjected to Cyclic and Seismic Loading", *ASCE Journal of Composites for Construction*, Vol. 20, No. 1, 4015021.

Tokyay, M. and Ozdemir, M. (1997). "Specimen Shape and Size Effect on the Compressive Strength of High Strength Concrete", *Cement and Concrete Research,* Vol. 27, No. 8, pp. 1281-1289.

Vecchio, F.J. (1999). "Towards Cyclic Load Modeling of Reinforced Concrete", *ACI Structural Journal*, Vol. 96, No. 2, pp. 193-202.

Vecchio, F.J. (2000). "Disturbed Stress Field Model for Reinforced Concrete: Formulation", *ASCE Journal of Structural Engineering,* Vol. 126, No. 8, pp. 1070-1077.

Vecchio, F.J. (2002). "Contribution of NLFEA to the Evaluation of Two Structural Concrete Failures", *ASCE Journal of Performance of Constructed Facilities,* Vol. 16, No. 3, pp. 110-115.

Vecchio, F.J. and Collins, M.P. (1986). "The Modified Compression-Field Theory for Reinforced Concrete Elements Subjected to Shear", *ACI Structural Journal,* Vol. 83, No. 2, pp. 219-231.

Vecchio, F.J. and Collins, M.P. (1993). "Compression Response of Cracked Reinforced Concrete", *ASCE Journal of Structural Engineering,* Vol. 119, No. 12, pp. 3590-3610.

Vecchio, F.J. and Shim, W. (2004). "Experimental and Analytical Re-Examination of Classic Concrete Beam Tests", *ASCE Journal of Structural Engineering,* Vol. 130, No. 3jia, pp. 460-469.

Wallace, B.J. and Krawinkler, H. (1985). "Small-Scale Model Experimentation on R/C Assemblies, US-Japan Research Program", Technical Report, No. 74, University of Stanford, C.A., U.S.A., 159 pp.

Wang, F.Y., Xu, Y.L., and Qu, W.L. (2014). "Mixed-Dimensional Finite Element Coupling for Structural Multi-Scale Simulation", *Finite Elements in Analysis and Design,* Vol. 92, No. 1, pp. 12-25.

Whitcomb, J.D. (1991). “Iterative Global/Local Finite Element Analysis”, *Computers and Structures*, Vol. 40, No. 4, pp. 1027-1031.

Wong, P.S., Trommels, H., and Vecchio, F.J. (2013). “VecTor2 and FormWorks User’s Manual, 2nd Edition”, Department of Civil Engineering, University of Toronto, Toronto, Canada, 311 pp.

Wong, R. and Vecchio, F.J. (2003). “Towards Modeling of Reinforced Concrete Members with Externally Bonded Fiber-Reinforced Polymer Composites”, *ACI Structural Journal,* Vol. 100, No. 1, pp. 47-55.

Yalcin, C. and Saatcioglou, M. (2000). “Inelastic Analysis of RC Columns”, *Computers and Structures*, Vol. 77, No. 5, pp. 539-555.

Yang, Y.S., Hsieh, S.H., and Hsieh, T-J. (2012). “Improving Parallel Substructuring Efficiency by Using a Multilevel Approach”, *ASCE Journal of Computing in Civil Engineering,* Vol. 26, No. 4, pp. 457-464.

Yang, Y.S., Hsieh, S.H., Wang, K.J., and Wang S.J. (2002). “Numerical Analysis Framework for Distributed Pseudo-Dynamic Tests”, *2nd International Conference on Structural Stability and Dynamics,* Singapore.

Zhan, H. (2015). “Development of a Generic Controller Interface Program, NICON, for Multi-Degrees-of-Freedom PSD Hybrid Simulation”, M.A.Sc. Thesis, Department of Civil Engineering, University of Toronto, Canada, 142 pp.

Zhan, H. and Kwon, O-S. (2015). “Actuator Controller Interface Program for Pseudo-Dynamic Hybrid Simulation”, *World Congress on Advances in Structural Engineering and Mechanics,* Incheon, Korea.

Zhu, Z., Ahmad, I., and Mirmirana, A. (2006). “Fiber Element Modeling for Seismic Performance of Bridge Columns Made of Concrete-Filled FRP Tubes”, *Engineering Structures,* Vol. 28, No. 14, pp. 2023-2035.

APPENDIX A

CRACK PATTERNS OF HYBRID SIMULATIONS

Table A.1 Crack development of test and analysis for the flexure-critical column

Load Stage	Specimen Front View	Specimen Back View (Reversed)	FE Analysis (Magnification Factor: 2)
Cycle 1 - Positive Peak			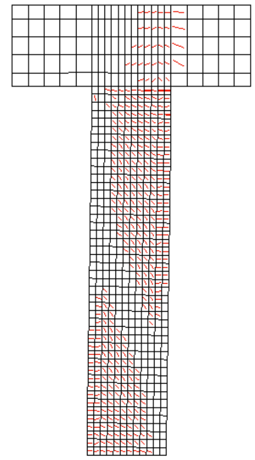
Cycle 1 - Negative Peak		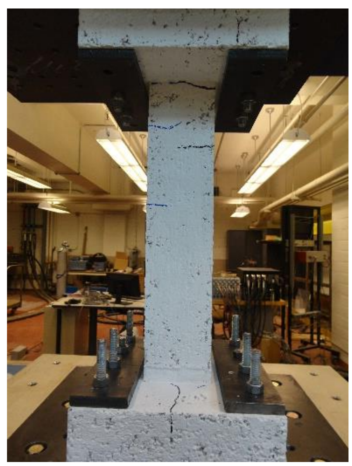	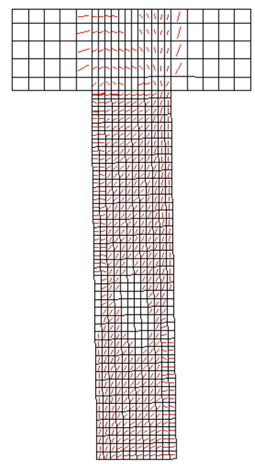
Cycle 2 - Positive Peak			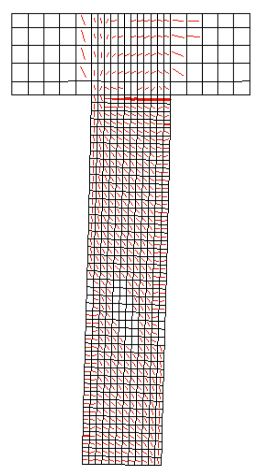

Table A.1 Crack development of test and analysis for the flexure-critical column (continued)

Load Stage	Specimen Front View	Specimen Back View (Reversed)	FE Analysis (Magnification Factor: 2)
Cycle 2 - Negative Peak		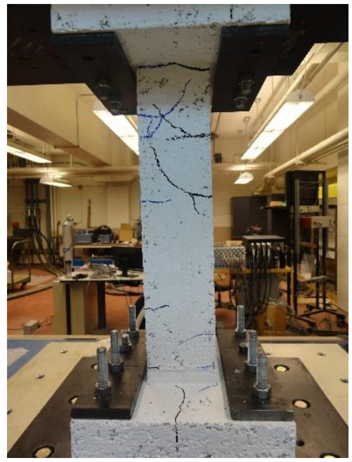	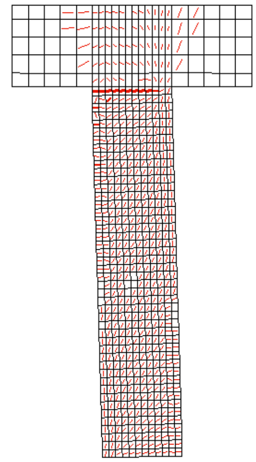
Cycle 3 - Positive Peak		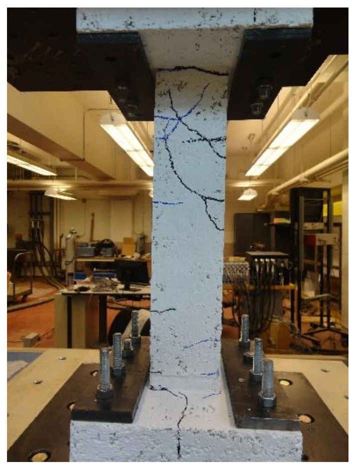	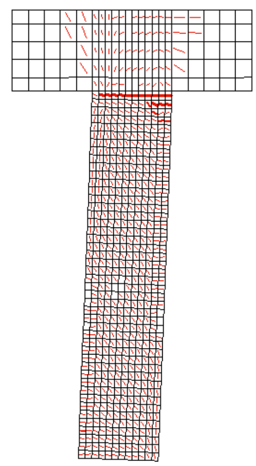
Cycle 3 - Negative Peak		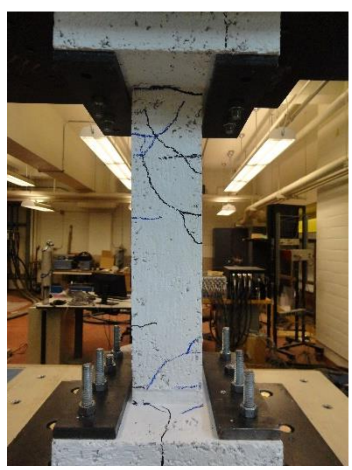	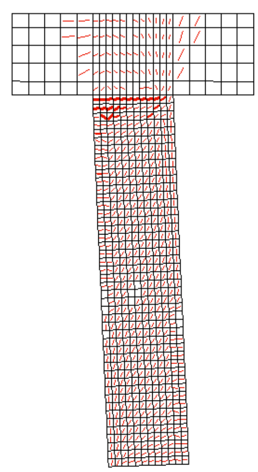

Table A.1 Crack development of test and analysis for the flexure-critical column (continued)

Load Stage	Specimen Front View	Specimen Back View (Reversed)	FE Analysis (Magnification Factor: 2)
Cycle 4 - Positive Peak		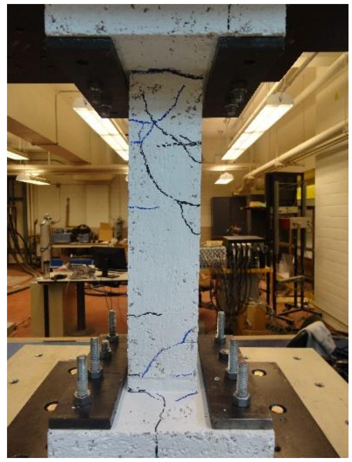	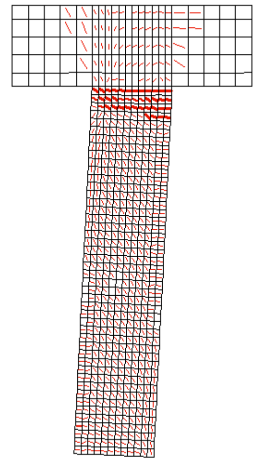
Cycle 4 - Negative Peak	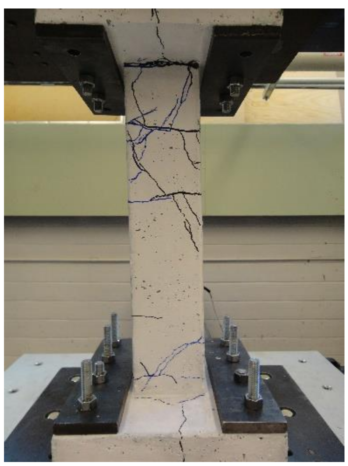	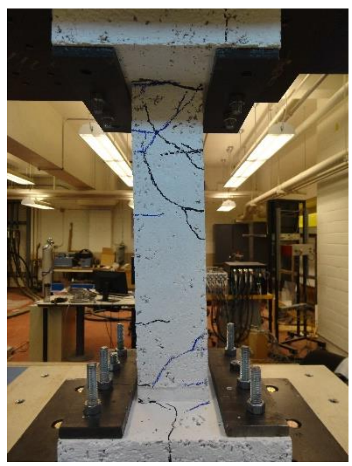	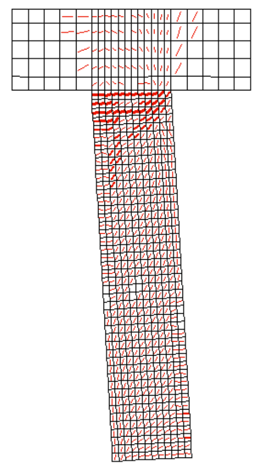
Cycle 5 - Positive Peak		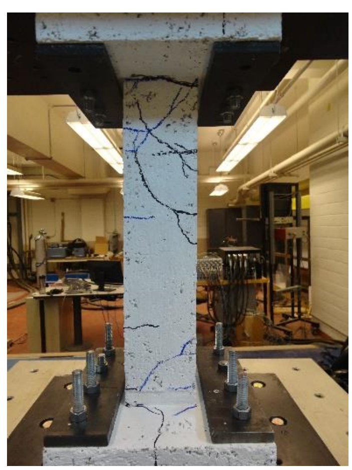	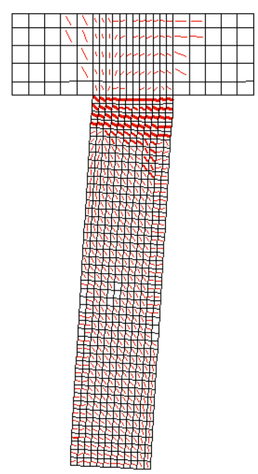

Table A.1 Crack development of test and analysis for the flexure-critical column (continued)

Load Stage	Specimen Front View	Specimen Back View (Reversed)	FE Analysis (Magnification Factor: 2)
Cycle 5 - Negative Peak	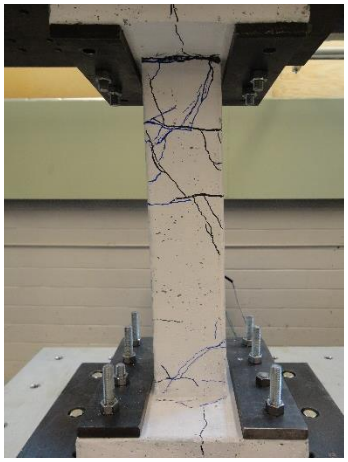	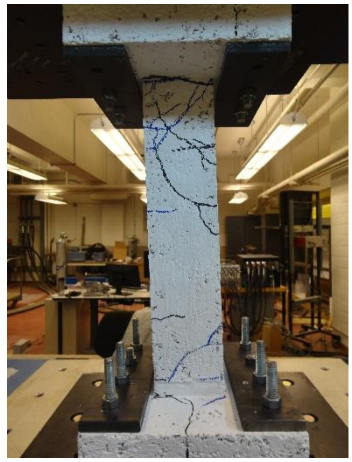	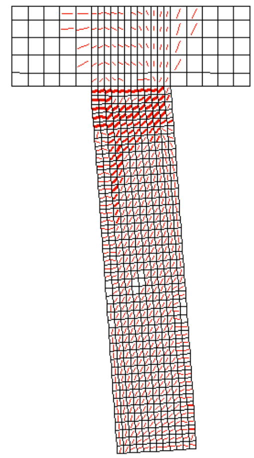
Cycle 6 - Positive Peak		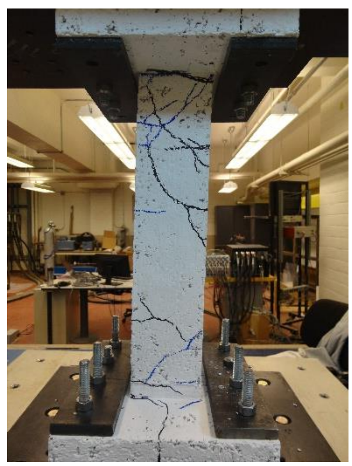	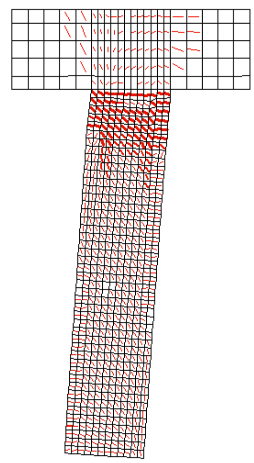
Cycle 6 - Negative Peak		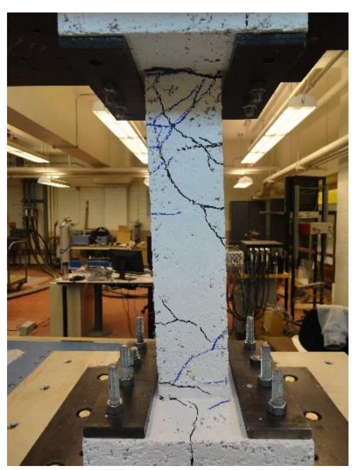	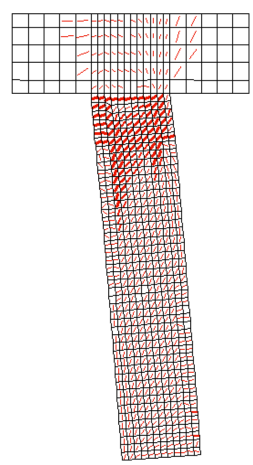

Table A.1 Crack development of test and analysis for the flexure-critical column (continued)

Load Stage	Specimen Front View	Specimen Back View (Reversed)	FE Analysis (Magnification Factor: 2)
Cycle 7 - Positive Peak	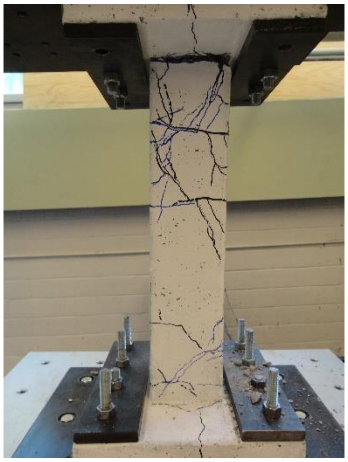	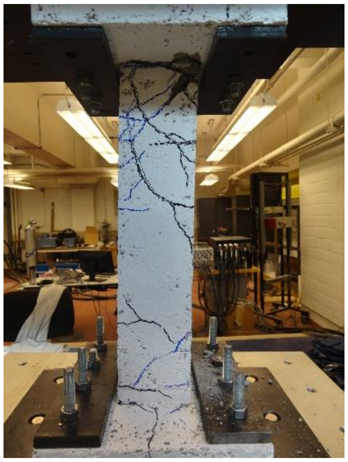	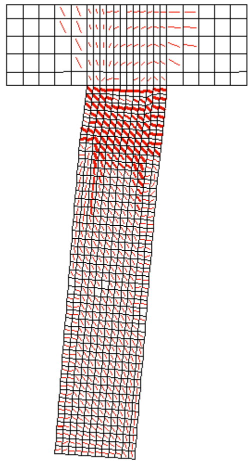
Cycle 7 - Negative Peak	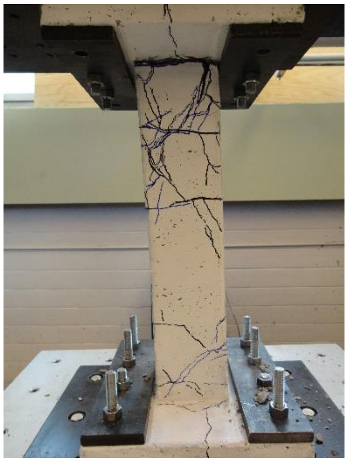	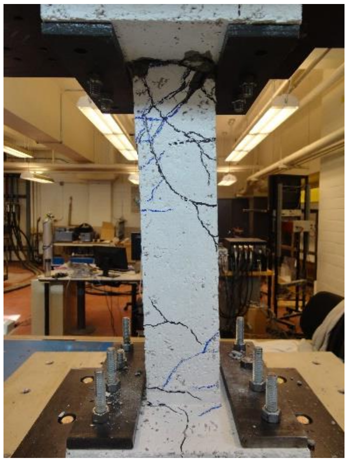	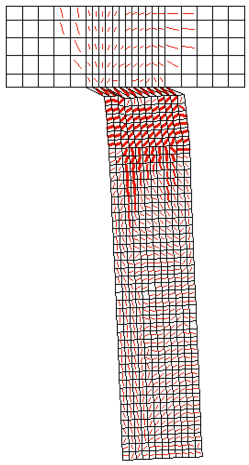

Table A.2 Crack development of test and analysis for the shear-critical column

Load Stage	Specimen Front View	Specimen Back View (Reversed)	FE Analysis (Magnification Factor: 2)
The crack development in the loading cycles 1 and 2 was negligible			
Cycle 3 - Positive Peak			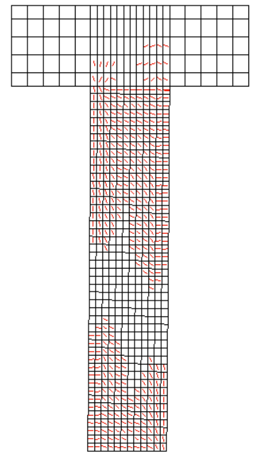
Cycle 3 - Negative Peak			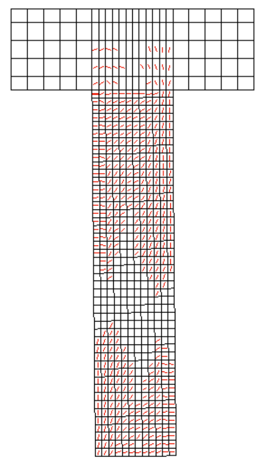
Cycle 4 - Positive Peak			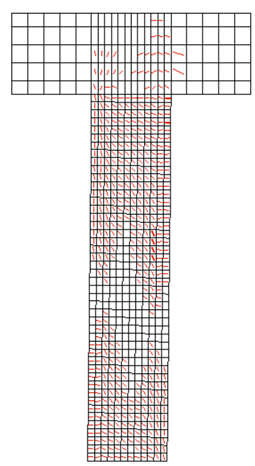

Table A.2 Crack development of test and analysis for the shear-critical column (continued)

Load Stage	Specimen Front View	Specimen Back View (Reversed)	FE Analysis (Magnification Factor: 2)
Cycle 4 - Negative Peak			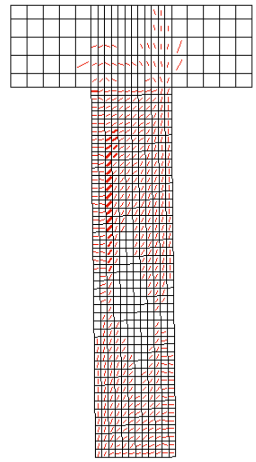
Cycle 5 - Positive Peak	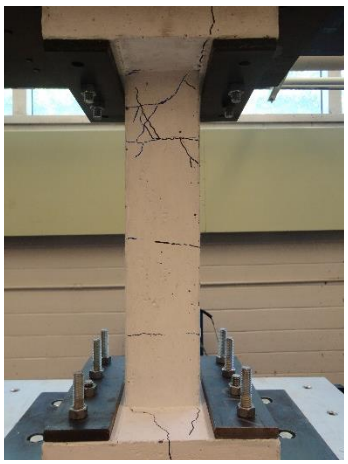	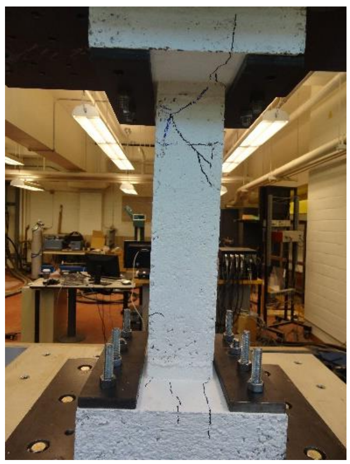	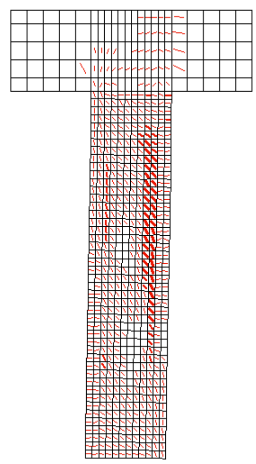
Cycle 5 - Negative Peak	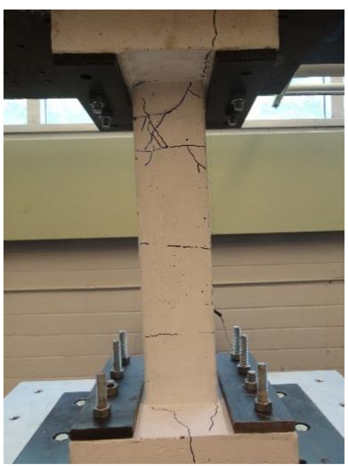	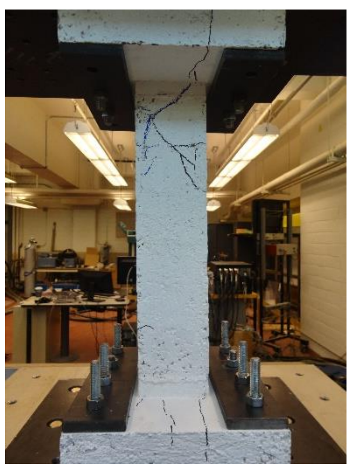	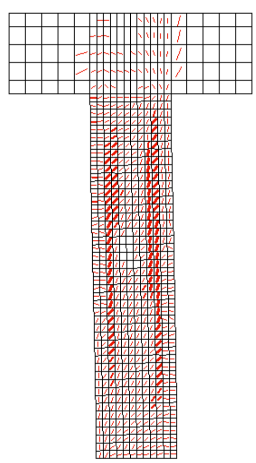

Table A.2 Crack development of test and analysis for the shear-critical column (continued)

Load Stage	Specimen Front View	Specimen Back View (Reversed)	FE Analysis (Magnification Factor: 2)
Cycle 6 - Positive Peak			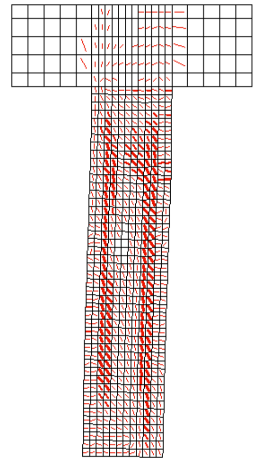
Cycle 6 - Negative Peak		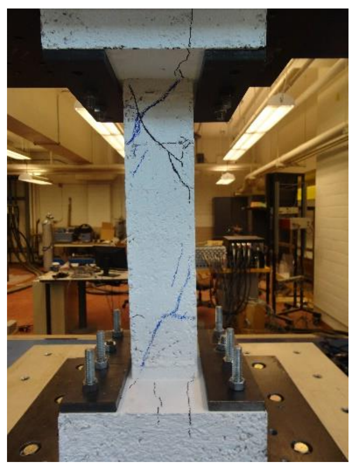	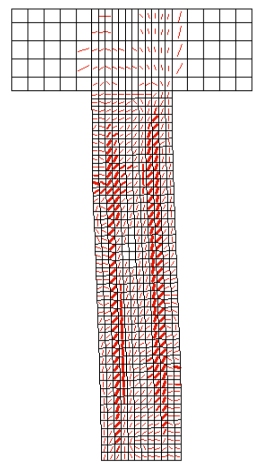
Cycle 7 - Positive Peak	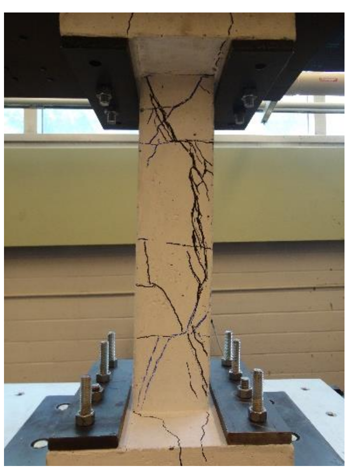	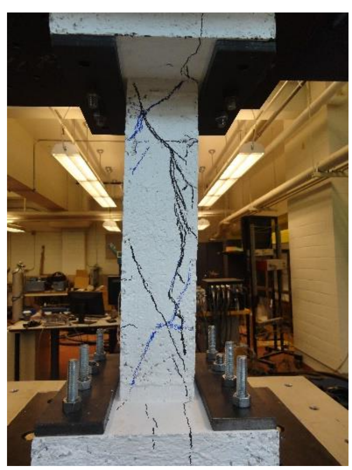	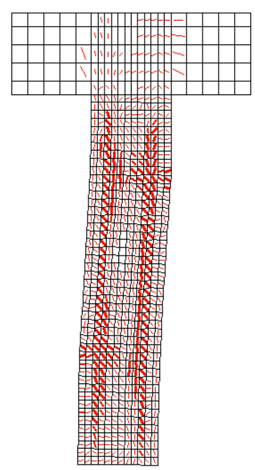

Table A.2 Crack development of test and analysis for the shear-critical column (continued)

Load Stage	Specimen Front View	Specimen Back View (Reversed)	FE Analysis (Magnification Factor: 2)
Cycle 7 - Negative Peak		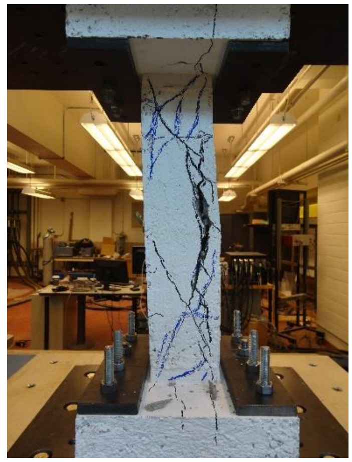	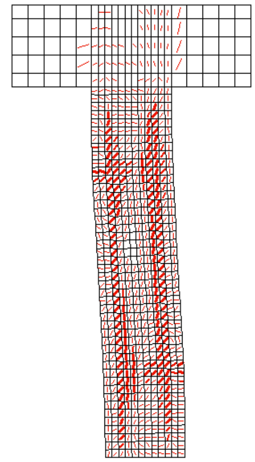

Table A.3 Crack pattern of the Duong frame first-storey beam

Displacement of 10 mm in forward cycle	
Model Beam Front View	
Model Beam Back View (Reversed)	
Prototype Beam	
FE Analysis (Magnification Factor: 10)	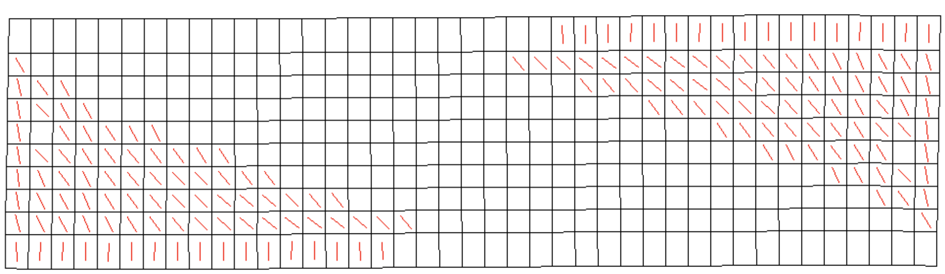

Table A.3 Crack pattern of the Duong frame first-storey beam (continued)

Displacement of 20 mm in forward cycle	
Model Beam Front View	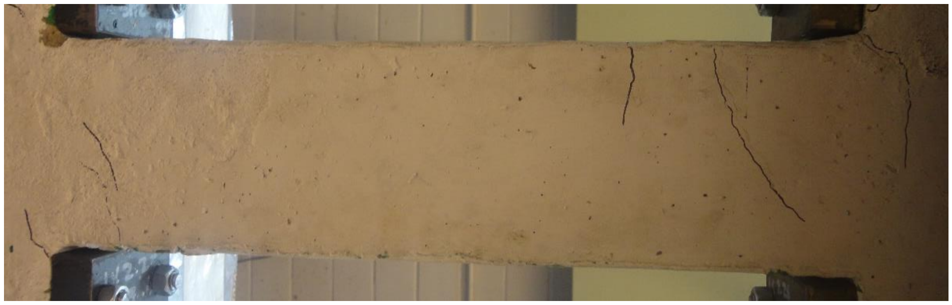
Model Beam Back View (Reversed)	
Prototype Beam	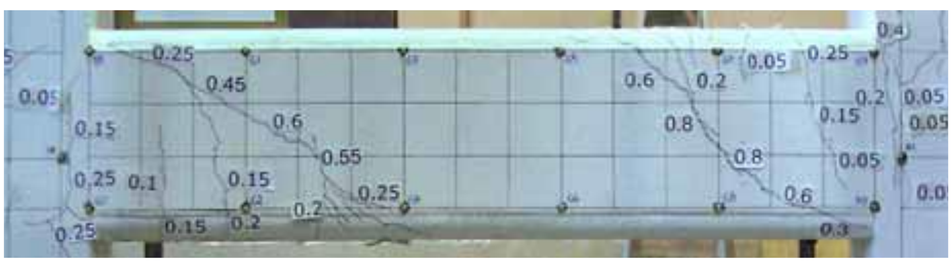
FE Analysis (Magnification Factor: 10)	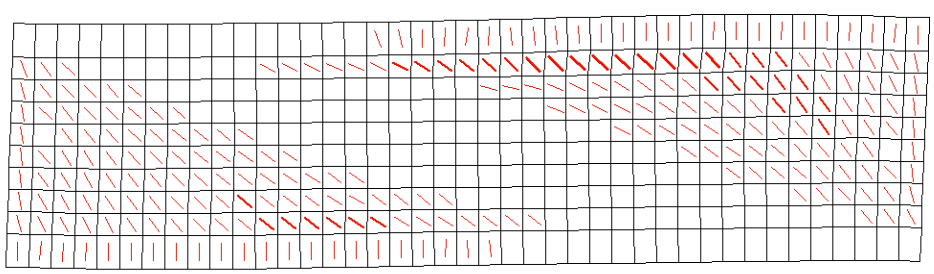

Table A.3 Crack pattern of the Duong frame first-storey beam (continued)

Displacement of 30 mm in forward cycle	
Model Beam Front View	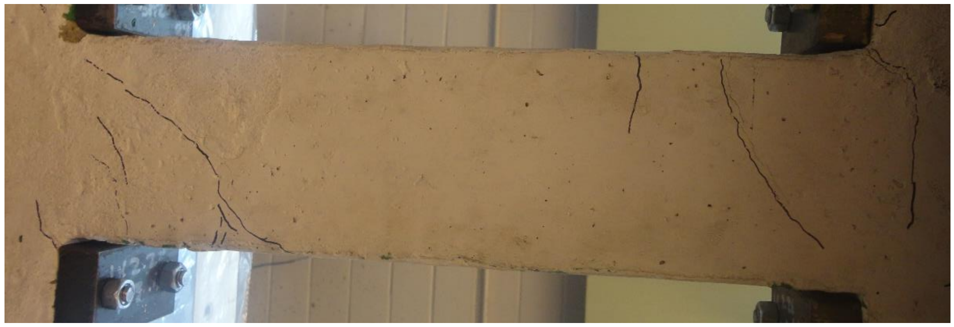
Model Beam Back View (Reversed)	
Prototype Beam	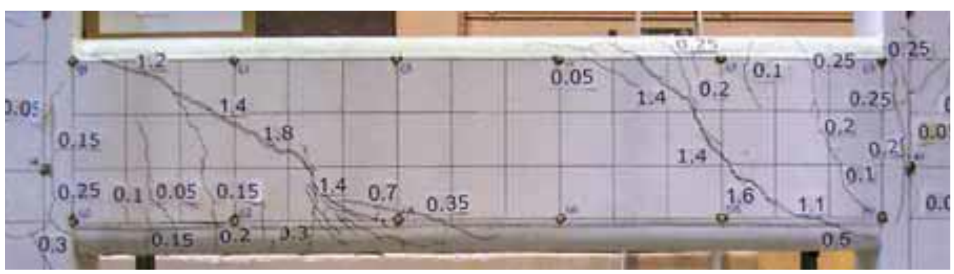
FE Analysis (Magnification Factor: 10)	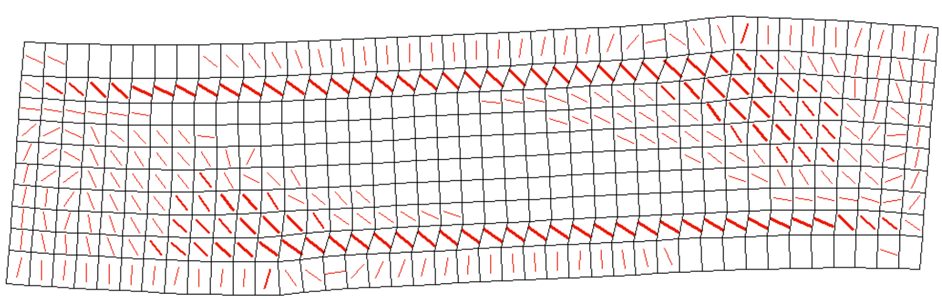

Table A.3 Crack pattern of the Duong frame first-storey beam (continued)

Displacement of 45 mm in forward cycle	
Model Beam Front View	
Model Beam Back View (Reversed)	
Prototype Beam	
FE Analysis (Magnification Factor: 10)	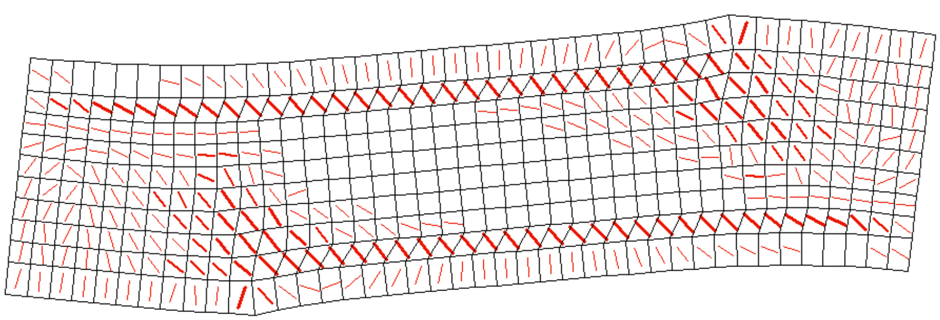

Table A.3 Crack pattern of the Duong frame first-storey beam (continued)

Displacement of 25 mm in backward cycle	
Model Beam Front View	
Model Beam Back View (Reversed)	
Prototype Beam	
FE Analysis (Magnification Factor: 10)	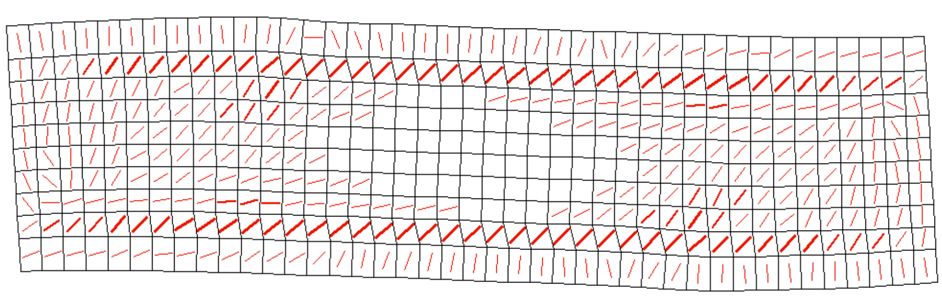

Table A.3 Crack pattern of the Duong frame first-storey beam (continued)

<table>
<tr><td colspan="2">Displacement of 35 mm in backward cycle</td></tr>
<tr><td>Model Beam
Front View</td><td>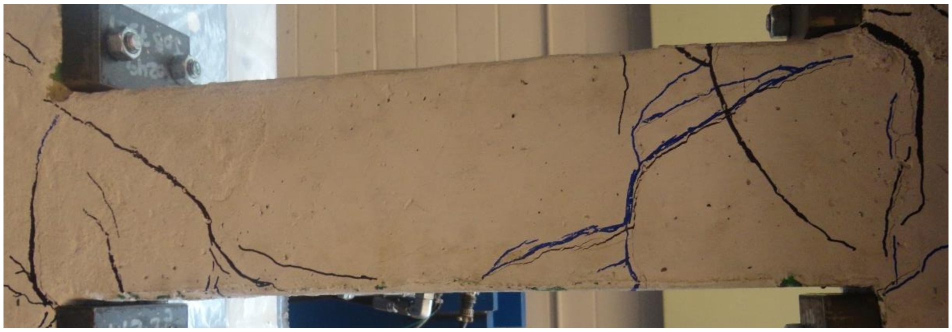</td></tr>
<tr><td>Model Beam
Back View (Reversed)</td><td></td></tr>
<tr><td>Prototype Beam</td><td>Not Reported</td></tr>
<tr><td>FE Analysis
(Magnification Factor: 10)</td><td>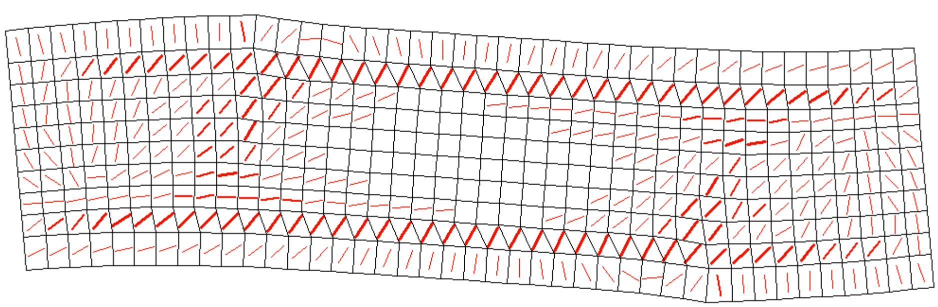</td></tr>
</table>

Table A.3 Crack pattern of the Duong frame first-storey beam (continued)

Displacement of 40 mm in backward cycle	
Model Beam Front View	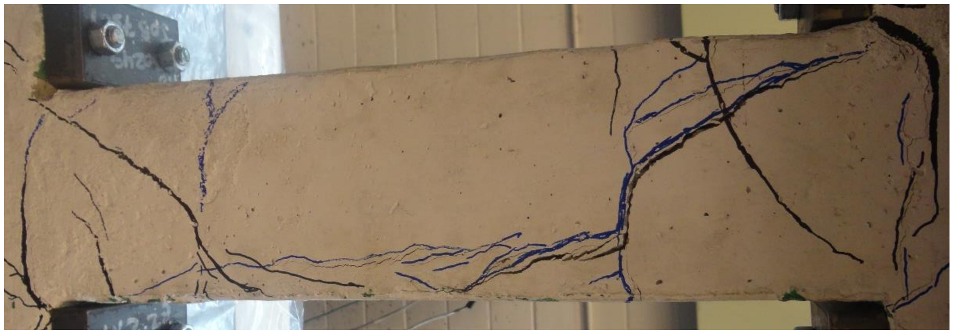
Model Beam Back View (Reversed)	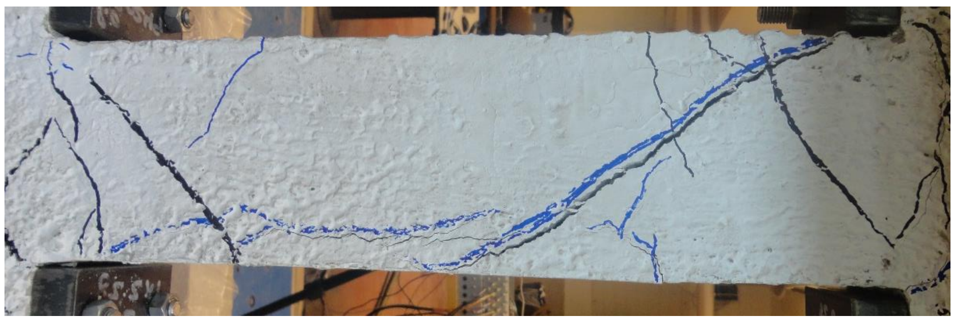
Prototype Beam	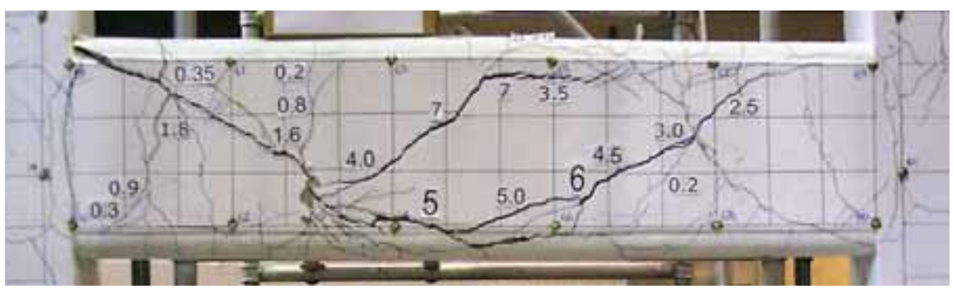
FE Analysis (Magnification Factor: 10)	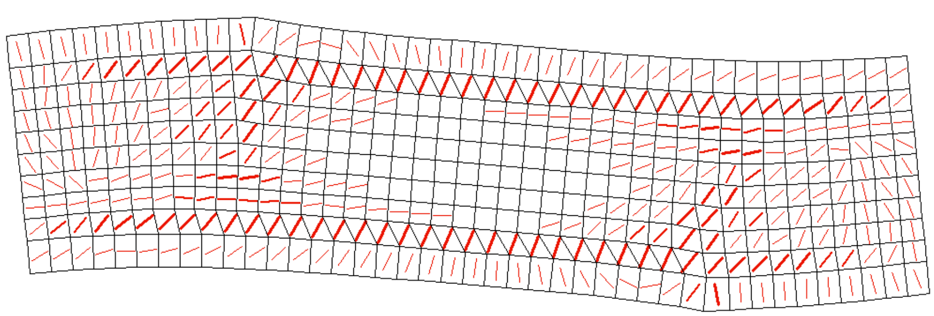

APPENDIX B

AN EXAMPLE OF COMMAND AND MEASURED DISPLACEMENTS

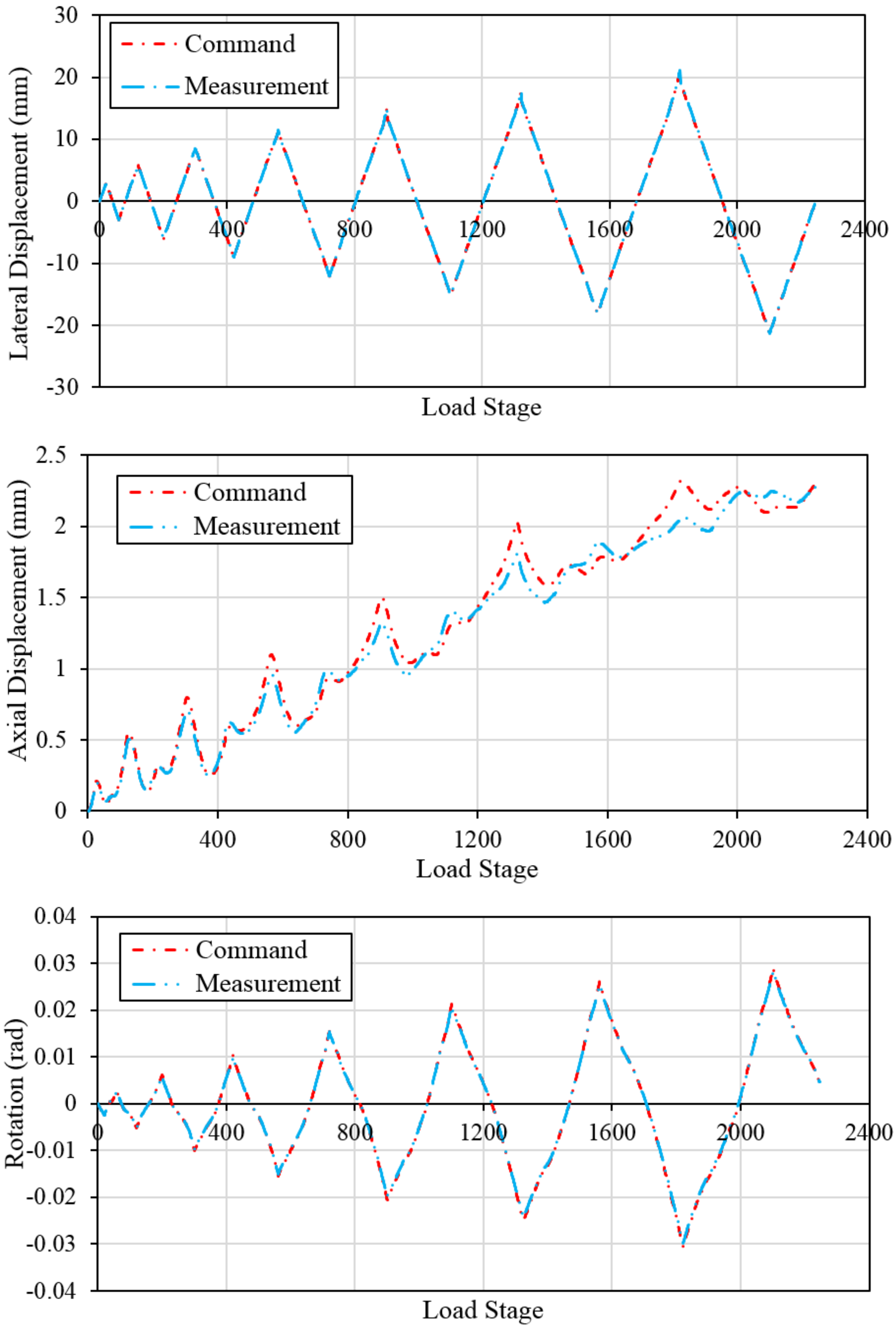

Figure B.1 Command and measured scaled displacements for flexural-critical one-storey frame

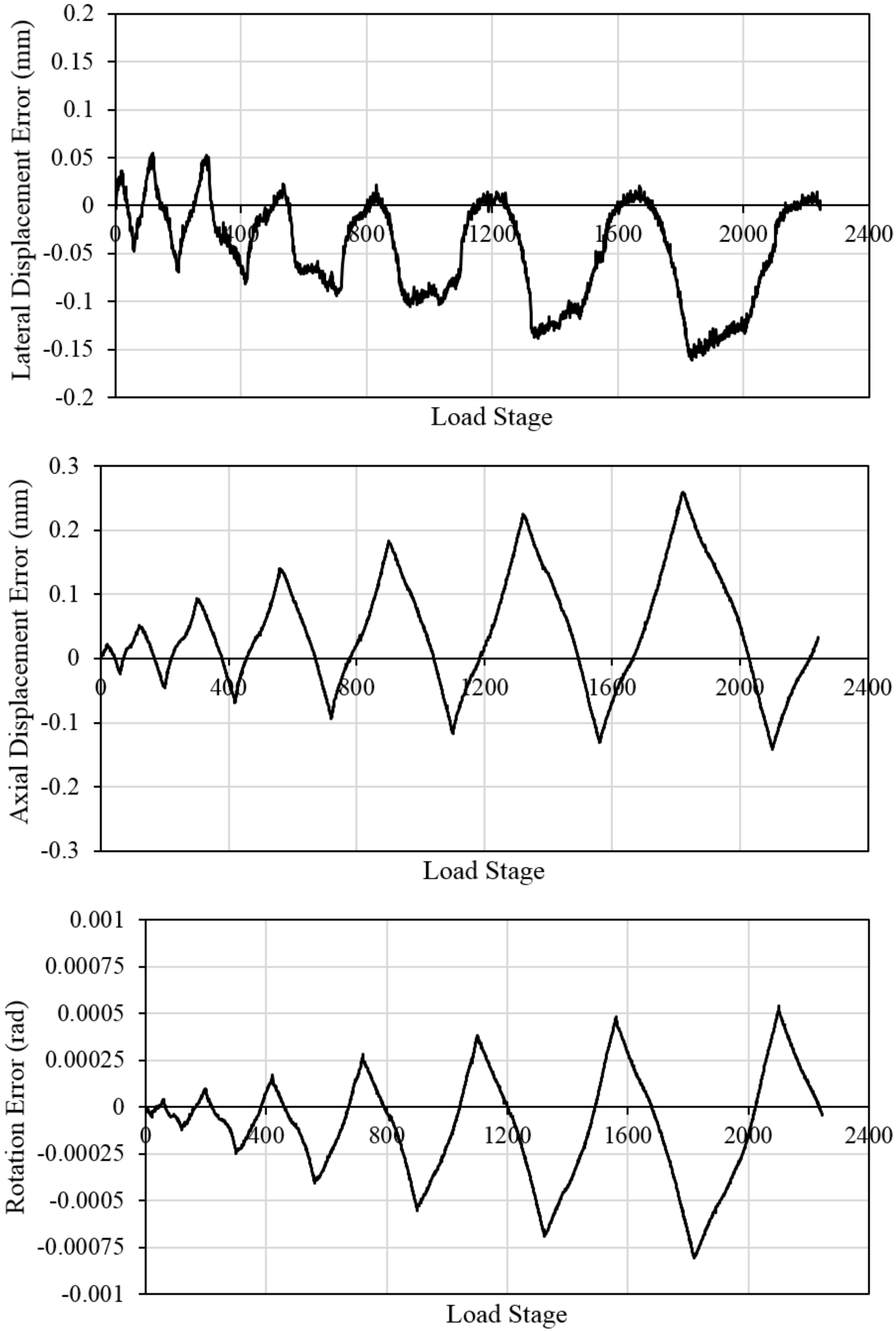

Figure B.2 Displacement errors for flexural-critical one-storey frame